UNIVERSITAT POLITÈCNICA DE CATALUNYA

Escola Tècnica Superior

d'Enginyeria de Camins, Canals i Ports de Barcelona

Institut Flumen – CIMNE

PhD Dissertation

SPACEBORNE SAR IMAGERY FOR MONITORING THE INUNDATION IN THE DOÑANA WETLANDS

Author:

Belén Martí-Cardona

Advisor:

Dr. Josep Dolz Ripollés

Co-advisor:

Dr. Carlos López Martínez

Dissertation submitted to obtain the degree of

DOCTOR OF PHILOSOPHY
BY THE UNIVERSITAT POLITÈCNICA DE CATALUNYA

CIVIL ENGINEERING PROGRAM

Barcelona, April 2014

To Adrià, Miguel, Juan and Santiago,
my Ph.D. in love and life

▪ ABSTRACT

Doñana wetlands, located in Southwest Spain, undergo yearly cycles of inundation in fall and drying out during the spring season. As for any wetland ecosystem, the Doñana's sustainability depends critically on its water resources. Important monitoring and modeling efforts have been made since the 1990's in order to assess the ecosystem health, to partially restore the Doñana's natural hydrologic scheme, to estimate threats associated to nearby socio-economic activities and climate change, and to design adaptation strategies for ensuring its sustainability.

This PhD dissertation inscribes within those efforts. Numerous satellite images of Doñana marshes were requested between 2006 and 2010 in order to obtain regional, synoptic observations of the inundation evolution. The final aim was to further current knowledge of the wetland's hydrology and to calibrate the existing two-dimensional hydraulic model of the marshes. A high observation frequency was of special interest during the marshes filling period, when rainfall is more frequent and hydrodynamic phenomena happen faster. The images were acquired by the C-band radar sensor ASAR, on board the Envisat satellite of the European Space Agency. The C-band capacity to penetrate clouds was particularly suitable to observe the flooding process, since this is associated to overcast weather. The ASAR images were ordered at six different incidence angles so as to increase the observation frequency, and most of them in HH/VV polarization configuration.

A detailed observation of the wetland filling up was achieved during the 2006-2007 hydrologic cycle. Backscattering temporal signatures of the main land cover types in Doñana were derived for this year and for the different available incidence angles and polarizations. The signatures were analyzed with the aid of ground-truth data in order to identify the effect of flooding on the backscattering coefficient. Conclusions on the feasibility to discriminate emerged versus flooded land were drawn for the different incidence angles, land cover types and phenological stages: Intermediate incidence angles (ASAR IS3 and IS4) came up as the most appropriate single swaths to discriminate open water surface in the marshland deepest areas. Flood mapping in pasture lands, the most elevated regions, is feasible at steep to mid incidence angles (ASAR IS1 to IS4). In the medium elevation zones, colonized by large helophytes, shallow incidence angles (ASAR IS6 and IS7) enable more accurate flood delineation during the vegetation growing phase

up to approximately mid-April, when the penetration capacity at these swaths might become insufficient.

Due to the complex casuistic of the Doñana covers' backscattering, flood mapping from a single ASAR acquisition often resulted unfeasible. Flood mapping was then tackled by the synergistic use of the ASAR scenes with the Doñana's digital terrain model and vegetation map. The use of irregular filtering neighborhoods adapted to the topography drastically improved the ASAR image filtering, since natural edges tend to follow terrain contours. Next, clustering and classification algorithms using ASAR data together with the elevation and vegetation maps were designed. These algorithms operate independently on the different Doñana's sub-basins because the pixels elevation is more accurately related to the cover classes within them. Vegetation and elevation maps plus the acquired knowledge of Doñana's backscattering characteristics were initially used to select seed pixels with high confidence on their class membership. Then, a region growing algorithm extends the seed regions with new pixels based on their planimmetric adjacency and backscattering distance to the seeds.

Frequent flood mapping from the ASAR scenes enabled the identification of several events for the calibration of the marshes hydraulic model. This research work also revealed other target information enclosed in the radar backscattering, such as the helophyte vegetation developmental degree or the capacity to discriminate among certain plant communities.

Learnings from this research are expected to be applied and furthered with upcoming polarimetric data of the Doñana wetland from the C-band Sentinel-1 constellation and Radarsat-2 satellite, the L-band ALOS-2/PALSAR-2 system and the X-band future Spanish mission PAZ.

- **RESUMEN**

Las marismas de Doñana, situadas en el suroeste de la Península Ibérica, experimentan ciclos anuales de inundación en otoño y secado en primavera. Como en cualquier humedal, la sostenibilidad de Doñana depende críticamente de sus recursos de agua. Desde la década de los noventa se han realizado importantes esfuerzos de monitorización y modelación para evaluar la salud del ecosistema marismeño y restaurar en lo posible su régimen hidrológico natural, para prever riesgos derivados de las actividades socio-económicas próximas y del cambio climático, y para diseñar estrategias de adaptación que garanticen su sostenibilidad.

La presente tesis doctoral forma parte de estos esfuerzos. Entre los años 2006 y 2010 se encargó la adquisición expresa de numerosas imágenes satelitales de Doñana con el objeto de obtener observaciones regionales y sinópticas de la evolución de la superficie inundada en el humedal. Con estas observaciones se pretendía avanzar en el conocimiento de la hidrodinámica de las marismas y calibrar el modelo hidráulico bidimensional de las mismas. Lograr una frecuencia de observación elevada durante el llenado de las marismas fue un requisito de especial interés, pues es durante este período cuando la lluvia es más abundante y los procesos hidrodinámicos suceden a mayor velocidad. Las imágenes fueron adquiridas por el sensor radar en banda C ASAR, a bordo del satélite Envisat de la Agencia Espacial Europea. La capacidad de la banda C para atravesar la cobertura nubosa resultó particularmente apropiada para monitorizar con detalle el proceso de llenado, ya que éste se halla asociado a la presencia de nubes. Las imágenes ASAR se solicitaron en siete ángulos de incidencia diferentes para incrementar la frecuencia de observación y la mayoría de ellas fueron adquiridas con la configuración de polarizaciones HH/VV.

Durante el año hidrológico 2006-2007 se consiguió una monitorización detallada del proceso de llenado. Para este ciclo se elaboraron signaturas temporales de los principales tipos de cubiertas en Doñana, en los distintos ángulos de incidencia y polarizaciones disponibles. Las signaturas se analizaron con la ayuda de datos de verdad-terreno para identificar el efecto de la inundación sobre el coeficiente de retrodispersión y se extrajeron conclusiones sobre la posibilidad de discriminar superficies emergidas e inundadas en función del ángulo de incidencia, tipo de cobertura vegetal y fase fenológica: ángulos de incidencia intermedios, como los IS3 e IS4 de ASAR, resultaron ser los más apropiados para discriminar en una única imagen superficies de agua libre. La cartografía

de inundación en los paciles, las regiones más elevadas, es factible usando ángulos reducidos y medios (entre IS1 e IS4 de ASAR). En las zonas de elevación intermedia, colonizadas por grandes helófitos, los ángulos de incidencia elevados (IS6 e IS7 de ASAR) permiten una delimitación de la inundación más precisa durante el desarrollo de la vegetación hasta aproximadamente mediados de abril, cuando la capacidad de penetración de estos ángulos puede resultar insuficiente.

Dada la compleja casuística de la retrodispersión de las cubiertas de Doñana, a menudo resultó inviable delinear la inundación en toda la marisma a partir de una única adquisición de ASAR. La cartografía de inundación se abordó entonces mediante el uso sinérgico de los datos ASAR con el modelo digital del terreno y el mapa de vegetación de Doñana. El uso de entornos de procesado irregulares adaptados a la topografía mejoró drásticamente el filtrado de las imágenes, ya que los bordes naturales tienden a seguir las curvas de nivel del terreno. A continuación se diseñaron algoritmos de agrupación y clasificación de píxeles que utilizan los datos ASAR junto con la cota del terreno y el mapa de vegetación, y que se aplican independientemente en las distintas subcuencas de Doñana, porque dentro de ellas existe una relación más precisa entre la cota de los píxeles y la clase de cubierta. Los mapas de elevación y vegetación, más el conocimiento adquirido sobre las características de retrodispersión de Doñana se utilizaron inicialmente para escoger píxeles germen o de origen con elevada confianza en su clase de pertenencia. A continuación, un algoritmo iterativo extiende las regiones germen, incorporando los píxeles adyacentes que son además próximos en distancia de retrodispersión.

La cartografía frecuente de inundación a partir de las escenas ASAR permitió identificar distintos eventos de calibración para el modelo hidrodinámico de las marismas de Doñana. Esta investigación también puso de manifiesto que la retrodispersión radar aporta datos adicionales sobre el estado de las marismas, como es el grado de desarrollo de las especies helófitas o la capacidad de discriminar ciertas comunidades vegetales.

Es de desear que los conocimientos derivados de este estudio puedan ser aplicados y extendidos con los datos polarimétricos de Doñana que serán adquiridos en breve por modernos radares satelitales. Se trata del sensor canadiense Radarsat-2 y de la constelación europea Sentinel-1, ambos operando en banda C, del sistema japonés ALOS-2/PALSAR-2, en banda L, y de la futura misión española PAZ, en banda X.

▪ RESUM

Els aiguamolls de Doñana, situats al sud-oest de la Península Ibèrica, experimenten cicles anuals d'inundació a la tardor i d'assecament a la primavera. Com en qualsevol zona humida, la sostenibilitat de Doñana depèn fonamentalment dels seus recursos hídrics. Des de la dècada dels noranta s'han portat a terme importants esforços de seguiment i modelització per a avaluar la salut de l'ecosistema i restaurar tant com sigui possible el seu règim hidrològic natural, per a preveure riscos derivats de les activitats sòcio-econòmiques i del canvi climàtic, i per a dissenyar estratègies d'adaptació que garanteixin la seva sostenibilitat.

La present tesi doctoral forma part d'aquests esforços. Entre 2006 i 2010 s'encarregà l'adquisició expressa de nombroses imatges satel·litals de Doñana amb l'objecte d'obtenir observacions regionals i sinòptiques de l'evolució de la superfície inundada als aiguamolls. Amb aquestes observacions es pretenia avançar en el coneixement de la hidrodinàmica del conjunt humit i calibrar el model hidràulic bidimensional del mateix. Aconseguir una freqüència d'observació elevada durant l'ompliment dels aiguamolls fou un requisit d'especial interès, ja que durant aquest període la pluja és més abundant i els processos hidrodinàmics són més ràpids. Les imatges foren adquirides pel sensor radar en banda C ASAR, a bord del satèl·lit Envisat de l'Agència Espacial Europea.

La capacitat de la banda C per a travessar la nuvolositat resultà particularment adient per a monitoritzar en detall el procés d'ompliment, ja que aquest està associat amb la presència de núvols. Les imatges ASAR se sol·licitaren en set angles d'incidència diferents per a augmentar la freqüència d'observació, i la majoria d'elles foren adquirides amb la configuració de polaritzacions HH/VV.

Durant l'any hidrològic 2006-2007 s'aconseguí un seguiment detallat del procés d'ompliment. Per a aquest cicle es desenvoluparen signatures temporals dels principals tipus de cobertes de Doñana, en els diferents angles d'incidència i polaritzacions disponibles. Les signatures s'analitzaren amb l'ajuda de dades de veritat-terreny per a identificar l'efecte de la inundació en el coeficient de retrodispersió i s'extragueren conclusions sobre la possibilitat de discriminar superfícies emergides i inundades en funció de l'angle d'incidència, tipus de cobertura vegetal i fase fenològica: angles d'incidència intermitjos, com els IS3 i IS4

d'ASAR, resultaren ser els més apropiats per a discriminar superfícies d'aigua lliure en una sola imatge. La cartografia d'inundació als paciles, les regions més elevades, és factible utilitzant angles d'incidència reduïts i intermitjos (entre IS1 i IS4 d'ASAR). En les zones d'elevació intermèdia, colonitzades per grans helòfits, els angles d'incidència grans (IS7 i IS6 d'ASAR) permeten una delimitació de la inundació més precisa durant el desenvolupament de la vegetació fins a aproximadament mitjans d'abril, quan la capacitat de penetració d'aquests angles pot resultar insuficient.

Donada la complexa casuística de la retrodispersión de les cobertes de Doñana, la cartografia d'inundació dels aiguamolls sencers a partir d'una sola imatge ASAR fou sovint inviable. Aquesta cartografia s'abordà llavors mitjançant l'ús sinèrgic de les dades ASAR amb el model digital del terreny i el mapa de vegetació de Doñana. L'ús d'entorns de processat irregulars adaptats a la topografia millorà dràsticament el filtrat de les imatges, ja que les vores naturals tendeixen a seguir les corbes de nivell del terreny. Seguidament es dissenyaren algoritmes d'agrupació i classificació de píxels que utilitzen dades ASAR, la cota del terreny i el mapa de vegetació, i que s'apliquen independentment a les diferents sub-conques de Doñana, perquè a dins d'elles existeix una relació més acurada entre la cota dels píxels i el tipus de coberta. Els mapes d'elevació i vegetació, més el coneixement adquirit sobre les característiques del retrodispersió de Doñana s'utilitzaren inicialment per a seleccionar píxels germen o d'origen amb elevada confiança en la seva classe de pertinença. A continuació, un algoritme iteratiu expandeix les regions germen, incorporant-hi els píxels adjacents que són, a més a més, propers en distància de retrodispersió.

La cartografia freqüent d'inundació a partir de les escenes ASAR permeté identificar diferents esdeveniments de calibració per al model hidrodinàmic dels aiguamolls de Doñana. Aquest treball de recerca també posà de manifest que la retrodispersión radar aporta dades addicionals sobre l'estat dels aiguamolls, ara com el grau de desenvolupament de les espècies helòfites o la capacitat de discriminar certes comunitats vegetals.

És d'esperar que els coneixements derivats d'aquest estudi puguin ser aplicats i ampliats amb les dades polarimètriques de Doñana que seran adquirides properament per moderns radars satel·litals: es tracta del sensor canadenc Radarsat-2 i de la constel·lació europea Sentinel-1, ambdós operant en banda C, del sistema japonès ALOS-2/PALSAR-2, en banda L, i de la futura missió espanyola PAZ, en banda X.

▪ ACKNOWLEDGEMENTS

To express my gratitude to the people and organizations that have been key for the completion of this PhD dissertation, I would like to go back to the year 2004. I was studying a Master of Science in water resources management at the University of California funded by the fellowship program of the Obra Social la Caixa. That adventure diverted my professional trajectory from the numerical modeling of water resources towards the application of remote sensing techniques in the same field. I will always be grateful to the Obra Social la Caixa for making that possible.

Having just arrived in California, I did not know what remote sensing was. On the first day of the second quarter, I ran into Javier, a Spanish student who was also undertaking graduate studies. He said that he was going to the presentation of a course on remote sensing. This was not on my lengthy list of pre-selected courses to complete that quarter, but for some reason I decided to attend the presentation with Javier. The Earth surface images that I saw that day and their application potential captivated me to the point of restructuring my schedule in order to accommodate the remote sensing course. After that first one, I took other courses in remote sensing and GIS. Afterwards, Professor Schladow gave me the opportunity to use optical and thermal images to complete the end-of-master article. I would like to acknowledge the wonderful freedom offered by the University of California to graduate students for customizing their master programs. I would also like to give special thanks to Professor Schladow for his confidence that allowed me to apply the newly acquired knowledge of remote sensing.

Back in Barcelona, I wrote an email to Professor Josep Dolz, Director of the Institut Flumen and advisor of this thesis, whom I knew from my undergraduate studies at the Civil Engineering School of the Universitat Politècnica de Catalunya. Still convinced that Flumen would be interested in my experience in hydraulics, I slipped the phrase remote sensing into the picture. Josep Dolz is one of those people capable of being aware of diverse technical and social worlds, as well as finding connections and synergies among them. Josep had references on remote sensing, which I imagine were filed as potentially interesting in his mind. After learning that I had studied that discipline, Josep decided to take a chance on remote sensing in Flumen. My deepest gratitude to Josep Dolz for the risk he took to open a new research line at Flumen and, especially, for the confidence he placed in me and has continued to keep over the years. In a civil engineering department, my

main occasion for contact and interaction with the remote sensing field has been conferences. Josep Dolz encouraged and facilitated my attendance to these events.

My next appreciation goes to Carlos López Martínez, co-advisor of this doctoral thesis. Carlos is a world-renowned expert in radar polarimetry. When, in the boldness of our ignorance, we decided to use SAR images for the purpose of observing the Doñana marshes, we turned to Carlos for technical advice. Far from treating us as intruders in a particularly technical field, Carlos has always shown interest in our applications and has been constantly accessible and collaborative. Carlos also gave me temperance and confidence when I worried about the fickleness and caprice of the actual data against the soft elegance of the theoretical curves.

I must dedicate a special thanks to the research staff of the Estación Biológica de Doñana: to Javier Bustamante and Ricardo Díaz-Delgado for their scientific advice and the opportunity to participate with them in two research projects. These projects represented a unique opportunity to interact with experts in the botany and ecology of the marshes' ecosystem. This interaction gave me perspective on the potential contribution of our work with SAR images for the purposes of conservation in Doñana. Many thanks to David Aragonés, always on the other end of the phone and many emails, who provided me with ancillary data that has been essential for the execution of this study. Thanks also to Rocío Fernández and Isabel Afán for kindly responding to my inquiries. My gratitude to Fernando Ibáñez who provided me, on several occasions, with the peculiar means of transportation needed in Doñana: the tame, yet mischievous horses for traveling long distances along the flooded marshland, as well as the fantastic Santana 4x4 with which we crossed sand dunes and immersed in thick waters to levels that I'd rather not reveal. And my sincere acknowledge to the ranger from the Estación Biológica, Alfredo Chico, who accompanied me for long hours in the marshes.

Of great importance has been the collaboration with the Espacio Natural de Doñana. Carlos Urdiales provided us with specific knowledge and data very useful for this job. Abel Valero and Diego García enthusiastically participated in the hydrodynamic modeling and monitoring of the Doñana flood extent evolution. They also walked beside me great distances along the muddy marshland, not allowing extreme temperatures, thirst, or hungry mosquitoes to falter their friendly mood at any time.

I must say the same about my Flumen colleagues who suffered from my eagerness for exploration at least once: Quim, Anaïs, Gabriel and Kat – thank you guys! I was lucky to be able to count on you and I hope that time makes us forget the weariness of those days, leaving the residue of that life experience in a privileged environment.

The complicity and affection of my doctoral colleagues at the Institut Flumen has been equally important: Marina, Hans, Rodrigo, Sole, Georgina, Irene, Klaudia, Úrsula, Jose Luís, Jordi, both Carlos, Eduard, Edu, Gonzalo, Jannette, Gabriel, Kat. Beyond our mutual technical support, I enjoyed their friendship and conversations around the tupperware. During the long time that I couldn't see an end to this work, or even trust that one existed, my colleagues have been the indispensable moral support for the long-distance runner. Hopefully, I can provide the same support for you guys one day, too. My gratitude, as well, to my Flumen colleagues who are not in the PhD student offices, but close enough to make us always feel their support for the team: Ernest, Martí, Manuel, Cesca, Cèlia, Juan and Daniel.

I sincerely acknowledge Professor Juan José Egozcue for our long instructive talks on spatial statistics. Thank you very much to Vicente and Juan for their altruist IT and programming assistance, and to Alberto, who kindly helped me test his SAR data filter on my ASAR scenes. I also wish to dedicate an affectionate thanks to Graeme and Kenton for their kind advice on English writing.

▪ AGRADECIMIENTOS

Para expresar mi gratitud a las personas y entidades que han sido claves en la realización de esta tesis doctoral, desearía retroceder hasta el año 2004. Por aquel entonces cursaba un Master of Science sobre gestión de recursos de agua en la University of California, gracias al programa de ayudas para estudios en el extranjero de la Obra Social "la Caixa". Aquella aventura cambió mi trayectoria profesional de la modelación numérica de recursos de agua hacia la aplicación de la teledetección en el mismo campo. A la Obra Social "la Caixa" estaré siempre agradecida por posibilitarme la realización de dichos estudios.

Recién llegada a California, no sabía lo que era la teledetección. El día en que comenzaban las asignaturas del segundo trimestre tropecé con Javier, un estudiante español que también cursaba estudios de postgrado. Me dijo que iba a la presentación de la asignatura Remote Sensing. Ésta no figuraba en mi dilatada lista de asignaturas preseleccionadas para completar el trimestre. Pero por alguna razón decidí acompañar a Javier a la presentación. Las imágenes de la superficie de la Tierra que vi aquel día y las posibilidades de aplicación de las mismas me cautivaron hasta el punto de reestructurar los horarios del trimestre para dar cabida a la asignatura de teledetección. Tras esta asignatura, tomé otros cursos en teledetección y GIS. Y el Prof. Schladow me brindó la oportunidad de usar imágenes ópticas y térmicas para completar el artículo final de máster. Aquí desearía reconocer la maravillosa libertad que ofrece la University of California a los alumnos de postgrado para la confección de planes de estudio a medida. Y quisiera agradecer también al Prof. Schladow su confianza, que me permitió comenzar a aplicar los conocimientos de teledetección recientemente adquiridos.

De vuelta en Barcelona escribí un correo electrónico al profesor Josep Dolz, director de esta tesis, al que conocía desde mis estudios de grado en la Escola Tècnica Superior d'Enginyeria de Camins, Canals i Ports de la Universitat Politècnica de Catalunya. Aún convencida de que el perfil que podía interesar a Flumen, su grupo de investigación, era mi lado hidráulico, deslicé la palabra teledetección en aquel correo. Josep Dolz es una de aquellas personas capaces de percatarse de mundos diversos, técnicos y sociales, y de hallarles conexiones y sinergias. Josep tenía referencias sobre la teledetección, que imagino estaban archivadas en su mente con la etiqueta de interés potencial. Y tras leer que había aprendido sobre esta disciplina decidió dar una oportunidad a la teledetección en Flumen. Mi más profundo agradecimiento a Josep Dolz por el riesgo que asumió al abrir

una nueva línea de investigación en su grupo, y especialmente por la confianza que depositó en mí y que ha mantenido durante estos años. Desde un departamento de ingeniería civil, mi principal oportunidad de contacto e interacción con el mundo de la teledetección han sido los congresos. Josep Dolz no sólo no me negó nunca la asistencia a congresos, sino que siempre me animó a participar y facilitó mi asistencia a los mismos.

Mi siguiente agradecimiento es para Carlos López Martínez, co-director de la tesis doctoral. Carlos es un reconocido experto mundial en polarimetría radar. Cuando, en el atrevimiento de nuestra ignorancia, decidimos utilizar imágenes SAR para los objetivos de observación de las marismas de Doñana, acudimos a Carlos en busca de asesoramiento técnico. Lejos de tratarnos como osados aprendices de una disciplina particularmente técnica, Carlos se ha mostrado siempre accesible, colaborativo e interesado por nuestras aplicaciones. Carlos me ha aportado además templanza cuando me preocupaba por la volubilidad y capricho de los datos reales frente a la suavidad de las curvas teóricas.

Debo dedicar un agradecimiento especial al personal investigador de la Estación Biológica de Doñana: a Javier Bustamante y a Ricardo Díaz-Delgado por su asesoramiento científico y por la posibilidad de participar con ellos en dos proyectos de investigación. Estos proyectos supusieron una ocasión extraordinaria para interactuar con expertos en la botánica y ecología del ecosistema marismeño. Esta interacción me proporcionó perspectiva sobre la contribución potencial nuestro trabajo con imágenes SAR para los fines de conservación en Doñana. Muchísimas gracias a David Aragonés, siempre al otro lado del email y del teléfono para facilitarme datos auxiliares que han sido esenciales en la ejecución de este estudio. También a Rocío Fernández e Isabel Afán, por responder amablemente a mis consultas. Mi sincero agradecimiento para Fernando Ibáñez quién me facilitó en diversas ocasiones los peculiares medios de transporte necesarios en Doñana: los caballos mansos, pero también experimentados y traviesos, para recorrer largas distancias por la marisma inundada. Y también los fantásticos vehículos Santana 4x4, con los que atravesé dunas de arena y me sumergí en charcos con el agua hasta niveles que prefiero no revelar. Gracias igualmente al guarda de la Estación Biológica Alfredo Chico que me acompañó durante largas jornadas por la marisma.

Muy importante ha sido la colaboración con el Espacio Natural de Doñana: Carlos Urdiales nos aportó conocimientos específicos y datos de gran utilidad para este trabajo. Abel Valero y Diego García participaron con entusiasmo en los trabajos de modelación hidrodinámica y de seguimiento de la inundación en Doñana, y caminaron a mi lado

decenas de kilómetros por la marisma, sin que las temperaturas extremas, la sed o los mosquitos hambrientos menguaran en ningún momento su excelente humor.

Y lo mismo he de decir de los compañeros de Flumen, que sufrieron en algún momento mis ansias de exploración: Quim, Anaïs, Gabriel y Kat. Gracias chicos! Fuí afortunada de contar con vuestra compañía y espero que el tiempo haga olvidar el cansancio de aquellas jornadas y deje el poso de la experiencia vital en un entorno privilegiado.

Igualmente importante ha sido para mí la complicidad y afecto de mis compañeros doctorandos del Institut Flumen: Marina, Hans, Rodrigo, Sole, Georgina, Irene, Klaudia, Úrsula, José Luís, Jordi, los dos Carlos, Eduard, Edu, Gonzalo, Jannette, Gabriel, Kat. Más allá del soporte técnico que nos intercambiamos, he disfrutado de su amistad y de sus conversaciones entorno a la fiambrera. Durante el largo tiempo en que no vi una meta clara para este trabajo, y ni siquiera confié en que ésta existiera, mis compañeros han sido el soporte moral imprescindible para el corredor de larga distancia. Ojalá pueda daros algún día ese apoyo a vosotros también. Mis gracias sinceras también a los que estáis más allá de la oficina de doctorandos, pero suficientemente cerca para hacernos sentir vuestro respaldo de equipo: Ernest, Martí, Manuel, Cesca, Cèlia, Juan, Daniel y Beniamino.

Al profesor Juan José Egozcue de la UPC le agradezco francamente nuestras charlas tendidas sobre estadística espacial, con las que ganó mi admiración. Muchísimas gracias a Vicente y a Juan por su altruista ayuda informática, y a Alberto, quien me ayudó a probar su filtro para imágenes polarimétricas con mis imágenes ASAR. También deseo dedicar un afectuoso agradecimiento a Graeme y Kenton por su amable asistencia en la redacción en lengua inglesa.

TABLE OF CONTENTS

INDEX OF FIGURES

24

Formerly a marginal land, it became during the 20th century the battle field where developmental economic and romantic conservationist arguments came into a clash. In this land it has been possible to substantiate that not everything has a price and that not all prices, even if affordable, should be paid.

Cristina Narbona, 2005

Chapter 1:
Introduction

1.1   *Doñana National Park Wetlands*

The Doñana wetlands are located in the Southern Spanish region of Andalucía, on the right bank of the Guadalquivir River, near its mouth on the Atlantic Ocean coast (Fig. 1.1). The wetlands occupy an area of 31,145 ha and constitute the core part of the Doñana complex fluvial-coastal ecosystem, which extends over 108,087 ha.

The great diversity of the Doñana biotopes holds a significant number of mammal, reptile amphibian, fish and insect species, along with about 900 plant species (García-Novo and Marín-Cabrera, 2005; Ramos and Soriguer, 2002; Rodríguez, 2002; Cobo et al., 2002; Fernández et al., 1994; Rivas-Martínez et al., 1980). Especially significant is Doñana's ornithological value: the site is located on an important bird migration route between Europe and Africa, and it is estimated that over five hundred thounsand waterfowls of about 200 species pass through this region every year (Máñez and Garrido, 2002; Butler, 2008).

In 1969, 54,252 ha of the Doñana ecosystem, including the marshland area, were declared National Park. Surrounding areas totaling 53.835 ha were protected under the status of Natural Park in 1989. Both, National and Natural Parks, were designated as a single environmental entity named *Espacio Natural de Doñana* for management purposes in 2006, which is since then responsibility of the Consejería de Medio Ambiente of the Junta de Andalucía (Andalusian Government).

Doñana has been internationally recognized by different environmental protection treaties and programmes, and catalogued as:

- Biosphere Reserve under UNESCO's Man and the Biosphere Programme (1981);
- Wetland of international importance, Ramsar Covention (1982);
- Zone for the Special Protection of Birds (ZEPA, 1988);
- UNESCO's World Heritage site (1994)

Additionally, the zone hosts the natural monuments of the Asperillo cliff, the Acebuches (wild olive trees) of El Rocío and the Centenarian Pine Tree of Mazagón.

Fig. 1.1. Location of the Espacio Natural de Doñana and its wetlands: a) Espacio Natural de Doñana (hatched in green) within the Spanish region of Andalucía; b) Doñana wetlands (hatched in blue) within the Espacio Natural de Doñana (delineated by a green line). Adapted from Urdiales et al., 2010.

1.2 Background. Why this Thesis?

Water supply is the primary strategic basis for the sustainability of any wetland ecosystem. Hence, wetland conservation, management, and restoration necessarily involve monitoring its hydrologic system.

From the beginning of the 19th century until the middle of the 20th numerous anthropogenic transformations seriously altered the natural hydrologic scheme of the Doñana basin and therefore the sustainability of its valuable wildlife habitat. Several reaches of the Guadalquivir River were channelized, dykes built and terrains poldered for navigation and irrigation purposes (Plan Almonte-Marismas).The locally called "cortas" or shortcut channels, aimed at facilitating maritime transportation up to Seville, reduced the navigation distance between this city and the Guadalquivir mouth by 50 km. The most relevant corta for Doñana's hydrology, the Corta Fernandina, was built in 1815 and detached the Brazo de la Torre watercourse from the Guadalquivir River, impeding the latter's flow contribution to the marshes (Urdiales et al., 2010; Menanteau, 1984).

On the other hand, the intensive agricultural occupation of the site during the 20th century reduced the marshes area to one third of its natural extent: from approximately 185,000 ha at the beginning of the 19th century to 31,145 ha at present (Fig. 1.2; Urdiales et al., 2010; Menanteau, 1984).
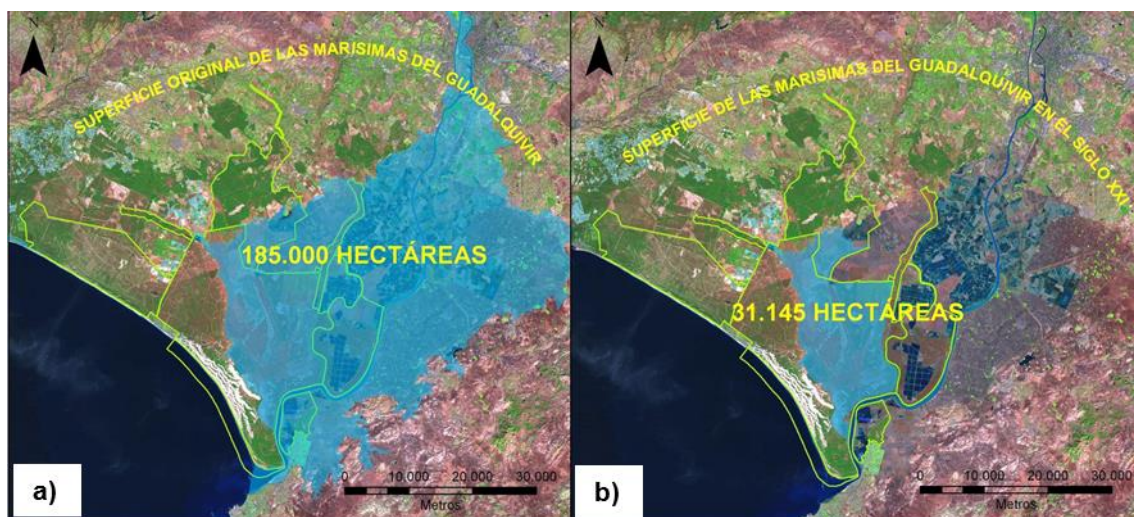
Fig. 1.2. Doñana marshes extent in 1800 (a) and in 2010 (b). Source: Urdiales et al., 2010.

The severe degradation of Doñana's marshland environment gave rise to an initial hydrological restoration project in the 1980's: the *Plan de Regeneración Hídrica de Doñana*. This project prioritized recovering the volume of water discharged into the

marshes versus other hydrological aspects which, according to some authors, led to the excessive inundation of elevated zones (Urdiales et al., 2010; Rodríguez-Ramírez, et al., 2005).

In April 1998, the Aznalcollar dam failure released 5 million tons of mining pollution into the Guadiamar River, tributary of the National Park. The existing levee between Doñana and the Guadalquivir River was then lengthened, and the marshes became completely detached from the Guadalquivir and Guadiamar river inflows. At this point the maximum transformation of Doñana's natural hydrologic scheme was reached. In terms of water inflows, the marshes had gone from a fluvial-tidal-pluvial system into basically a pluvial one (Dolz and Velasco, 1990; Rodríguez-Ramírez et al., 2005).

Following the Aznalcollar accident, the Spanish Ministry of the Environment promoted the ambitious project called *Doñana 2005* (Saura et al., 2001) aimed at the restoration of the marshes natural hydrologic scheme. This project has become the framework for all water related actions in Doñana's basin. Within the Doñana 2005 framework, the Institut Flumen of the Universitat Politècnica de Catalunya was commissioned to develop a two-dimensional hydrodynamic model of the marshes (Bladé and Gómez, 2006). Once calibrated, the model would provide the Park's authorities with a reliable tool for the prediction of the wetland response to proposed restoration actions within Doñana's basin. At present the Institut Flumen is also developing a hydrologicl model of the basin, for the simulation of the flows discharged into the marshes after a rainfall event.

A network of five permanent gauging stations was installed and operated in Doñana marshes by the Institut Flumen from 2004 to 2010 (Ramos Fuertes, 2012). These stations took continuous meteorological and hydraulic measurements for the monitoring of water-related processes and for the calibration of the hydrodynamic model. However, given the extreme flatness of the marshes terrain (Ibáñez, 2008), hydrodynamic phenomena are essentially two-dimensional. Slight changes of the water surface shape, such as those induced by sustained winds, can cause the flooded surface to advance or retreat hundreds of meters (Martí-Cardona et al., 2012; Ramos Fuertes et al., 2013). The area affected by these phenomena cannot be captured by the one-dimensional point data obtained at the gauging stations. Thus, the rigorous understanding of the two-dimensional hydrodynamic processes and the calibration of the corresponding model necessitated a more synoptic approach, with regional observations of the wetland flood extent at different instants of the hydrologic year.

The exploration of remote sensing techniques as a tool for the regional and periodic observation of the marshes was the starting point of the research work presented in this document. An assessment of the available satellite sensors (Martí-Cardona and Dolz, 2005) pointed to the Advanced Synthetic Aperture Radar (ASAR), on board the Envisat satellite of the European Space Agency (ESA, 2006), as being the most suitable instrument for monitoring the Doñana's flood evolution. ASAR proved particularly suitable because the detailed observation of the inundation process, when water velocities and hydrodynamic phenomena are faster, was of particular interest for the calibration of the numerical model. This process is rapid and coincides with overcast weather. ASAR's C-band microwave radiation can penetrate cloud cover, haze and even rainfall, so the sensor was able to collect data under almost all weather conditions. Additionally, ASAR's pointable capability enabled up to 14 image acquisitions of the site per 35-day orbit cycle. Thus, ASAR was capable to provide the required frequent observations of the Doñana marshes during the flooding process.

The PhD thesis developed throughout this document focuses on the use of Envisat/ASAR images to produce frequent flood maps of the Doñana wetlands. Initially, polarimetric backscattering characteristics of the Doñana's land cover types are thoroughly analyzed for the different ASAR incidence angles and phenological stages of the marshes (Martí-Cardona et al., 2010). Algorithms are then developed for the effective filtering of the images and for combining the ASAR data with ancillary spatial information in order to derive the flood maps (Martí-Cardona et al., 2013).

Frequent mapping of the inundation extent, together with the data from the network of gauging stations, furthered our understanding of Doñana's water dynamics and enabled the identification of several events for the calibration and validation of the marshes hydraulic model. Furthermore, this research work revealed other target information enclosed in the radar backscattering, and therefore other potential applications of the SAR data for the monitoring of the Doñana wetland ecosystem, such as the assessment of the helophyte vegetation development or the discrimination between plant communities.

1.3   Basic Concepts of Radar Remote Sensing

This section presents some general concepts of radar remote sensing with the aim to facilitate the comprehension of the rest of the document to the reader unfamiliar with this technique.

The term radar originates from the acronym of "RAdio Detection And Ranging". Imaging radars, on board aircrafts or satellites, emit pulses of electromagnetic radiation that illuminate an area on the Earth surface and measure the backscattered signal. The pulses are sent out orthogonally to the flight or azimuth direction, and at an angle to the vertical direction, referred to as the **incidence angle** (Fig. 1.3).

The radar system records the **time delay** between the transmission and the echo reception, as well as the **amplitude** and **phase** of the reflected signal. The time delay between the emission and reception determines the distance to the target. The amplitude is related to the amount of power reflected by the target. As the sensor's platform moves, the collection of successive backscattered signals enables the construction of a two-dimensional image of the Earth surface.

Synthetic aperture radar (SAR) systems modulate the frequency of the emitted pulses and exploit the echo Doppler effect, consequence of the platform-target relative movement, for greatly increasing the spatial resolution of the images.

(a) Propagation of one radar pulse (indicating the wavefront location at time intervals 1–17)

(b) Resulting antenna return
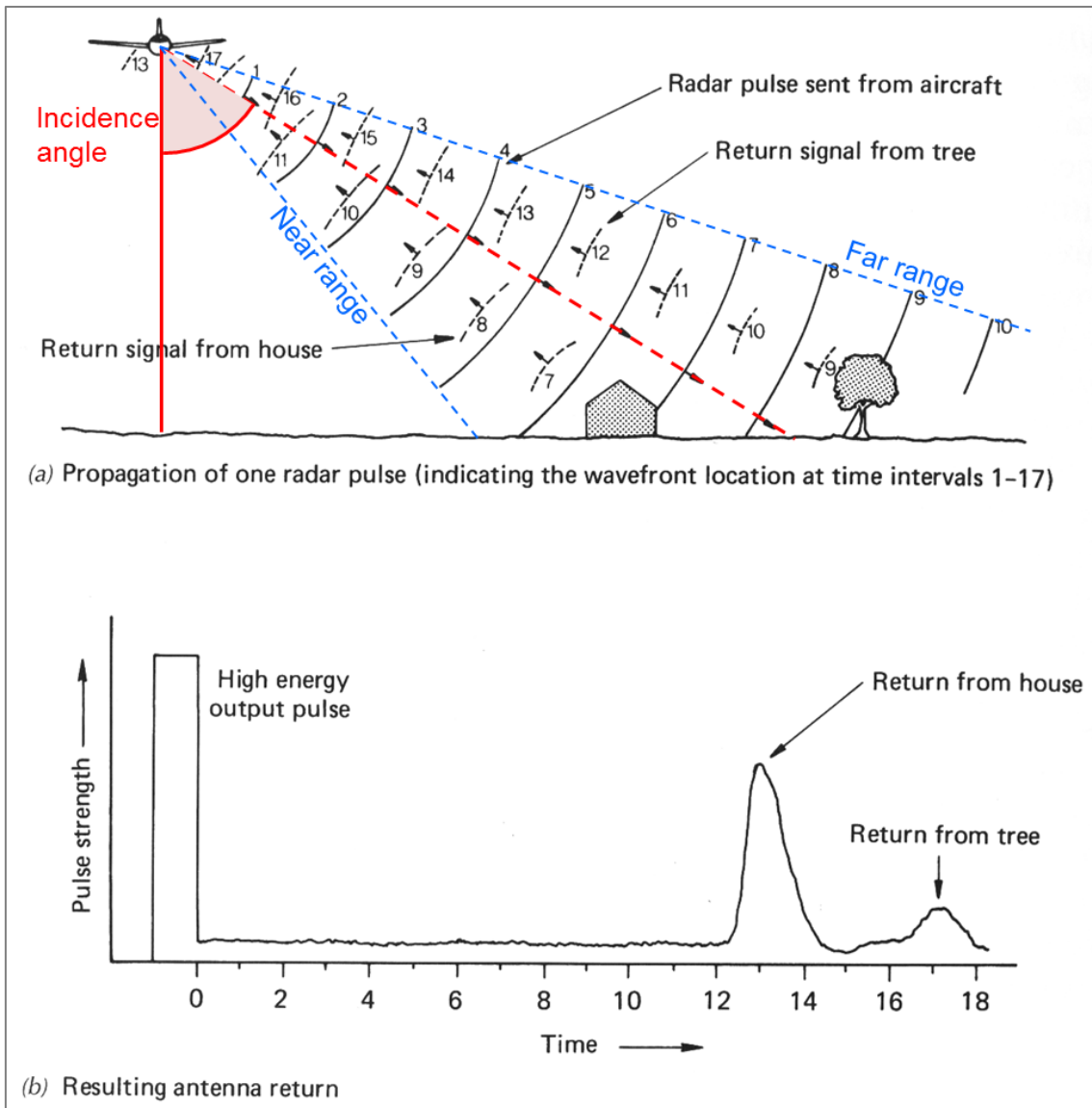
Fig. 1.3. The radar image acquisition.

Radar frequencies: the microwaves

The frequencies used by the radar systems correspond to the microwave region of the electromagnetic spectrum, which encompasses wavelengths between 1 mm and 1 m approximately. This region is sub-divided into narrower bands named with letters, as indicated in Fig. 1.4.

Since radars provide their own source of illumination, they can acquire images during the day and night, indistinctly. On the other hand, thanks to their relatively long wavelengths, microwaves are capable to penetrate clouds, fog, aerosols and, in most cases, rainfall. Hence, radar images can be acquired at any time, and under almost any weather condition.
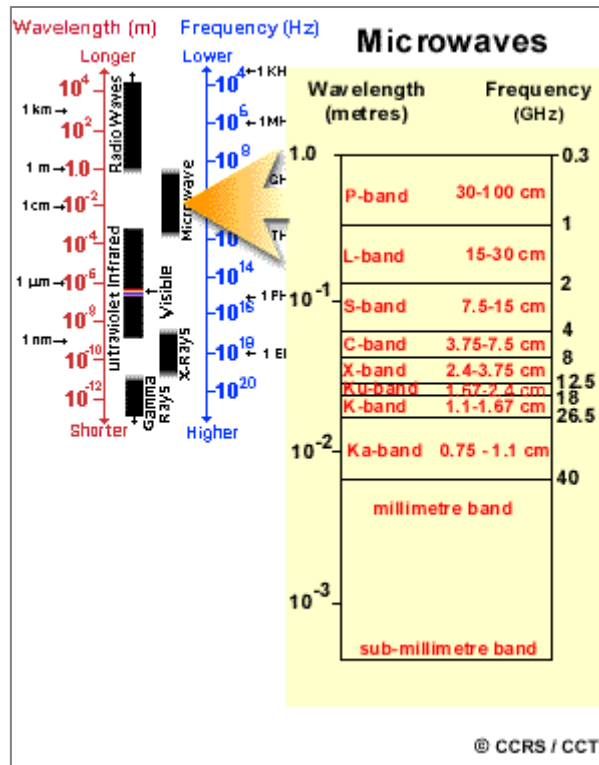
Fig. 1.4. The microwave spectral region and sub-bands.

Polarization

In an electromagnetic wave, the electric and magnetic fields oscillate in perpendicular directions, both orthogonal to the direction of propagation (Können, 1985). By convention, the polarization of the electromagnetic wave refers to the orientation of the electric field (IEEE Standards Board, 1993). Most radar systems emit and receive microwaves whose electric fields oscillate in a single plain (linearly polarized radiation), typically in the vertical (V) and horizontal (H) plain. These waves are referred to as vertically and horizontally polarized, respectively. Depending on the polarization of the emitted and received signal, the radar polarization configuration is designated as: **VV** and **HH** (like-polarization), and **HV** and **VH** (cross-polarization). For monostatic radars such as the Envisat/ASAR instrument, HV and VH data are equivalent.

The science of acquiring, processing and analyzing the polarization state of an electromagnetic wave is known as **polarimetry**. In radar applications, the differential behavior of the polarizations is used to characterize the target (Kostinski and Boerner, 1986; Lee and Pottier 2009; Mishchenko et al., 2011).
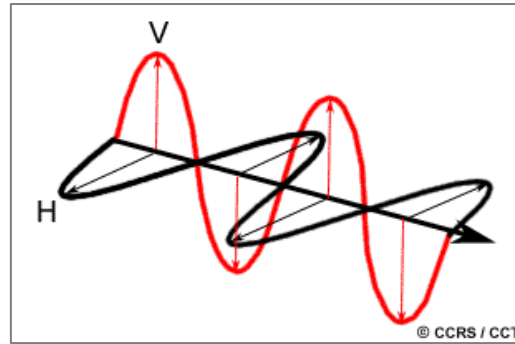
Fig. 1.5. Vertical and horizontal polarization.

<u>Main factors governing the radar backscattering:</u>

The radar backscattering depends on the system acquisition configuration and on the target characteristics.

- **Acquisition parameters:**

The backscatter from a given target depends on the radar frequency band (e.g. C, X, L, etc.), and on the incidence angle and polarization of the radar pulse. SAR images obtained with different combinations of those acquisition parameters can yield different and complementary information of the same area.

- **Target characteristics:**

In natural environments, the radar backscatter is largely controlled by the land surface roughness, the terrain dielectric constant and the vegetation structure. The radar signal increases with the complex dielectric constant of the scattering surface. This constant measures a material's capacity to conduct the electric current in the microwave region, and depends to a great extent on its moisture content. Thus, in general, the higher the soil moisture, the brighter it appears on a SAR image. On the other hand, the backscatter from open water and bare soil areas of similar moisture content depends basically on their surface roughness magnitude in relation to the radar wavelength and incidence angle. If the acquisition parameters are fixed, the microwave backscattering increases with the surface roughness. The polarization state of the backscattered signal usually provides information of the vegetation canopy structure. Vertically polarized radiation, for example, interacts to a larger extent with vertically oriented elements such as trunks or stalks, while the cross-polarized signal is often indicative of multiple reflections within the vegetation volume and related to its biomass (Fig. 1.6).
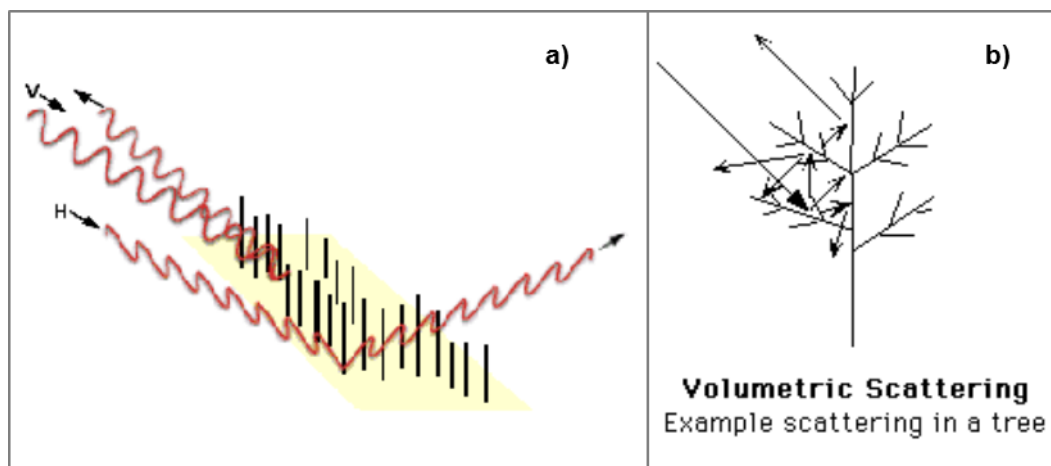
Fig. 1.6. Schematic of the interaction between the polarized microwave radiation and the vegetation canopy: a) the vertically polarized waves interact more strongly with vertical elements than the horizontally polarized ones; b) multiple scattering within a vegetation volume. Adapted from ESA, 2006.

Speckle

Speckle refers to the granular noise appearing in SAR images. It is caused by the constructive and destructive interference of waves reflected from the numerous elementary scatterers within every image resolution cell (Goodman, 1976; Oliver and Quegan 2004). The speckle noise greatly complicates the SAR images interpretation, segmentation and classification.

1.4   References

Bladé, E., & Gómez, M. (2006). Modelación del flujo en lámina libre sobre cauces naturales. Análisis integrado en una y dos dimensiones. (E. Bladé & M. Gómez, Eds.). Barcelona: CIMNE.

Butler, J. (2008). A Birdwatching Guide to Doñana. Bloomington, IN: Trafford Publishing.

Cobo, M. D., Sánchez Gullón, E. and García Murillo, P. (2002). Flora y Vegetación. In V. García Canseco (Ed.), Parque Nacional de Doñana (pp. 108–174). Talavera de la Reina: Canseco Editores SL.

Dolz, J., & Velasco, E. (1990). Análisis cualitativo de las cuencas vertientes al Parque Nacional de Doñana. Informe de la Sección de Ingeniería Hidráulica e Hidrológica, Departament d'Enginyeria Hidràulica, Marítima i Ambiental de la Universitat Politècnica de Catalunya, Barcelona.

ESA, 2006. EnviSat ASAR Product Handbook, Issue 2.1, March 2006, European Space Agency.

Fernández, C., Herrera, M., Sánchez, F. J., & Ariza, J. C. (1994). Inventario de las especies de peces del Parque Nacional de Doñana. Biología, ecología y conservación. ICONA.

García-Novo, F., & Marín-Cabrera, C. (2005). Doñana: agua y biosfera. Madrid, España: Confederación Hidrográfica del Guadalquivir, Ministerio de Medio Ambiente.

Goodman, J. W., 1976. Some Fundamental Properties of Speckle, Journal of the Optical Society of America, 66, 11, 1145-1150.

Ibáñez, E. (2008). Validación de Modelos Digitales del Terreno de precisión a partir de datos Láser Escáner Aerotransportado; Aplicación a la Marisma del Parque Nacional de Doñana. PhD dissertation. Universitat Politècnica de Catalunya.

IEEE Standards Board, 1993. IEEE Standard Definitions of Terms for Antennas, IEEE Std 145-1993(R2004), New York, NY: Institute of Electrical and Electronics Engineers, Inc. ISBN 1-55937-317-2.

Können, G. P., 1985. Polarized light in Nature, New York, NY: Cambridge University Press.

Kostinski, B. and Boerner, W. M., 1986. On foundations of radar polarimetry, IEEE Transactions on Antennas and Propagation, vol. AP-34, no. 12, pp. 1395 – 1403.

Lee, J. S. and Pottier, E., 2009. Polarimetric Radar Imaging: From Basics to Applications. Optical Science and Engineering, Boca Ratón, FL: CRC Press, Taylor and Francis Group. ISBN: 1420054988, 9781420054989

Máñez, M., & Garrido, H. (2002). Avifauna. In V. (coord. . García (Ed.), Parque Nacional de Doñana (pp. 231–316). Canseco Editores.

Martí-Cardona, B, Tran, T. D., Bladé-Castellet, E., Dolz-Ripollés, J., Neale, C. M. U., & Cosh, M. H. (2012). ASAR/ENVISAT images for the calibration of the wind hydrodynamic effect on Donana wetlands. Remote Sensing and Hydrology, 352, 459–463.

Martí-Cardona, B., & Dolz, J. (2005). Teledetección de la lámina de agua en la marisma de Doñana. Estudio comparativo de sensores. Flumen Internal Report.

Martí-Cardona, Belen, Dolz-Ripollés, J., & López-Martínez, C. (2013). Wetland inundation monitoring by the synergistic use of ENVISAT/ASAR imagery and ancilliary spatial data. Remote Sensing of Environment, 139, 171–184. doi:10.1016/j.rse.2013.07.028

Martí-Cardona, Belen, López-Martínez, C., Dolz-Ripollés, J., & Bladé-Castellet, E. (2010). ASAR polarimetric, multi-incidence angle and multitemporal characterization of Doñana wetlands for flood extent monitoring. Remote Sensing of Environment, 114(11), 2802–2815. doi:10.1016/j.rse.2010.06.015

Menanteau, L. (1984). Evoluvión histórica y consecuencias morfológicas de la intervención humana en las zonas húmedas: el caso de las marismas del Guadalquivir. (pp. 43–76). Madrid, España: Dirección General de Medio Ambiente, Ministerio de Obras Públicas y Urbanismo.

Mishchenko, M.I., Yatskiv, Y.S., Rosenbush, V.K., and Videen, G., (Eds.), 2011. Polarimetric Detection, Characterization and Remote Sensing, Proceedings of the NATO Advanced Study Institute on Special Detection Technique (Polarimetry) and Remote Sensing Yalta, Ukraine 20 September - 1 October 2010, Series: NATO Science for Peace and Security Series C: Environmental Security.

Narbona, C. (2005). Presentación. In F. García-Novo & C. Marín-Cabrera (Eds.), Doñana: Agua y Biosphera. (pp. 7–8). Madrid: Ministerio de Medio Ambiente.

Oliver, C. and Quegan, S, 2004. Understanding Synthetic Aperture Radar Images, Raleigh, NC: SciTech Publishing Inc.

Ramos, B., & Soriguer, R. C. (2002). Mamíferos. In Parque Nacional de Doñana (pp. 231–316.). Canseco Editores.

Ramos Fuertes, A. (2012). Hidrometeorología y balance térmico de la marisma de Doñana. PhD dissertation. Universitat Politècnica de Catalunya. Retrieved from http://www.tdx.cat/handle/10803/110548

Ramos Fuertes, A., Martí-Cardona, B., Bladé Castellet, E., & Dolz, J. (2013). Envisat/ASAR images for the calibration of the wind drag action in Doñana wetlands 2D hydrodynamic model. Under review. Remote Sensing.

Rivas-Martínez, S., Costa, M., Castroviejo, S., & Valdés, E. (1980). Vegetación de Doñana (Huelva , España). Lazaroa, 2, 5–180.

Rodríguez, E. (2002). Anfibios y reptiles. In V. García (Ed.), Parque Nacional de Doñana (pp. 213–230). Canseco Editores.

Rodríguez-Ramírez, A., Yáñez-Camacho, C., Gascó, C., Clemente-Salas, L., & Antón, M. . (2005). Colmatación natural y antrópica de las marismas del Parque Nacional de Doñana: Implicaciones para su manejo y conservación. Rev. Cuaternario y Geomorfología, 19(3-4), 37–48.

Saura, J., Bayán-Jardín, B., Casas, J., Ruíz, A., & Urdiales, C. (2001). Documento marco para el desarrollo del proyecto Doñana 2005. Regeneración hídrica de las cuencas y cauces vertientes a las marismas del Parque Nacional de Doñana.

Urdiales, C., García, D., Valero, A., & Fernández, J. M. (2010). Seguimiento de la inundación en la marisma de Doñana: resultados del ciclo 2009/2010 y efecto del dique de la Montaña del Río en el proceso de inundación. In J. Ojeda, M. F. Pita, & I. Vallejo (Eds.), (pp. 1146–1156). Sevilla: Secretariado de Publicaciones de la Universidad de Sevilla.

Chapter 2:
Objectives

Numerous Envisat/ASAR images of the Doñana National Park wetlands were ordered between 2006 and 2010 for the completion of this research. The images were collected, processed and analyzed with the aid of ground truth data and diverse ancillary information. In an initial study preceding this research, the first image and field data acquisitions were used to explore the capacity of the SAR satellite images to observe the marshes flood extent in overcast conditions. This initial study determined the most suitable polarization configuration for such observation. Once the capacity of the SAR images to detect flooding in the Doñana wetland was corroborated, frequent Envisat/ASAR acquisitions were ordered over the site in the appropriate polarization configuration and at the seven sensor's incidence angles in order to achieve a high observation frequency.

The main objective of the present research is the use of the Envisat/ASAR imagery to produce flood maps of the Doñana wetlands and to achieve a detailed monitoring of the inundation evolution throughout a hydrologic cycle. Frequent observations of the marshes flood extent, derived from the exhaustive Envisat/ASAR image time series, will further our current knowledge of the hydrologic processes taking place in the site and will provide the spatial data needed to calibrate the existing two-dimensional hydrodynamic model of the wetland. Especial attention is paid to the observation of the filling up process, during the rainy period, because the faster hydrologic phenomena taking place during this period provide valuable spatial calibration data for hydrodynamic modeling purposes.

The presented main research goals are attained through the completion of subsequent tasks with the specific objectives as follows:

➢ The first objective is to characterize and understand the polarimetric, multi-incidence angle and multi-temporal C-band backscattering behavior from the

Doñana's main land cover types, to identify the effect of the inundation on the backscattering coefficient and to assess the feasibility of the ASAR scenes for monitoring the marshes flood extent at the different incidence angles of the sensor.

➢ The subsequent objective consists on developing a tool able to derive flood maps from the ASAR images for different incidence angles and marshes phenological stages. This tool should be applicable to images from different hydrological cycles. It should also be robust enough to capture spatial changes in the vegetation spatial distribution, which might be affected by the on-going hydrologic restorations activities. The developed algorithm will be applied to map the inundation evolution during the 2006-2007 hydrologic year.

➢ Given the hydrodynamic application pursued by this research, an additional goal is to identify hydrologic events appropriate for the calibration of the two-dimensional hydrodynamic model of the Doñana wetlands.

➢ The acquired insight of the Doñana's land cover types backscattering behavior will be used to identify those hydrologic and biophysical characteristics of the wetlands that the C-band SAR data are sensitive to, therefore providing a potential data source.

"It's sort of like sediment of rocks" (regarding technological innovation). "You're building up a mountain and you get to contribute your little layer of sedimentary rock to make the mountain that much higher. People on the surface will stand on it, but no one will see your sediment. It will only be appreciated by that rare geologist".

Steve Jobs, 1994

Chapter 3:
State of the Art

3.1 Introduction

Chapter 3 presents a thorough literature review on the core objective of this research, which is the wetland observation and flood detection from remote sensing SAR images. However, as an applied research, this work made use of multiple concepts and techniques from a wide variety of disciplines such as hydrology, statistics or SAR signal and digital image processing. Amongst these techniques, the speckle filtering of the ASAR images became crucial in order to produce proper flood maps from the satellite scenes. A significant effort was made to achieve accurate speckle filtering and the authors developed a specific filter that best suited the flood mapping goal. Thus, although filtering development was not initially among the research objectives, an examination of the main speckle filtering techniques became compelling and a general review of them is included in Section 3.3 of this chapter.

3.2 SAR Remote Sensing of Wetlands

Radar systems have been used for wetland characterization since the 1970's (Waite and MacDonald, 1971). In addition to their day and night, and all-weather imaging capabilities, SAR systems can provide unique, valuable information on wetland biophysical parameters, such as soil and vegetation moisture (Ballester-Berman et al., 2013; Pierdicca et al., 2009; Hajnsek et al., 2003; Kasischke et al., 2003; Wickel et al., 2001; Ulaby et al.,

---

1986), and vegetation structure, phenology and biomass (López-Sánchez et al., 2014; López-Sánchez et al., 2012; Bouvet et al., 2009; López-Sánchez and Ballester-Berman, 2009; Touzi et al., 2007; Grings et al., 2005; Moreau and Le Toan, 2003; Le Toan et al., 1997; Dobson et al., 1992; Le Toan et al., 1992; Ulaby et al., 1986). The radar signal is also capable to partially penetrate vegetation canopies and detect standing water underneath (Martínez and Le Toan, 2007; Rosenqvist et al., 2002; Ramsey, 1998; Hess et al., 1995; Hess et al., 1990; Richards et al., 1987; Krohn et al., 1983). Moreover, the flatness of the wetlands terrain minimizes undesirable topographic effects on the radar returns. Five review articles by Henderson and Lewis (2008), Ramsey (1998), Schmullius and Evans (1997), Kasischke et al. (1997) and Hess et al. (1990) considering 261 papers from 1965 to 2007 summarize most of the current knowledge concerning radar-wetland interactions. These reviews evidence the complexity of the SAR-wetland relationships, highly influenced by the structure and density of the vegetation in relation to the observation wavelength and incidence angle. Despite this complexity, some generally agreed conclusions of the reviewed papers are gathered as follows:

L-band is considered more appropriate than C and X bands for flood detection in forested wetlands (Bourgeau-Chavez et al., 2001; Costa et al., 1998; Hess et al., 1995; Wang et al., 1995; Hess et al., 1990). The L-band longer wavelength facilitates the penetration of the radar signal through the forest canopy and the interaction with the soil or water surface underneath, while C and X bands returns come primarily from the branches and leaves. The latter wavelengths are better suited for flood mapping in herbaceous marshes (Bourgeau-Chavez et al., 2001; Costa et al., 1998; Pope et al., 1997; Kasischke et al., 1997; Ramsey, 1995). In general for all bands, steep incidence angles favor the radar signal penetration through the canopy, while increases in biomass or incidence angle intensify the signal-canopy interactions to the detriment of penetration (Grings et al., 2005; Costa, 2004; Ramsey, 1998; Costa et al., 1998; Hess et al., 1990). Subcanopy flood detection can be enhanced by the double bounce of the radar waves between trunks and water surface in forests (Martínez and Le Toan, 2007; Ramsey, 1998; Kasischke et al., 1997; Hess et al., 1990; Richards et al., 1987), and between vertical stalks and water surface in herbaceous wetlands (Lang, 2008; Grings et al., 2006; Grings et al., 2005; Kasischke et al., 2003; Parmuchi et al., 2002; Townsend, 2002; Ramsey, 1998; Pope et al., 1997).

Kandus et al. (2001) and Töyrä et al. (2001) suggested a combination of incidence angles: steep ones for subcanopy flooding detection and shallow angles to delineate open water, since wind-roughened water surface can be confused with emerged land at low incidence

angles. Novo et al. (1998) also pointed at the interest of multi-incidence angle imagery to retrieve biophysical parameters of several macrophyte species in the Amazon.

Temporal variability is inherent to most wetland environments. Some authors have advocated the importance of multi-temporal imagery to capture the flood and vegetation temporal patterns, since this information is of great relevance for numerous fields of research and for efficient wetland managing (Henderson and Lewis, 2008; Costa and Telmer, 2006; Kandus et al., 2001; Brown et al., 1996). An L-band imagery time series spanning two years was successfully analyzed by Rosenqvist et all. (2002) to model the spatial and temporal variation of inundation in the Central Brazilian Amazon. A four-year long L-band set was used by Martínez and Le Toan (2007) to monitor the flood extent dynamics and spatial distribution of broad land cover types in the Amazon flood plain. Grings et al. (2005) utilized multi-temporal C-band data to observe and model herbaceous vegetation growth in the Parana River Delta, Argentina. Töyrä and Pietroniro (2005) combined C-band SAR and optical data from 1996 to 2001 to derive a flood duration map of the Peace–Athabasca Delta, in Canada. Kasischke et al. (2003) used 22 C-band scenes over a 25-month period to monitor hydrologic conditions in South Florida wetlands. Nevertheless, despite the cited studies and a few others (Pottier et al., 2012; Marechal et al., 2011; Wang, 2004; Crevier et al., 1996; Morrissey et al., 1996), most research assessing change in wetlands is restricted to image acquisition opportunities and fail to capture temporal patterns.

Several authors have investigated the utility of fully polarimetric SAR data for wetland characterization. Most early studies used data from the NASA's AirSAR and Shuttle Imaging Radar (SIR-C), and from the Canadian Space Agency's Convair 580 (Pope, 1994; Hess, 1995; Pope, 1997; Sokol et al., 1998; Bourgeau-Chavez, 2001). These studies pointed to the phase difference between the horizontal and vertical like-polarizations as the most informative parameter for flood detection in vegetated areas. The launch of satellite sensors with fully polarimetric capabilities, such as the L-band ALOS/PALSAR (Rosenvisq et al., 2004), the X-band TerraSAR (Werninghaus and Buckreuss, 2010) and the C-band RADARSAT-2 (Morena et al., 2004) in 2006 and 2007, signified a breakthrough in the use of polarimetric systems for Earth observation. At present, the SAR data decomposition into the different backscattering mechanisms is considered the most effective method for target characterization (Touzi et al., 2004; Boerner et al., 1998; Cloude and Pottier, 1996). Several studies have applied such decomposition to satellite SAR images for wetland characterization, demonstrating the usefulness of fully polarimetric data for wetland

observation and mapping (Pottier et al., 2012; Marechal et al., 2011; Touzi et al., 2009; Boerner and Yamaguchi, 2008; Touzi et al., 2007). Unfortunately, information such as the target's backscattering mechanisms decomposition or the phase difference between polarizations cannot be obtained from the dual-pol incoherent SAR data used in this work. However, it is fair saying that none of the abovementioned fully polarimetric satellite systems can provide, in fully polarimetric mode, observations of the entire Doñana marshes at the temporal frequency achieved with ASAR.

3.3   Speckle Filtering

As explained in Section 1.3, the speckle refers to the granular noise appearing in SAR images. This noise greatly complicates the SAR images interpretation, segmentation and classification. A considerable number of filters have been proposed to smooth deleterious effects of speckle. Oliver and Quegan (2004), Touzi (2002) or Lee et al. (1994) provide a thorough review of them.

The boxcar or moving averaging window speckle filter is one of the simplest methods, but has the drawback of treating equally homogeneous and heterogeneous regions, hence smearing edges with the subsequent resolution loss. The median (Pratt, 1978) or sigma (Lee, 1983) filters are computationally simple while improving the edge blurring effect, but fail to include and benefit from specific SAR speckle properties (Oliver and Quegan, 2004; Goodman, 1975).

Minimum mean square error (MMSE) methods adapt the filtering degree to the pixel neighborhood homogeneity level, dependent of the on intensity fluctuations within. Three well known MMSE speckle filters, widely implemented in SAR processing software are:
- Lee filter (Lee, 1980), later improved by the refined Lee filter (Lee, 1981);
- Kuan filter (Kuan et al., 1985);
- Frost (Frost et al., 1982).

Other approaches make use of the Bayes criterion to relate the observed pixel intensity to its despeckled value. When this approach assumes knowledge of the intensity probability density function (PDF), it is referred to as the Maximum A Posteriori (MAP) estimate.

Gamma MAP (Lopes et al. 1993) and Gaussian MAP (Kuan et al. 1987) are examples of Bayesian algorithms.

More sophisticated methods apply the filters above in a multi-resolution fashion, adapting the filtering window size and shape to the structural features in the scene. Among these methods it is worth mentioning: the Crimmins filter (Crimmins, 1985), structural Gamma MAP filter (Lopes et al. 1993), refined Lee filter (Lee, 1981), structural multi-resolution MMSE and Frost filters (Touzi, 2002).

A novel multi-scale SAR data filtering technique was proposed by Alonso et al. 2010. The technique relies on a multi-scale representation of the SAR image by means of a Binary Partition Tree (BPT) (Salembier and Garrido, 2000). Filtering and segmentation tasks are carried out jointly by pruning the BPT according to a region homogeneity criterion.

Finally, it is worth mentioning, for the implications in this research, that none of the methods above make use of prior knowledge or ancillary information of the imaged target. They have been developed to be applied on stand-alone SAR images.

3.4   References

Alonso-González, A., López-Martínez, C. and Salembier, P., 2010. *Filtering And Segmentation Of Polarimetric SAR Images With Binary Partition Trees*, IEEE International Geoscience and Remote Sensing Symposium (IGARSS), 25-30 July, Hawaii, 4043-4047.

Ballester-Berman, J. D., Vicente-Guijalba, F. and Lopez-Sanchez, J. M., 2013. *Polarimetric SAR Model For Soil Moisture Estimation Over Vineyards At C-Band*, Progress In Electromagnetics Research, Vol. 142, pp. 639-665.

Boerner, W. -M. and Yamaguchi, Y., 2008. *Recent Advances In POL-SAR & POLIN-SAR Imaging Of Natural Habitats And Wetland Remote Sensing*, IEEE International Conference on Geoscience and Remote Sensing Symposium, 2, 293–294, 7-11 July, Boston, MA, U.S.A: IGARSS 2008.

Boerner, W. M., Mott, H., Luneburg, E., Livingstone, C., Brisco, B., Brown, R. J., Paterson, J. S., Cloude, S. R., Krogager, E., Lee, J. S., Schuler, D. L., Van Zyl, J. J., Randall, D., Budkewitsch, P. and Pottier, E., 1998. *Polarimetry In Radar Remote Sensing: Basic And Applied Concepts*, in Manual of Remote Sensing: Principles and Applications of Imaging Radar, 3, R. A. Ryerson, Ed. Hoboken, NJ: Wiley, ch. 5, 271–356.

Bourgeau-Chavez, l., Kasischke, E., Brunzell, S., Mudd, J., Smith, K. and Frick, A., 2001. *Analysis Of Space-Borne SAR Data For Wetland Mapping In Virginia Riparian Ecosystems*, International Journal of Remote Sensing, 22, 3665–3687.

Bouvet, A., Le Toan, T. and Lam-Dao, N., 2009. *Monitoring Of The Rice Cropping System In The Mekong Delta Using ENVISAT/ASAR Dual Polarization Data*, IEEE Trans. Geosci. Remote Sens., vol. 47, no. 2, pp. 517–526.

Brown, R., Brisco, B., D'Iorio, M., Prevost, C., Ryerson, R. and Singhroy, V., 1996. *RADARSAT Applications: Review Of Globesar Program*, Canadian Journal of Remote Sensing, 22, 404–419.

Cloude, S. R. and Pottier, E., 1996. *A Review Of Target Decomposition Theorems In Radar Polarimetry*, IEEE Transactions on Geoscience and Remote Sensing, 34, 2, 498–518.

Costa, M. and Telmer, K., 2006. *Utilizing SAR Imagery And Aquatic Vegetation To Map Fresh And Brackish Lakes In The Brazilian Pantanal Wetland*, Remote Sensing of Environment, 105, 204–213.

Costa, M., 2004. *Use Of SAR Satellites For Mapping Zonation Of Vegetation Communities In The Amazon Floodplain*, International Journal of Remote Sensing, 25, 1817–1835.

Costa, M., Novo, E., Ahern, E., Mitsuo, E. I. I., Mantovani, J. and Ballester, M., 1998. *The Amazon flood plain through Radar eyes: Lago Grande de Monte Alegre case study*, Canadian Journal of Remote Sensing, 24, 339–349.

Crevier, Y. , Pultz, T. , Lukowski, T. and Toutin, T., 1996. *Temporal Analysis Of ERS-1 SAR Backscatter For Hydrology Applications*, Canadian Journal of Remote Sensing, 22 , 65-77.

Crimmins, T. R., 1985. *Geometric Filter For Reducing Speckle*, Applied Optics, 24, 438-1443.

Dobson, M. C., Ulaby, F. T., Le Toan, T., Beaudoin, A., Kasischke, E. S. and Christensen, N. L., 1992. *Dependence Of Radar Backscatter On Coniferous Forest Biomass*, IEEE Transactions on Geoscience and Remote Sensing, 30, 412–415.

Frost, V. S., Stiles, J. A., Shanmugan, K. S. and Holtzman, J. C., 1982. *A Model For Radar Images And Its Application To Adaptive Digital Filtering Of Multiplicative Noise*, IEEE Transactions on Pattern Analyses and Machine Intelligence, PAMI-4, 157–166.

Goodman, J. W., 1976. *Some Fundamental Properties Of Speckle*, Journal of the Optical Society of America, 66, 11, 1145-1150.

Grings, F. M., Ferrazzoli, P., Jacobo-Berlles, J. C., Karszenbaum, H., Tiffenberg, J. and Pratolongo, P., 2006. *Monitoring Flood Conditions In Marshes Using EM Models And Envisat ASAR Observations*, IEEE Transactions on Geoscience and Remote Sensing, 44, 936–942.

Grings, F., Ferrazzoli, P., Karszenbaum, H., Tiffenberg, J., Kandus, P. and Guerriero, L., 2005. *Modeling Temporal Evolution Of Junco Marshes Radar Signatures*, IEEE Transactions on Geoscience and Remote Sensing, 43, 2238–2245.

Hajnsek, I., Pottier, E. and Cloude, S.R. 2003. *Inversion of Surface Parameters from Polarimetric SAR*, IEEE Transactions on Geoscience and Remote Sensing, 41, 4, 727-745.

Henderson, F. M. and Lewis, A. J., 2008. *Radar Detection Of Wetland Ecosystems: A Review*, International Journal of Remote Sensing, 29, 5809–5835.

Hess, L., Melack, J., Filoso, S. and Wang, Y., 1995. *Delineation Of Inundated Area And Vegetation Along The Amazon Floodplain With The SIR-C Synthetic Aperture Radar*, IEEE Transactions on Geoscience and Remote Sensing, 33, 896–904.

Hess, L., Melack, J. and Simonet, D., 1990. *Radar Detection Of Flooding Beneath The Forest Canopy: A Review*, International Journal of Remote Sensing, 11, 1313–1325.

Jobs, S., 1994. *Steve Jobs on his Legacy*, interview by Silicon Valley Historical Association (http://www.youtube.com/watch?v=zut2NLMVL_kandfeature=player_embedded).

Kandus, P., Karszenbaum, H., Pultz, T., Parmuchi, G. and Bava, J., 2001. *Influence Of Flood Conditions And Vegetation Status On The Radar Backscatter Of Wetland Ecosystems*, Canadian Journal of Remote Sensing, 27, 651–662.

Kasischke, E., Smith, K., Bourgeau-Chavez, L., Romanowicz, E., Brunzell, S. and Richardson, C., 2003. *Effects Of Seasonal Hydrologic Patterns In South Florida Wetlands On Radar Backscatter Measured From ERS-2 SAR Imagery*, Remote Sensing of Environment, 88, 423–441.

Kasischke, E., Melack, J. and Dobson, M., 1997. *The Use Of Radars For Ecological Applications: A Review*, Remote Sensing of Environment, 59, 141–156.

Krohn, D. M., Milton, N. M. and Segal, D. B., 1983. *SEASAT Synthetic Aperture Radar (SAR) Response To Lowland Vegetation Types In Eastern Maryland And Virginia*, Journal of Geophysical Research, 88, 1937–1952.

Kuan, D. T., Sawchuk, A. A., Strand, T. C. and Chavel, P., 1987. *Adaptive Restoration Of Images With Speckle*, IEEE Transactions on Acoustics, Speech and Signal Processing, ASSP-35, 373–383.

Kuan, D. T., Sawchuk, A. A., Strand, T. C. and Chavel, P., 1985. *Adaptive Noise Smoothing Filter For Images With Signal-Dependent Noise*, IEEE Transactions on Pattern Analyses and Machine Intelligence, PAMI-2, 165–177.

Lang, M. W., Kasischke, E. S., Prince, S. D. and Pittman, K. W., 2008. *Assessment of C-band synthetic aperture radar data for mapping and monitoring Coastal Plain forested wetlands in the Mid-Atlantic Region, USA*, Remote Sensing of Environment, 112, 11, 4120-4130.

Le Toan, T., Ribbes, F., Wange, L. F., Floury, N., Ding, N. and Kong, K. H., 1997. *Rice Crop Mapping And Monitoring Using ERS-1 Data Based On Experiment And Modeling Results*, IEEE Transactions on Geoscience and Remote Sensing, 35, 41–56.

Le Toan, T., Beaudoin, A., Riom, J. and Guyon, D., 1992. *Relating Forest Biomass To SAR Data", IEEE Transactions On Geoscience And Remote Sensing*, 30, 403–411.

Lee, J. S., Jurkevicha, L., Dewaeleb, P., Wambacqb, P. and Oosterlinckb, A., 1994*. Speckle Filtering Of Synthetic Aperture Radar Images: A Review*, Remote Sensing Reviews, 8, 4, 313-340.

Lee, J. S., 1983. *A Simple Speckle Smoothing Algorithm For Synthetic Aperture Radar Images*, IEEE Transactions on System Man Cybernetics, 13, 85-89.

Lee, J. S., 1981. *Refined Filtering Of Image Noise Using Local Statistics*, Computer Graphics and Image Processing, 15, 380–389.

Lee, J. S., 1980. *Digital Image Enhancement And Noise Filtering By Use Of Local Statistics*, IEEE Transactions on Pattern Analysis and Machine Intelligence, PAMI-2, 165–168.

Lopes, A., Nezry, E., Touzi, R. and Laur, H., 1993. *Structure Detection And Statistical Adaptive Speckle Filtering In SAR Images*, International Journal of Remote sensing, 14, 1735–1758.

Lopez-Sanchez, J. M., Vicente-Guijalba, F., Ballester-Berman, J. D. and Cloude, S. R., 2014. *Polarimetric Response Of Rice Fields At C-Band: Analysis And Phenology Retrieval*, IEEE Trans. on Geoscience and Remote Sensing, vol.PP, no.99, pp.1,17, doi: 10.1109/TGRS.2013.2268319.

Lopez-Sanchez, J. M., Hajnsek, I. and Ballester-Berman, J. D., 2012. *First Demonstration Of Agriculture Height Retrieval With Polinsar Airborne Data*, IEEE Geoscience and Remote Sensing Letters, Vol. 9, No. 2, pp. 242-246.

Lopez-Sanchez, J. M. and Ballester-Berman, J. D., 2009. *Potentials of Polarimetric SAR Interferometry for Agriculture Monitoring*, Radio Science, Vol. 44, No. 2, doi: 10.1029/2008RS004078.

Martínez, J. and Le Toan, 2007. *Mapping Of Flood Dynamics And Spatial Distribution Of Vegetation In The Amazon Floodplain Using Multitemporal SAR Data*, Remote Sensing of Environment, 108, 209–223.

Moreau, S. and Le Toan, T., 2003. *Biomass Quantification Of Andean Wetland Forages Using ERS Satellite SAR Data For Optimizing Livestock Management*, Remote Sensing of Environment, 84, 477–492.

Morrissey, L. , Durden, S. , Livingston, G. , Stearn, J. and Guild, L., 1996. *Differentiating Methane Source Areas In Arctic Environments With Multitemporal ERS-1 SAR Data*, IEEE Transactions on Geoscience and Remote Sensing, 34, 667-672.

Marechal, C., Pottier, E., Allain-Bailhache, S., Méric, S., Hubert-Moy, L. and Corgne, S., 2011. *Mapping Dynamic Wetland Processes With A One Year RADARSAT-2 Quad Pol Time-Series*, Proceedings of the IEEE International Conference on Geoscience and Remote Sensing Symposium, IGARSS 2011, 24–29 July, Vancouver, 126–129.

Morena, L. C., James, K. V. and Beck, J., 2004. *An introduction to RADARSAT-2 Mission*, Canadian Journal of Remote Sensing, 30, 3, 221–234.

Novo, E. M., Costa, M. F. and Mantovani, J., 1998. *Exploratory Survey On Macrophyte Biophysical Parameters In Tropical Reservoirs*, Canadian Journal of Remote Sensing, 24, 367–375.

Oliver, C. and Quegan, S, 2004. *Understanding Synthetic Aperture Radar Images*, Raleigh, NC: SciTech Publishing Inc.

Parmuchi, M., Karsenbaum, H. and Kandus, P., 2002. *Mapping Wetlands Using Multitemporal RADARSAT-1 Data And A Decision-Based Classifier*, Canadian Journal of Remote Sensing, 28, 175–186.

Pierdicca, N., Pulvirenti, L. and Bignami, C., 2010. *Soil Moisture Estimation over Vegetated Terrains using Multitemporal Remote Sensing Data*, Remote Sensing of Environment, 114, 440–448.

Pope, K., Rejmankova, E., Paris, J. and Woodruff, R., 1997. *Detecting Seasonal Flooding Cycles In Marshes Of The Yucatan Peninsula With SIR-C Polarimetric Radar Imagery*, Remote Sensing of Environment, 59, 157–166.

Pope, K. O., Rey-Benayas, J. M. and Paris, J. F., 1994. *Radar Remote Sensing Of Forest And Wetland Ecosystems In The Central American Tropics*, Remote Sensing of Environment, 48, 2, 205–219.

Pottier, E., Marechal, C., Allain-Bailhache, S., Méric, S., Hubert-Moy, L. and Corgne, S., 2012. *On The Use Of Fully Polarimetric RADARSAT-2 Time-Series Datasets For Delineating And Monitoring The Seasonal Dynamics Of Wetland Ecosystem*, Proceedings of the IEEE International Conference on Geoscience and Remote Sensing Symposium, IGARSS 2012, 23-27 July, Munich, 107-110

Pratt, W. K., 1978. *Digital Image Processing*, New York: Wiley.

Ramsey, E. I., 1998. *Radar Remote Sensing Of Wetlands*, In R. Lunetta, and C. Elvidge (Eds.), Remote sensing change detection: environmental monitoring methods and applications, 211–243, Chelsea, MI: Ann Arbor Press.

Ramsey, E., III, 1995. *Monitoring Flooding In Coastal Wetlands By Using Radar Imagery And Ground-Based Measurements*, International Journal of Remote Sensing, 16, 2495–2505.

Richards, J. A., Woodgate, P. W. and Skidmore, A. K., 1987. *An Explanation of Enhanced Backscattering from Flooded Forest*, International Journal of Remote Sensing, 7, 1093-1100.

Rosenqvist, A., Shimada, M. and Watanabe, M., 2004. *ALOS PALSAR: Technical Outline And Mission Concepts,* 4th International Symposium on Retrieval of Bio- and Geophysical Parameters from SAR Data for Land Applications, Nov. 16-19, Innsbruck, Austria.

Rosenqvist, A., Forsberg, B., Pimentel, T., Rauste, Y. and Richey, J., 2002. *The Use Of Spaceborne Radar Data To Model Inundation Patterns And Trace Gas Emissions In The Central Amazon Floodplain*, International Journal of Remote Sensing, 23, 1303–1328.

Salembier, P. and Garrido, L., 2000. *Binary Partition Tree As An Efficient Representation For Image Processing, Segmentation And Information Retrieval*, 9, 4, 561–576.

Schmullius, C. and Evans, D., 1997. *Synthetic Aperture Radar (SAR) Frequency And Polarization Requirements For Applications In Ecology, Geology, Hydrology, And*

Oceanography: A Tabular Status Quo After SIR-C/X-SAR, International Journal of Remote Sensing, 18, 2713–2722.

Sokol, J., McNairn, H., Pultz, T., Touzi, R. and Livingstone, C., 1998*. Monitoring Wetland Hydrology With Airborne Polarimetric Radar*, in Proceedings of the Canadian Symposium of Remote Sensing, Calgary, AB, Canada, 111–114.

Touzi, R., Deschamps, A. and Rother, G., 2009. *Phase Of Target Scattering For Wetland Characterization Using Polarimetric C-Band SAR*. IEEE Transactions on Geoscience and Remote Sensing, 47, 3241–3261.

Touzi, R., Deschamps, A. and Rother, G., 2007. *Wetland Characterization using Polarimetric RADARSAT-2 Capability*, Canadian Journal of Remote Sensing, 33, 1, S56-S67.

Touzi, R., Boerner, W. M., Lee, J. S. and Luneberg, E., 2004. *A Review Of Polarimetry In The Context Of Synthetic Aperture Radar: Concepts And Information Extraction,*" Canadian Journal of Remote Sensing, 30, 3, 380–407.

Touzi, R., 2002. *A Review Of Speckle Filtering In The Context Of Estimation Theory*, IEEE Transactions on Geoscience and Remote Sensing, 11, 2392–2404.

Touzi, R., Lopes, A., & Bousquet, P. (1988). A statistical and geometrical edge detector for SAR images. IEEE Trans. Geosci. Remote Sensing, 26, 764–773.

Townsend, P. A., 2002. *Relationships Between Forest Structure And The Detection Of Flood Inundation In Forested Wetlands Using C-Band SAR*, International Journal of Remote Sensing, 23, 3, 443-460.

Töyrä, J. and Pietroniro, A., 2005. *Towards Operational Monitoring Of A Northern Wetland Using Geomatics-Based Techniques*, Remote Sensing of Environment, 97, 174–191.

Töyrä, J., Pietroniro, A. and Martz, L. W., 2001. *Multisensor Hydrologic Assessment Of A Freshwater Wetland*, Remote Sensing of Environment, 75, 162–173.

Ulaby, F. T., Moore, R. K. and Fung, A. K., 1986. *Microwave Remote Sensing: Active And Passive III. From Theory To Applications*, Norwood, MA: Artech House.

Waite, W. and MacDonald, H., 1971. *Vegetation Penetration with K-band Imaging Radars*, IEEE Transactions on Geoscience and Remote Sensing, 9, 147–155.

Wang, Y., 2004. *Seasonal Change In The Extent Of Inundation On Floodplains Detected By JERS-1 Synthetic Aperture Radar Data*, International Journal of Remote Sensing, 25, 13, 2497-2508.

Wang, Y., Hess, L. L., Filoso, S. and Melack, J. M., 1995. *Understanding The Radar Backscattering From Flooded And Nonflooded Amazonian Forests: Results From Canopy Backscatter Modeling*, Remote Sensing of Environment, 54, 324–332.

Werninghaus, R. and Buckreuss, S., 2010. *The Terrasar-X Mission And System Design*, IEEE Transactions on Geoscience and Remote Sensing, 48, 2, 606-614.

Wickel, A. J., Jackson, T. J. and Wood, E. F., 2001. *Multitemporal Monitoring Of Soil Moisture With RADARSAT SAR During The 1997 Southern Great Plains Hydrology Experiment*, International Journal of Remote Sensing, 22, 1571–1583.

Water is the blood of the planet. It is always the same water flowing from the sky to the land and from the land to the sky in a continuous cycle, painting landscapes and chiseling living architectures.

Cristina Narbona, 2005

Chapter 4:
Description of the Study Site

4.1. Introduction

Doñana wetlands are located in the Southwest of the Iberian Peninsula, on the colmated paleo-estuary of the Guadalquivir River (Fig. 1.1). The wetlands have an extent of 31,145 ha and constitute a core part of a larger and complex fluvio-coastal ecosystem, which holds multiple environmental protection titles, as explained in Chapter 1. The Doñana's protected areas were declared a single environmental entity named Espacio Natural de Doñana for management purposes in 2006 and they are since then the responsibility of the Andalusian Government.

Literature and on-going research on Doñana is extensive and varied. Doñana is notable for the great diversity of its biotopes, including marshlands, coastal dunes, Mediterranean chaparral, or cork oak and olive tree woodlands, among others (García-Novo and Marín-Cabrera, 2005). Whilst flooded, Doñana marshes create a crucial migration passage, breeding and wintering site for more than 500,000 waterfowl each year, including about 200 bird species (Butler, 2008; Máñez & Garrido, 2002). The park is also home to twelve endangered species of flora and fauna, such as the Iberian imperial eagle (*Aquila adalberti*) and the Iberian lynx (*Lynx pardina*) (Muriel et al., 2012; Perez de Ayala et al., 2011; Palomares et al., 2011; Delibes et al., 1991). From the geomorphological perspective, Doñana's formation history is an exciting account happening at a geologically breathtaking pace and conveying the readers to the Tartesian, Phoenician and Roman ancient civilizations (Rodríguez-Vidal, 2005; Periáñez and Abril, 2013; Bayán Jardín, 2005; Ruiz et al., 2004; Rodriguez-Ramirez et al., 1996).   From the hydrology point of view, the Park's marshes have been an emblem of the confrontation between the 20th century

developmental and conservationist approaches (Urdiales et al., 2010; Bayán Jardín, 2005; Menanteau, 1984).

It becomes evident that Doñana's description can be tackled from the point of view of numerous disciplines. The description included in this chapter focuses on those aspects relevant for the methods developed in the rest of the thesis and for the achievement of the research goals. The description begins with the marshes formation process, which is responsible for the actual marshland morphology and enlightens some of the on-going colmating transformations. Following, Doñana's hydrology and flooding cycles are described, since they are directly related to these research goals. Finally, the close relationship between Doñana's topography, hydroperiod and land cover types is emphasized. This relationship is exploited in ensuing chapters for the ASAR scenes filtering and classification.

4.2. Geomorphology: The Marshes Formation, an On-Going Process

The entire Espacio Natural de Doñana lies within the lower Guadalquivir River basin, a physiographical unit that has undergone dynamic and still active geological processes. Towards the end of the Tertiary Age the lower Guadalquivir basin sank and a deep sea occupied Doñana's current location (Rodriguez-Ramirez et al., 1996; Bayán Jardín, 2005). The accumulation of blue loam and sand deposits throughout the Quaternary period resulted in the formation of the Guadalquivir estuary. Coastal bars were then developed nearby the estuary by eolian sands and marine sediment deposition. The progressive closure of the estuary by the growing coastal bars led to the formation of the Guadalquivir lagoon, known as *Ligur* by the Phoenicians and *Lingustinus* by the Romans (Periáñez and Abril, 2013; Urdiales et al., 2010; Rodríguez-Vidal, 2005; Bayán Jardín, 2005; Ruiz et al., 2004; Rodriguez-Ramirez et al., 1996).

The present marsh environment resulted from continental sediments colmating the lagoon with an upper-most layer of 50 to 100 m thick of fine silts and grey-bluish clays. The tidal influence on the marshes decreased as a consequence of the sediment deposit rise. The on-going colmation process drives Doñana wetlands towards the formation of a large and dry coastal plain, where the sand dunes, currently between the marshland and

the ocean, will advance into the continent (Rodríguez-Vidal, 2005). Such an evolutionary trend, common to most tidal estuaries, can only be modified by anthropogenic activities, or by the sea level rise, as the one resulting from the greenhouse effect.

4.3. Hydrology: Doñana's Annual Flooding Cycles

4.3.1 INFLOWS AND OUTFLOWS IN THE DOÑANA MARSHES

Before the Aznalcollar dam failure, in 1998, the surface areas draining into the Doñana marshes totaled approximately 283,000 ha (Dolz and Velasco, 1990; Urdiales et al., 2010). In 1998 the wetland inflows from the Guadiamar reach were diverted into the Brazo de la Torre in order to prevent the entrance of mining pollution into the National Park. Since then, the Doñana marshes collect the surface waters from a basin of 129,895 ha, represented in Fig. 4.1. The main inflows into the marshes come from direct precipitation and run-off, and from the discharge of the tributaries: La Rocina, El Partido, Cañada Mayor and Guadiamar (Urdiales et al., 2010; Custodio et al., 2006, Fig. 4.2). These streams drain part of Doñana's surface basin, and receive their baseflow from the aquifer system number 27, sub-unity of Almonte-Marismas (Custodio et al., 2008; Suso and Llamas, 1993; Machuca et al., 1992). Such groundwater contribution helps prolong the tributary inflows and the marshes flood duration after the end of the rainy periods.

Of less importance than the abovementioned water sources is the discharge from the sand dunes free aquifer, which can take place directly at the emplacements called "retuertas" (Fig. 4.3), and through the tributaries of Soto Chico y Soto Grande creeks (Casas and Urdiales, 1995). Some inflows are also received from the marshes underlying semi-confined aquifer, through small upwellings locally known as "ojos" (Fig. 4.3 and Fig. 4.4). This contribution is, however, irrelevant for the marshes water balance (Suso and Llamas, 1993).
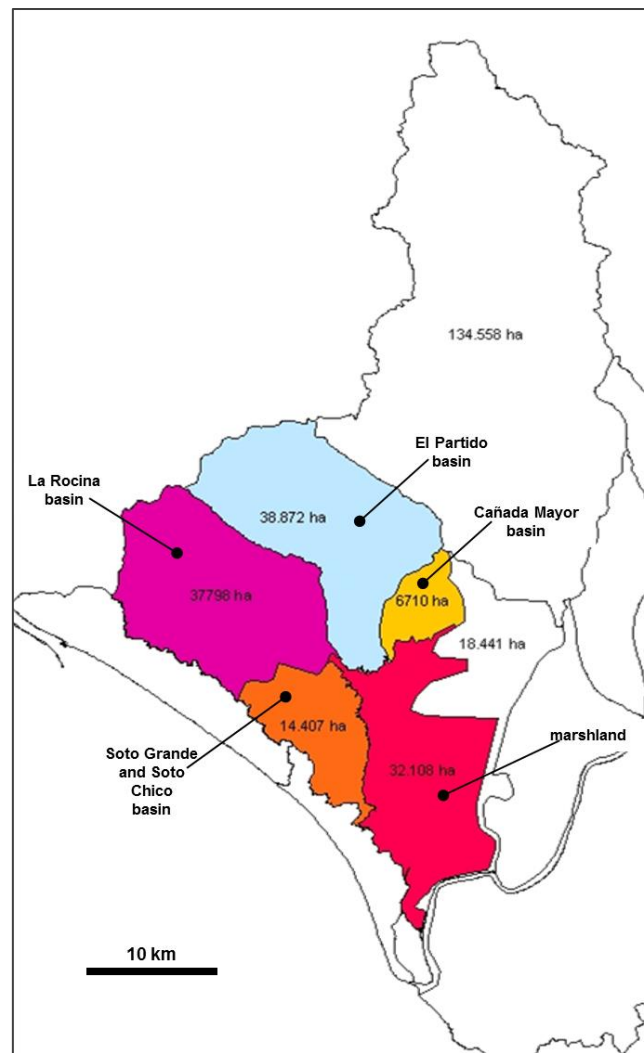
Fig. 4.1. Surface basins draining into Doñana marhes. Map courtesy of Mr. C. Urdiales.

Another way of water exchange takes place through the sluices in the Montaña del Río, the levee detaching the marshes from the Guadalquivir River. The direction of this exchange depends on the relative marshes and river water levels, the latter being mostly driven by the ocean tides. The wind drag action has also been observed to play a role in the flow direction through the Montaña del Río, as discussed in Section 10.6. Again, this flow exchange has a reduced repercussion over the wetland water balance due to the small size of the levee sluices.

Outflows from the marshes are basically caused by evaporation and evapotranspiration. The infiltration losses are negligible due to the impervious clay soil layer covering the marshland (Fig. 4.3; Custodio et al., 2008; Suso and Llamas, 1993; Machuca et al., 1992). The flood stage decrease rate was quantified from continuous in-situ records of water

level as varying linearly from 2 to 27 mm/day between March and July, in absence of precipitation (Ramos Fuertes, 2012).
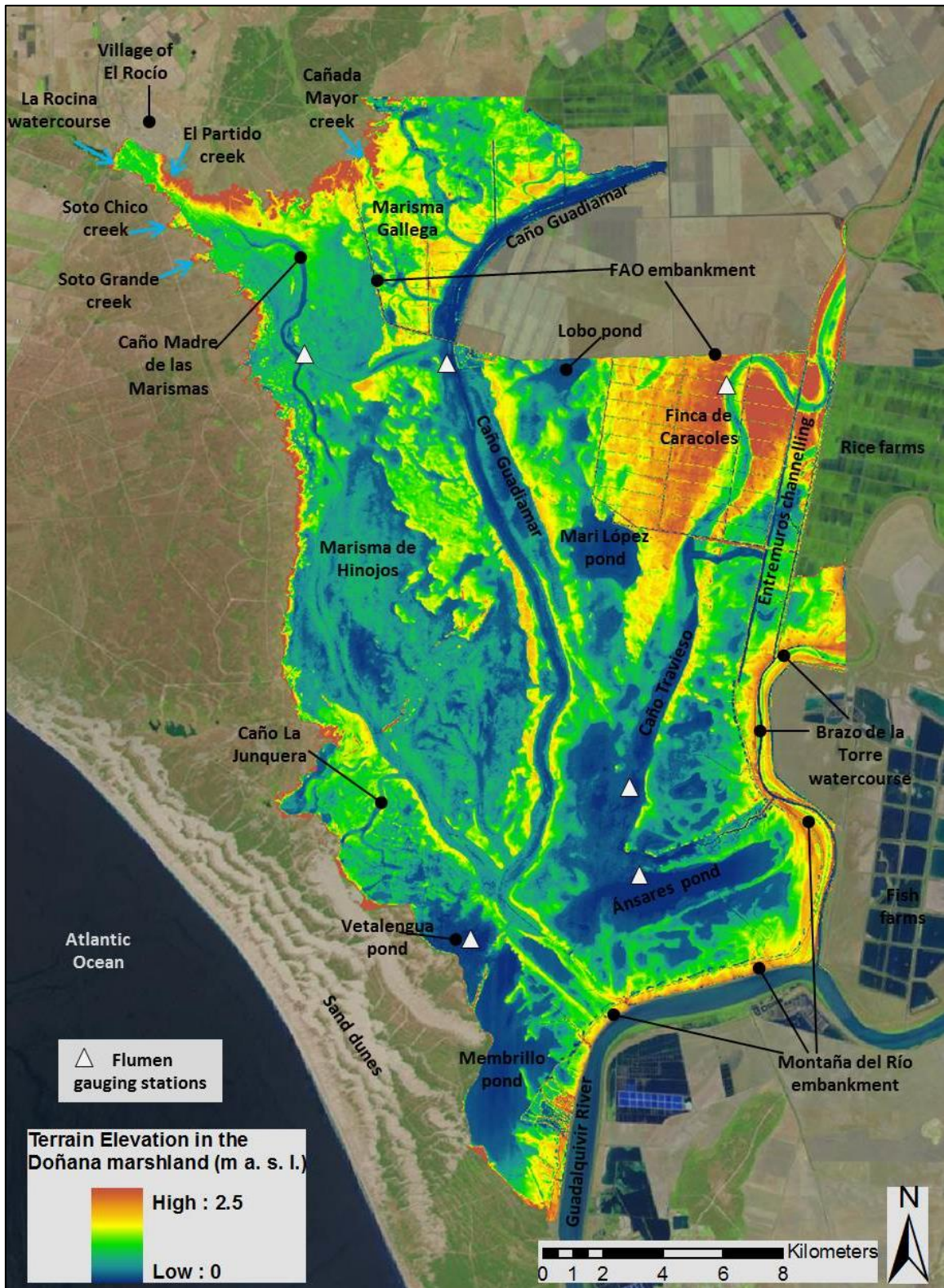
Fig. 4.2. Digital terrain model of the Doñana marshland overlaying a Landsat natural color image, and location of the main ponds and watercourses.
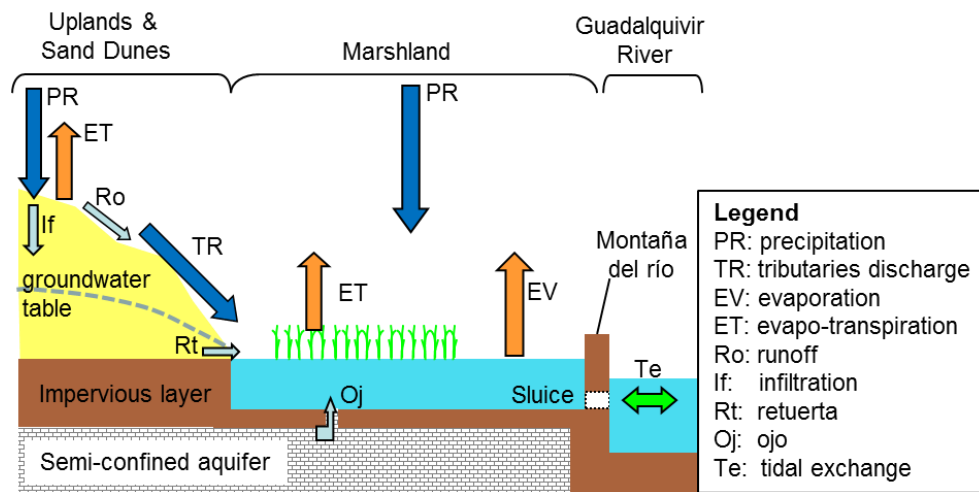
Fig. 4.3. Schematic of inflows and outflows in Doñana wetlands. Adapted from Estación Biológica de Doñana - CSIC, 2010.

Fig. 4.4. "Ojo" or local upwelling from the marshes underlying semi-confined aquifer, near the Vetalengua pond.

4.3.2 DOÑANA WETLANDS FLOODING CYCLES

Doñana wetlands undergo yearly cycles of inundation and drying out. Every summer the marshes dry out completely (Fig. 4.5a) with the exception of the Cerrado-Garrido and Lobo ponds, where water might be pumped from the underlying aquifer, and arrive from the Guadiamar watercourse, which drains irrigation water from the nearby croplands.

At the beginning of the hydrologic year, in September and October, the initial rainfall events dampen the marshes soil. After its saturation flooded areas start appearing at the terrain troughs. The ASAR scenes from the hydrologic years 2006-2007, 2007-2008 and 2008-2009 showed that the first large water bodies were formed at the Membrillo and Ánsares ponds by direct precipitation and run-off, before the inflows from the tributary streams reached their sub-basins.

During the fall and the winter the marshes inundation increases progressively as a result of the above-mentioned inflows, the direct precipitation and the tributary discharges being the main ones (Fig. 4.5b). The maximum flood extent varies considerably amongst years depending on the precipitation (Beltrán, 2006; Aragonés et al., 2005; Clemente et al., 2004; Rodríguez-Ramirez and Clemente-Salas, 2002; Bayán and Dolz, 1995). According to Aragonés et al. 2005, who analyzed Doñana's flood extent evolution using a time series of 224 Landsat images from 1975 to 2004, the maximum flood extent is achieved between December and March, and the largest water surface observed in the study period was of 25,424 ha.

From the beginning of March, new green helophyte vegetation emerges at some of the flooded areas and experiences rapid growth throughout the spring season, virtually concealing the water surface by the end of May (Fig. 4.5c). Simultaneously, the evaporation and evapotranspiration losses cause a constant decrease in the flood extent during the spring (Ramos Fuertes, 2012), until the marshes dry out again in July.

Fig. 4.6 shows the evolution of the water surface elevation and accumulated precipitation for the 2006-2007 hydrologic cycle, as recorded at two gauging stations in Doñana marshes (Ramos Fuertes, 2012; Martí-Cardona et al., 2010). The acquisition date of the contemporary ASAR scenes is also indicated.
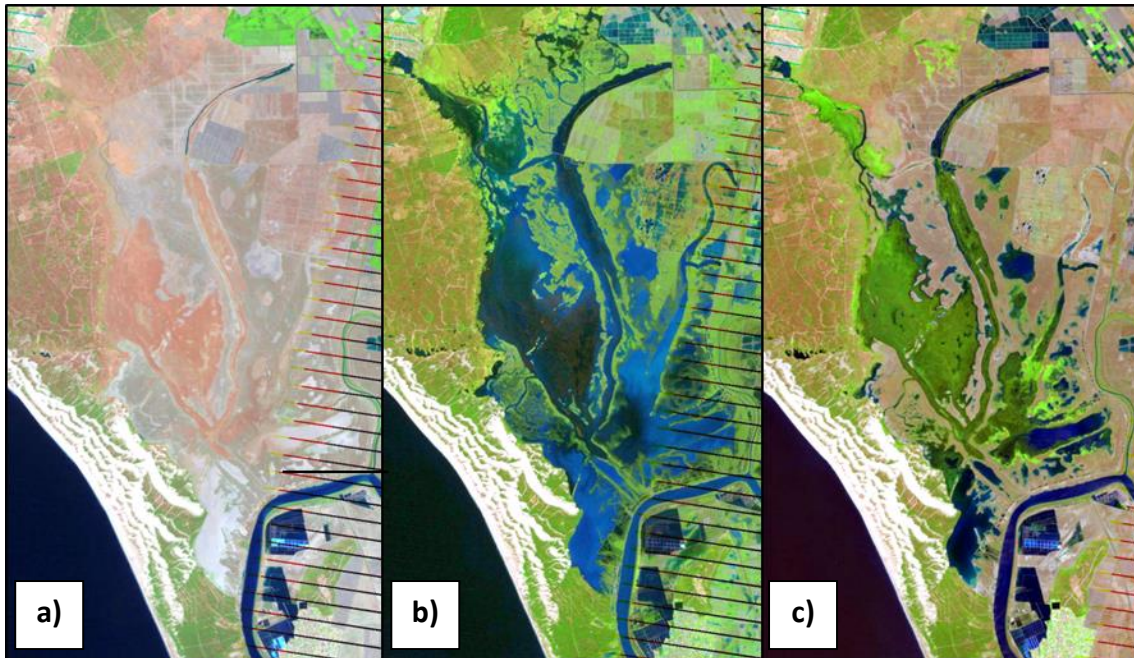
Fig. 4.5. Natural color Landsat scenes of Doñana wetlands (RGB composite of bands 5, 4, 3) acquired on: a) 30 August 2006; b) 20 December 2006; c) 29 May 2007.
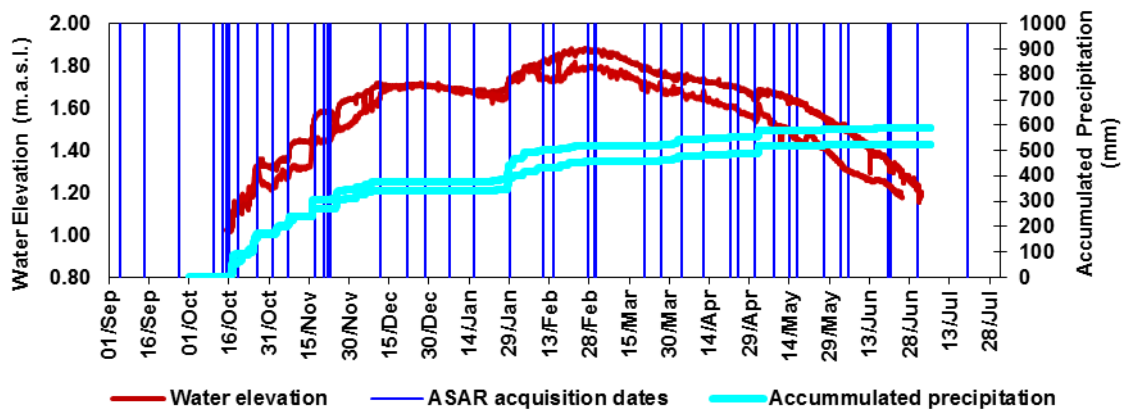
Fig. 4.6. Water elevation and cumulated precipitation at two gauging stations in Doñana marshes throughout the 2006-2007 hydrologic cycle.

Fig. 4.7 depicts the temporal distribution of the cumulated rainfall in Doñana for the hydrological years between 1970 and 2010 (Urdiales et al., 2010). This figure illustrates the large variability of the precipitation regime, which was empirically related to the marshes flood extent with significant accuracy by Beltrán (2006).
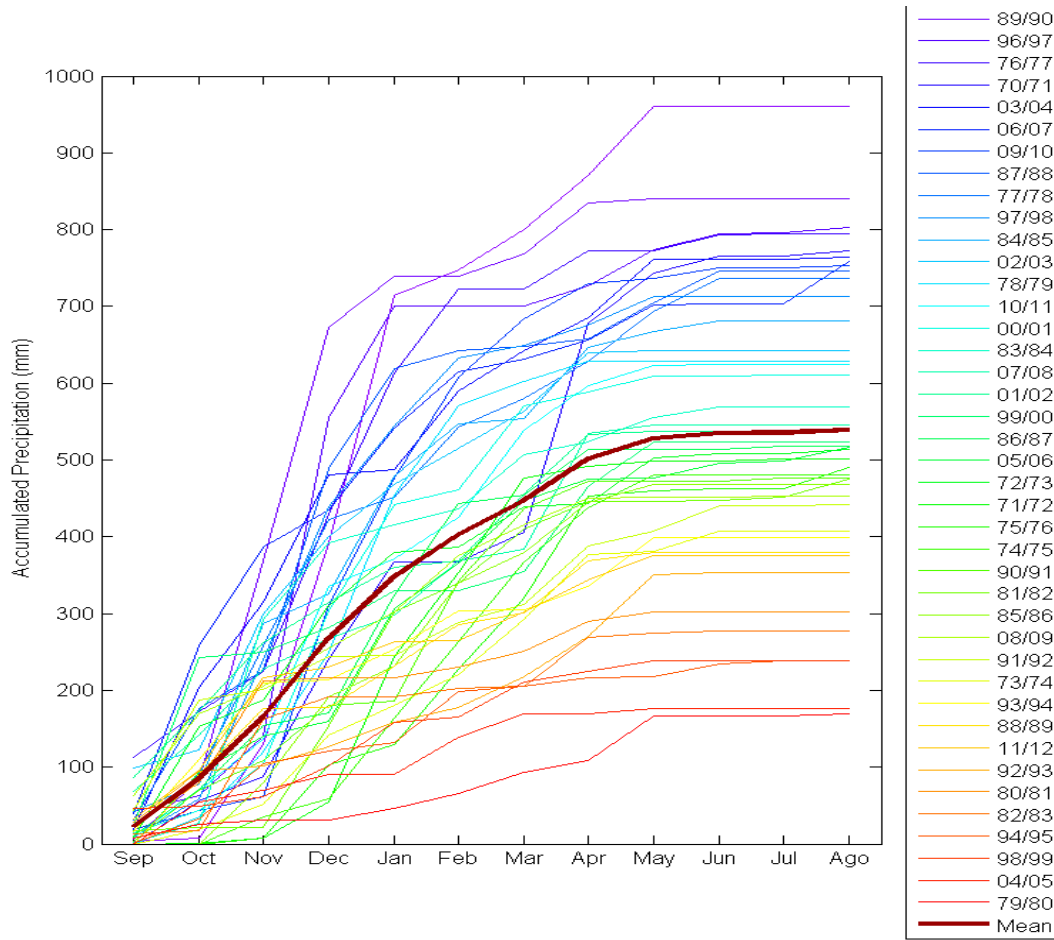
Fig. 4.7. Monthly accumulated precipitation evolution in Doñana for the hydrologic years from 1970 to 2012. Data courtesy of Mr. C. Urdiales.

4.4 Topography:
Driver of the Hydroperiod and the Vegetation Distribution

Fig. 4.8 shows a digital terrain model (DTM) of Doñana marshes and Fig. 4. 9 depicts the corresponding elevation histogram and cumulative histogram. As it can be appreciated in Fig. 4.8 and Fig. 4. 9 the marshes topography is extremely flat (Ibáñez, 2008; Mintegui et al., 2004), with a maximum elevation difference of 2.50 m and a well-defined frequency mode at the elevation of 1.40 m. Zone A in Fig. 4.8 was an agriculture parcel known as Finca de Caracoles, which was incorporated to the marshland in 2003. The topography of this zone was significantly modified between the generation of the DTM in 2002 and the ASAR acquisitions used in this study, so it was excluded from the analysis.
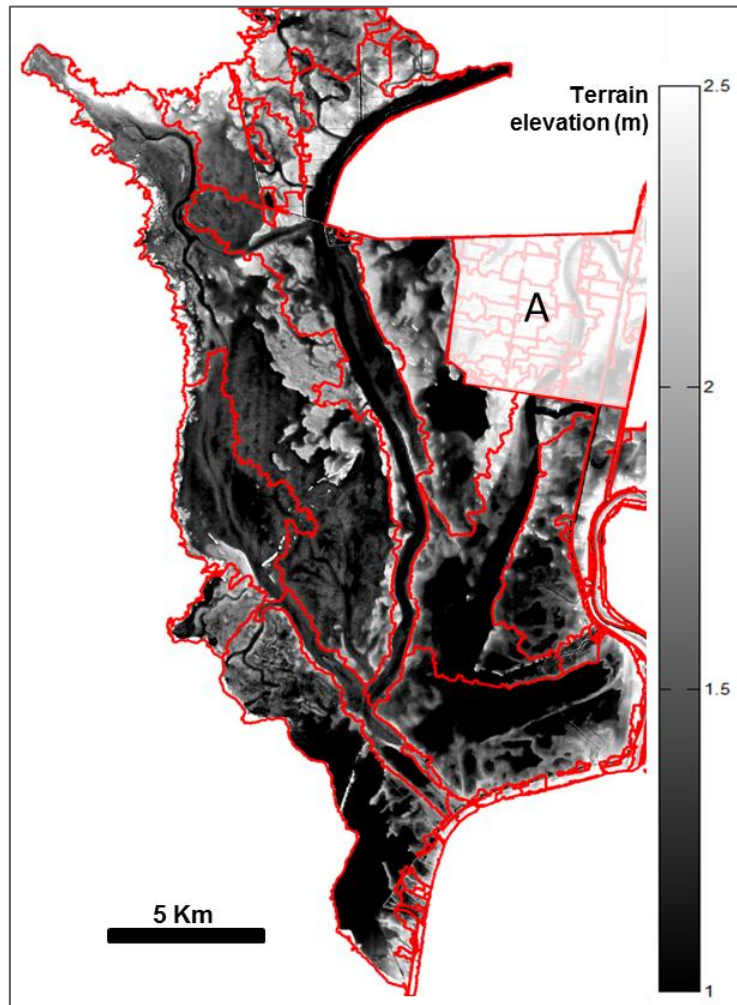
Fig. 4.8. Doñana marshes digital terrain model and sub-basins. Watersheds among sub-basins are shown in red. No accurate elevation data is available for area A.
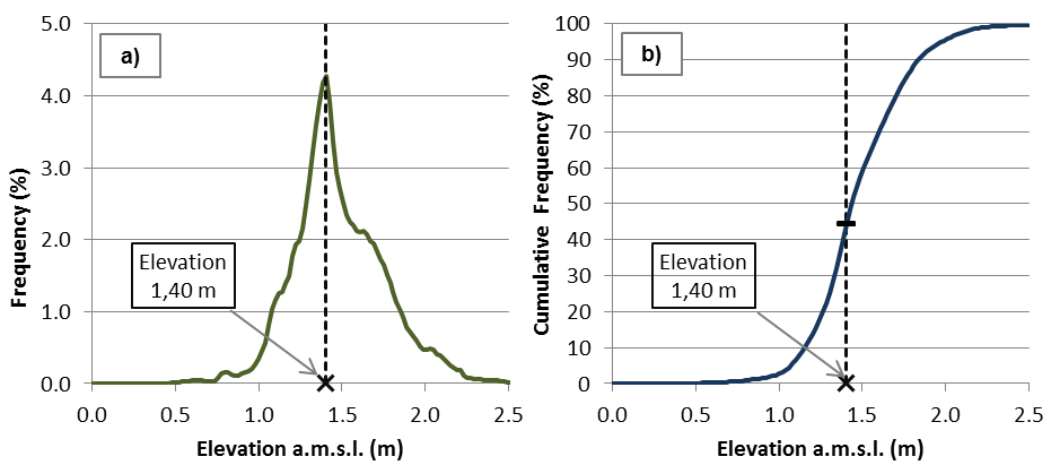
Fig. 4. 9. DTM elevation histogram (a) and cumulative histogram (b).

Despite its subtleness, the marshes topography has a critical effect on the hydroperiod, or time that each zone remains flooded, which in turn determines the vegetal species growing in it (Aragonés et al., 2005; Díaz-Delgado et al., 2006; García Viñas et al., 2005; Rodríguez-Ramirez and Clemente-Salas, 2002).

Attending to topographical and vegetation characteristics, Doñana marshes can be subdivided into three main area types (García Viñas et al., 2005; Mintegui et al., 2004): paciles, ponds centers and transition zones, which are described below, sketched in Fig. 4.10 and mapped in Fig. 4.15. This spatial categorization coincides with those land cover types yielding most distinctive C-band backscattering signatures and therefore more clearly discernible with Envisat/ASAR data (Martí-Cardona et al., 2010). The cartography of pond centers, transition zones and pacil areas in Fig. 4.15 was derived from the detailed map of vegetation communities produced by Luque et al. (2005), as explained in Chapter 5.
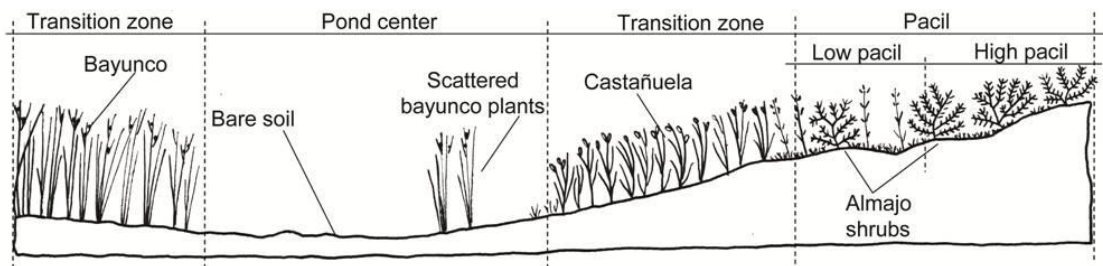
Fig. 4.10. Cross-section model of Doñana marshes. Source: Martí-Cardona et al., 2010.

The **centers of ponds and watercourses** are the deepest marshland areas, the first ones in flooding and the last ones in drying out (Fig. 4.11). In other words, they are the areas of longer hydroperiod. The centers of the ponds are formed by clayey bare soil, and virtually no vegetation develops in them at any time of the year (García Viñas et al., 2005).

The locally called **paciles**, the most elevated zones, are fluvio-tidal sediment bars located between ponds and watercourses (Fig. 4.12, Rodríguez-Ramirez and Clemente-Salas, 2002). The paciles only flood in wet years, when the water level in the marshes rises high enough. The vegetation found in the paciles is pasture land known as almajar. The almajar is dominated by the almajo plant (*Arthrocnemun macrostachyum*), shrub of height between 0.5 and 1.1 m, and percentage of coverage around 50% (García Viñas et al., 2005). When flooded, the water depth in the paciles rarely exceeds 0.2 m, so most of the almajo bush remains out of the water.

The **transition zones**, between paciles and ponds centers, are colmated watercourses. They flood almost every year and communities of large helophytes develop in them. These communities are largely dominated by two species: bayunco (*Scirpus litoralis*, Fig. 4.13) and castañuela *(Scirpus maritimus,* Fig. 4.14). The castañuela is an herb of triangular cross-section and height ranging from 0.6 to 1.0 m. The bayunco is reed-like, with circular cross-section, and often higher than 1.0 m. Both species start emerging from the water surface towards the end of February. They experience rapid growth throughout the spring season and in April and May form dense vegetation masses reaching 95% of surface coverage (García Viñas et al., 2005). The castañuela and the bayunco dry out and die during the summer. Their brown stems stick out of the water surface when the marshes flood in autumn, but they progressively putrefy and sink by the spring.
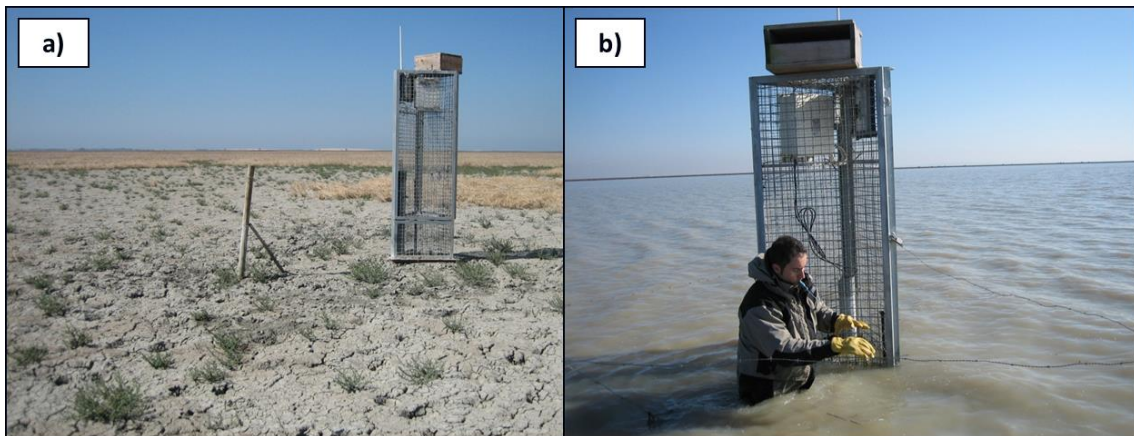
Fig. 4.11. Deep bare soil areas in ponds and water course centers: a) emerged in summer; b) during the flooding season;
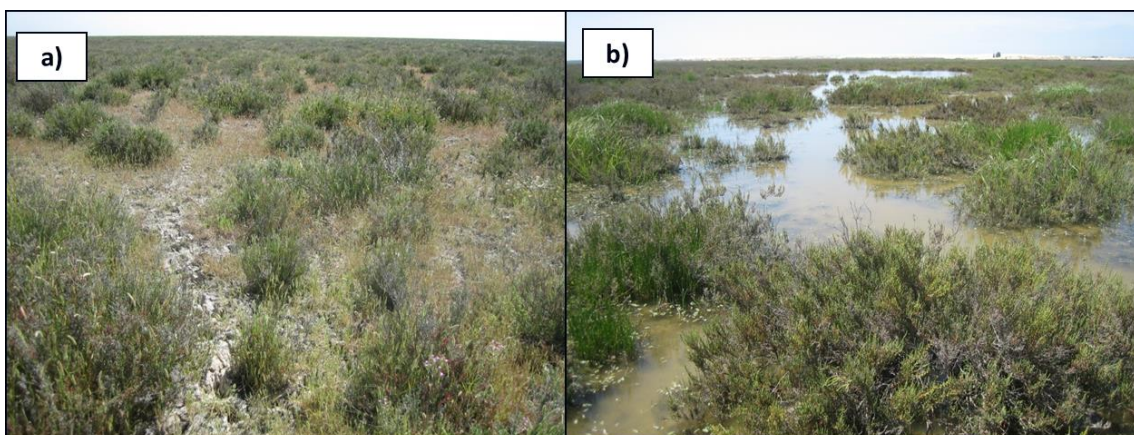
Fig. 4.12. Almajar in the paciles: a) emerged almajar; b) flooded almajar.

Other topographical units of minor extent than the above-mentioned ones are (Mintegui, 2004):

- *Vetas*, small and sandy elevated zones, remaining of the paleo-estuary beaches.
- *Hondones*, contiguous to some paciles, at a lower elevation.
- *Quebradas*, small steps adjacent to some watercourses, shaped by the fluvial erosion.

Fig. 4.13. Bayunco helophytes in the transition zones: a) dry bayunco at the end of the summer; b) brown bayunco at the beginning of the flooding period; c) new, green bayunco stems emerging from the water surface in spring.
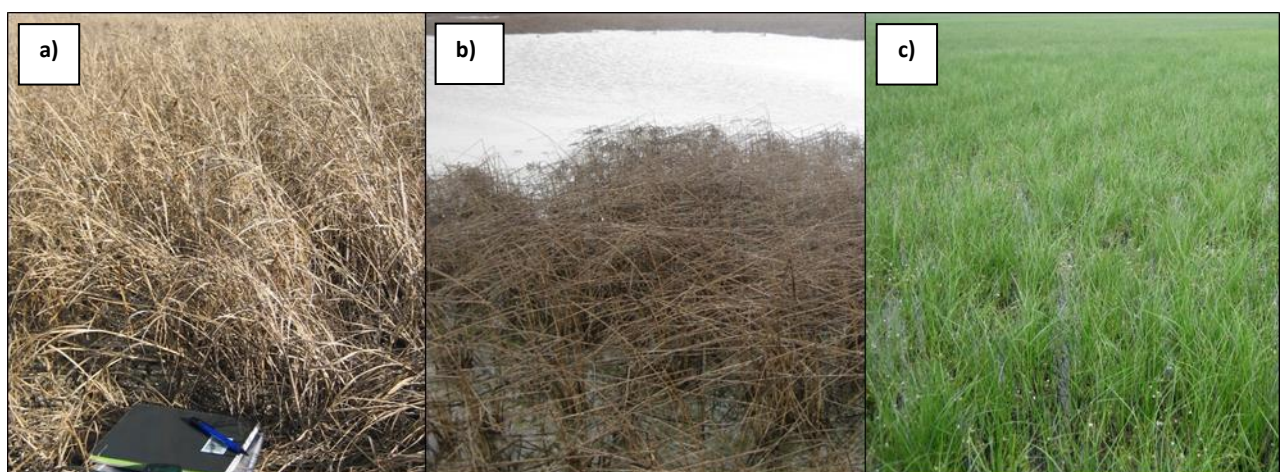
Fig. 4.14. Castañuela helophytes in the transition zones: a) dry castañuela at the end of the summer; b) brown castañuela at the beginning of the flooding period; c) new, green castañuela stems emerging from the water surface in spring.

Topographical elements resulting from the anthropogenic activity are listed below and indicated in Fig. 4.15:

- The *Montaña del Río* (River Mountain), a 3 m high earth levee that detaches the marshes from the Guadalquivir River. It was first built to compensate the degradation of the river's natural embankment caused by fluvial traffic swell. After the Aznalcollar dam failure in 1998, the Montaña del Río was prolonged up to the Entremuros in order to block the entrance of toxic mine spills into the marshes.

- The *FAO* and *Entremuros* embankments, limiting the natural marshes on the North and East, respectively.

- The *sacatierras* (soil-mining pits), small artificial ponds resulting from the soil extraction for building the earth embankments.

- The abandoned *San Rafael saltworks*.

- The *Alluvial fan of El Partido creek*. The canalization of El Partido creek and farming on its natural floodplains during the last decades largely increased the erosive and sediment transport processes in this watercourse. As a result, an alluvial deposition fan was rapidly formed at the mouth of El Partido creek in Doñana marshes (Sendra, 2002).

Another anthropogenic element in Doñana is the metallic fencing subdividing the marshes for cattle grazing allocation. Some of these fences can be seen in Fig. 4.16, while Fig. 4.15 indicates their location. Those fence reaches parallel to the Envisat trajectory and hence perpendicular to the SAR beam yield very high backscattering on the ASAR images, as illustrated by Fig. 4.17, and were masked out prior to filtering the images as explained in Chapter 8.
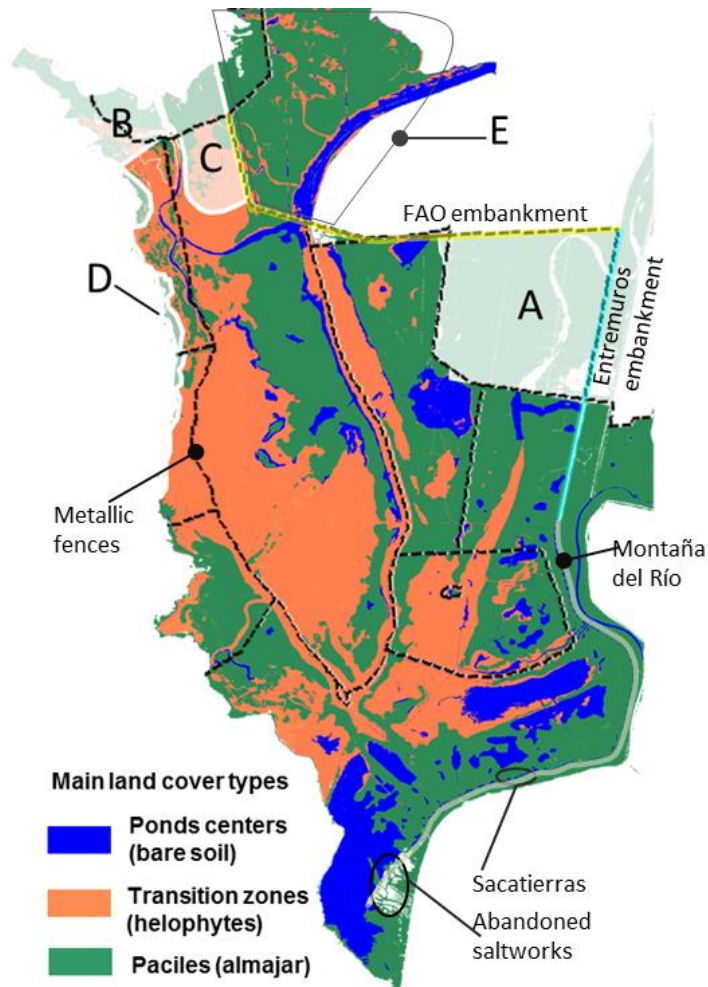
Fig. 4.15. Doñana main cover types. No vegetation cartography is available for areas A and B. No backscattering characterization was available for vegetation communities in C and D.

Fig. 4.16. Metallic fences in Doñana marshes.
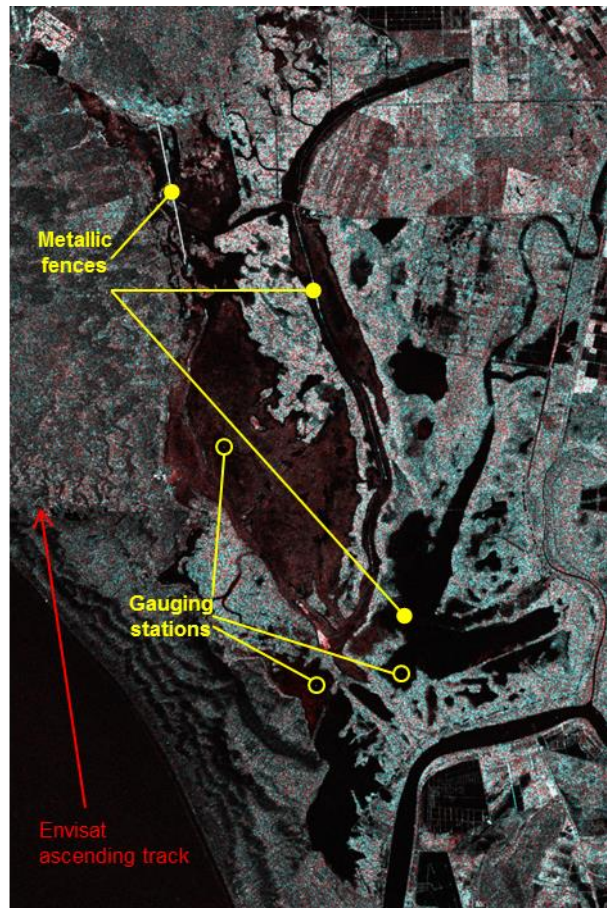
Fig. 4.17. ASAR scene from 22 Nov. 2006, at swath IS6 and ascending track. VV-polarization backscattered intensity is displayed in red and HH-polarization in cyan. Some metallic fence reaches appear bright. Some gauging stations with solar panels are also discernible.

4.4.1 COVER TYPES AND ELEVATION CORRESPONDENCE WITHIN SUB-BASINS

As revealed by the description above, Doñana cover types are intimately related to the hydroperiod, which in turn is closely related to the topography, so local troughs and crests exhibit the longest and shortest inundation periods respectively. This relationship becomes obvious in view of the morphological similarities among contours and land cover maps (e.g. Fig. 4.8 and Fig. 4.15). Nevertheless, when exploring the elevation ranges of the main cover types, significant overlapping is found. The reason is that troughs and crests can happen at different absolute elevations in different sub-basins, as illustrated by Fig. 4.18. However, the equivalence between terrain absolute elevation and hydroperiod, and consequently between absolute elevation and cover type, is closely achieved within sub-basins.

The red lines in Fig. 4.8 delineate the Doñana's sub-basins. These watersheds were determined based on the DTM so that local minima at each sub-basin were at least 0.40 m deeper than their surroundings. The value 0.40 m was one of the smallest thresholds for which the three main cover types (pond centers, transition zones and paciles) were represented in most of the segments, covering 90% of the marshes area.

Indicative of the relationship between elevation and cover type within sub-basins is the qualitative similarity among sub-basins terrain elevation histograms (Fig. 4.19). These histograms show a bi or three-modal shape, revealing two or three dominant ranges of elevations or plains within the sub-basin, which spatially match the abovementioned three main cover types. This relationship between the Doñana cover classes and the terrain elevation within sub-basins contributes valuable spatial information that is exploited for the classification and flood mapping algorithm of the ASAR scenes in Chapter 7.
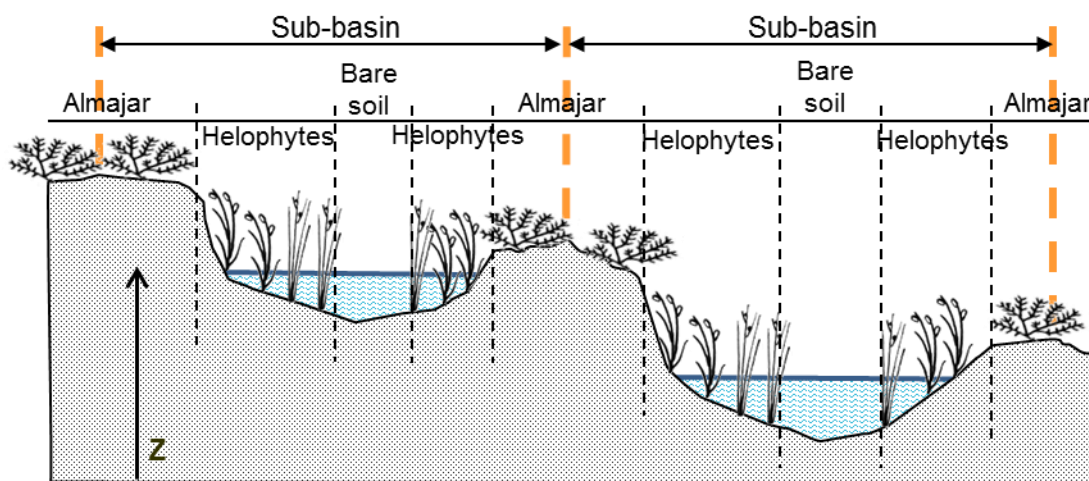
Fig. 4.18. Cross section model of Doñana marshes (vertical to horizontal scale ratio>>1): the same cover types happen at different elevations throughout the marshes, but a similar vertical sequence between vegetation communities is preserved within sub-basins.
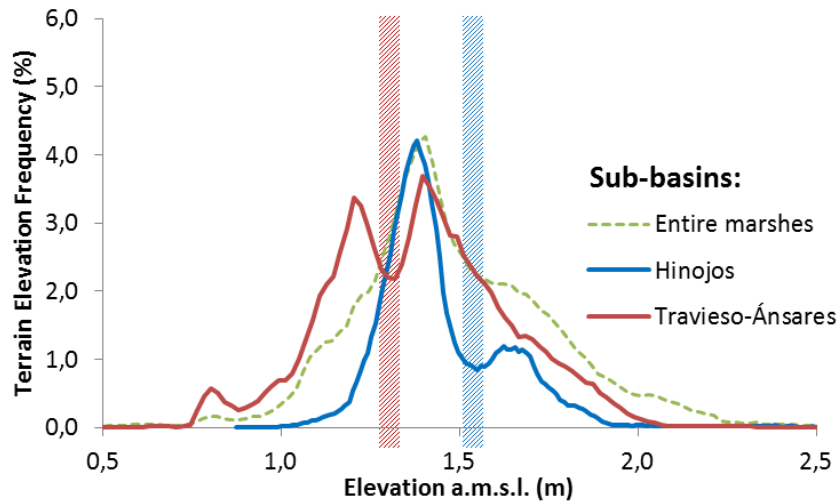
Fig. 4.19. Terrain elevation histograms for Hinojos and Travieso-Ánsares sub-basins The higher and lower modes correspond to paciles and transition zones or pond centers, respectively. The hatched bars indicate the transitional elevations between plains or cover classes, which happen at clearly different heights at the two sub-basins.

4.5 Conclusions

Those aspects of the above presented site description which are especially relevant for the development of this research are highlighted as follows:

Despite its subtleness, Doñana's micro-topography exerts an essential influence on the hydroperiod and, consequently, on the vegetation communities spatial distribution. Thus, the marshes DTM provides exquisite information for the determination of homogeneous neighborhoods following natural edges at each pixel position. This information is successfully exploited in Chapter 8 for filtering the speckle noise on the ASAR scenes.

Attending to topographical and vegetation characteristics, Doñana marshes can be subdivided into three main area types, paciles, ponds centers and transition zones, which yield discernible ASAR backscattering signatures (Martí-Cardona et al., 2010).

As shown in Section 4.4.1 the equivalence between terrain absolute elevation and hydroperiod, and consequently between absolute elevation and cover type, is closely achieved within sub-basins. This relationship between the Doñana cover classes and the terrain elevation within sub-basins contributes valuable spatial information that is used by a classification and flood mapping algorithm of the ASAR scenes in Chapter 9.

4.6 References

Aragonés, D., Díaz-Delgado, R., & Bustamante, J. (2005). Tratamiento de una serie temporal larga de imágenes Landsat para la cartografía de la inundación histórica de las marismas de Doñana. In M. Arbeló, A. González, & J. C. Pérez (Eds.), Teledetección. Avances en la Observación de la Tierra. Actas XI Congreso Nacional de Teledetección (pp. 407–410). Tenerife, Spain: Sociedad Española de Teledetección. Retrieved from http://www.ebd.csic.es/bustamante/publicaciones/Aragon?s_et_al_(2005)_XI_Congreso_Teledetecci?n_407-410.pdf

Bayán, B. J., & Dolz, J. (1995). Las aguas superficiales y la marisma del Parque Nacional de Doñana. Revista de Obras Públicas, 142(3340), 17–29.

Bayán Jardín, B. J. (2005). Los caminos del agua en la marisma: los cambios en la red hidrológica. In F. García-Novo & C. Marín-Cabrera (Eds.), Doñana: Agua y Biosphera. (pp. 143–147). Madrid: Confederación Hidrográfica del Guadalquivir, Ministerio de Medio Ambiente.

Beltrán, M. (2006). Development of water balance models of Doñana marshes using remote sensing determination of their flood extent.

Butler, J. (2008). A Birdwatching Guide to Doñana. Bloomington, IN: Trafford Publishing.

Clemente, L., García, L. V, Espinar, J. L., Cara, J. S., & Moreno, A. (2004). Las Marismas del Parque Nacional de Doñana. Investigación y Ciencia, 332.

Custodio, E., Dolz, J., & Manzano, M. (2006). Recursos de agua de la comarca de Doñana. Almonte, Huelva. Fundación Doñana 21.

Custodio, E., Manzano, M., & Montes, C. (2008). Perspectiva general del papel y gestión de las aguas subterráneas en el área de doñana, sudoeste de España. Boletin Geologico y Minero, 119(1), 81–92.

Delibes, M., Rodríguez, A., Laffitte, R., & Palomares, F. (1991). The status and distribution of the Iberian lynx Felis pardina (Temminck) in Coto Doñana Area, SW Spain. Biological Conservation. doi:10.1016/0006-3207(91)90136-W

Díaz-Delgado, R., Bustamante, J., Pacios, F., & Aragonés, D. (2006). Hydroperiod of Doñana marshes: natural or anthropic origin of inundation regime? In Proceeding of the 1st GlobWetland Symposium: Looking at Wetlands from Space. European Space Agency and Ramsar Convention.

Dolz, J., & Velasco, E. (1990). Análisis cualitativo de las cuencas vertientes al Parque Nacional de Doñana. Informe de la Sección de Ingeniería Hidráulica e Hidrológica, Departament d'Enginyeria Hidràulica, Marítima i Ambiental de la Universitat Politècnica de Catalunya, Barcelona.

García Viñas, J. I. (2005). La vegetación en la marisma del Parque Nacional de Doñana en relación con su régimen hidráulico.

García-Novo, F., & Marín-Cabrera, C. (2005). Doñana: agua y biosfera. Madrid, España: Confederación Hidrográfica del Guadalquivir, Ministerio de Medio Ambiente.

Ibáñez, E. (2008). Validación de Modelos Digitales del Terreno de precisión a partir de datos Láser Escáner Aerotransportado; Aplicación a la Marisma del Parque Nacional de Doñana. PhD dissertation. Universitat Politècnica de Catalunya.

Machuca, M. M., Geta, J. A. L., Vílches, L. L., Gómez, R. M., Robles, R. C., & Fiaño, I. C. (1992). Hidrogeologia del Parque Nacional de Doñana y su entorno (p. 64). Madrid: Instituto Tecnólogico Geominero de España.

Máñez, M., & Garrido, H. (2002). Avifauna. In V. (coord. . García (Ed.), Parque Nacional de Doñana (pp. 231–316). Canseco Editores.

Martí-Cardona, B., López-Martínez, C., Dolz-Ripollés, J., & Bladé-Castellet, E. (2010). ASAR polarimetric, multi-incidence angle and multitemporal characterization of Doñana wetlands for flood extent monitoring. Remote Sensing of Environment, 114(11), 2802–2815. doi:10.1016/j.rse.2010.06.015

Menanteau, L. (1984). Evoluvión histórica y consecuencias morfológicas de la intervención humana en las zonas húmedas: el caso de las marismas del Guadalquivir. (pp. 43–76). Madrid, España: Dirección General de Medio Ambiente, Ministerio de Obras Públicas y Urbanismo.

Mintegui, J. A., Robredo, J. C., & García, J. I. (2004). Importancia de los trabajos de campo en la confección del modelo del terreno para aplicaciones en ecología. Investigación Agraria: Sistemas y Recursos Forestales, Fuera de s, 164–175.

Muriel, R., Ferrer, M., Casado, E., Madero, A., & Calabuig, C. P. (2012, October 29). Asentamiento y reproducción con éxito de águilas imperiales ibéricas Aquila adalberti reintroducidas en la provincia de Cádiz (España). Sociedad Espanola de Ornitologia. Retrieved from http://hdl.handle.net/10261/59095

Narbona, C. (2005). Presentación. In F. García-Novo & C. Marín-Cabrera (Eds.), Doñana: Agua y Biosphera. (pp. 7–8). Madrid: Ministerio de Medio Ambiente.

Palomares, F., Rodríguez, A., Revilla, E., López-Bao, J. V., & Calzada, J. (2011). Assessment of the conservation efforts to prevent extinction of the Iberian lynx. Conservation biology : the journal of the Society for Conservation Biology, 25, 4–8. doi:10.1111/j.1523-1739.2010.01607.x

Perez de Ayala, R., Guzman, N., Iglesias, M. C., Pereira, P., Simón, M., García, F. J., … Robles, F. (2011). Estimation of the Iberian lynx (Lynx pardinus) population in the Doñana area, SW Spain, using capture–recapture analysis of camera-trapping data. European Journal of Wildlife Research. doi:10.1007/s10344-010-0440-7

Periáñez, R., & Abril, J. M. (2013). Modeling tsunami propagation in the Iberia–Africa plate boundary: Historical events, regional exposure and the case-study of the former Gulf of Tartessos. Journal of Marine Systems, 111-112, 223–234. doi:10.1016/j.jmarsys.2012.11.005

Ramos Fuertes, A. (2012). Hidrometeorología y balance térmico de la marisma de Doñana. PhD dissertation. Universitat Politècnica de Catalunya. Retrieved from http://www.tdx.cat/handle/10803/110548

Rodríguez-Ramirez, A., & Clemente-Salas, L. (2002). Geomorfología (pp. 19–42). Talavera de la Reina, Spain: Canseco Editores.

Rodriguez-Ramirez, A., Rodriguez-vidal, J., Cticeres, L., & De, J. R. (1996). Recent coastal evolution of the dorana national park (sw spain), 15(96), 803–809.

Rodríguez-Vidal, J. (2005). La evolución geomorfológica de Doñana. In F. García-Novo & C. Marín-Cabrera (Eds.), Doñana: Agua y Biosphera. (pp. 129–131). Madrid: Confederación Hidrográfica del Guadalquivir, Ministerio de Medio Ambiente.

Ruiz, F., Rodríguez-Ramírez, A., Cáceres, L. M., Rodríguez Vidal, J., Carretero, M. I., Clemente, L., ... Abad, M. (2004). Late Holocene evolution of the southwestern Doñana National Park (Guadalquivir Estuary, SW Spain): a multivariate approach. Palaeogeography, Palaeoclimatology, Palaeoecology, 204(1-2), 47–64. doi:10.1016/S0031-0182(03)00721-1

Suso, J., & Llamas, M. R. (1993). Influence of Groundwater Development on the Donana-National-Park Ecosystems (Spain). Journal of Hydrology, 141(1-4), 239–269.

Urdiales, C., García, D., Valero, A., & Fernández, J. M. (2010). Seguimiento de la inundación en la marisma de Doñana: resultados del ciclo 2009/2010 y efecto del dique de la Montaña del Río en el proceso de inundación. In J. Ojeda, M. F. Pita, & I. Vallejo (Eds.), (pp. 1146–1156). Sevilla: Secretariado de Publicaciones de la Universidad de Sevilla.

It is a capital mistake to theorize before one has data. Insensibly, one begins to twist facts to suit theories, instead of theories to suit facts.

Arthur Conan Doyle, 1887

Chapter 5:
Experimental Data

5.1   Introduction

This chapter describes the data used throughout the completion of the present research. It begins with the description of the Advanced Synthetic Aperture Radar's (ASAR) imagery, whose interpretation and processing is the corner stone of this work. Next, the ground truth data acquisition is explained. This section has a personal connotation for the author. Many kilometers were trailed in the muddy marshes for ground-truthing, often in adverse weather conditions and in absolute loneliness, but always driven by the wish to know the real world behind the backscattering coefficients and the aspiration to properly interpret the imagery data, so the derived land cover products suited the facts.

In addition to the ground truth, the terrain elevation data, the existing vegetation maps and the on-site water level and wind records also aided the interpretation of the ASAR images and the backscattering characterization of Doñana's land cover types, object of subsequent chapters. The terrain elevation and the vegetation maps were used again in the flood mapping algorithm, presented in Chapter 9. ASAR inundation results were compared to those obtained from Landsat images, when acquisitions of both sensors coincided on cloud free dates. The ground truth data, the terrain elevation model, the vegetation cartography, the on-site hydro-meteorological records and the Landsat flood maps used in this research are presented in the sections as follows.

5.2   The Envisat/ASAR Sensor

The Advanced Synthetic Aperture Radar (ASAR) sensor was installed on board the Envisat satellite of the European Space Agency (ESA). Envisat was launched in 2002 and was operative until its failure in 2012. It flew in a sun-synchronous polar orbit of about 800-km altitude and had a repeat cycle of 35 days (ESA, 2006). ASAR imaged the Earth surface by transmitting and receiving electromagnetic radiation at C-band (5.34 GHz) and could be operated in different measurement modes and incidence angles.

The ASAR images acquired during the completion of this study were ordered in the Alternated Polarization (AP) and Image (IM) acquisition modes, and were received respectively in the form of Alternated Polarization Ellipsoid Geocoded (ASA_APG_1P) and Image Mode Precision (ASA_IMP_1P) products. Both products are multi-look, ground-range projected digital images, with a spatial resolution (range x azimuth) of approximately 30 m x 30 m, and their footprints covered the entire marshes area in virtually all cases. Other ASAR's acquisition modes were discarded due to its coarser spatial resolution.

In the AP and IM modes, the ASAR's imaging swath could be selected by changing the beam incidence angle and the elevation beam width amongst seven predetermined swaths designated as IS1 to IS7. Fig. 5.1 illustrates the seven ASAR's swaths and Table 5.1 shows the incidence angle range and the equivalent number of looks of the corresponding image products. In the AP mode, the ASAR sensor acquired data in two of the three polarization channels as follows: HH, VV and HV. In the HH and VV channels, also referred to as like-polar channels, the sensor antenna used respectively horizontally or vertically polarized radiation, and the same polarization was used for transmitting and receiving. HV is the cross-polar channel, where the transmitted and received pulses have different polarization. In the IM acquisition mode only one like-polar channel could be used, either HH or VV.
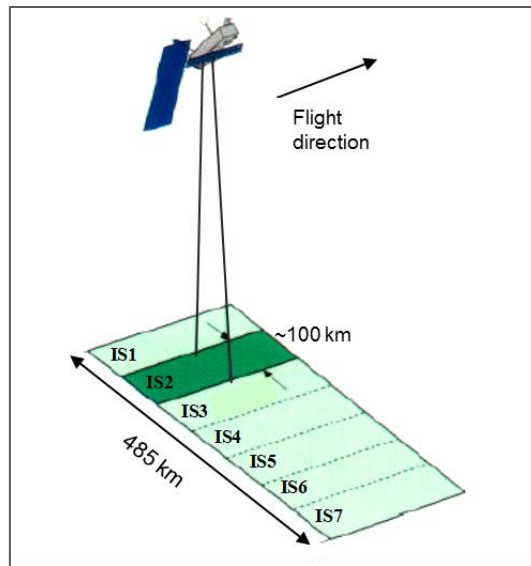
Fig. 5.1. Envisat/ASAR predetermined incidence angles, labeled as IS1 to IS7. Adapted from ESA, 2006.

Table 5.1. Predetermined ASAR swaths, incidence angle range and equivalent number of looks (ENL) of the Alternated Polarization (AP) and Image (IM) modes' ground projected image products.

ASAR swath	Incidence angle from near to far range (°)	ENL of IM image products	ENL of AP image products
IS1	15.0 – 22.9	3.95	1.76
IS2	19.2 – 26.7	3.95	1.73
IS3	26.0 – 31.4	3.95	2.25
IS4	31.0 – 36.3	3.95	2.66
IS5	35.8 – 39.4	3.95	3.30
IS6	39.1 – 42.8	3.95	3.78
IS7	42.5 – 45.2	3.95	3.73

5.2.1 WHY USING ASAR?

The Institut Flumen initiated the exploration of remote sensing techniques as a tool for the regional and periodic observation of the Doñana marshes at the end of the year 2005. An assessment of the available satellite sensors was carried out (Martí-Cardona and Dolz, 2005) and pointed to the Envisat/ASAR sensor as being the most suitable instrument for monitoring Doñana's flood evolution.

Detailed observation of the Doñana flooding process was of particular interest to capture two-dimensional data for the calibration of the marshes hydrodynamic model. This process is usually rapid, so frequent imagery is needed to monitor it. On the other hand, the flooding tends to coincide with overcast weather. In the abovementioned assessment of satellite sensors, ASAR was considered the most suitable instrument to provide the required frequent observations of Doñana during the filling period for the main two reasons as follows:

- The ASAR's pointable capability enabled up to 14 image acquisitions of Doñana per 35-day orbit cycle.
- The C-band radiation can penetrate cloud cover, haze, dust and all but heavy rainfall, so ASAR was able to collect data under almost any weather condition and the observation frequency would not be impaired during rainy periods.

5.3   Selection of the Imaging Configuration and Study Period

In December 2005, the Institut Flumen signed a Category-1 User Agreement with the ESA, hence becoming entitled to order ASAR data at the required configurations. The ASAR scene planning began in the early 2006. Several scenes were ordered and acquired in different polarizations and incidence angles between February and June 2006 (Period 1 in Fig. 5.2). Ground truth data campaigns were undertaken coinciding with selected ASAR acquisitions over Doñana. Archived Doñana ASAR scenes were also collected. Simultaneously, a thorough literature review on the SAR observation of wetland environments was carried out. Preliminary conclusions regarding the suitability of the ASAR's polarization and incidence angle configurations for flood mapping in Doñana marshes were drawn in Martí-Cardona et al. (2006).

In broad outlines, these results indicated the beneficial use of dual polarization data (Alternated Polarization mode) for land cover mapping in Doñana, versus single polarization data (Image mode), despite the higher equivalent number of looks (ENL) of the latter product, shown in Table 5.1. The suitability of the incidence angle depended largely on the marshes flood and phenological stage, as well as on the wind conditions, since these determine the open water surface roughness. However, the incidence angles were not exclusive to capture Doñana's marshland on a given date, and could be all used in order to increase the observation frequency.

Figs. 5.3 and 5.4 illustrate some of the initial understanding of the ASAR scenes achieved by contrasting the image data with the ground truth, in-situ water level records and Landsat data derived flood maps (Aragonés et al., 2005), and from the knowledge attained from the literature review. The ASAR acquisition planning during the subsequent hydrologic year, from September 2006 to August 2007 (Period 2 in Fig. 5.2), was designed according to those preliminary findings.

The methodology developed in this thesis focuses on the 2006-2007 hydrologic year, with special attention to the flooding process, because a large ASAR image data set was acquired during this period. It was also a wet year during which the paciles, the marshes' highest areas, flooded partially. Additionally, a significant amount of ground truth was collected coinciding with the ASAR acquisitions and continuous series of on-site water level and meteorological records were registered at five permanent gauging stations (Ramos Fuertes, 2012). Such a complete and miscellaneous dataset provides valuable information for the interpretation of the ASAR scenes, and for the validation of the derived products. Furthermore, frequent flood mapping from the ASAR scenes would provide a detailed spatial insight on Doñana's flood dynamics*. The 2006-2007 hydrological year was hence selected as the study period, and special attention was paid to the flooding process, between October and mid-April.* However none of the developed algorithms in this research make assumptions related to the particular flood evolution during the 2006-2007 year, so they can be extrapolated to images acquired on different cycles.

ASAR images were also ordered over Doñana between 2008 and 2010, although at lower temporal frequency than on the 2006-2007 cycle. Some of these images have also been processed in order to retrieve spatial data on specific events for hydrodynamic calibration or conservation purposes.

Envisat/ASAR scenes of Doñana
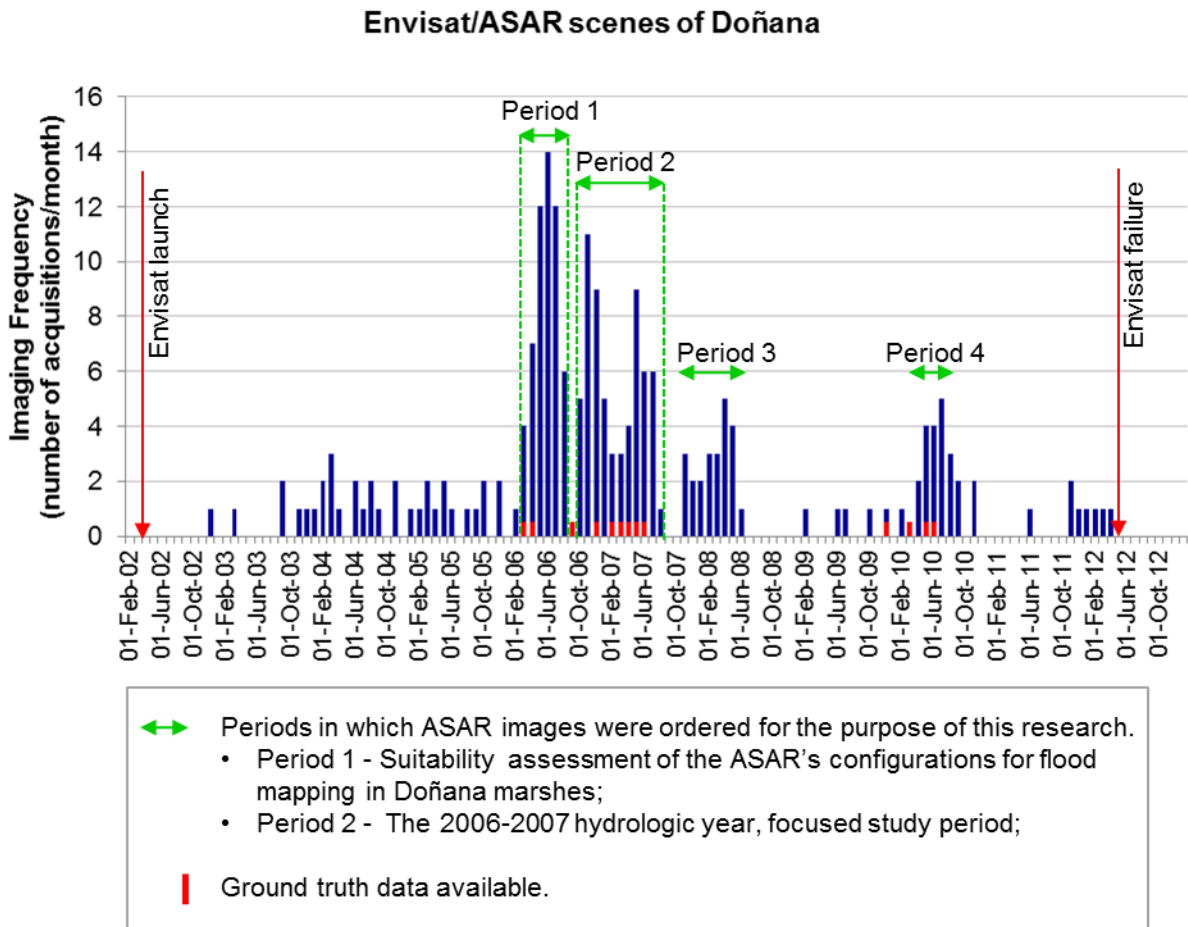
Fig. 5.2. Number of ASAR IM and AP images of Doñana marshes acquired per month during the Envisat's operative life. The green arrows indicate the images ordered for the purpose of this research.
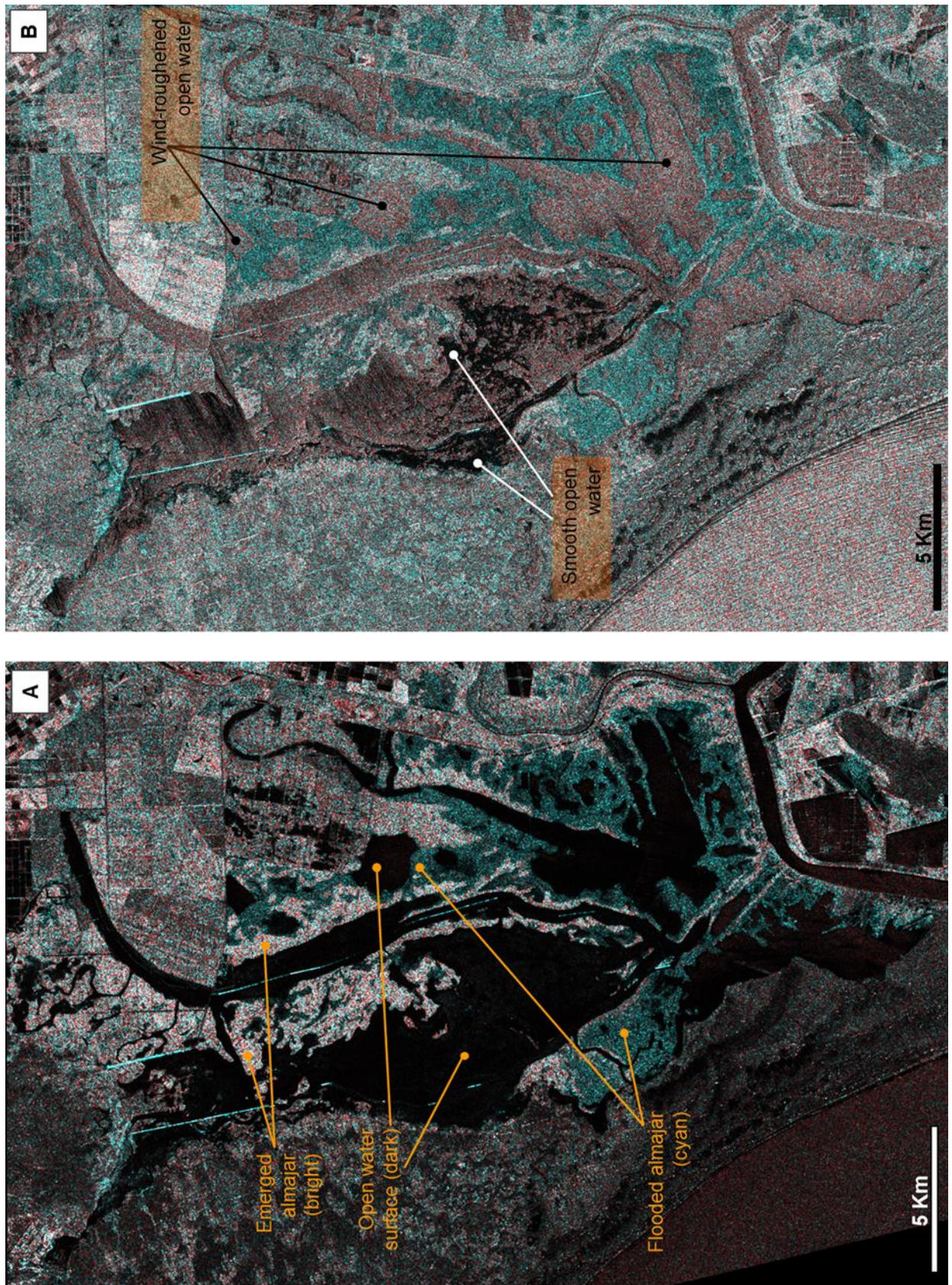
Fig. 5.3. Preliminary interpretation of the Doñana ASAR scenes: a) ASAR image from 21 Dec. 2006, swath IS3, AP mode HH/VV polarizations; b) ASAR image from 10 Feb. 2007, swath IS2, AP mode HH/VV polarizations. . In both images HH backscattering is displayed in cyan and the VV in red.
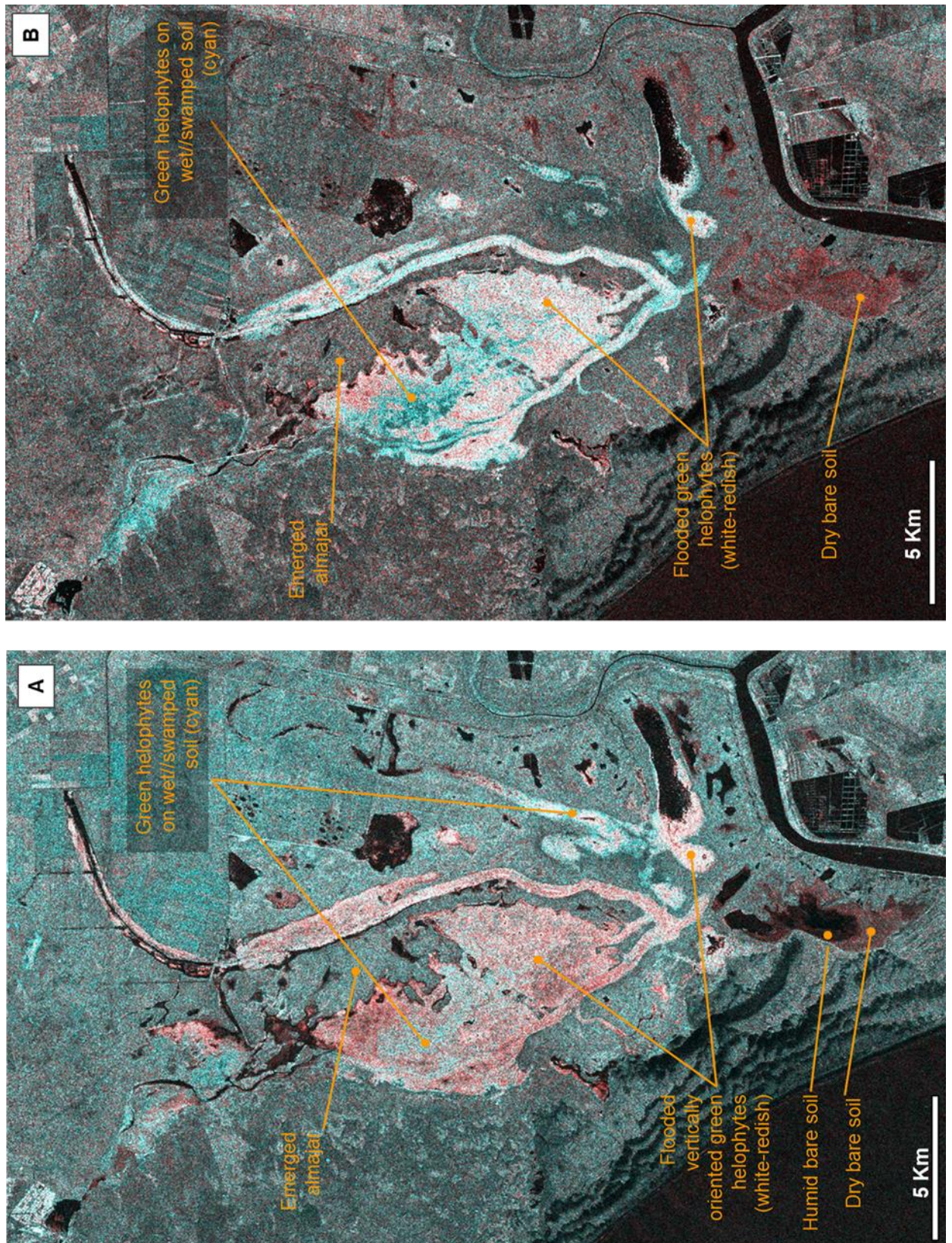
Fig. 5.4. **Preliminary interpretation of the Doñana ASAR scenes: a) ASAR image from 18 Abr. 2006, swath IS6, AP mode HH/VV polarizations; b) ASAR image from 12 May. 2006, swath IS5, AP mode HH/VV polarizations. In both images HH backscattering is displayed in cyan and VV in red.**

5.4   ASAR Imagery

The calendar in Fig. 5.5 indicates in green color the ASAR acquisition dates over Doñana marshland during the study period. The ASAR operation mode, incidence angle and polarization configuration of the acquisitions is also specified. The dates highlighted in orange correspond to potential ASAR observations at the indicated incidence angles. Most of the Doñana feasible observations at the seven ASAR's swaths (in green and orange in Fig. 5.5) were initially requested in order to achieve high imaging frequency, especially during the fall, when the flood extent changes more rapidly. However, the observation opportunities were restricted by conflicts with other users' ASAR configuration orders. Some requests were also rejected by ESA due to satellite operation maneuvers and other diverse technical reasons.   Additionally, swath IS5 experienced technical irregularities during the study period, and the corresponding requested acquisitions were cancelled.

As it can be observed in Fig. 5.5, the majority of the ASAR scenes were ordered in the AP mode and HH/VV polarization configuration, in accordance with the preliminary assessment of the ASAR's suitability for monitoring Doñana marshes (Martí-Cardona et all., 2006). Consequently, this research is mostly concerned with this data type. Ascending and descending tracks were used indifferently, in virtue of the terrain flatness and the horizontal isotropy of the vegetation. Phase data were discarded due to the incoherency between ASAR polarization channels and between different acquisition dates on distributed targets.

Fig. 4.4 in Chapter 4 shows the ASAR image acquisition dates during the study period together with the cumulated precipitation and water level evolution in Doñana at two different gauging stations. This figure manifest the higher observation frequency achieved during the marshes flooding, when the water levels were rising. The number of available images per swath in the 2006-2007 hydrologic year is summarized in Table 5.2.   A complete inventory of all existing Envisat/ASAR scenes over Doñana in the Alternated Polarization and Image acquisition modes during the sensor's operative life is included in Annex 1 to this document.

Mo.	Tu.	We.	Th.	Fr.	Sa.	Su.
04-Sep-06 IM HH, I1	05-Sep-06 AP HH/VV, I6	06-Sep-06	07-Sep-06 I3	08-Sep-06 I4	09-Sep-06	10-Sep-06 I4
11-Sep-06 I3	12-Sep-06	13-Sep-06 I6	14-Sep-06 AP_HH/HV, I1	15-Sep-06	16-Sep-06	17-Sep-06
18-Sep-06	19-Sep-06	20-Sep-06	21-Sep-06 I7	22-Sep-06	23-Sep-06 I2	24-Sep-06 I5
25-Sep-06	26-Sep-06 I3	27-Sep-06 AP HH/VV, I4	28-Sep-06	29-Sep-06 I5	30-Sep-06 I2	01-Oct-06
02-Oct-06 I7	03-Oct-06	04-Oct-06	05-Oct-06	06-Oct-06	07-Oct-06	08-Oct-06
09-Oct-06 IM_HH, I1	10-Oct-06 AP_HH/VV, I6	11-Oct-06	12-Oct-06 IM HH, I3	13-Oct-06 AP_HH/VV, I4	14-Oct-06	15-Oct-06 AP_HH/VV, I4
16-Oct-06 AP_HH/HV, I3	17-Oct-06	18-Oct-06 I6	19-Oct-06 AP_HH/HV, I1	20-Oct-06	21-Oct-06	22-Oct-06
23-Oct-06	24-Oct-06	25-Oct-06	26-Oct-06 AP HH/VV, I7	27-Oct-06	28-Oct-06 IM HH, I2	29-Oct-06 AP_HH/VV, I5
30-Oct-06	31-Oct-06 I3	01-Nov-06 AP_HH/VV, I4	02-Nov-06	03-Nov-06 AP_HH/VV, I5	04-Nov-06 I2	05-Nov-06
06-Nov-06 AP_HH/VV, I7	07-Nov-06	08-Nov-06	09-Nov-06	10-Nov-06	11-Nov-06	12-Nov-06
13-Nov-06 I1	14-Nov-06 I6	15-Nov-06	16-Nov-06 IM_HH, I3	17-Nov-06 AP_HH/VV, I4	18-Nov-06	19-Nov-06 I4
20-Nov-06 AP_HH/HV, I3	21-Nov-06	22-Nov-06 AP_HH/VV, I6	23-Nov-06 AP_HH/HV, I1	24-Nov-06	25-Nov-06	26-Nov-06
27-Nov-06	28-Nov-06	29-Nov-06	30-Nov-06 I7	01-Dec-06	02-Dec-06 IM_HH, I2	03-Dec-06 AP_HH/VV, I5
04-Dec-06	05-Dec-06 I3	06-Dec-06 I4	07-Dec-06	08-Dec-06 I5	09-Dec-06 I2	10-Dec-06
11-Dec-06 AP HH/VV, I7	12-Dec-06	13-Dec-06	14-Dec-06	15-Dec-06	16-Dec-06	17-Dec-06
18-Dec-06 I1	19-Dec-06 I6	20-Dec-06	21-Dec-06 AP_HH/VV, I3	22-Dec-06 I4	23-Dec-06	24-Dec-06 I4
25-Dec-06 I3	26-Dec-06	27-Dec-06 I6	28-Dec-06 AP_HH/HV, I1	29-Dec-06	30-Dec-06	31-Dec-06
01-Jan-07	02-Jan-07	03-Jan-07	04-Jan-07 I7	05-Jan-07	06-Jan-07 AP_HH/VV, I2	07-Jan-07 AP_HH/VV, I5
08-Jan-07	09-Jan-07 I3	10-Jan-07 I4	11-Jan-07	12-Jan-07 I5	13-Jan-07 I2	14-Jan-07
15-Jan-07 AP_HH/VV, I7	16-Jan-07	17-Jan-07	18-Jan-07	19-Jan-07	20-Jan-07	21-Jan-07
22-Jan-07 I1	23-Jan-07 I6	24-Jan-07	25-Jan-07 I3	26-Jan-07 I4	27-Jan-07	28-Jan-07 I4
29-Jan-07 AP HH/VV, I3	30-Jan-07	31-Jan-07 I6	01-Feb-07 I1	02-Feb-07	03-Feb-07	04-Feb-07
05-Feb-07	06-Feb-07	07-Feb-07	08-Feb-07 I7	09-Feb-07	10-Feb-07 AP HH/VV, I2	11-Feb-07 I5
12-Feb-07	13-Feb-07 I3	14-Feb-07 AP_HH/VV, I4	15-Feb-07	16-Feb-07 I5	17-Feb-07 I2	18-Feb-07
19-Feb-07 I7	20-Feb-07	21-Feb-07	22-Feb-07	23-Feb-07	24-Feb-07	25-Feb-07

Fig. 5.5. Calendar of potential and successful ASAR acquisitions over Doñana during the 2006-2007 hydrologic year. The ASAR swath is indicated for all cases. The acquisition configuration is specified for the successful acquisitions. Ground truth collection dates are also shown.

Mo.	Tu.	We.	Th.	Fr.	Sa.	Su.
26-Feb-07 I1	27-Feb-07 AP_HH/VV, I6	28-Feb-07	01-Mar-07 AP_HH/VV, I3	02-Mar-07 AP_HH/VV, I4	03-Mar-07	04-Mar-07 I4
05-Mar-07 I3	06-Mar-07	07-Mar-07 I6	08-Mar-07 I1	09-Mar-07	10-Mar-07	11-Mar-07
12-Mar-07	13-Mar-07	14-Mar-07	15-Mar-07 I7	16-Mar-07	17-Mar-07 I2	18-Mar-07 I5
19-Mar-07	20-Mar-07 AP_HH/VV, I3	21-Mar-07 I4	22-Mar-07	23-Mar-07 I5	24-Mar-07 I2	25-Mar-07
26-Mar-07 AP_HH/VV, I7	27-Mar-07	28-Mar-07	29-Mar-07	30-Mar-07	31-Mar-07	01-Apr-07
02-Apr-07 I1	03-Apr-07 AP_HH/VV, I6	04-Apr-07	05-Apr-07 I3	06-Apr-07 I4	07-Apr-07	08-Apr-07 I4
09-Apr-07 I3	10-Apr-07	11-Apr-07 AP_HH/VV, I6	12-Apr-07 I1	13-Apr-07	14-Apr-07	15-Apr-07
16-Apr-07	17-Apr-07	18-Apr-07	19-Apr-07 I7	20-Apr-07	21-Apr-07 AP_HH/VV, I2	22-Apr-07 I5
23-Apr-07	24-Apr-07 AP_HH/VV, I3	25-Apr-07 I4	26-Apr-07	27-Apr-07 I5	28-Apr-07 I2	29-Apr-07
30-Apr-07 AP_HH/VV, I7	01-May-07	02-May-07	03-May-07	04-May-07	05-May-07	06-May-07
07-May-07 I1	08-May-07 AP_HH/VV, I6	09-May-07	10-May-07 AP_HH/VV, I3	11-May-07 I4	12-May-07	13-May-07 AP_HH/VV, I4
14-May-07	15-May-07	16-May-07 AP_HH/VV, I6	17-May-07 I1	18-May-07	19-May-07	20-May-07
21-May-07	22-May-07	23-May-07	24-May-07 I7	25-May-07	26-May-07 AP_HH/VV, I2	27-May-07 I5
28-May-07	29-May-07 I3	30-May-07 I4	31-May-07	01-Jun-07 I5	02-Jun-07 AP_HH/VV, I2	03-Jun-07
04-Jun-07 AP_HH/VV, I7	05-Jun-07	06-Jun-07	07-Jun-07	08-Jun-07	09-Jun-07	10-Jun-07
11-Jun-07 I1	12-Jun-07 I6	13-Jun-07	14-Jun-07 AP_HH/VV, I3	15-Jun-07 I4	16-Jun-07	17-Jun-07 I4
18-Jun-07	19-Jun-07	20-Jun-07 AP_HH/VV, I6	21-Jun-07 AP_HH/VV, I1	22-Jun-07	23-Jun-07	24-Jun-07
25-Jun-07	26-Jun-07	27-Jun-07	28-Jun-07 I7	29-Jun-07	30-Jun-07 AP_HH/VV, I2	01-Jul-07 I5
02-Jul-07	03-Jul-07 I3	04-Jul-07 I4	05-Jul-07	06-Jul-07 I5	07-Jul-07 I2	08-Jul-07
09-Jul-07 I7	10-Jul-07	11-Jul-07	12-Jul-07	13-Jul-07	14-Jul-07	15-Jul-07
16-Jul-07 AP_HH/VV, I1	17-Jul-07 I6	18-Jul-07	19-Jul-07 AP_HH/VV, I3	20-Jul-07 I4	21-Jul-07	22-Jul-07 I4

Successful acquisition	I1, I2, ...I7	ASAR predetermined swaths
Potential acquisition	AP	Alternated Polarization acquisition mode
Ground truth collected	IM	Image acquisition mode
	HH, VV	Horizontal and vertical like-polar configuration
	HV	Cross-polar configuration

Fig. 5.5 cont. Calendar of potential and successful ASAR acquisitions over Doñana during the 2006-2007 hydrologic year. The ASAR swath is indicated for all cases. The acquisition configuration is specified for the successful acquisitions. Ground truth collection dates are also shown.

Table 5.2. Swath and number of the Alternated Polarization (AP) mode ASAR scenes targeted in this study.

ASAR swath	Number of images in AP mode	Polarization configuration
IS1	5	4 in HH/HV 1 in HH/VV
IS2	6	HH/VV
IS3	8	2 in HH/HV 6 in HH/VV
IS4	8	HH/VV
IS5	3 (not used)	HH/VV
IS6	9	HH/VV
IS7	7	HH/VV

5.5   Ground Truth Data

Ground truth data were collected on 28 days between March 2006 and June 2010. Table 5.3 lists the dates of the ground truth acquisition campaigns and the concurrent or closest ASAR scenes. On average the data consisted of 8-km long transects with 150 m spaced sampling points. The transects were undertaken on foot or on horseback riding. A total of 1,099 points were sampled. Flood stage, percentage of water, soil and vegetation coverage, and type of plant community were recorded at each point. Several photographs were also taken at the sampling locations. Persons or man-made objects such as note books or pencils were often included in the pictures for scale reference. A geographical information system data base (GIS) was built with the ground truth data for visualization, management and archiving purposes.

Fig. 5.6 shows the location of the sampling points for each ground truth acquisition campaign. Fig. 5.7 illustrates the information contained in the GIS database for each point. The ground truth data provided precious information for the correct interpretation of the ASAR scenes and the corresponding backscattering characterization of Doñana land cover types. Later on, it provided the needed spatial data for validating the classification algorithms developed in this research work.

Table 5.3. Dates of ground truth acquisition campaigns and concurrent ASAR scenes.

Ground truth data				ASAR images			
Acquisition date			Number of sampling points	Acquisition mode	Acquisition start time	Swath	Polarization configuration
13-Mar-06	14-Mar-06		77	ASA_IM	13-03-2006 22:09:37	IS1	HH
				ASA_IM	14-03-2006 10:23:39	IS6	HH
17-Apr-06			47	ASA_AP	17-04-2006 22:09:39	IS1	HH/VV
				ASA_AP	18-04-2006 10:23:41	IS6	HH/VV
27-Apr-06	28-Apr-06		61	ASA_AP	26-04-2006 22:26:43	IS6	HH/VV
				ASA_AP	27-04-2006 10:40:44	IS1	HH/VV
18-Sep-06	19-Sep-06	20-Sep-06	100	ASA_AP	14-09-2006 10:40:44	I1	HH/HV
20-Dec-06	21-Dec-06		32	ASA_AP	21-12-2006 22:15:28	IS3	HH/VV
13-Feb-07	14-Feb-07		65	ASA_AP	10-02-2007 22:12:33	IS2	HH/VV
				ASA_AP	14-02-2007 10:32:17	IS4	HH/VV
01-Mar-07	02-Mar-07		101	ASA_AP	01-03-2007 22:15:24	IS3	HH/VV
				ASA_AP	02-03-2007 10:29:27	IS4	HH/VV
03-Apr-07	04-Apr-07	05-Apr-07	160	ASA_AP	03-04-2007 10:23:42	IS6	HH/VV
09-May-07	10-May-07		113	ASA_AP	08-05-2007 10:23:46	IS6	HH/VV
				ASA_AP	10-05-2007 22:15:10	IS3	HH/VV
20-Jun-07	21-Jun-07		85	ASA_AP	20-06-2007 22:26:21	IS6	HH/VV
				ASA_AP	21-06-2007 10:40:37	IS1	HH/VV
23-Dec-09			37				HH/VV
24-Mar-10			42	ASA_AP	23-03-10 10:23	IS6	HH/VV
15-May-10	16-May-10		54		15-05-2010 22:12:20	IS2	HH/VV
					16-05-2010 10:26:23	IS5	HH/VV
28-Jun-10	29-Jun-10	30-Jun-10	125	ASA_AP	25-06-2010 22:23:41	IS5	HH/VV
					26-06-2010 10:37:44	IS2	HH/VV
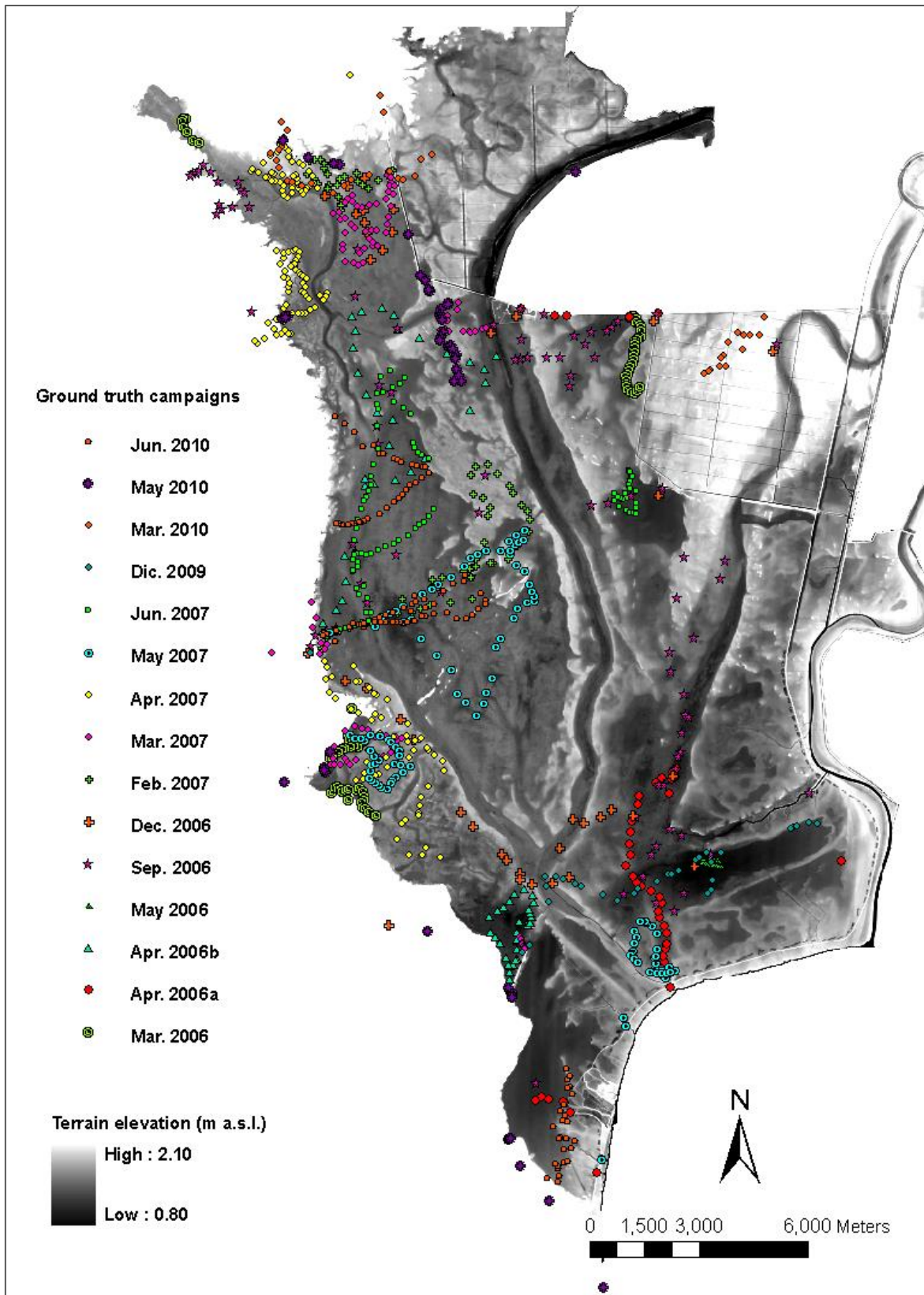
Fig. 5.6. Location of the sampling points and digital terrain model (DTM).
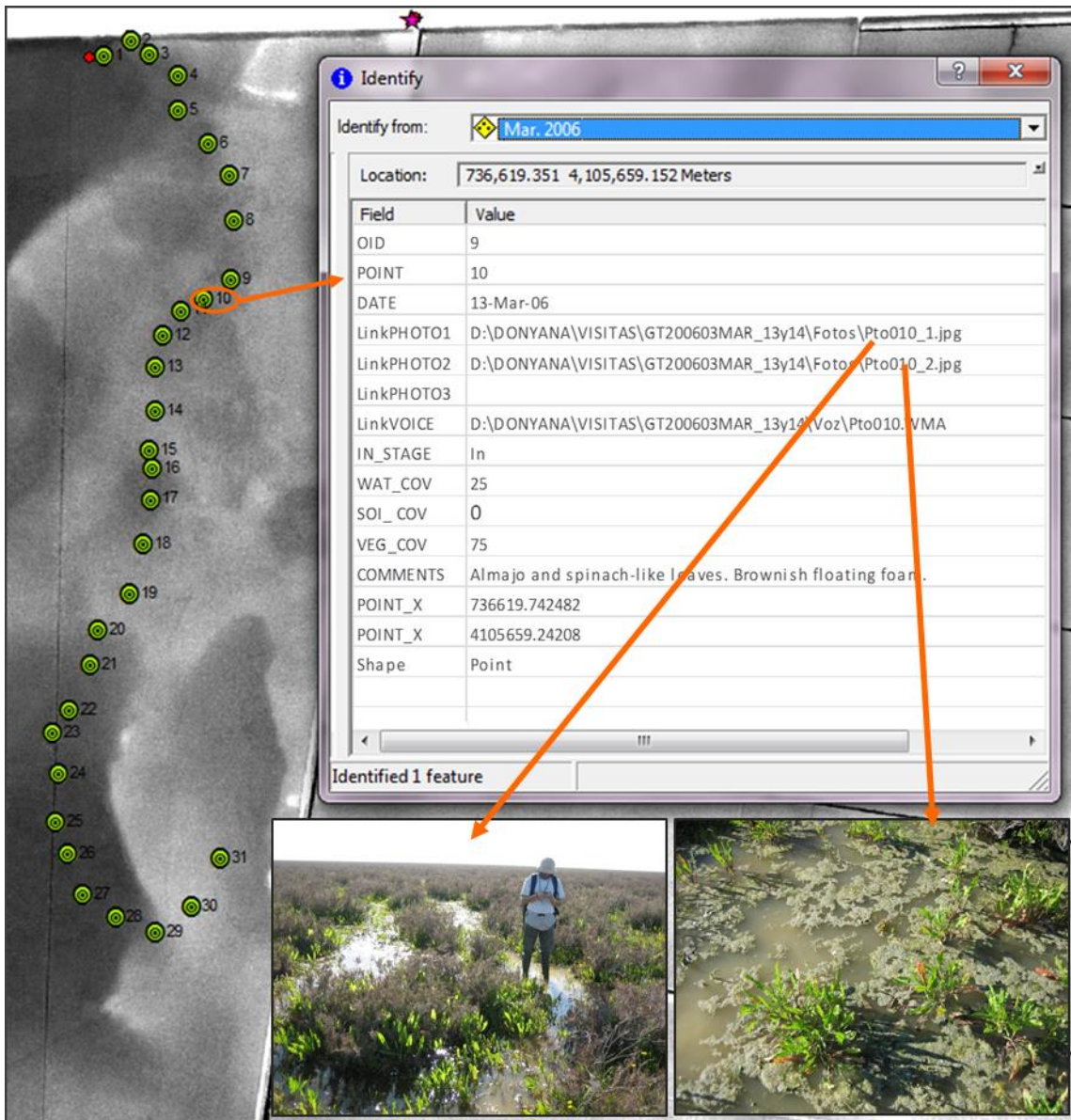
Fig. 5.7. Ground truth GIS and photographic data base: example of the information collected at each sampling point.

5.6   Digital Terrain Model

In September 2002 a LIDAR survey flight was conducted over Doñana marshes. The LIDAR data set was used to generate a digital terrain model (DTM) of 2.00 m^2 and 0.15 m planimetric and elevation resolution respectively (Ibáñez, 2008). The DTM pixel size was resampled at 12.5 x 12.5 m^2 in order to match the ASAR image products' pixel dimension and facilitate the conjunctive use of both data sources. Doñana's DTM is depicted in Fig. 5.6.

5.7   Hydrometeorological Field Data

A network of permanent hydrometeorological gauging stations was installed in September 2004 and operative until September 2010. The stations acquire 10-minute records of water level, water temperature, rainfall, wind direction and velocity, air temperature and humidity, soil temperature and incident and reflected visible and near infrared radiation (Ramos Fuertes, 2012).

The water levels measured at the time of the image acquisitions together with the marshes DTM were used to produce approximate flood maps in the neighborhood of the gauging stations, which helped interpret the ASAR data. Wind records and ASAR images acquired during persistent wind episodes were also used for calibrating the wind drag action in the marshes 2D hydrodynamic model, as discussed in Chapter 10 and Annex 6.

5.8   Vegetation Cartography

The Doñana marshes vegetal species have been surveyed and described within the framework of several studies and projects (Luque et al., 2005; García-Novo and Marín-Cabrera, 2005; Garcia-Murillo et al., 2007). This study used the detailed cartography of vegetation communities produced by Luque et al. (2005), which delineates the spatial distribution of over 100 different plant communities. The vegetation polygons in the Luque et al. (2005) map, represented in Fig. 5.8, were progressively merged to determine the spatial distribution of the broad categories almajar, helophytes and bare soil described in Chapter 4.   These are three main cover types in Doñana yielding a distinctive

backscattering response on the ASAR images, as observed in Martí-Cardona et al. 2010. Fig. 4.15 depicts the map of almajar, helophytes and bare soil obtained from the merging operations.

It has to be stressed that the Luque et al. (2005) map did not consider the Marisma Gallega area, designated as zone E in Fig. 4.15. In order not to exclude such a large area in the wetland from the research and ensuing flood mapping algorithm, the three abovementioned categories were approximately mapped in zone E, based on the terrain relative elevation, the backscattering characteristics and on-site observations in this zone.

Furthermore, none of the referred vegetation surveys mapped the strongly anthropized plant communities in regions A and B in Fig. 4.13, reason why these areas were not considered in the present research.
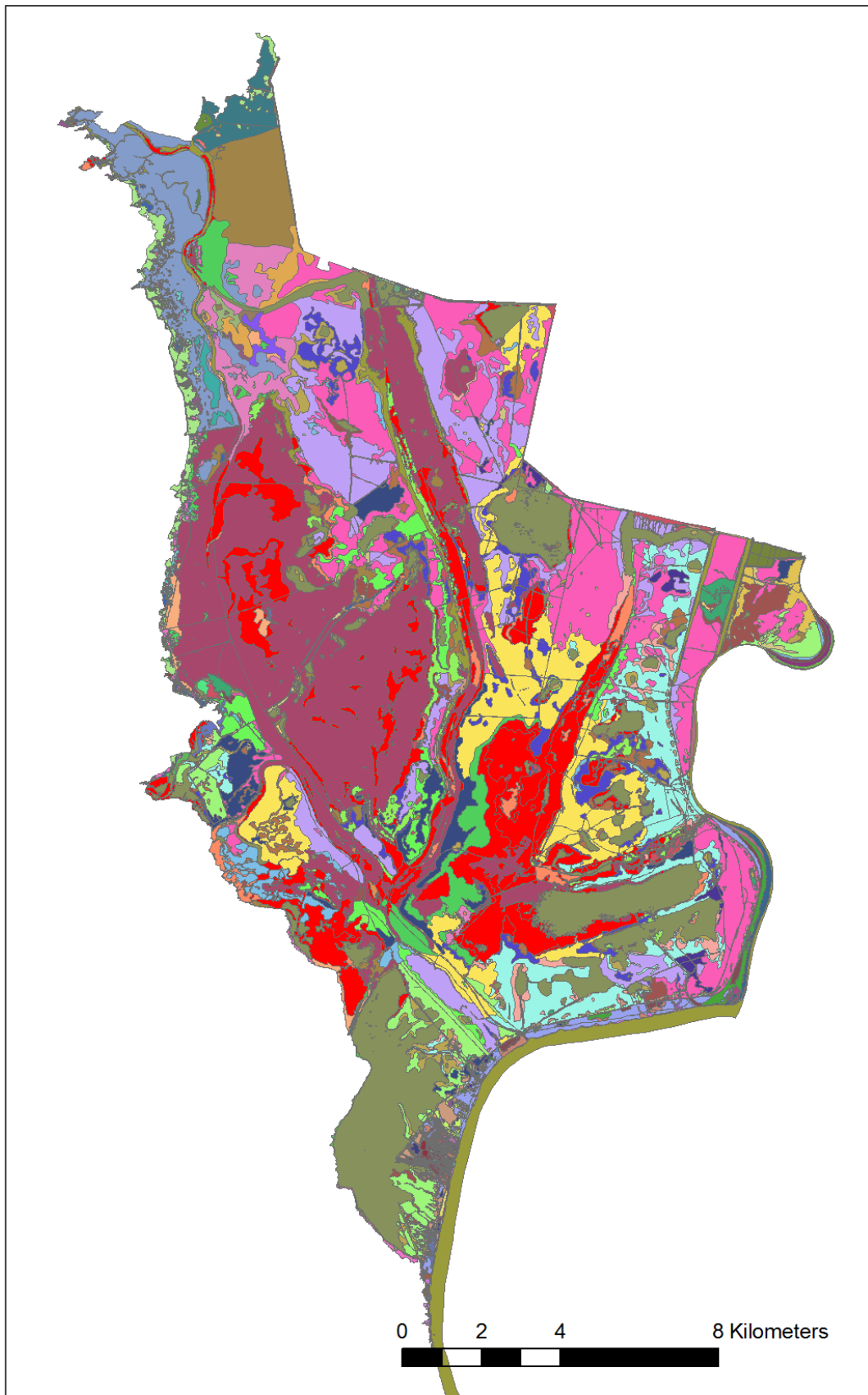
Fig. 5.8. Vegetation cartography of the Doñana wetland according to Luque et al., 2005. (the legend of vegetation communities is included in the next two pages).

Legend for Fig. 5.

- Arrozales
- Banda de necromasa con acompañantes
- Borde de caño con Spartina densiflora
- Caminos
- Canal artificial
- Casas
- Charcas
- Comunida de Eleocharis palustris y Scirpus maritimus
- Comunidad de Arthrocnemum macrostachyum y Scirpus maritimus en baja cobertura
- Comunidad de Arthrocnemum macrostachyum con Damasonium alisma en baja cobertura
- Comunidad de Arthrocnemum macrostachyum con Juncus subulatus
- Comunidad de Arthrocnemum macrostachyum con Juncus subulatus en zona mareal
- Comunidad de Arthrocnemum macrostachyum y Damasonium alisma con alta cobertura en zona marea
- Comunidad de Arthrocnemum macrostachyum y Damasonium alisma en alta cobertura
- Comunidad de Arthrocnemum macrostachyum y Juncus subulatus con baja cobertura en zona mareal
- Comunidad de Arthrocnemum macrostachyum y Juncus subulatus en baja cobertura
- Comunidad de Arthrocnemum macrostachyum y Sarcocornia perennis subsp. alpini
- Comunidad de Arthrocnemum macrostachyum, Damasonium alisma y Juncus subulatus
- Comunidad de Arthrocnemum macrostachyum, Damasonium alisma y Lythrum sp.
- Comunidad de Arthrocnemum macrostachyum, Damasonium alisma, Lythrum sp. y Juncus subulatus
- Comunidad de Arthrocnemum macrostahyum y Hordeum marinum acompañada de pastizal
- Comunidad de Cressa cretica en baja cobertura
- Comunidad de Crypsis aculeata y Cynodon dactylon con baja cobertura
- Comunidad de Cynodon dactylon y Damasonium alisma
- Comunidad de Damasonium alisma acompañado de Polypogon monspeliensis y Heliotropium supinum
- Comunidad de Damasonium alisma, Lythrum sp. y Cynodon dactylon
- Comunidad de Eleocharis palustris y Scirpus maritimus con baja cobertura
- Comunidad de Eleocharis paulstris y Cynodon dactylon con baja cobertura
- Comunidad de Heliotropium supinum
- Comunidad de Hordeum marinum acompañada de Plantago lanceolata y Trifolium sp.
- Comunidad de Hordeum marinum acompañado de pastizal denso
- Comunidad de Hordeum marinum y Plantago coronopus con abundante suelo desnudo
- Comunidad de Inula crithmoides y Arthrocnemum macrostachyum
- Comunidad de Inula crithmoides y Spartina densiflora
- Comunidad de Inula crithmoides, Puccinellia stenophylla y Sarcocornia fruticosa
- Comunidad de Inula crithmoides, Spartina densiflora y Limoniastrum monopetalum
- Comunidad de Juncus maritimus con Cynodon dactilon y otras gramineas acompañantes
- Comunidad de Limoniastrum monopetalum con Pistacia lentiscus
- Comunidad de Limoniastrum monopetalum y Arthrocnemum macrostachyum
- Comunidad de Limonium diffusum con Limonium ferulaceum
- Comunidad de Limonium ferulaceum y Lytrum tribracteatum acompañado de pastizal
- Comunidad de Lythrum tribracteatum
- Comunidad de Sarcocornia fruticosa con Sarcocornia perennis subsp. alpini
- Comunidad de Sarcocornia fruticosa y Halimione portulacoides
- Comunidad de Sarcocornia fruticosa y Spartina densiflora
- Comunidad de Sarcocornia perennis subsp. alpini con acompañantes
- Comunidad de Sarcocornia perennis subsp. perennis acompañada de Sarcocornia fruticosa
- Comunidad de Scirpus litoralis en baja cobertura
- Comunidad de Scirpus maritimus y Cressa cretica
- Comunidad de Scirpus maritimus con Arthrocnemum macrostachyum en alta cobertura
- Comunidad de Scirpus maritimus en baja cobertura
- Comunidad de Scirpus maritimus y Arthrocnemum macrostachyum en zona mareal
- Comunidad de Scirpus maritimus y Eleocharis palustris
- Comunidad de Scirpus maritimus y Eleocharis palustris en zona mareal
- Comunidad de Scirpus maritimus y Sarcocornia perennis subsp. alpini
- Comunidad de Scirpus maritimus, Arthrocnemum macrostachyum y Damasonium alisma
- Comunidad de Spartina densiflora y Halimione portulacoides

Legend for Fig. 5. (cont.)

Comunidad de Spartina densiflora y Phragmites australis

Comunidad de Typha latifolia con acompañantes

Comunidad dominada por Eryngium corniculatum

Comunidad dominada por Scirpus maritimus en alta cobertura en zona mareal

Comunidad dominada por Suaeda splendens

Comunidad dominana por Sarcocornia fruticosa

Cristalizadores

Cubetas con Arthrocnemum macrostachyum con baja cobertura en zona mareal

Cubetas con Arthrocnemum macrostachyum en cobertura media

Cubetas con vegetación halófila inferior al 10 % de cobertura

Explanadas de Sarcocornia perennis subsp. alpini y Damasonium alisma

Extensiones de Arthrocnemum macrostachyum

Extensiones de Arthrocnemum macrostachyum en zona mareal

Extensiones de Cressa cretica

Fangos desnudos

Juncus acutus en alta cobertura con pocas acompañantes

Limoniastrum monopetalum acompañado de halófilas arbustivas y herbáceas

Limoniastrum monopetalum acompañado de pastizal

Lucios

Monticulos con Silybum marianum acompañado de otros cardos

Muro de Limoniastrum monopetalum

Muro de nitrófilas

Muro intermedio con Arthrocnemum macrostachyum y Suaeda vera

Muro mareal con Halimione portulacoides y Sarcocornia fruticosa

Muros altos con Suaeda vera

Pastizal continuo de Scirpus litoralis

Pastizal de Cynodon dactylon acompañado de Ammi visnaga y Opuntia megacantha

Pastizal de Cynodon dactylon con acompañantes

Pastizal de Cynodon dactylon y legumiosas

Pastizal de Eleocharis palustris con Cynodon dactilon

Pastizal de Hordeum marinum

Pastizal de Scirpus litoralis acompañado de Cressa cretica

Pastizal de gramíneas y Plantago coronopus

Pastizal de vera

Pastizal de vera en arenas

Pastizal denso de Phragmites australis

Pastizales continuos de Scirpus maritimus

Pastizales mixtos de Scirpus maritimus y Scirpus litoralis en alta cobertura

Pastizales mixtos de Scirpus maritimus y Scirpus litoralis en baja cobertura

Pozas sin vegetación

Pradera de Halopeplis amplexicaulis

Praderas de Salicornia ramosissima

Praderas de Sarcocornia perennis subsp. alpini

Praderas de Sarcocornia perennis subsp. alpini en marisma alta

Rodales de Juncus maritimus

Río y Canales mareales

Sabinar

Spartina densiflora acompañada de quenopodiáceas de marisma media-baja

Suelo desnudo

Suelo desnudo con Suaeda vera y poblaciones de Narcissus serotinus y Narcissus sp.

Suelo desnudo con escasa vegetación dispersa

Suelo desnudo con escasa vegetación dispersa en zona mareal

Tarajal de plantación

Unidad de Pteridium aquilinum

Vegetación en cubetas hipersalinas

Vera de marisma con Juncus acutus, Rubus ulmifolius y Cynodon

Vetas con pastizal halófilo

5.9   Landsat Imagery

Landsat Thematic Mapper and Enhanced Thematic Mapper images of Doñana from Landsat 5 and Landsat 7 satellites, together with flood maps derived from them (Bustamante et al., 2009; Aragonés et all, 2005) were sporadically used throughout this research, when the ASAR and Landsat acquisitions coincided on cloud free dates. Initially, the comparison among both image types assisted the interpretation of the ASAR data, while later on this comparison helped validate the ASAR derived flood maps. Fig. 5.9 shows an early comparison between both data sources: the Envisat/ASAR scene from 10 February 2006, one of the first images ordered during the execution of this study, is shown at the background. The green line represents the inundation boundary extracted from the Landsat 5 image of 11 February 2006. The radar backscattering change between flooded and emerged surfaces becomes obvious, suggesting the sensitivity of the radar images to the flooding state. These sort of early comparisons greatly motivated further investigation and guided the initial ground truth campaigns.
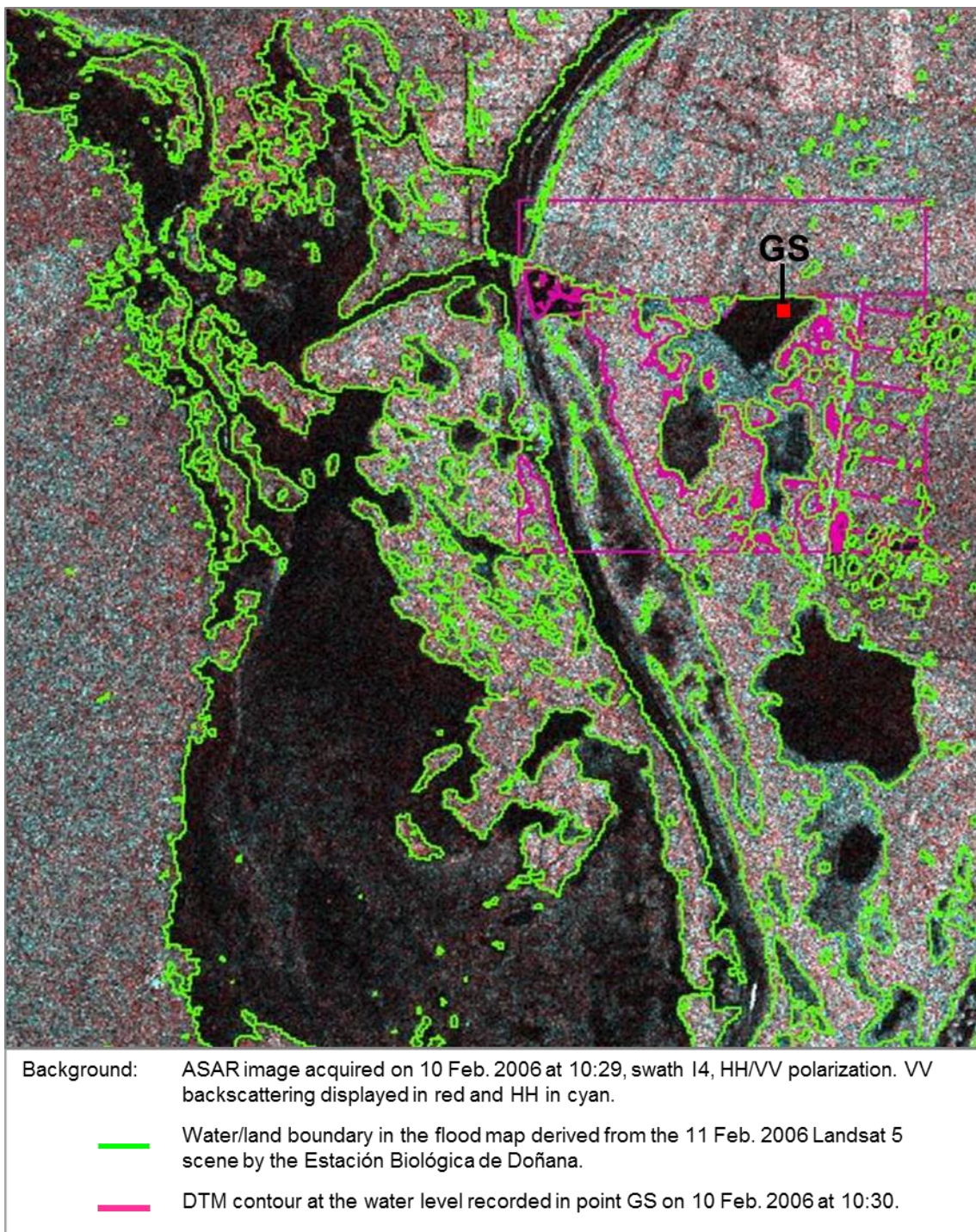
Fig. 5.9. Comparison among an Envisat/ASAR image, concurrent water elevation records and the flood boundary extracted from a nearly simultaneous Landsat 5 image.

5.10 References

Aragonés, D., Díaz-Delgado, R. and Bustamante, J., 2005. Tratamiento de una Serie Temporal Larga de Imágenes Landsat para la Cartografía de la Inundación Histórica de las Marismas de Doñana, XI Congreso Nacional de Teledetección, sep. 2005, Puerto de la Cruz, Tenerife, Spain.

Bustamante, J., Pacios, F., Díaz-Delgado, R., and Aragonés, D., 2009. Predictive Models of Turbidity and Water Depth in the Doñana Marshes using Landsat TM and ETM+ Images, Journal of Environmental Management, 2219-2225.

Doyle, A. C., 1887. A Study in Scarlet, Sherlock Holms series 1, Ward, Lock & Co, London, United Kingdom.

ESA, 2006. EnviSat ASAR Product Handbook, Issue 2.1, March 2006, European Space Agency.

García-Novo, F. and Marín-Cabrera, C., 2005. Doñana: Agua y Biosfera, Ministerio de Medio Ambiente, Madrid, Spain.

García-Murillo, P., Fernández-Zamudio, R., Cirujano, S. and Sousa, S., 2007. Flora y Vegetación de la Marisma de Doñana en el Marco del Proyecto de Restauración Ecológica Doñana 2005, Limnetica, 2, 319-330.

Ibáñez, E., 2008. Validación de Modelos Digitales del Terreno de Precisión a partir de Datos Láser Escáner Aerotransportado; Aplicación a la Marisma del Parque Nacional de Doñana, PhD Thesis, Universitat Politècnica de Catalunya, Barcelona, Spain.

Luque, C.J., Rubio-Casal, A.E., Álvarez, A.A., Muñoz, J., Vecino, I., Doblas, D., Leira, P., Redondo, S., Castillo, J., Mateos, E., Castellanos, E. and Figueroa, E., 2005. Memoria de Vegetación: Parque Nacional de Doñana. Proyecto de Cartografía y Evaluación de la Flora y Vegetación Halófita y de los Ecosistemas de Marismas que se encuentren dentro de la Red de Espacios Naturales Protegidos de Andalucía, Consejería de Medio Ambiente de la Junta de Andalucía & Universidad de Sevilla, Sevilla, Spain.

Martí-Cardona, B. & Dolz, J., 2005. La Teledetección como Herramienta de Monitorización de las Marismas de Doñana. Informe sobre Aplicaciones y Viabilidad. Internal report, Flumen, Universitat Politècnica de Catalunya, Barcelona, Spain.

Martí-Cardona, B. and Dolz., J., 2006. Progress report of project ESDJ0110: Monitoring of the Flooding and Dry-Out Processes in Doñana National Park for the Calibration, Refinement and Operation of the Hydrodynamic Model of its Marshes, submitted at ESA PI portal, July 2006.

Martí-Cardona, B., Dolz-Ripollés, J. and Gili-Ripoll, J., 2006. Monitoring of the Flooding and Dry-Out Processes in Doñana National Park for the Calibration, Refinement and Operation of the Hydrodynamic Model of its Marshes, Proceedings of the 1st GlobWetland Symposium: Looking at Wetlands from Space, ESA, 19-20 Oct., Frascati, Italy.

Martí-Cardona, B., López-Martínez, C. and Dolz-Ripollés, J., 2010. ASAR Polarimetric, Multi-Incidence Angle and Multitemporal Characterization of Doñana Wetlands for Flood Extent Monitoring, Remote Sensing of Environment, 114, 2802–2815.

Ramos Fuertes, A., 2012. Hidrometeorología y Balance Térmico de la Marisma de Doñana, PhD dissertation, Universitat Politècnica de Catalunya, Barcelona, Spain.

Chapter 6:
Preprocessing
of the ASAR Scenes

The radar power reflected by a target on the Earth's surface and received by the antenna depends on the SAR system configuration (transmitted power, frequency, incidence angle, polarization, antenna gain), on the propagation losses and on the target characteristics (basically material, dielectric constant, geometry and orientation regarding the SAR beam direction). Through the calibration process, the power backscattered from the different resolution cells on the Earth is normalized by the transmitted power, and is corrected for propagation losses, for antenna pattern and range spreading loss, and for the elevation angle change across range on a single acquisition (Oliver and Quegan, 2004; Freeman, 1992). For distributed targets, such as virtually the entire Doñana marshland area, the resultant calibrated value is referred to as the backscattering coefficient or σ^0. This coefficient is a physical quantity directly related to the ground target characteristics for a given incidence angle, frequency and polarization. It represents the proportion of the incident power that is reflected by the resolution cell per unit surface. The backscattering coefficient's physical units are m^2/m^2. However, due to its large dynamic range, σ^0 is normally expressed and graphed in decibel units (dB).

As indicated in Chapter 4, the Envisat/ASAR images of the 2006-2007 hydrological cycle were received geo-referenced from ESA. However, the synergistic use of the DTM and the images for filtering and flood mapping required a precise co-registration amongst both spatial data sources, and a refinement of the geocoding was needed to attain it.

Chapter 6 explains the process applied to the ASAR scenes to achieve their absolute calibration and their accurate co-registration to the existing DTM.

6.2. Absolute Calibration of the ASAR Scenes

All the images were received from ESA as radar brightness (i.e. antenna elevation gain and range spreading loss corrected but with no elevation angle compensation), and geo-referenced (ASA_APG_1P product; ESA, 2006). To perform the absolute image calibration and derive the radar backscattering coefficient σ^0 over distributed targets the following expression was applied at each image pixel (Rosich and Meadows, 2004):

$$\sigma^0 = \frac{DN^2}{K}\sin(\alpha)$$

where:

> K is an absolute calibration constant, which is derived from measurements over precision transponders and delivered for each image and polarization by ESA;
>
> DN^2 is the pixel intensity value;
>
> A is the local incidence angle at each pixel. The derivation of this angle is explained in the subsequent sections.

6.2.1 DERIVATION OF THE LOCAL INCIDENCE ANGLE BASED ON THE WGS84 ELLIPSOID

The local incidence angle is provided by ESA in the Geolocation Grid Annotated Data Set Record (LADS) for every scene granule. The LADS contain the local incidence angle based on the ellipsoid WGS84 at 11 points across range, also referred to as tie points, every 10 Km in the azimuth direction. A quadratic polynomial was fitted to the variation of the tie points' incidence angle versus sample numbers. This polynomial was then evaluated at every sample number to obtain the incidence angles at all range locations in the scene. The analysis was performed using the incidence angles for the mid-azimuth tie points and considering them constant in azimuth, as recommended in Rosich and Meadows (2004).

6.2.2 EFFECT OF THE TERRAIN SLOPE ON THE BACKSCATTERING COEFFICIENT

The local incidence angle derived as indicated in Section 6.2.1 is based on the WGS84 ellipsoid. The terrain slope in the SAR beam direction modifies the local incidence angle as illustrated by Fig. 6.1. Thus, to perform a precise absolute image calibration and derive the radar backscattering coefficient σ^0, knowledge of the local terrain slope is generally required. However, given the flatness of Doñana's topography flat terrain was assumed, i.e., the increment of the WGS84 incidence angle due to the terrain slope was neglected.
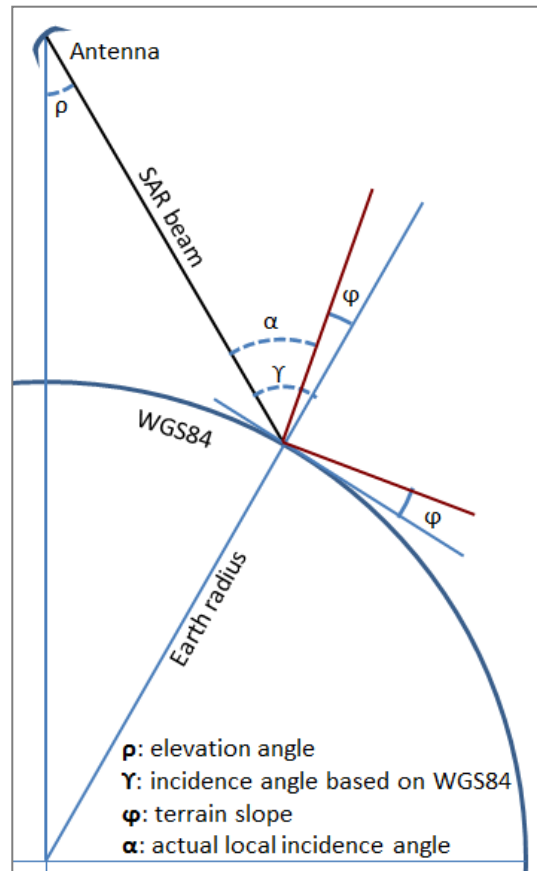
Fig. 6.1. SAR viewing geometry and effect of the terrain slope (φ) over the local incidence angle (α).

Fig. 6.2 depicts the Doñana's terrain in the SAR beam direction for the Envisat ascending track. Fig. 6.3 shows the terrain slope histogram in the same direction. The σ^0 relative error due to the flat terrain assumption is also plotted for IS1 and IS7 ASAR swaths. These plots reveal that the error is highest at the steepest incidence angle of swath IS1, but it keeps under 2.5% in 98% of the marshland area. The same error decreases below 1% for the same percentage of the area at IS7 images. The error takes intermediate values for swaths from IS2 to IS6.
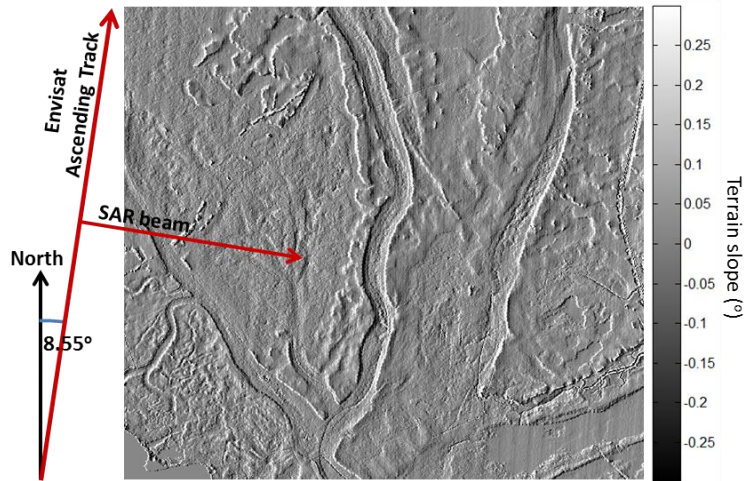
Fig. 6.2. Terrain slope in Doñana marshes (angle φ in Fig. 6.1), computed in the SAR beam direction.
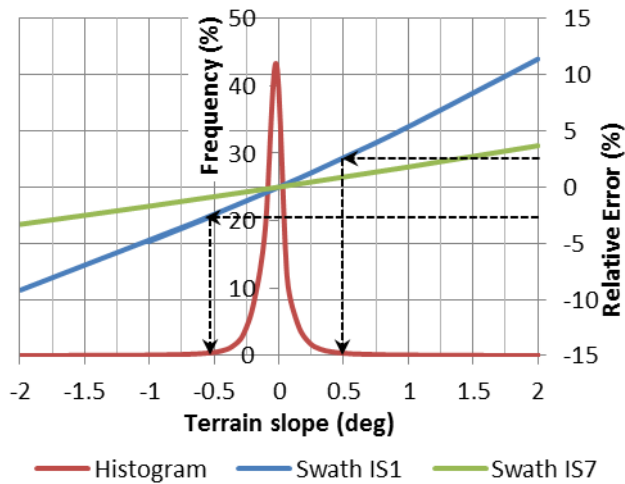
Fig. 6.3. Histogram of the terrain slope facing the SAR beam (φ in Fig. 6.1) in Envisat ascending track, and relative error in the backscattering coefficient computation due to neglecting the slope at swaths IS1 and IS7.

6.3. *Image and DTM Co-Registration*

It has been stressed in Chapter 4 that Doñana cover types are strongly related to the terrain topography. This relationship is exploited in Chapter 8 to select likely homogeneous filtering regions based on the marshes DTM.

The synergistic use of the DTM and the ASAR imagery required an accurate co-registration between both spatial data sources. However, misco-registrations were observed between the elevation model and the geocoded ASAR scenes, as exemplified by Fig. 6.4. A fragment of Doñana's DTM encompassing a winding watercourse is represented in Fig. 6.4a. The same area on the HH polarization ASAR image of 27 Feb. 2007 is shown in Fig. 6.4b. Both, the model and the satellite image, are represented in U.T.M. projection, zone 29, WGS84 datum. The 1.4 m contour, highlighted in yellow, closely follows the limits of the watercourse in Fig. 6.4a. When overlaid on the ASAR image in Fig. 6.4b, the yellow contours evidence a clear shift with regard to the dark watercourse. This shift had important effects on the quality of the DTM-base filtering, especially in the vicinity of small features such as narrow watercourses, as illustrated by Fig. 6.8 and Fig. 6.9.
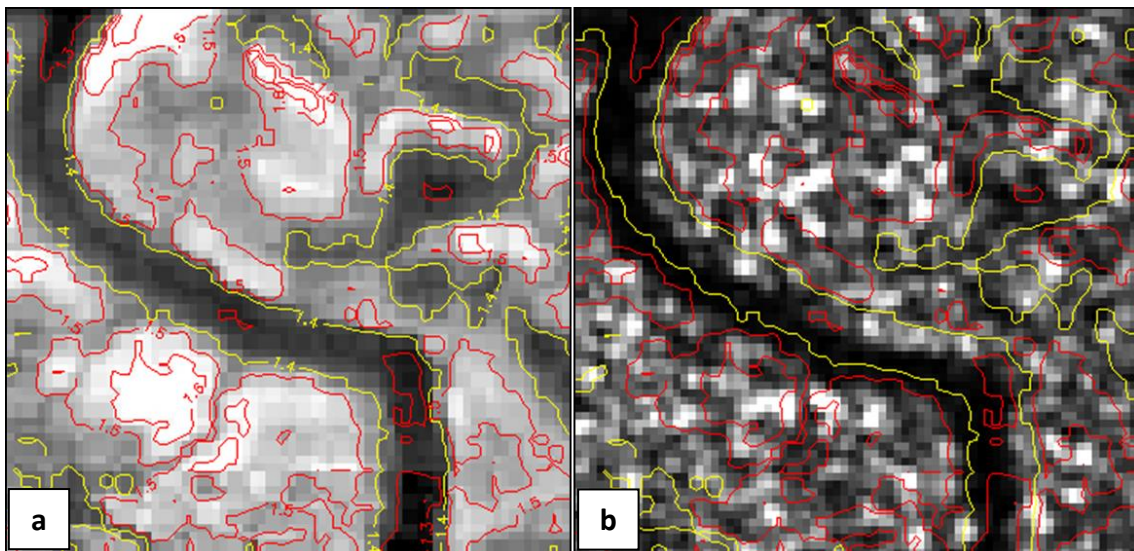
Fig. 6.4. Misco-registration between the elevation model and an ASAR image: a) Fragment of Doñana's DTM; b) same area on the HH ASAR scene from 27 Feb. 2007. Both images are represented in U.T.M. projection, zone 29, WGS84 datum. The red and yellow lines depict the DTM contours at 0.1 m increment.

The ASAR scenes acquired with the same geometry, i.e. the same incidence angle and track (ascending or descending), could be co-registered by simply sliding over each other a few rows or columns. Co-registration among different tracks and swaths was attempted by means of several software tools which searched for correlated pixel neighborhoods between pairs of images. None of the automated methods however yielded satisfactory results. This is presumably a consequence of the substantial changes in the marshes backscattering values between acquisition dates, due to changes in soil moisture, flood extent, surface water roughness and/or plant phenology. These changes, which add up to

those derived from the mere incidence angle variation, obscure the determination of correlated neighborhoods.

The coregistration was finally carried out by manually selecting ground control points (GCP) on the DTM (base image) and on one radar scene for each ASAR swath and track (warp image). Between 80 and 100 GCPs were selected for each case, meeting different authors' recommendations (Jensen, 1996; Liu and Mason, 2009). Fig. 6.5 and Fig 6.6 show the GCPs selected on the DTM and the images of 12 Dec. 2006 and 27 Feb. 2007.

Given that the geometric differences between the Envisat scenes and the DTM were subtle (approximately equivalent to a few pixels shift and a slight rotation) a first degree polynomial function was considered appropriate to define the coordinate transformation between them. The coefficients of the transformation polynomial were computed by minimum mean square error regression between the coordinates of the GCPs in the warp and base image (Chuvieco, 1990; Liu and Mason, 2009). During the GCP selection process, the points were purged so that the overall mean square error did not exceed 0.8 pixels. Fig. 6.7 shows the errors corresponding to the GCPs used for the geometric correction of the 12 Dec. 2006 image. Resampling of the pixel values was undertaken by means of the nearest neighbor method (Jensen, 1996; Liu and Mason, 2009). This is an appropriate resampling option for slight modifications of the image geometry, and it was particularly interesting in this case for preserving the statistical properties of the data.
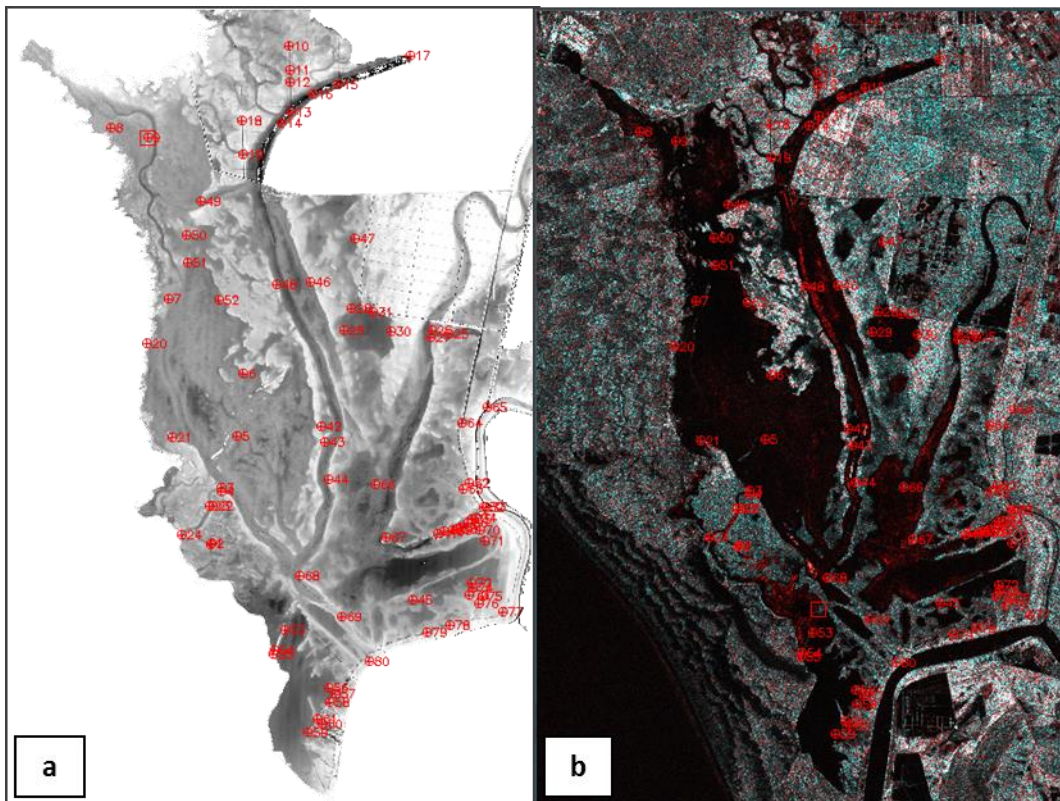
Fig. 6.5. Example of ground control points selection: a) marshes DTM used as the base image; b) ASAR scene from 27 Feb. 2007, swath IS6, descending track. VV is displayed in red and HH in cyan.
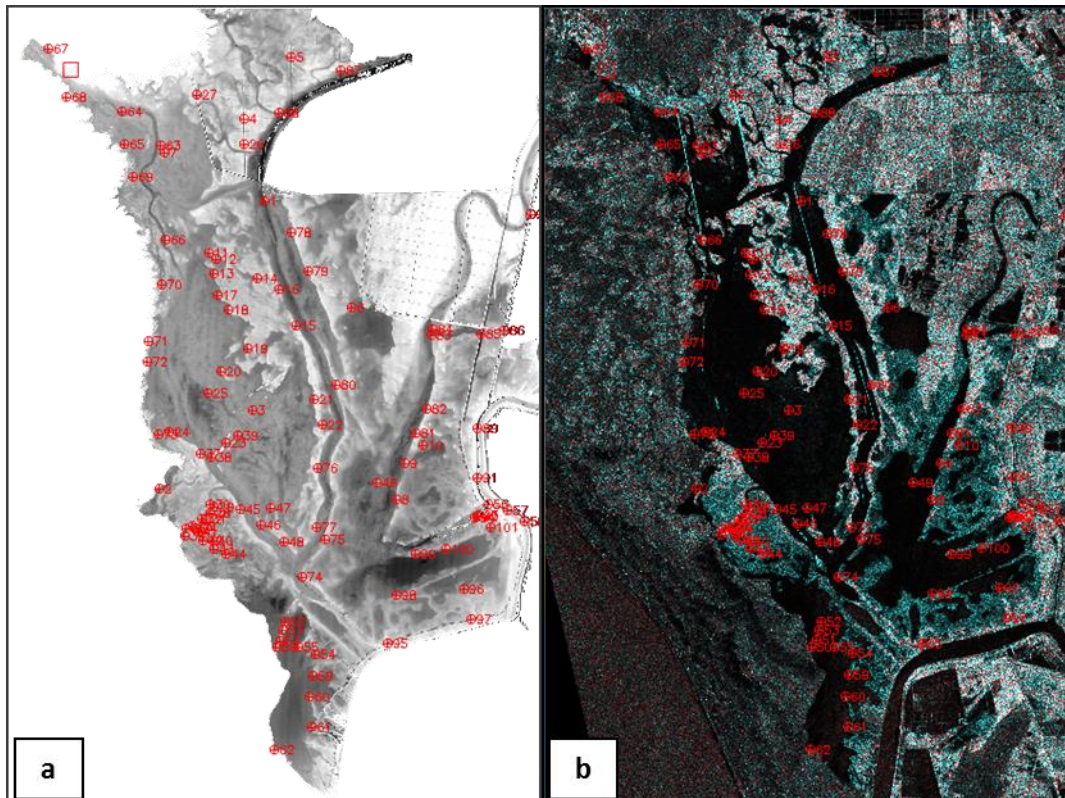
Fig. 6.6. Example of ground control points selection: a) marshes DTM used as the base image; b) ASAR scene from 12 Dec. 2006, swath IS3, ascending track. VV is displayed in red and HH in cyan.
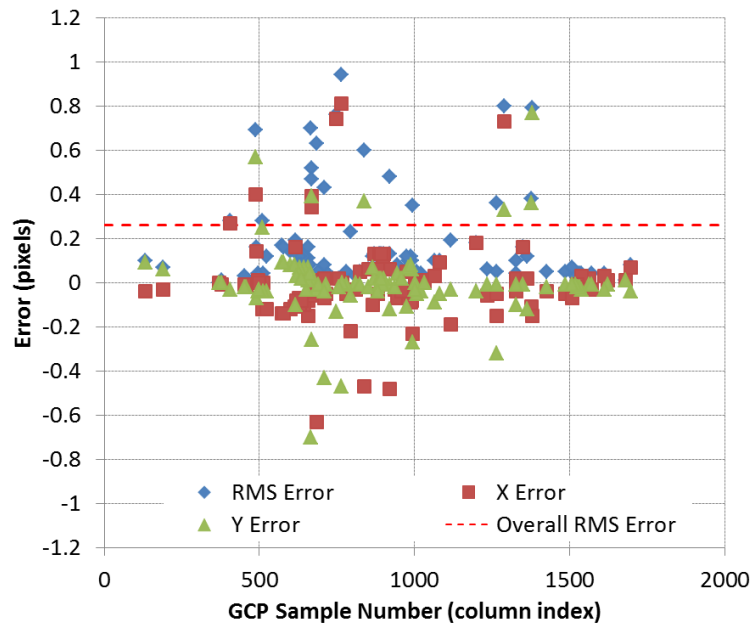
Fig. 6.7. X, Y and absolute co-registration residual errors for the 12 Dec. 2006 image GCP, depicted at each GCP warp image sample number.

Fig. 6.8 and Fig. 6.9 illustrate the benefits of an accurate coregistration between the DTM and the ASAR images. Fig. 6.8a and Fig. 6.9a are fragments of the ASAR scene from 27 Feb. 2007. Fig. 6.8b and Fig. 6.9b show the result of applying the DTM-based filter introduced in Chapter 8, using the original ASAR geocoding as received from ESA. Fig. 6.8c and Fig. 6.9c depict the result of applying the same filter after co-registering the ASAR scene to the DTM. It can be seen that the few-pixel shift between the satellite image and the DTM georeferences causes clear distortion of the watercourse in Fig. 6.8b, while the stream and other spatial features are significantly better defined in vignettes "c".

This research also made use of other spatial data sets, such as vegetation maps, which were also carefully co-registered to the DTM by the same GCP selection procedure as for the remote sensing images.
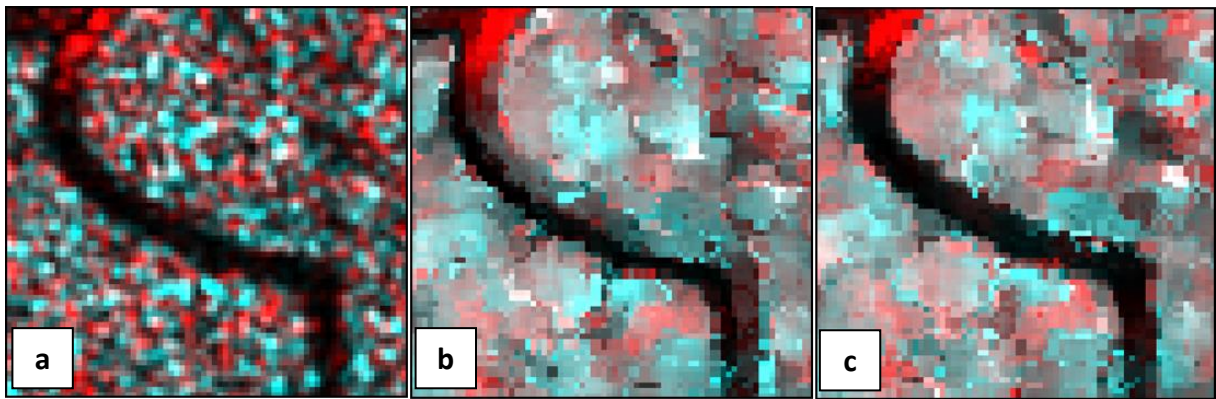
Fig. 6.8. **DTM and ASAR scenes co-registration effects on the image filtering: a) piece of the ASAR scene from 27 Feb. 2007, VV displayed in red and HH in cyan; b).result of applying the DTM-based filter before refining the co-registration; c) filtered image after refining the co-registration.**
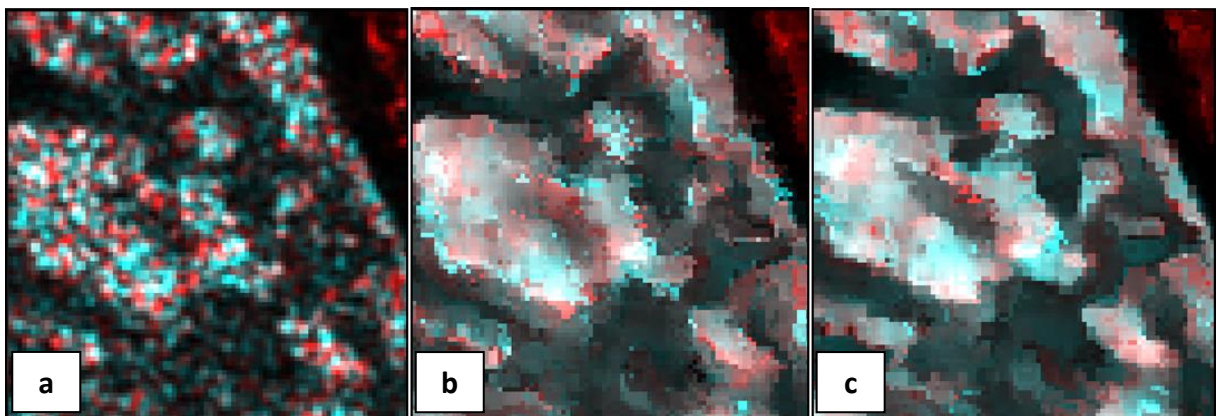
Fig. 6.9. **DTM and ASAR scenes co-registration effects on the image filtering: a) piece of the ASAR scene from 27 Feb. 2007, VV displayed in red and HH in cyan; b).result of applying the DTM-based filter before refining the co-registration; c) filtered image after refining the co-registration.**

6.4. References

Chuvieco, E., 1990. Fundamentos de Teledetección Espacial, Madrid, Spain: Ediciones Rialp.

ESA, 2007. ASAR Product Handbook, Issue 2.2: European Space Agency. (https://earth.esa.int/handbooks/asar/).

Freeman, A., 1992. SAR Calibration: an Overview, IEEE Transactions on Geoscience and Remote Sensing, Vol. 30, 1107-1121.

Jensen, J. R., 1996. Introductory Digital Image Processing: A Remote Sensing Perspective, 2nd edn., Englewood Cliffs, N.J., U.S.A.: Prentice-Hall.

Liu, J. G. and Mason, P., 2009. Essential Image Processing and GIS for Remote Sensing, Chapter 9, Chichester, U.K.: Wiley-Blackwell.

Oliver, C. and Quegan, S., 2004. Understanding Synthetic Aperture Radar Images, Chapter 2, Raleigh, N.C., U.S.A.: SciTech Publishing.

Rosich, B., and Meadows, P., 2004. Absolute Calibration of SAR Level-1 Products Generated with PF-ASAR, Issue 1.5: ESA Technical note, (https://earth.esa.int/c/document_library/get_file?folderId=38042&name=DLFE-661.pdf).

Chapter 7:
Backscattering Characterization of Doñana's Land Cover Types

7.1. Introduction

The objectives of this chapter are to characterize and understand the backscattering behavior of Doñana's land cover types, and to assess the feasibility of the ASAR scenes to monitor the marshes flood extent. To this aim, backscattering temporal signatures of Doñana main land cover types are determined at every available polarization and incidence angle throughout an entire hydrological cycle. Polarimetric behavior of the signatures is analyzed with the aid of extensive site data and plausible physical explanations to the observed backscattering features are suggested, based on the state of the art on radar-wetland interactions. Special attention is paid to the effect of the inundation on the classes' backscattering characteristics and conclusions regarding the flood mapping feasibility are drawn for each incidence angle. These conclusions are used in Chapter 9 to delineate inundation in Doñana from the ASAR scenes.

7.2 Methodology

The backscattering temporal behavior was characterized for the three main area types in Doñana, described in Chapter 4: paciles, ponds centers and transition zones. The subsequent sections describe the selection of the study period, the regions of interest (ROIs) representative of the different covers, and the determination of the corresponding flooding periods and temporal backscattering signatures.

7.2.1 STUDY PERIOD

The multi-incidence, polarimetric and temporal backscattering characterization of Doñana land covers was performed with the ASAR image time series from the 2006-2007 hydrological cycle for the reasons explained in Chapter 5 and summarized as follows:

The highest number of ASAR acquisitions over Doñana was achieved during this period;

The greatest ground truth data set was also acquired during the 2006-2007 cycle;

It was a wet year in which it was possible to observe partially flooded paciles;

A continuous series of water level and meteorological records were collected at Doñana gauging stations (Ramos Fuertes, 2012; Ramos Fuertes et al., 2009).

7.2.2 ROIS DEFINITION

Once the images were calibrated, 15 ROIs representative of the main land cover types in Doñana were selected. Fig. 7.1 shows the polygons defining these ROIs. The polygons include roughly 1,000 pixels each (15.6 ha), and were selected so that they comprised approximately flat areas with homogeneous vegetation. The ROIs are distributed as follows:

3 out of the 15 ROIs are located in the ponds centers and characterize the land cover class designated as *Deep Bare Soil*.

7 ROIs were defined in the transition zones. 4 of them correspond to communities dominated by the Castañuela, and characterize the class called *Castañuela*. The Bayunco is the main vegetation species found in the other 3 ROIs, which represent the class *Bayunco*.

5 ROIs are located in the paciles. 2 of them were defined in areas of almajar that flooded during the study period and have been designated as *Low Pacil*. The other 3 occupy slightly higher areas which did not flood and represent the class *High Pacil*.

The ROIs homogeneity was checked at every image by ensuring that their intensity coefficient of variation agreed with the Gamma theoretical one for uniform targets. This was almost always the case except on a few dates, at the beginning of the Bayunco emergence, when plants can start patching the water surface unevenly.
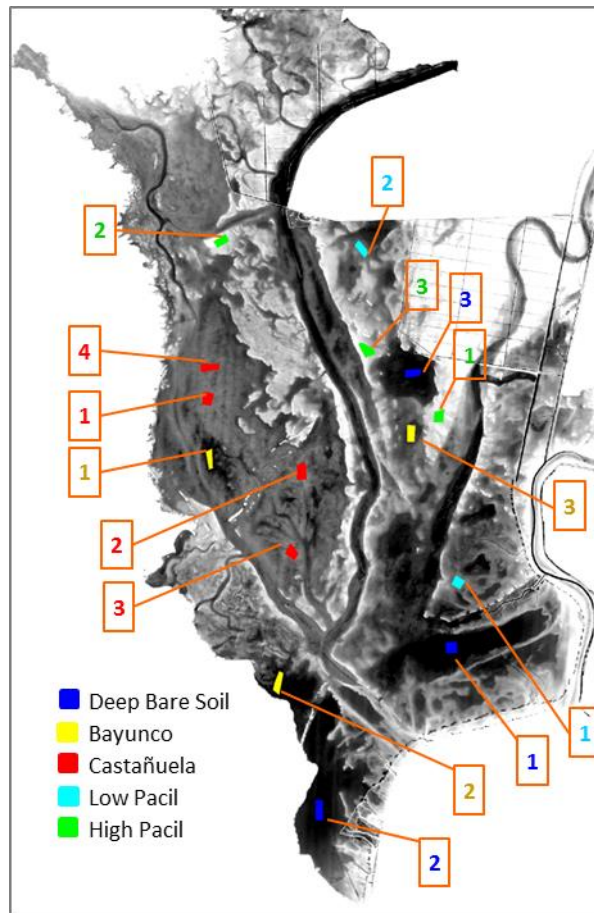
Fig. 7.1. ROIs representative of Doñana's main cover types, displayed over the DTM.

.

7.2.3 DETERMINATION OF THE ROIS FLOODING PERIOD

The analysis of the inundation effect on the ROIs backscattering characteristics required knowledge of each region flooding period. Ground truth data plus the DTM and the water level records were used to determine the dates on which the different ROIs flooded and emerged during the study period. Water level records were obtained from the Flumen's hydro-meteorological stations. Additional flood stage data were collected from the Espacio Natural de Doñana's gauging stations and from the site notes of the Estación Biológica de Doñana rangers (EBD-CSIC, 1971-Present). Landsat scenes were also used to aid the determination of the ROIs flooding period.

Given the extent of the ROIs (about 16 ha), these can take a few days to flood or emerge completely. The beginning and end of the flooding period were selected as the dates on which 50% of the regions area was below the closest water level, that is, as the dates on

which water elevation records nearby reached the ROI's terrain median elevation. Fig. 7.2 illustrates this selection.
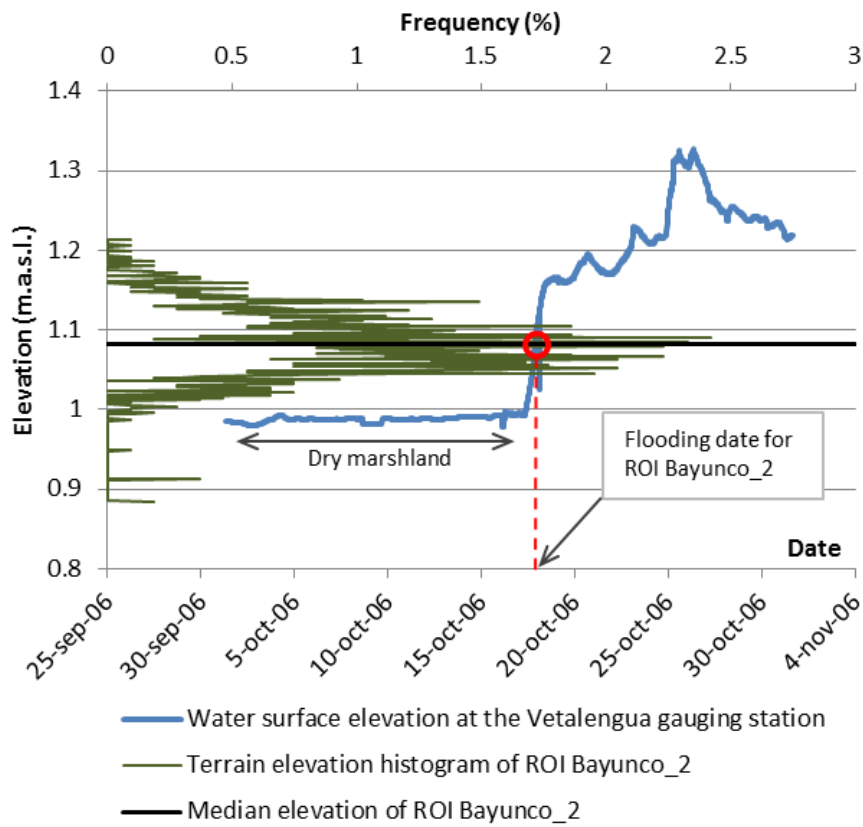
Fig. 7.2. Flooding date for ROI Bayunco 2, nearby the Vetalengua gauging station.

It has to be stressed that despite the data gathering effort, the extrapolation of the point water levels to the closest ROI's was unavoidable. Since this extrapolation could introduce certain error, the determined flooding periods should be taken as approximate. Given that the flooding and emergence dates for ROIs of the same class were quite close and that there is a few days uncertainty about them, a common average beginning and ending dates were chosen for every class. This class single flooding period simplifies its representation together with the ROIs backscattering signatures in the subsequent sections.

7.2.4 DETERMINATION OF THE BACKSCATTERING TEMPORAL SIGNATURES

For uniform distributed targets, the mean intensity represents the minimum variance unbiased estimator of the target's radar cross section (Goodman 1975). Accordingly, the temporal signatures were determined by computing the backscattering coefficient arithmetic mean of the pixels in each ROI for all available images and polarizations. Plots showing the average coefficient evolution for each class, incidence angle and polarization along the hydrologic year 2006-2007 were drawn and are presented in the next section in dB units. HH and VV backscattering ratios were also graphed, in order to analyze the polarimetric behavior of the land cover types.

7.3   Results and Discussion

The backscattering characteristics of the different land cover types observed before, during and after the inundation are presented and discussed in the following sub-sections:

7.3.1 LAND COVER TYPE: DEEP BARE SOIL

Deep Bare Soil ROIs consist on either even clayey soil, when they are emerged, or open water, when inundated (see Fig. 4.8 in Chapter 4). The dominant backscattering mechanism in both cases is surface scattering. Consistently with this mechanism, the temporal signatures of this class show higher σ^0 in VV than in HH polarization at all swaths, both before and after the inundation. A lineal regression of σ^0HH (dB) versus σ^0VV (dB) showed a similar consistency in the HH and VV relative behavior for the six ASAR incidence angles, with a slope $\Delta\sigma^0$VV/$\Delta\sigma^0$HH of 0.92 and R^2=0.93. Fig. 7.3 depicts the HH and VV relative behavior on the bare soil regions.

Fig. 7.4 shows the Deep Bare Soil backscattering signatures at ASAR swaths IS1 to IS7. These class ROIs were emerged in only 8 of the 43 ASAR images and virtually in all cases the backscattering coefficient of the emerged bare soil was higher than that from the flooded surface at the same swath and polarization.
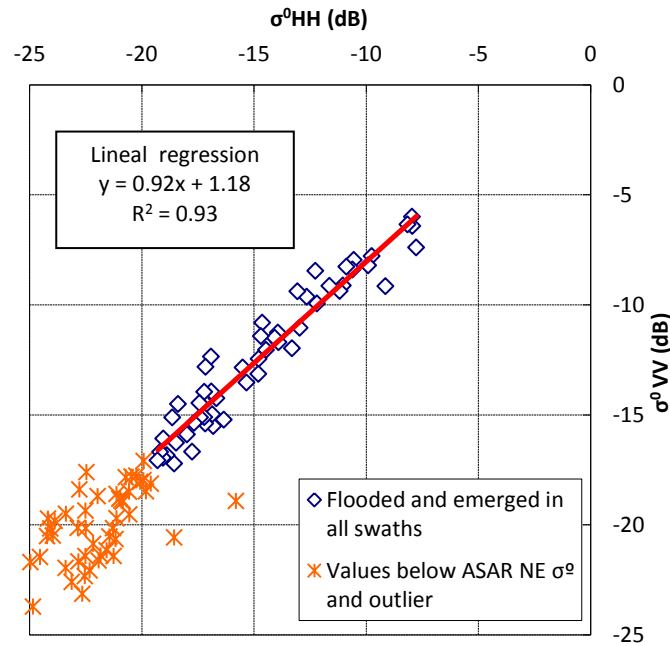
Fig. 7.3. σ^0HH and σ^0VV relative behavior for flooded and emerged bare soil regions at all ASAR swaths.

When the Deep Bare Soil ROIs are flooded, their backscattering is highly dependent on the wind-induced surface roughness at steep incidence angles (Leconte & Pultz, 1991; Brown et al., 1996; Kandus et all., 2001; Töyrä et all., 2001; Henderson & Lewis, 1998). Backscattering values have been compared with the wind velocity averaged for the six hours prior to each image acquisition, which is approximately the wind responsible for the water surface roughness at that time. The results showed that above a mean wind velocity of about 1.5 m/s there is a positive correlation between wind speed and σ^0 at swaths IS2, IS3 and IS4 (there are not enough data at IS1). Fig. 7.4b, Fig. 7.4c and Fig. 7.4d illustrate this correlation.

Under low wind conditions the open water σ^0 is very small, often below the ASAR noise equivalent σ^0, what can be explained by the fact that the incident radar beam is specularly reflected away from the sensor by the smooth water surface. Large incidence angles of swaths IS6 and IS7 also induce high amount of specular reflection (Leconte & Pultz, 1991; Brown et al., 1996; Kandus et all., 2001; Töyrä et all., 2001; ; Henderson & Lewis, 1998). Thus, backscattering at these swaths is generally low (under -15 dB) and less correlated with the wind speed than swaths IS2 to IS4 (Fig. 7.4e and Fig. 7.4f).

Backscattering differences between emerged and flooded Deep Bare Soil have been found to be lower in HH than in VV polarization. The minimum observed σ^0HH change before

and after the inundation is lowest at IS1 and IS6. The smallest σ^0 difference at IS1 was observed on a windy day and can be explained by the high sensitivity of steep incidence angles to the water surface roughness. In the case of IS6 images, the shallow incidence angle causes high amount of specular reflection of the radar beam not only on the open water but also on the smooth bare clayey soil. Therefore, the σ^0 differences and, hence, the separability between emerged and flooded surface are smaller at IS1 and IS6 than at IS3 and IS4. Fig. 7.5 illustrates the separability of flooded versus emerged Deep Bare Soil at swaths IS3, IS4 and IS6.
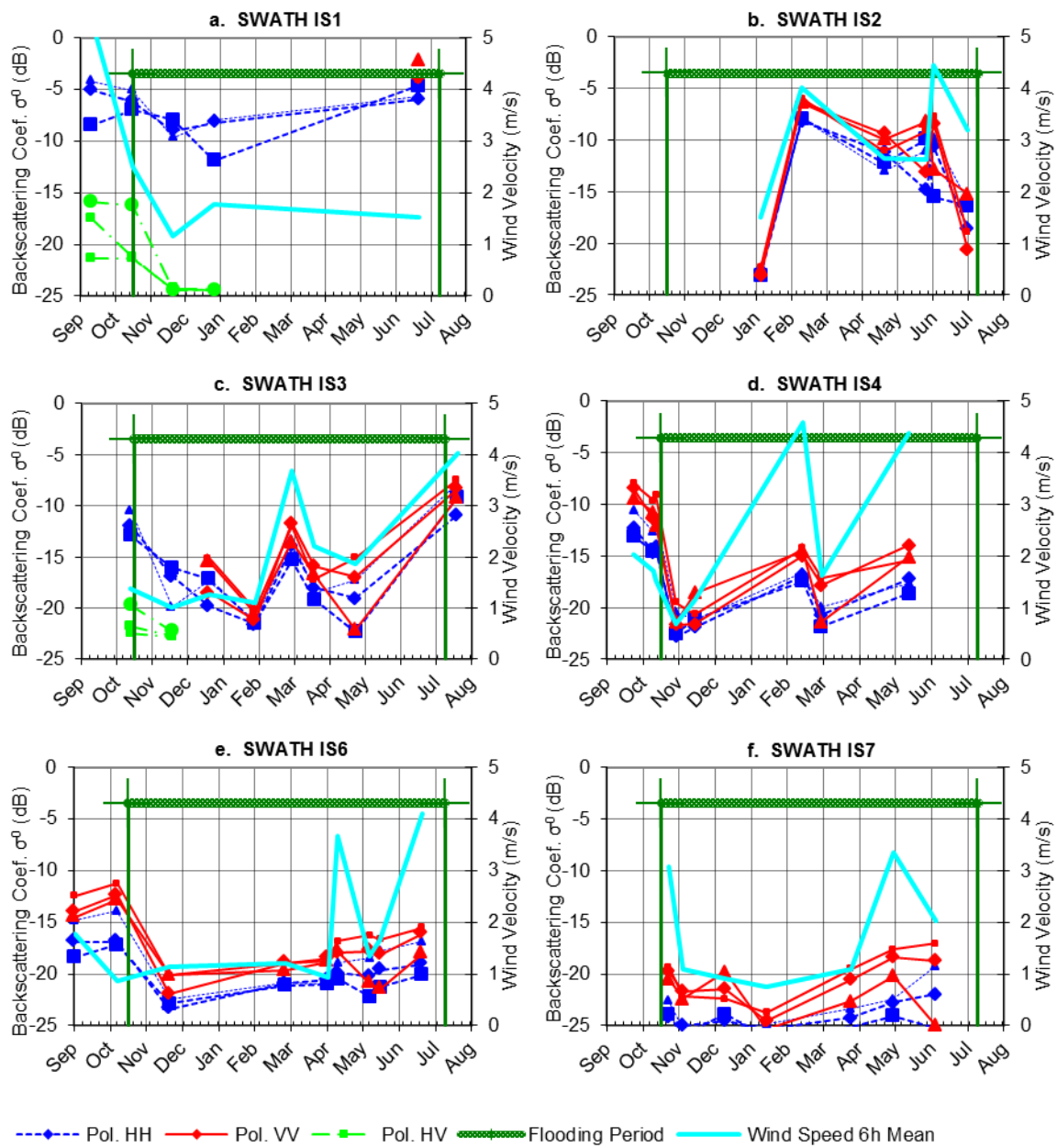
Fig. 7.4. Deep Bare Soil ROIs σ0HH and σ0VV evolution during the 2006-2007 hydrologic cycle at swaths IS3 (a), IS4 (b) and IS6 (c). Wind velocity averaged for the 6 hours prior to each image acquisition is also represented.
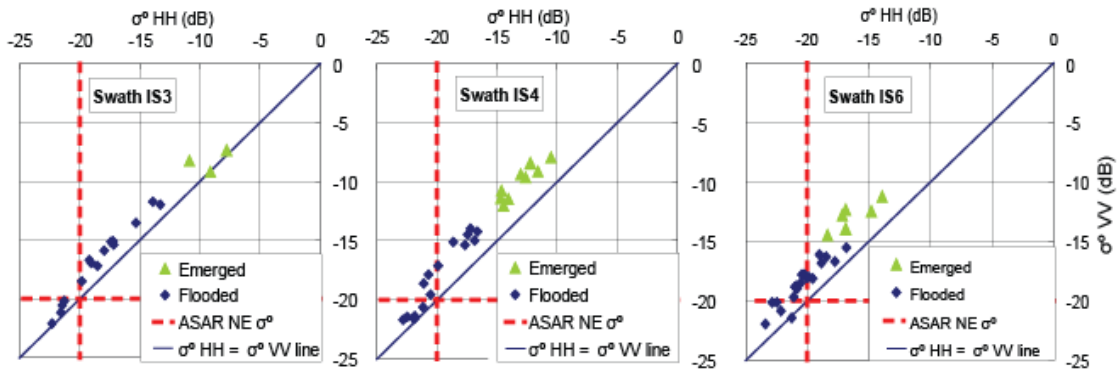
Fig. 7.5. Scatter plots of σ⁰HH vs. σ⁰VV in the Deep Bare Soil ROIs at swaths IS3, IS4 and IS6.

The number of cross-polarized data is limited to 6 images at swaths IS1 and IS3. σ^0HV values are in all cases low or below the ASAR noise equivalent σ^0. The backscattering mechanism of the Deep Bare Soil class is surface scattering on a relatively smooth surface throughout the study period. This mechanism induces little depolarization of the electromagnetic radiation, what explains the low observed σ^0HV.

7.3.2 LAND COVER TYPES: HIGH PACIL AND LOW PACIL

The High Pacil ROIs did not flood during the study period, although they occasionally became swamped after strong rainfall events, such as the one on 28 January 2007, only a few hours before the IS3 image acquisition on 29 January (Fig. 7.6c). The ROIs of class Low Pacil were flooded approximately from 11 November 2006 to 10 May 2007. Fig. 4.9 in Chapter 4 portrays flooded and emerged pacil areas.

Fig. 7.6 depicts the High and Low Pacil backscattering coefficient evolution at ASAR swaths IS1 to IS7during the 2006-2007 hydrologic cycle. Right after the summer the soil is very dry everywhere in the pacil and the backscattering coefficients of Low and High Pacil are close to each other. Focusing on the High Pacil ROIs, a similar backscattering temporal pattern is observed in them for all swaths: σ^0HH and σ^0VV take their lowest values at the beginning of the hydrologic year, when the soil is dry. They rise during the marshes flooding period, due presumably to the higher soil humidity, and go down again from April on, when the soil progressively dries out again. The High Pacil ratio σ^0HH/σ^0VV shows a moderate increase during the flooding period at all swaths (Fig. 7.7a), and no significant effect of the incidence angle is observed on this parameter.

When the Low Pacil floods, σ^0 experiences a significant drop at swaths IS2, IS3 and IS4 with regard to those of the High Pacil (Fig. 7.6b, Fig. 7.6c, Fig. 7.6d), and this drop is more acute in VV than in HH. The σ^0 decrease could be explained by the lost of the surface scattering from bare soil and short pasture, which get covered by water and therefore induce forward reflection of the radar beam. A sound interpretation for the differential behavior between polarizations would be that double bounce is the dominant backscattering mechanism and that it is higher at HH than at VV polarization (Wang et all., 1995). This polarimetric response of the almajo would be explained by a preferential orientation of the almajo stems, but has not been explored in detail yet.

At large incidence angles of swaths IS6 and IS7 polarimetric effects of the flooded Low Pacil signature are reduced (Fig. 7.6e, Fig. 7.7f). This could be explained by the fact that the path length through the almajo bushes increases and the direct volume backscattering mechanism becomes dominant. The differential behavior between polarizations is a key backscattering characteristic to discriminate emerged versus flooded pacil. Fig. Fig. 7.8 illustrates the reduction of polarimetric differences, and therefore separability, with the incidence angle increase.

Soon after the flooding period, in June, the ratio $\sigma^0 HH / \sigma^0 VV$ of the Low and High Pacil takes again similar values (Fig. 7.7), but the backscattering coefficient from the Low Pacil is greater than that from the High Pacil (Fig. 7.6), presumably as a result of the rather higher humidity of the just unflooded soil.
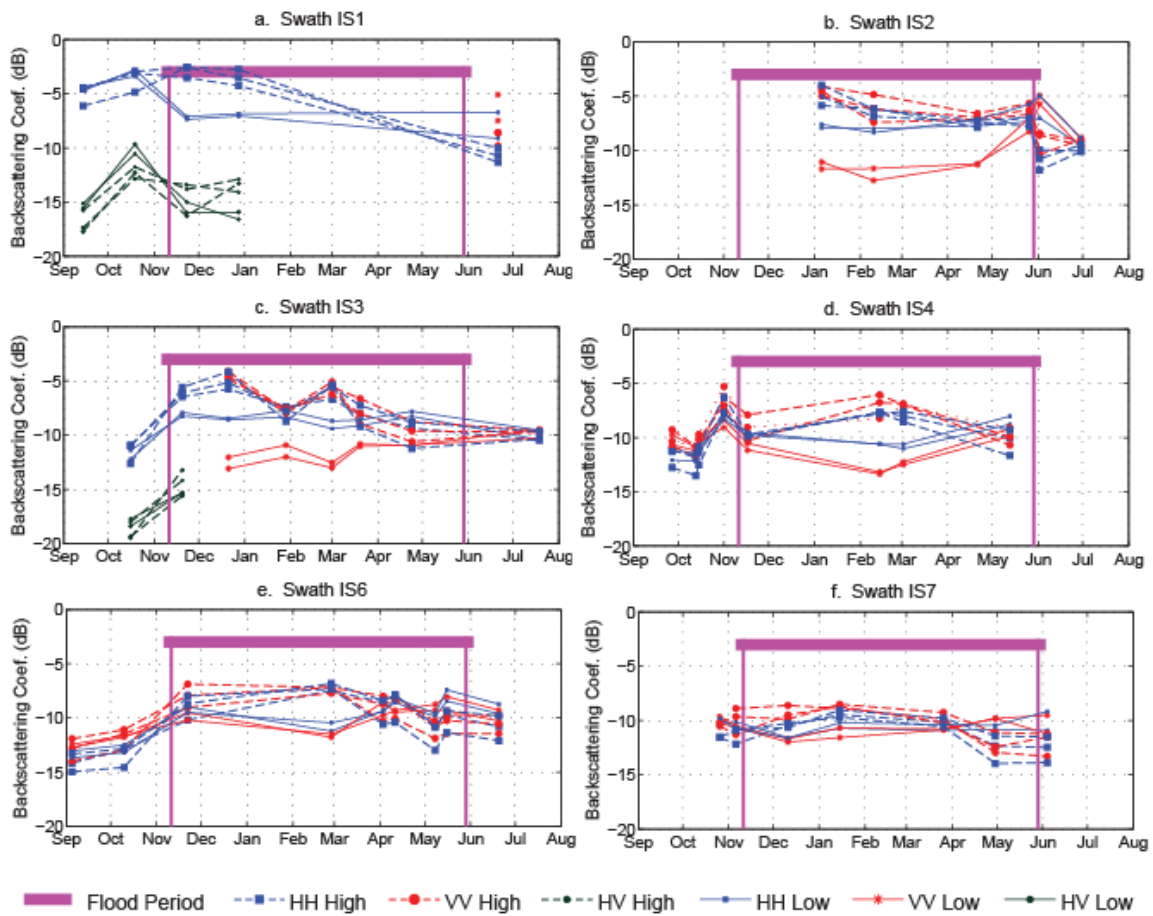
Fig. 7.6. High and Low Pacil ROIs σ0HH and σ0VV evolution during the 2006-2007 hydrologic cycle at swaths IS1, IS2, IS3, IS4, IS6 and IS7.
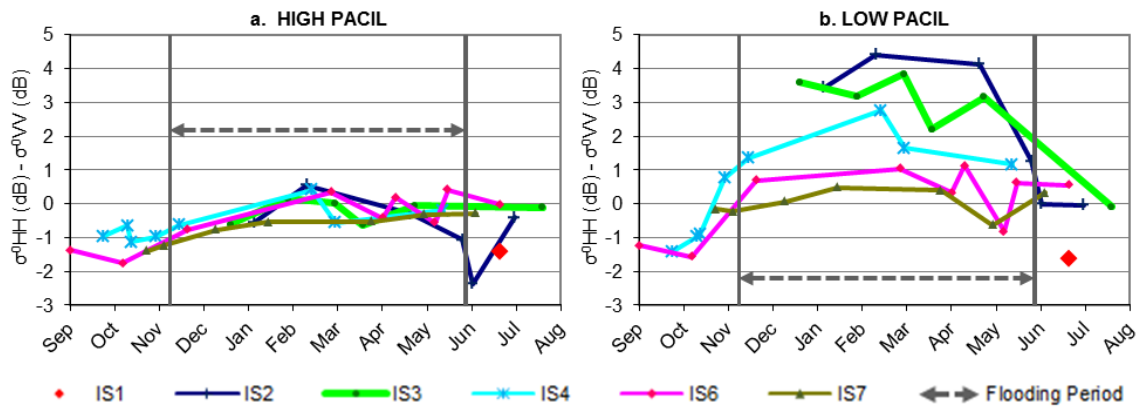
Fig. 7.7. High and Low Pacil ROIs σ0HH/σ0VV ratio evolution during the 2006-2007 hydrologic cycle at swaths IS1, IS2, IS3, IS4, IS6 and IS7.
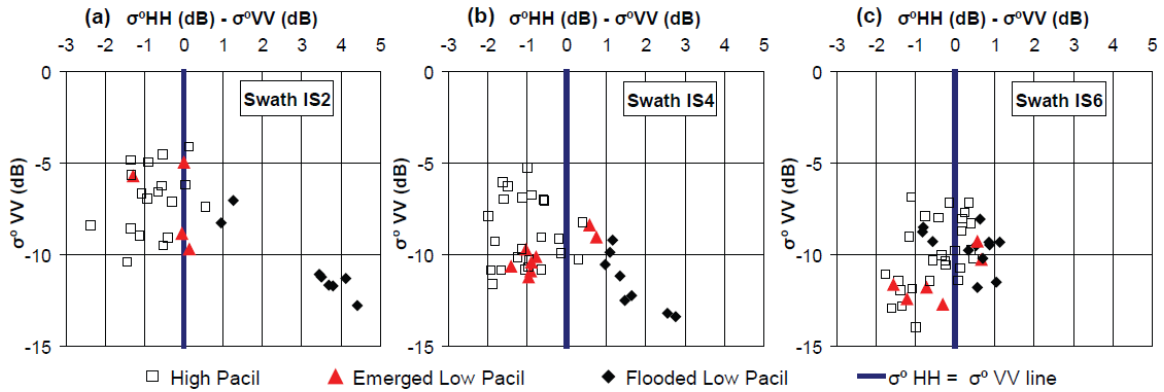
Fig. 7.8. Scatter plots of σ0HH/σ0VV ratio versus σ0VV in the High and Low Pacil ROIs at swaths IS2, IS4 and IS6.

7.3.3 LAND COVER TYPES: BAYUNCO AND CASTAÑUELA

Fig. 7.9 depicts the Bayunco and Castañuela ROIs backscattering signatures during the 2006-2007 hydrologic cycle. Five stages are identifiable in these signatures, although images for at least one of the stages are missing at each swath. The stages depend on the ROIs water content (dry, wet, flooded) and the phenological phase of the vegetation (dry, green, density and emerging height). The five stages and the polarimetric multi-incidence angle radar response at each of them are discussed as follows:

Stage 1. In September, at the beginning of the hydrologic year, soil and vegetation are dry. Consistently with the reduced moisture content, the observed Bayunco and Castañuela backscattering is lower than in stages of wet soil or green emerged vegetation. Castañuela σ^0 ranges between -18 and -14 dB and Bayunco σ^0 between -16 and -11 dB at IS3, IS4 and IS6 (Fig. 7.9). The only available IS1 image in the same period shows σ^0 values substantially higher, in the order of -8 dB for the Castañuela and -5dB for the Bayunco. This high backscattering at IS1 could be due, in large part, to the summer cloudburst that took place in the night, 11 hours before the image acquisition, and that caused momentary soil and vegetation wetness.

Stage 2. From the beginning of the rainfall period, on 16 October 2006, until the inundation, in November, the Castañuela ROIs were permanently wet. The ASAR images in this period, at swaths IS1, IS4 and IS7, show backscattering values between -11 and -6 dB in the Castañuela ROIs, clearly higher than those for the previous dry soil stage (Fig. 7.9b1, Fig. 7.9b4, Fig. 7.9b6). The backscattering increment in this phase is assumed to be

wetness-induced and is well illustrated by the IS4 temporal signature (Fig. 7.9b4). Bayunco regions flooded earlier than Castañuela's and only one IS1 ASAR image was acquired between the beginning of the rainfall period and the inundation of two of the Bayunco ROIs (Fig. 7.9a1). Backscattering of the Bayunco ROIs at this second stage was about -4 dB, only 1 dB higher than in the previous stage, after a summer cloudburst.

Stage 3.   Bayunco and Castañuela ROIs flooded approximately on 25 October 2006 and 6 of November 2006, respectively. During this phase brown Bayunco and Castañuela stems stick out of the water surface in an amount dependant basically on the water depth and the time elapsed after the inundation (dry plants progressively putrefy and sink). A clear decrease in σ^0 is observed respect to stage 2 at all swaths, what can be explained by the partial forward reflection of the radar beam on the water surface.

Castañuela regions show lower backscattering than in the previous stage of emerged wet soil at IS3, IS4 and IS7 (Fig. 7.9b), but similar to the first dry soil phase at IS3, IS4 and IS6 (no data are available to perform the same comparison at the rest of the swaths). Unlike the Castañuela, Bayunco backscattering in this stage is always lower than in the previous ones, especially at HH polarization (Fig. 7.9a).

It is worth mentioning that the Castañuela and Bayunco ROIs water surface remains rather smooth even on windy days, presumably as a result of the wind energy attenuation effect of the submerged vegetation. High backscattering from roughened water surface clearly distinguishes the flooded bare soil areas from the flooded Bayunco and Castañuela on windy days at this stage, as illustrated by Fig. 7.10.
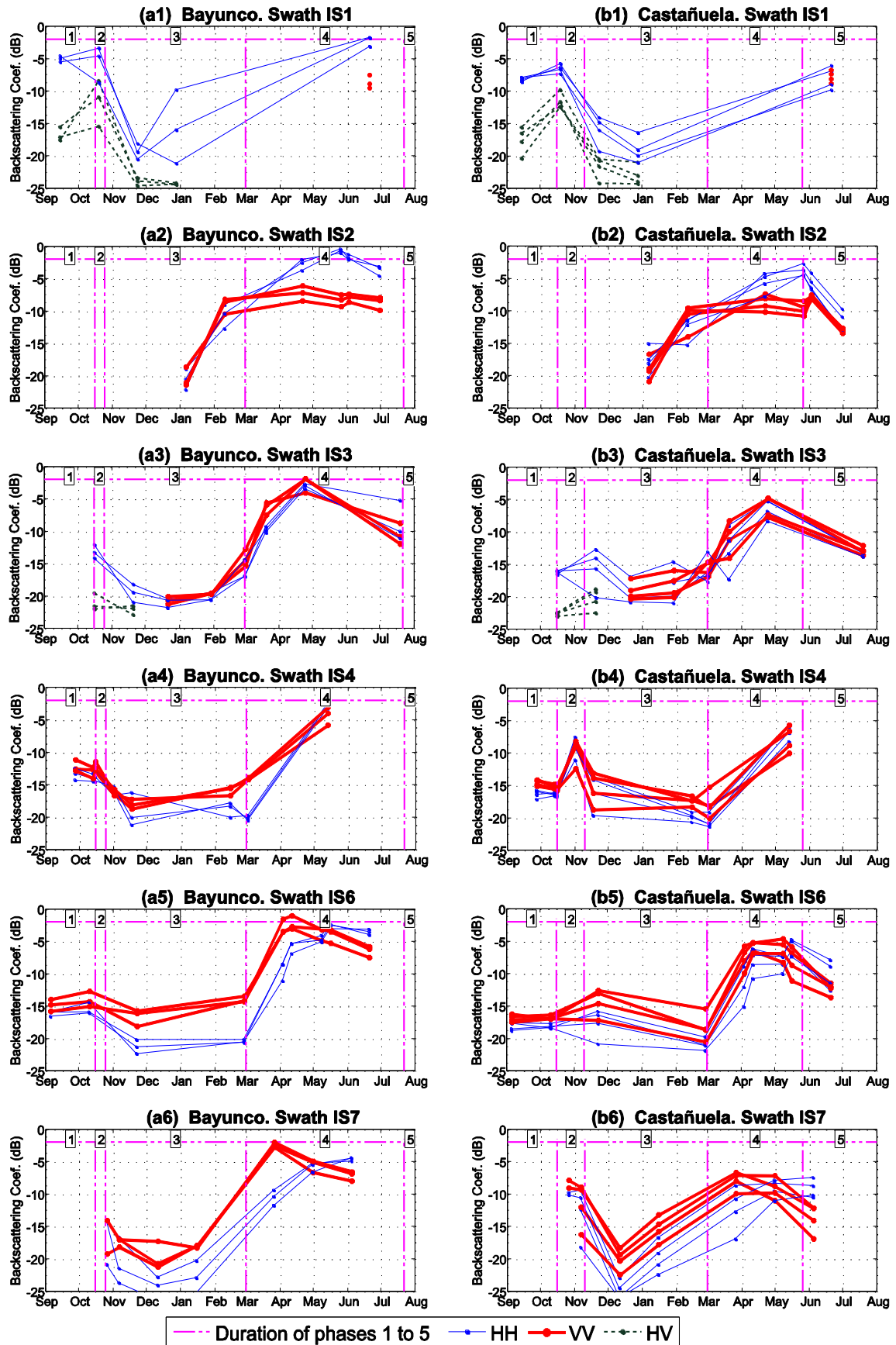
Fig. 7.9. Bayunco and Castañuela ROIs σ⁰HH and σ⁰VV evolution during the 2006-2007 hydrologic cycle at swaths IS1, IS2, IS3, IS4, IS6 and IS7.

Fig. 7.10. Envisat/ASAR image of Doñana from 23 Mar. 2006, at swath IS1 and HV/VV polarization configuration. HV and VV backscattering are displayed in red and cyan, respectively. In areas of submerged vegetation, the open water appears darker, i.e. the water surface is smoother.

Stage 4. In March, new green Bayunco and Castañuela plants start coming out of the water and experience rapid height and density growth during the spring months, while the water level drops steadily. Concurrently, radar brightness shows a steep increase, reaching values up to 18 dB higher than in the previous stage (Fig. 7.9 and Fig. 7.13). Such increase might be explained by the specular double bounce of the radar waves between growing stalks and water surface, and by the vegetation canopy volume scattering. A clear swath dependent polarimetric behavior is observed in this stage:

IS2 backscatter from flooded Bayunco and Castañuela is clearly higher in HH than in VV polarization (Fig. 7.9a2, Fig. 7.9b2). σ^0HH/σ^0VV increases at this swath with the plant growth reaching values above 7 and 5 dB for the Bayunco and Castañuela respectively. Bayunco σ^0VV reaches its maximum values around -7 dB in mid April, while σ^0HH continues to increase until the end of May, when it takes the highest values of about -0.6 dB. Backscattering from Castañuela follows the same temporal pattern: σ^0VV and σ^0HH maxima are achieved in mid-April and end of May with approximate values of -9 and -5 dB, respectively.

In contrast with swath IS2, Bayunco and Castañuela σ^0VV at IS6 and IS7 is higher than σ^0HH in March and April (Fig. 7.9a5, Fig. 7.9a6, Fig. 7.9b5, Fig. 7.9b6). However, as it has been observed at IS2, σ^0VV reaches a maximum value and starts decreasing earlier than σ^0HH, so that the latter becomes greater than σ^0VV towards mid-May. σ^0HH/σ^0VV increases in about 10 dB for both vegetation types in the course of this stage.

Polarimetric differences are lowest at swaths IS3 and IS4, but also in these cases σ^0VV is higher than σ^0HH in March and April (Fig. 7.9a3, Fig. 7.9a4, Fig. 7.9b3, Fig. 7.9b4). The imaging frequency at these swaths does not allow establishing a maxima time shift between polarizations, like for the rest of the incidence angles, although such maxima would fit the available data.

Strong differences between HH and VV backscattering, similar to the ones found in this study at swath IS2, were already spotted by Karszenbaum et al. 2000 and Grings et al. 2005 for flooded junco (i.e. reed-like vegetation comparable to the Bayunco), using ERS 2 (C-band, VV polarization and 23º incidence angle), Radarsat S1(C-band, HH polarization and 23.5º incidence angle) and Envisat IS1 (C-band, HH/VV polarization and 19º incidence angle) data. Grings et al. explained through C-band electromagnetic model simulation that during the junco growing phase the HH backscattering dominates over the VV one, as observed for the Bayunco and Castañuela, due to three processes: 1) junco bistatic specular scattering is higher in the case of H incident polarization than in the V one; 2) water surface bistatic specular scattering is higher at H polarization than at V; 3) junco attenuation is higher at V than at H. In the simulations, both HH and VV responses increase with the junco growth due mainly to the water surface-stalks double-bounce, up to a certain combination of vegetation height and density. Afterwards, further growth produces an increase in the attenuation and, hence, a decrease in σ^0. Their electromagnetic

simulations also showed that during the junco growth the maximum σ^0 at 23º incidence angle was first achieved in VV polarization, consistently with this study's results.

Grings et al.'s explanations of the junco backscattering behavior during the growing phase fit the observed Bayunco and Castañuela behavior in phase 4: σ^0 increases in virtue of the water-stalks double bounce up to a certain degree of plant development, after which the volume attenuation causes a decrease in $\sigma^0 VV$. The orientation of the Bayunco and Castañuela stems, preferently vertical, causes greater attenuation at VV radiation. As a result, $\sigma^0 VV$ starts decreasing for a smaller amount of emergent vegetation than $\sigma^0 HH$. The fact that Bayunco polarimetric effects are larger than the Castañuela's might be explained by the cylindrical shape and more vertical orientation of the first plant, which enhances the double bounce of the radar signal to a larger degree than the curved Castañuela leaves do (Grings et al., 2005; Grings et al., 2006).

A subsequent paper of the same authors, Grings et al. 2008, compared modeled $\sigma^0 HH$ and $\sigma^0 VV$ with ASAR signatures of flooded junco marshes at IS1 and IS3 incidence angles. Both, modeled simulations and experimental data showed that junco $\sigma^0 HH$ was clearly higher than $\sigma^0 VV$ at IS1 and IS3. In contrast, Doñana ASAR images show that $\sigma^0 HH$ at swaths IS3 to IS7 is lower than $\sigma^0 VV$ during most of the growing phase, and becomes only moderately higher at the end of the growing period, in May and June (Fig. 7.9, Fig. 7.13). Such discrepancy could be due to the different vegetation type's geometries, such as emerged stem height, stem orientation or stem density. The Bayunco and Castañuela abrupt polarimetric behavior change between swaths IS2 and IS3, needs to be further investigated.

Stage 5.   The Castañuela ROIs came out of water around 26 May 2007. A decrease of 3 to 7 dB in the total backscattering is observed at all swaths after the regions have emerged, except at swath IS7 and HH polarization (Fig. 7.9b). This decrease is probably due to the loss of water surface-stalks double bounce. At swaths IS6 and IS7, the HH backscattering coefficient, which had been smaller than the VV one all through the flooding stages 3 and 4, becomes now greater than the latter. At swath IS2 the $\sigma^0 HH / \sigma^0 VV$ trend is opposite: it was clearly above 0 during the stage 4 and drops abruptly to values around 0 (Fig. 7.11b) coinciding with the waters retreat. The same ratio is slightly affected at IS3, and remains with values close to 0 as in the previous stage.

The Bayunco ROIs came out of water between 6 and 26 July 2007. Despite the emerging time lag with respect to Castañuela, the same σ^0HH/σ^0VV trends on the same dates are observed (Fig. 7.11a), suggesting that the HH and VV relative behavior at this phenological stage does not depend on the inundation but basically on the radar-vegetation interaction. Only in the last image, on 19 July at IS3, it is possible to observe two of the Bayunco ROIs out of water. Both HH and VV σ^0 in this image are 7 to 10 dB lower than in the previous IS3 image, acquired three months earlier.

As mentioned before, HV data is limited to the beginning of the hydrologic year and to swaths IS1 and IS3. HV backscattering is below the ASAR noise equivalent σ^0 value in the two IS3 images. IS1 HV Bayunco and Castañuela σ^0 ranges between -20 and -15 dB in September, increases above -12 dB at the beginning of the rainy period, due to plant and soil moisture, and goes down below the ASAR noise equivalent σ^0 after the flooding.

Fig. 7.11 embodies the σ^0HH/σ^0VV evolution in the Bayunco and Castañuela ROIs through the five stages described above. It can be seen in this figure that the σ^0HH/σ^0VV ratio is swath dependant at all stages, decreasing for larger incidence angles until May, when the Castañuela and Bayunco reach their maximum above water height and density. Fig. 7.11 also reveals that polarimetric effects are lowest at IS3 and IS4 throughout the hydrologic cycle.
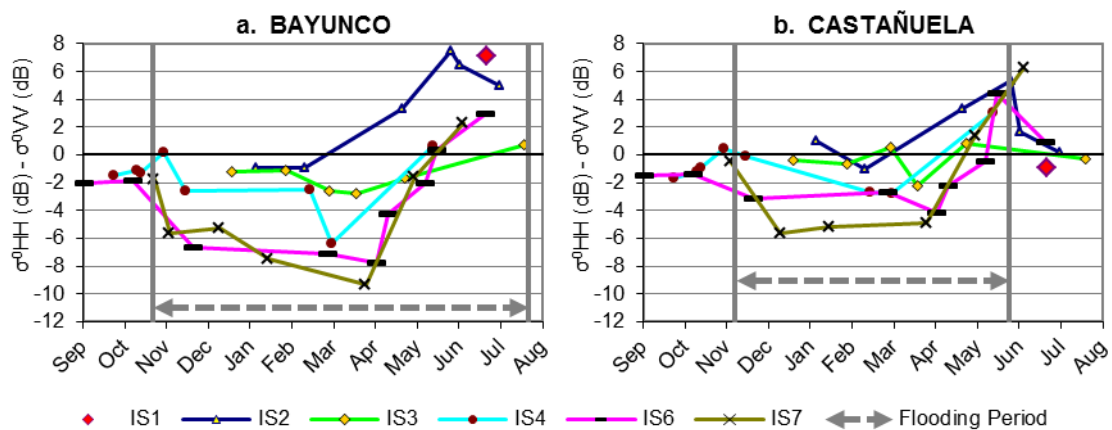
Fig. 7.11. Bayunco and Castañuela ROIs σ^0HH/σ^0VV ratio evolution during the 2006-2007 hydrologic cycle at swaths IS1, IS2, IS3, IS4, IS6 and IS7.

Despite the σ^0 differences related to incidence angle, polarization and vegetation structure, Fig. 7.9 shows a similar backscattering temporal pattern of Bayunco and Castañuela in all swaths. This pattern is sketched in Fig. 7.12.

Fig. 7.13 illustrates the separability among Bayunco and Castañuela stages based on the $\sigma^0 VV$ and $\sigma^0 HH/\sigma^0 VV$ ratio space. Flood detection feasibility is discussed in the following subsections.
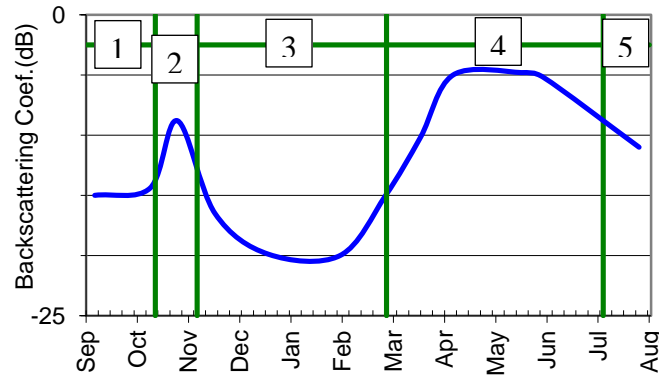
Fig. 7.12. Sketch of the temporal pattern and stages observed in the Bayunco and Castañuela backscattering signatures.

Flood delineation at the beginning of the flooding period

Delineating flooded Bayunco and Castañuela areas at the beginning of the flooding period is equivalent to discriminating the areas in stage 3 from those still in stage 2. There are few observations of stage 2 ROIs in this study's results: only Castañuela ROIs at swaths IS1, IS4 and IS7 (Fig. 7.9b1, Fig. 7.9b4, Fig. 7.9b6, Fig. 7.13b3, Fig. 7.13b5). In these observations the emerged and wet stage 2 areas show total backscattering of at least 5 dB higher than the flooded stage 3 ones. At swath IS7, backscattering decrease in stage 3 is accompanied by a shift in the $\sigma^0 HH/\sigma^0 VV$ ratio (Fig. 7.13b5), which enhances the contrast between stage 2 and 3. Backscattering differences similar to the ones commented for IS4 and IS7 have been observed for Castañuela at swaths IS2 and IS6, although unfortunately in areas that were not part of the selected control ROIs, and therefore are not represented in the included figures. In the unlikely case of adjacent Castañuela areas at stage 1 (dry vegetation and soil) and stage 3 (flooded vegetation), their mean backscattering coefficient may be confounded, as illustrated by the very close stage 1 and stage 3 points in Fig. 7.13b.
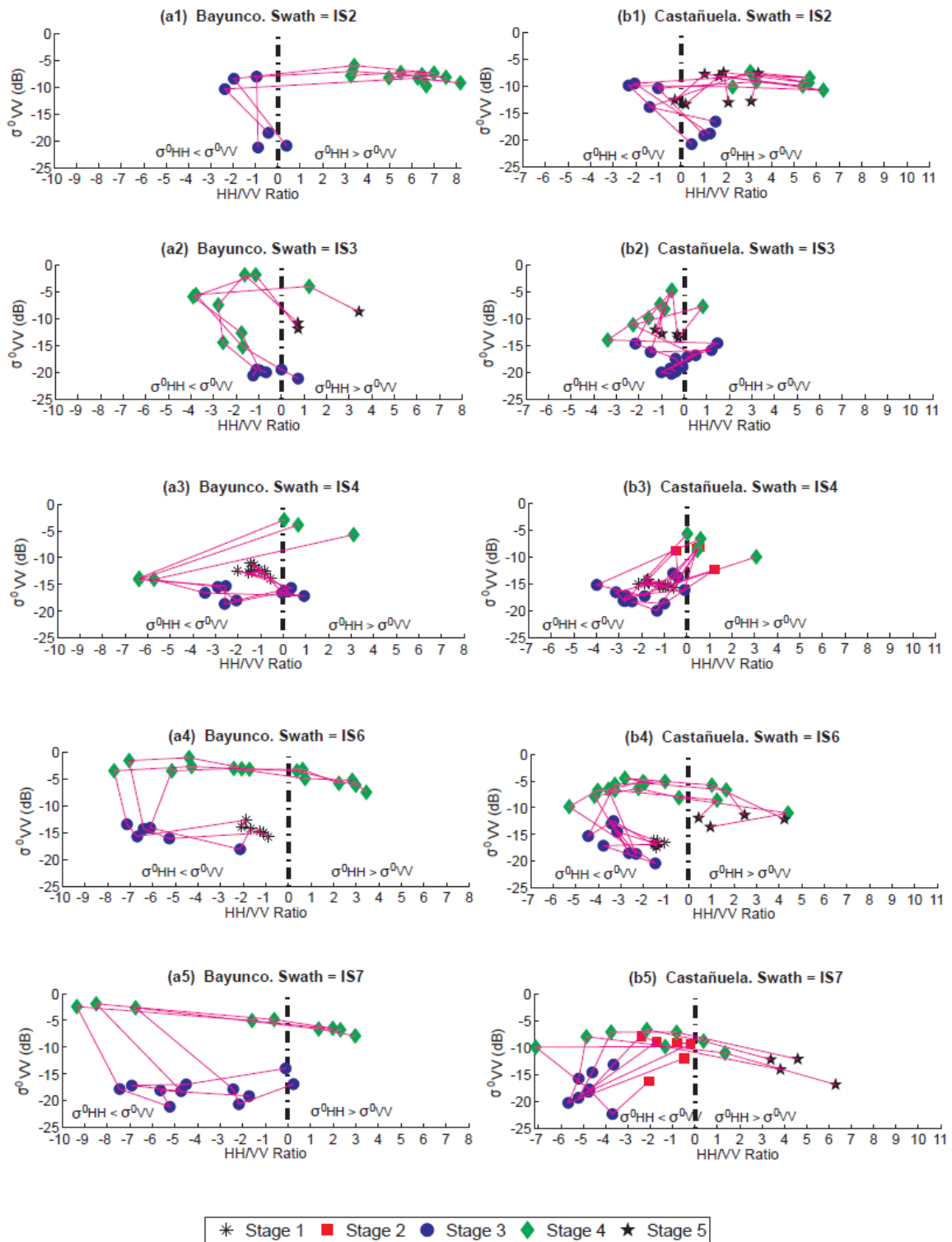
Fig. 7.13. Scatter plots of σ0HH/σ0VV ratio versus σ0VV in the Bayunco (a) and Castañuela (b) ROIs at swaths IS2, IS3, IS4, IS6 and IS7. Point marker types indicate different stages. Points corresponding to the same ROI are connected by a polyline.

Bayunco temporal signatures (Fig. 7.9a) show that at the beginning of the flooding period, HH backscattering from flooded Bayunco (stage 3) is clearly lower than that from the emerged plant (stages 1 or 2) in IS1, IS3, IS4 and IS6. This distinction is expected to be possible too at IS2 and IS7, since polarimetric effects and discrimination capacity is higher at these swaths than at IS3 and IS4. Fig. 7.13a shows that Bayunco stages 1 and 3 are close but still separable. Nevertheless, the distinction between emerged and flooded Bayunco is expected to be much clearer in the more likely case that areas at stage 3 are surrounded by others at stage 2 on the same ASAR image.

Flood delineation at the end of the flooding period

Discrimination between flooded and emerged Bayunco and Castañuela regions at the end of the flooding period consists on discerning among areas at stages 4 and 5. According to Fig. 7.9b, a significant drop in the Castañuela backscattering coefficient takes place between both stages. So a clear contrast between flooded and emerged green Castañuela areas is to be expected at all swaths, being the flooded ones brighter. However, Fig. 7.13b1, Fig. 7.13b2 reveal that the reduced backscattering coefficient of the unflooded Castañuela regions at swaths IS2 and IS3 could be confounded with that from flooded areas with delayed plant development (e.g. at the middle of stage 4). No stage 5 data is available at IS4 (Fig. 7.13b3), but the minor polarimetric differences at this swath lead to expect an analogous drawback. At IS6 and IS7 incidence angles. (Fig. 7.13b4, Fig. 7.13b5), a sustained increase in the HH/VV ratio along stage 4 prevents the confusion between stage 4 and 5 points.

Emerged green Bayunco was only observed on the last ASAR acquisition, at swath IS3. However, the more vertical orientation of this plant compared to the Castañuela exacerbates the polarimetric effects which facilitate the discrimination of the inundation at IS6 and IS7 in the Castañuela case. So Bayunco flood mapping is expected feasible at least at these swaths. Fig. 7.13a2 suggests that it could also be possible at IS3 and, by extension, at other swaths.

7.3.4 COMBINATION OF STEEP AND SHALLOW SWATHS

The discussion above refers to the flood detection feasibility on a single ASAR image. The versatility of the ASAR look direction allows observing Doñana at two different incidence angles with approximately 12 hours delay, 6 times per 35-day orbit cycle. The following combinations of 12 hour-shifted observation swaths are possible twice per orbit cycle: IS1/IS6, IS3/IS4 and IS2/IS5. Provided the marshes flood state does not experience rapid changes in the period between scene acquisitions (e.g. rainfall occurs), both images can be combined for flood detection and, hence, benefit from the valuable additional information from two different look directions. This image composition is especially interesting when combining steep and shallow incidence angles, that is IS1/IS6 and IS2/IS5 pairs, since they provide more complementary information than the IS3 and IS4 closer swaths.

Fig. 7.14 and Fig. 7.15 show three zones in the marshes observed at swaths IS6 and IS1. They correspond to the ASAR images indicated in Table 7.1, which were acquired with 12 hour and 14 minute lag. These ASAR scenes illustrate the advantage of combining swaths IS1 and IS6 respect to the use of either of the same swaths independently.

Table 7.1. Acquisition time, swath and polarization of the ASAR images in Fig. 7.14, Fig. 7.15 and Fig. 7.16.

Acquisition time	Swath	Polarization
20 Feb. 2008, 22:26:43	IS6	HH/VV
21 Feb. 2008, 10:40:45	IS1	HH/VV

Fig. 7.14a shows the extent of one flooded Deep Bare Soil pond with clarity. The extent of the same pond at IS1 (Fig. 7.15a) is less evident due to the increased backscattering from the roughened water surface, similar to that from the emerged bare soil in Fig. 7.15b. Flood and emerged bare soil are distinguishable at IS6 (Fig. 7.14a, Fig. 7.14b).
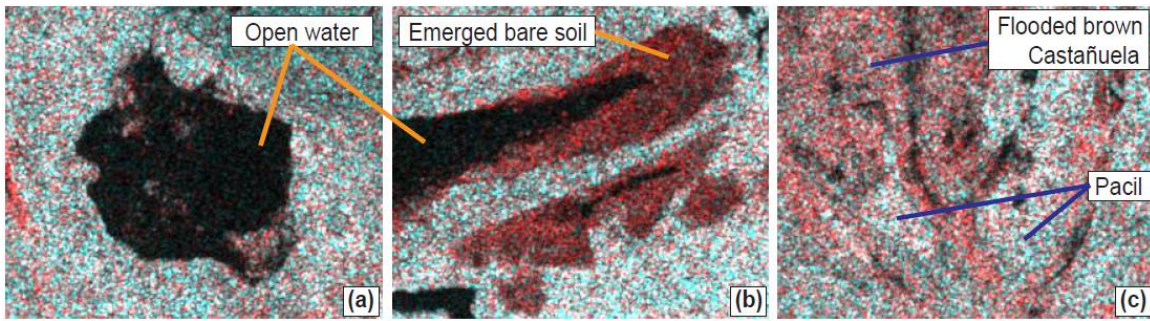
Fig. 7.14. **Doñana marshes areas extracted from the IS6 HH/VV ASAR amplitude scene on 20 February 2008: a) flooded Deep Bare Soil pond; b) partially flooded Deep Bare Soil pond; c) flooded brown Castañuela. VV amplitude is displayed in red and HH in green and blue.**
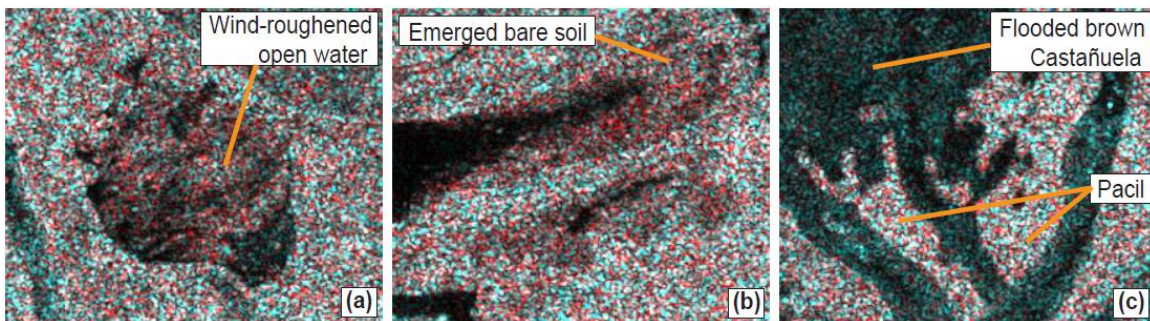
Fig. 7.15. **Doñana marshes areas extracted from the IS1 HH/VV ASAR amplitude scene on 21 February 2008: a) flooded Deep Bare Soil pond; b) partially flooded Deep Bare Soil pond; c) flooded brown Castañuela. VV amplitude is displayed in red and HH in green and blue.**
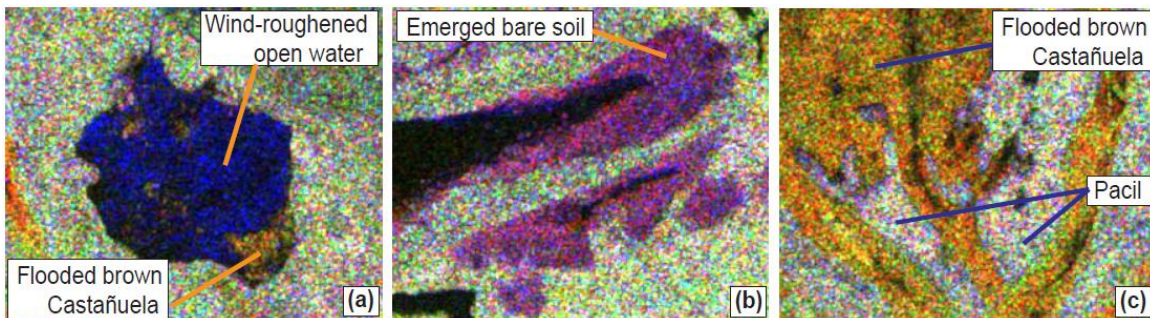
Fig. 7.16. **Doñana marshes areas extracted from the IS6 and IS1 HH/VV ASAR amplitude scenes on 20 and 21 February 2008: a) flooded Deep Bare Soil pond; b) partially flooded Deep Bare Soil pond; c) flooded brown Castañuela. IS6 VV amplitude is displayed in red, IS6 HH in green and IS1 VV in blue.**

The area in Fig. 7.14c and Fig. 7.15c corresponds to brown Castañuela in shallow inundation. In this condition a significant volume of Castañuela sticks out of the water surface, but their dry leaves have bent and lost vertical orientation compared to its young, green state. It yields high backscattering at IS6 (Fig. 7.14c), close to that from the same vegetation with emerged wet soil and close to that from the surrounding wet Pacil too. The same vegetation is more transparent at IS1, which shows low σ^0 values due to the

water surface underneath, and therefore discerns the inundation from the adjacent Pacil more neatly (Fig. 7.15c). If flooded Pacil areas were present on the same ASAR scenes, IS1 would also be advantageous respect to IS6 in order to discriminate them, as discussed in Section 7.3.2.

Fig. 7.16 represents the following channel combination from the IS1 and IS6 ASAR scenes: IS6-VV is displayed in red, IS6-HH in green and IS1-VV in blue. This figure reveals how the inundation can be delineated in the three area types thanks to the quasi-simultaneous observation at two different incidence angles. The use of two different swaths shows potential, not only for flood mapping within a given land cover type, but also to discriminate among cover types in Doñana and therefore to account for spatial distribution changes in them.

7.4 Conclusions

Conclusions on the flood mapping suitability of the various incidence angles for the different land cover types and phenological stages are presented as follows. These conclusions are used in sub-sequent chapters to derive Doñana flood maps from ASAR images which, in turn, further our understanding of Doñana's complex hydrologic system and make possible the calibration of the marshes hydrodynamic model.

Land cover type: Deep Bare Soil

Deep bare soil temporal signatures and 2D scatter plots obtained in this study indicate that flooding stages are separable at swaths IS3 and IS4. High amount of specular reflection can cause confusion between flooded and emerged bare soil at large incidence angles. Confusion also occurs at steep incidence angles on windy days due to increased backscattering from wave action.

Land cover type: Low Pacil and High Pacil

Flooding in the pacil is clearly detectable at swaths IS2, IS3 and IS4, and presumably at IS1 (there is not enough data at this swath). The indicators of this class inundation are a significant backscattering decrease in both polarizations and a steep increase in the $\sigma^0 HH/\sigma^0 VV$ ratio, as a result of a larger drop at VV than at HH. The smaller the incidence

angle the higher the σ^0HH/σ^0VV value and therefore the distinction of flooded versus emerged pacil areas on a single image. At swaths IS6 and IS7 backscattering differences between flooded and emerged pacil are subtle. Hence, when water levels in the marshes are high enough to reach pacil areas, swaths IS6 and IS7 are not appropriate for flood mapping.

Land cover type: Bayunco and Castañuela

Flooded brown Castañuela can be discriminated at all incidence angles, except IS3, when the surrounding emerged regions are wet, because σ^0HH from the inundated areas is considerably lower than that from the emerged wet soil. There is no data for the same assertion about IS3. In the unlikely case of adjacent Castañuela areas of flooded and emerged dry soil, the inundation may not be separable. Delineating inundation in brown Bayunco areas is feasible at all swaths provided that HH data is available, since σ^0HH is always lower for flooded than for emerged brown Bayunco. In spring and summer images, backscattering from green flooded Castañuela is substantially higher than that from the emerged plant at all swaths. However, certain confusion between emerged and low vegetated flooded areas can occur at IS2 and IS3. At IS6 and IS7 incidence angles the sustained increase in the HH/VV ratio at the end of the hydrologic year (Fig. 7.13b4, Fig. 7.13b5) prevents the same confusion. Although no data on unflooded green Bayunco ROIs is available, flood mapping is expected to be feasible at least at IS6 and IS7, because polarimetric effects enabling flood detection in the Castañuela case are more accused in the Bayunco areas.

Summarizing, during the first part of the flooding period, if the marshes water level is high enough to flood the Paciles, steep incidence angles are preferred because of their sensitivity to inundation in the Almajar areas. The main drawback of steep incidence angles at this stage is that wind-roughened open water surfaces can be confused with emerged areas. During the drying period, when the paciles are out of the water flooded area is decreasing at transition zones, large incidence angles of IS6 and IS7 show increased capacity to discriminate between flooded and emerged helophytes, in virtue of their higher differential polarimetric behavior than steeper swaths. In the case of the ASAR product used in this study, the IS6 and IS7 incidence angles have the additional advantage of a higher number of looks over steeper swaths and, therefore, less speckle noise than the latter.

Combination of 12 hour-delayed ASAR images at steep and shallow incidence angles offer better flood detection capabilities than any single swath scene at all stages. Such acquisition combination was possible at least 4 times in 35 days, which is a satisfactory observation frequency for Doñana flood extent monitoring.

New satellite radar systems such as ALOS-PALSAR, RADARSAT-2 or TerraSAR-X provide fully polarimetric data, which has been proved to be advantageous for wetland monitoring (Touzi, 2006; Boerner & Yamaguchi, 2008; Touzi et al., 2009; Hong et al., 2010). Despite the doubtless added value data of these systems compared to the ASAR amplitude data used in this study, none of them can provide, in fully polarimetric mode, observations of the entire marshes at the temporal frequency achieved with ASAR. Both, temporal frequency and complete Doñana coverage were key requisites for this study's final goals.

7.5 References

Aragonés, D., Díaz-Delgado, R., & Bustamante, J. (2005). Tratamiento de una serie temporal larga de imágenes Landsat para la cartografía de la inundación histórica de las marismas de Doñana. Proceedings of the XI Congreso Nacional de Teledetección, 21-23 Sep., Tenerife, Spain: Asociación Española de Teledetección.

Bayán-Jardín, B., & Dolz-Ripollés, J. (1995). Las aguas superficiales y la marisma del Parque Nacional de Doñana. Revista de Obras Públicas, 3340, 17-29.

Bladé, E., & Gómez, M. (Eds.), (2006). Modelación del flujo en lámina libre sobre cauces naturales. Análisis integrado en una y dos dimensiones. Monografía CIMNE, 97. Barcelona, Spain: CIMNE.

Boerner, W.-M. & Yamaguchi, Y. (2008). Recent advances in POL-SAR & POL-IN-SAR imaging of natural habitats and wetland remote sensing. IEEE International Conference on Geoscience and Remote Sensing Symposium, IGARSS 2008, 7-11 July, Boston, MA, U.S.A., 2, 293-294.

Bourgeau-Chavez, l., Kasischke, E., Brunzell, S., Mudd, J., Smith, K. & Frick, A. (2001), Analysis of space-borne SAR data for wetland mapping in Virginia riparian ecosystems. International Journal of Remote Sensing, 22, 3665–3687.

Brown, R., Brisco, B., D'Iorio, M., Prevost, C., Ryerson, R., & Singhroy, V. (1996). RADARSAT applications: review of GlobeSAR program. Canadian Journal of Remote Sensing, 22, 404-419.

Bustamante, J., Pacios, F., Díaz-Delgado, R., & Aragonés, D. (2009). Predictive models of turbidity and water depth in the Doñana marshes using Landsat TM and ETM+ images. Journal of Environmental Management, 2219-2225.

Grings, F., Ferrazzoli, P., Karszenbaum, H., Tiffenberg, J., Kandus, P., Guerriero, L. & Jacobo-Berlles, J.C. (2005). Modeling temporal evolution of junco marshes radar signatures. IEEE Transactions on Geoscience and Remote Sensing, 43, 2238 – 2245.

Henderson, F.M. & Lewis, A.J. (2008). Radar detection of wetland ecosystems: a review. International Journal of Remote Sensing, 29, 5809-5835.

Henderson, F.M. & Lewis, A.J. (1998). Principles and applications of imaging radar. Somerset, NJ: John Wiley and Sons, Inc.

Hess, L., Melack, J., Filoso, S. & Wang, Y. (1995). Delineation of inundated area and vegetation along the Amazon floodplain with the SIR-C synthetic aperture radar. IEEE Transactions on Geoscience and Remote Sensing, 33, 896–904.

Hess, L., Melack, J. & Simonet, D. (1990). Radar detection of flooding beneath the forest canopy: a review. International Journal of Remote Sensing, 11, 1313–1325.

Hong, S.-H., Wdowinski, S., & Kim, S.-W. (2010). Evaluation of TerraSAR-X observations for wetland InSAR application. IEEE Transactions on Geoscience and Remote Sensing, 48, 864-873.

Ibañez, E., & Gili-Ripoll, J. (2008). Validación de modelos digitales del terreno de precisión a partir de datos láser escáner aerotransportado; Aplicación a la marisma del parque nacional de Doñana. PhD Thesis, Universitat Politècnica de Catalunya, Barcelona, Spain.

Kandus, P., Karszenbaum, H., Pultz, T., Parmuchi, G., & Bava, J. (2001). Influence of flood conditions and vegetation status on the radar backscatter of wetland ecosystems. Canadian Journal of Remote Sensing, 27, 651-662.

Kasischke, E., Smith, K., Bourgeau-Chavez, L., Romanowicz, E., Brunzell, S. & Richardson, C. (2003). Effects of seasonal hydrologic patterns in south Florida wetlands on radar backscatter measured from ERS-2 SAR imagery. Remote Sensing of Environment, 88, 423–441.

Karszenbaum, H., Kandus, P., Martínez, J.M., Toan, T.L., Tiffenberg, J., & Parmuchi, G. (2000). ERS-2, RADARSAT SAR backscattering characteristics of the Paraná River delta wetlands, Argentina. Proceedings of the ERS –ENVISAT symposium. Looking down to Earth in the new millennium. 16 – 20 Oct., Gothemburg, Sweden: ESA.

Kasischke, E.; Melack, J. & Dobson, M. (1997). The use of radars for ecological applications: a review. Remote Sensing of Environment, 59, 141–156.

Krohn, D. M., Milton, N. M., and Segal, D. B. (1983). SEASAT synthetic aperture radar (SAR) response to lowland vegetation types in eastern Maryland and Virginia. Journal of Geophysical Research, 88, 1937–1952.

Le Toan, T., Ribbes, F., Wange, L.F., Floury, N., Ding, N. & Kong, K.H. (1997). Rice crop mapping and monitoring using ERS-1 data based on experiment and modeling results. IEEE Transactions on Geoscience and Remote Sensing, 35, 41-56.

Le Toan, T., Beaudoin, A., Riom, J., & Guyon, D. (1992). Relating forest biomass to SAR data. IEEE Transactions on Geoscience and Remote Sensing, 30, 403–411.

Leconte, R. & Pultz, T. (1991). Evaluation of the potential of Radarsat for flood mapping using simulated satellite SAR imagery. Canadian Journal of Remote Sensing, 17, 241-249.

Luque, C.J., Rubio-Casal, A.E., Álvarez, A.A., Muñoz, J., Vecino, I., Doblas, D., Leira, P., Redondo, S., Castillo, J., Mateos, E., Castellanos, E. & Figueroa, E. (2005). Memoria de Vegetación: Parque Nacional de Doñana. Proyecto de Cartografía y Evaluación de la Flora y Vegetación Halófita y de los Ecosistemas de Marismas que se encuentren dentro de la Red de Espacios Naturales Protegidos de Andalucía. Sevilla, Spain: Consejería de Medio Ambiente de la Junta de Andalucía & Universidad de Sevilla.

Martí-Cardona, B., Dolz-Ripollés, J. & Gili-Ripoll, J. (2006). Monitoring of the Flooding and Dry-Out Processes in Doñana National Park for the Calibration of the Hydrodynamic Model of its Marshes. Proceedings of 1st GlobWetland Symposium: Looking at Wetlands from Space, 19-20 Oct., Frascati, Italy: ESA.

Martínez, J. & Le Toan, T. (2007). Mapping of flood dynamics and spatial distribution of vegetation in the Amazon floodplain using multitemporal SAR data. Remote Sensing of Environment, 108, 209-223.

Menanteau, L. (1984). Evolución histórica y consecuencias morfológicas de la intervención humana en las zonas húmedas: el caso de las marismas del Guadalquivir. In Las zonas húmedas en Andalucía (pp. 43-76). Madrid, Spain: Dirección General de Medio Ambiente, Ministerio de Obras Públicas y Urbanismo.

Moreau, S. & Le Toan, T., 2003, Biomass quantification of Andean wetland forages using ERS satellite SAR data for optimizing livestock management. Remote Sensing of Environment, 84, 477-492.

Novo, E.M., Costa, M.F. & Mantovani, J. (1998). Exploratory survey on macrophyte biophysical parameters in tropical reservoirs. Canadian Journal of Remote Sensing, 24, 367-375.

Parmuchi, M., Karsenbaum, H. & Kandus, P. (2002). Mapping wetlands using multitemporal RADARSAT-1 data and a decision-based classifier. Canadian Journal of Remote Sensing, 28, 175-186.

Peinado, M., Martínez, J.M., Parras, C., Bartolomé, C., Álvarez, J., & De La Cruz, M. (1990). Nuevas plantas y nuevas áreas para la flora de Andalucía Occidenta. Lagascalia, 16, 125-129.

Pierdicca, N., Pulvirenti, L., & Bignami, C. (2010). Soil moisture estimation over vegetated terrains using multitemporal remote sensing data. Remote Sensing of Environment, 114, 440-448.

Pope, K., Rejmankova, E., Paris, J. & Woodruff, R. (1997). Detecting seasonal flooding cycles in marshes of the Yucatan peninsula with SIR-C polarimetric radar imagery. Remote Sensing of Environment, 59, 157–166.

Ramos, A., Martí-Cardona, B., Rabadà, J., & Dolz-Ripollés, J. (2009). Teledetección e Información Hidrometeorológica de Campo en la Marisma de Doñana. Proceedings of Jornadas de Ingeniería del Agua. 27-28 Oct., Madrid, Spain: CEDEX.

Ramsey, E.I. (1998). Radar remote sensing of wetlands. In R. Lunetta, & C. Elvidge (Eds.), Remote sensing change detection: Environmental monitoring methods and applications (pp. 211-243). Chelsea, MI: Ann Arbor Press.

Ramsey, E. III (1995). Monitoring flooding in coastal wetlands by using radar imagery and ground-based measurements. International Journal of Remote Sensing, 16, 2495-2505.

Rivas-Martínez, S., Costa, M., Castroviejo, S., & Valdés-Bermejo, E. (1980). Vegetación de Doñana (Huelva, España). Lazaroa, 2, 5-189.

Rodríguez-Ramirez, A., & Clemente-Salas, L. (2002). Geomorfología. In Parque Nacional de Doñana (pp. 19-42). Talavera de la Reina, Spain: Canseco Editores.

Rosenqvist, A., Forsberg, B., Pimentel, T., Rauste, Y. & Richey, J. (2002). The use of spaceborne radar data to model inundation patterns and trace gas emissions in the central Amazon floodplain. International Journal of Remote Sensing, 23, 1303-1328.

Rosich, B., & Meadows, P. (2004). Absolute Calibration of SAR Level-1 Products Generated with PF-ASAR, v.1.4. ESA Technical note: ESA.

Saura, J., Bayán-Jardín, B., Casas, J., Ruíz, A., & Urdiales, C. (2001). Documento marco para el desarrollo del proyecto Doñana 2005. Regeneración hídrica de las cuencas y cauces vertientes a las marismas del Parque Nacional de Doñana. Madrid, Spain: Ministerio de Medioambiente.

Schmullius, C. & Evans, D. (1997). Synthetic aperture radar (SAR) frequency and polarization requirements for applications in ecology, geology, hydrology, and oceanography: a tabular status quo after SIR-C/X-SAR. International Journal of Remote Sensing, 18, 2713–2722.

Touzi, R. (2006). Wetland characterization using polarimetric RADARSAT-2 capability. IEEE International Conference on Geoscience and Remote Sensing Symposium, IGARSS 2006, 31 July –4 Aug., Denver, CO, U.S.A., 1639-1642.

Touzi, R., Deschamps, A., & Rother, G. (2009). Phase of target scattering for wetland characterization using polarimetric C-band SAR. IEEE Transactions on Geoscience and Remote Sensing, 47, 3241-3261.

Töyrä, J. & Pietroniro, A. (2005). Towards operational monitoring of a northern wetland using geomatics-based techniques. Remote Sensing of Environment, 97, 174-191.

Töyrä, J., Pietroniro, A., & Martz, L.W. (2001). Multisensor hydrologic assessment of a freshwater wetland. Remote Sensing of Environment, 75, 162-173.

Ulaby, F.T., & Dobson, M.G. (1989). Handbook of radar scattering statistics for terrain. Norwood, MA: Artech House.

Ulaby, F.T., Moore, R.K., & Fung, A.K. (1986). Microwave remote sensing: active and passive III. From theory to applications. Norwood, MA: Artech House.

Wang, Y., Hess, L.L., Filoso, S., & Melack, J.M. (1995). Understanding the radar backscattering from flooded and nonflooded Amazonian forests: Results from canopy backscatter modeling. Remote Sensing of Environment, 54, 324-332.

Wickel, A. J., Jackson, T. J., & Wood, E. F. (2001). Multitemporal monitoring of soil moisture with RADARSAT SAR during the 1997 Southern Great Plains hydrology experiment. International Journal of Remote Sensing, 22, 1571–1583.

Chapter 8:
Image Filtering

8.1   Introduction

Delineation of the flooded areas on the Doñana ASAR images required filtering the scenes to smooth out backscattering fluctuations owing to speckle and texture within cover classes. It is well-known that the utility of radar images for land cover mapping is seriously undermined by the speckle phenomenon and literature on SAR image filtering is vast. Some benchmarks are Lee (1980); Frost et al. (1982) and Kuan et al. (1985). The all-purpose filtering methods proposed by these and other authors are applied in sliding rectangular windows, which need to encompass locally stationary neighborhoods so that the filtered value does not smear edges or mix up backscattering values from different cover types.

Given the strong correlation between Doñana's cover types and its topography, neighboring pixels at the same elevation are very likely to belong to the same class. Hence, the DTM provides precious clues for choosing homogeneous filtering neighborhoods, which will be large in flat areas and will become smaller as the terrain gets steeper. Irregular filtering neighborhoods defined in this way are more likely to follow natural edges than square or other fixed-geometry windows used by general purpose methods.

This chapter describes the filtering procedure applied to the Doñana ASAR images under the guidance of the DTM. Results are compared to those obtained by filtering the images with common speckle filters. The ASAR scenes filtered under the DTM guidance are the starting point for the segmentation and classification methods presented in Chapter 9 for flood mapping purposes.

8.2 Methodology

8.2.1 FILTERING NEIGHBORHOOD SELECTION

Irregular filtering neighborhoods were selected at every image location, P, based on the pixels relative elevation, so that:

- The elevation of pixels in the neighborhood was less than 25 mm apart from that of P.

- All pixels in the neighborhood were connected to pixel P (through 8-pixel neighborhood connection).

- The pixels lay within a 13x13 pixel window centered at the pixel to be filtered, P.

Fig. 8.1 sketches the DTM-based neighborhood selection and Fig. 8.2 shows the resulting filtering neighborhood size at each pixel location, indicative of the smoothing degree potentially achievable by the DTM-based filtering. The resulting regions are up to 169 (i.e. 13x13) pixels large in the flattest areas and down to 1 pixel in the steepest zones, with an average size of 59 pixels. The region's size frequency is shown by the corresponding histogram in Fig. 8.3. Since the neighborhoods are based on the DTM, they were computed once, stored as templates for each pixel position, and then used to filter out all ASAR scenes.
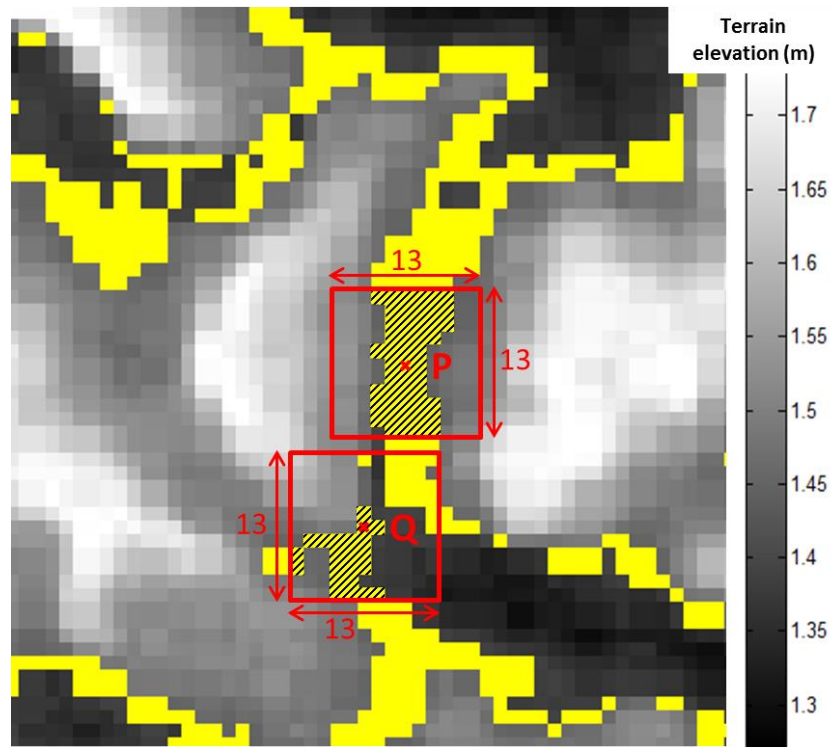
Fig. 8.1. Filtering neighborhood selection. The grey-scale image in the background is a segment of Doñana's DTM. Pixels P and Q are at 1.42 m of elevation. Pixels at an elevation +- 25mm apart from that of P and Q are highlighted in yellow. The hatched area indicates P's and Q's filtering neighborhoods.
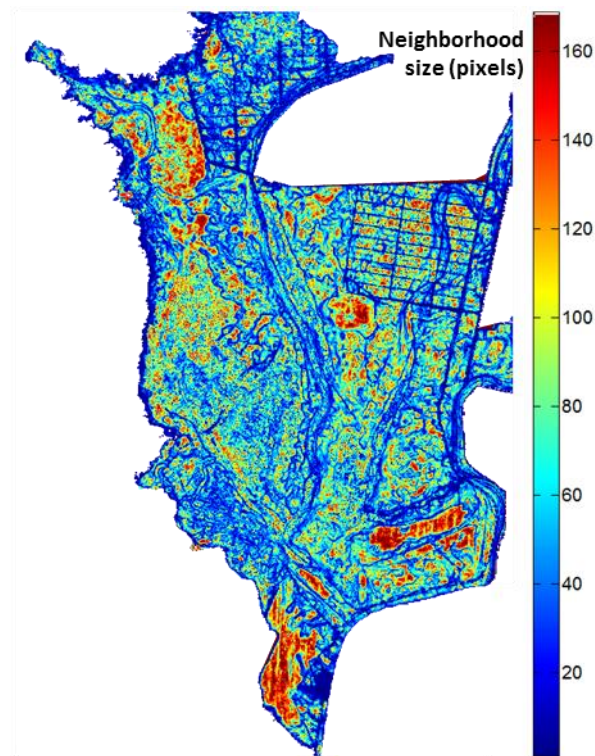
Fig. 8.2. Filtering neighborhood size at each pixel for a 13x13 pixel frame window.

In addition to elevation, planimetric distance is also an important variable to account for when trying to define homogenous neighborhoods, since land cover type in a positively auto-correlated variable (King et al., 2005; Overmars et al., 2003; Getis, 2010; Legendre and Legendre, 1998; Ord & Getis, 1995; Griffith, 1987). Thus, 13x13 pixel windows were used to constrain the spatial extent of the neighborhoods. Otherwise their definition would only rely on the pixels relative elevation and could expand spatially for elongated distances, following terrain contours.

Regarding the 13x13 pixel window size, this is consistent with the terrain slopes and the elevation increment threshold of 25 mm. Given the most frequent slopes found in Doñana marshes (see Fig. 6.3 in Chapter 6) a considerable number of filtering regions within 5x5 or 7x7 windows are only constrained by the window itself, and not by the elevation increment threshold, which suggests that the corresponding pixels could have larger associated filtering regions and therefore be further filtered. This is illustrated by the large number of pixels (i.e. number of filtering regions) cumulated at the maximum region size of 25 and 49 pixels, in the 5x5 and 7x7 frame window histograms of Fig. 8.3.
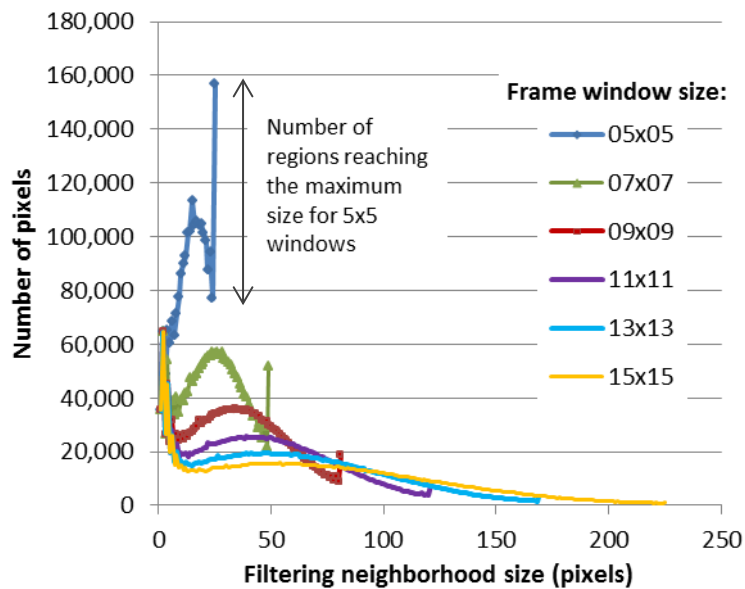
Fig. 8.3. Histograms of the filtering neighborhood size for different frame window sizes.

In view of Fig. 8.3, 11x11, 13x13 and 15x15 pixel frame windows are rather equivalent options in terms of the resulting neighborhood sizes and therefore filtering degree.

8.2.2 MASKING OF METALLIC FENCES

As explained in Chapter 4, several metallic fences sub-divide the marshes area for cattle grazing allocation. Those fence reaches oriented in a direction perpendicular to the SAR beam yield very high backscattering on the ASAR images. Pixels affected by this high backscattering were masked out prior to the image filtering. For this purpose, narrow regions overlapping the fences trajectory were defined, and image pixels within these regions showing backscattering coefficients higher than 0.2 m^2/m^2 were disregarded for the filtered values computation.

8.2.3 NON-STATIONARITY DETECTION

Given the relationship between natural edges and terrain contours, the perimeter of DTM-based neighborhoods tends to follow natural boundaries, and the likelihood of such neighborhoods to ride over different cover types is much lower than if fixed-shape filtering windows are used. Accordingly, a higher number of filtering regions exceed the homogeneity threshold CVm (defined below) when using square processing regions instead of DTM-based ones, as exemplified by Fig. 8.4.
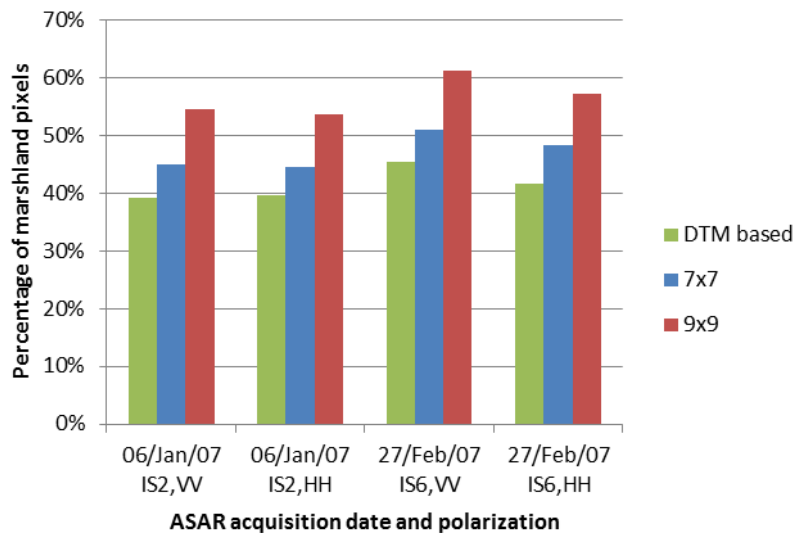
Fig. 8.4. Percentage of marshland pixels whose associated filtering regions exceed the homogeneity threshold in two ASAR scenes, for 7x7 and 9x9 pixel processing windows, and for 13x13 DTM-based neighborhoods.

Despite the adjustment of DTM-based neighborhoods to natural boundaries, the flood perimeter can be located on approximately flat areas and pass through the middle of the defined filtering regions. Consequently, a method for detecting heterogeneities within the DTM-processing regions was implemented and applied prior to computing the filtered value.

The method first assesses the filtering neighborhood stationarity by means of the coefficient of variation, CV, computed as the standard deviation of the neighborhood intensities divided by the mean. The CV is a SAR image heterogeneity index used by well-known speckle filters (Lee, 1980; Frost et al., 1982; Lee, 1983; Kuan et al., 1985; Touzi et al., 1988; Lopes et al., 1990; Nezry et al., 1991; Lopes et al., 1993; Touzi, 2002). Based on the speckle properties derived by Goodman 1975, the theoretical speckle CV mean of a homogeneous area in an L-look intensity image is $CV_m = 1/\sqrt{L}$. Here, filtering neighborhoods with $CV < CV_m$ were considered homogeneous, and the filtered value assigned to the central pixel P was the neighborhood intensity mean, which represents the minimum variance unbiased estimator of the region's radar cross section.

Higher CV's can be due to the presence of an edge, in which case the neighborhood should be split so that the computation of the filtered value avoids using backscattering intensities from two different cover classes. Nevertheless, large CV values can also be due to high contrast textures happening within single cover types. High CV's due to texture, similar to others due to soft edges, have been spotted in Doñana ASAR images in areas of emerging helophytes (Martí-Cardona et al., 2012; Martí-Cardona et al., 2010). In order to distinguish between the abovementioned situations, i.e. a soft edge between two different covers and texture within a single one, the Ds structural operator proposed by Martí-Cardona et al. (2012), was used in this study. In addition, Ds provides an increased sensitivity to soft or transitional edges compared to the CV.

Ds represents the first order central moment of an image neighborhood, normalized by the total intensity. More intuitively, Ds represents the distance in pixels between region's geometrical and intensity centroids. The latter coincides with what would be the neighborhood gravity center if the pixel values were masses. The Ds distance provides a measurement of the intensities spatial imbalance, so that Ds yields small values for isotropic distributions (where geometrical and intensity centroids would be almost coincident) and large ones when high and low intensities are preferentially clustered in

two different segments of the neighborhood. Additionally, the orthogonal to the segment defined by both centroids provides a likely edge direction.

Fig. 8.5 tries to shed light over the Ds concept, while Fig. 8.6 compares the sensitivity of the Ds and CV values to the presence of an edge in the processing window. The Ds parameter definition was presented in Martí-Cardona (2012). A thorough discussion on this parameter's properties and usefulness is included in Annex 7, and will hopefully be found in the scientific literature by Martí-Cardona et al., 2014.
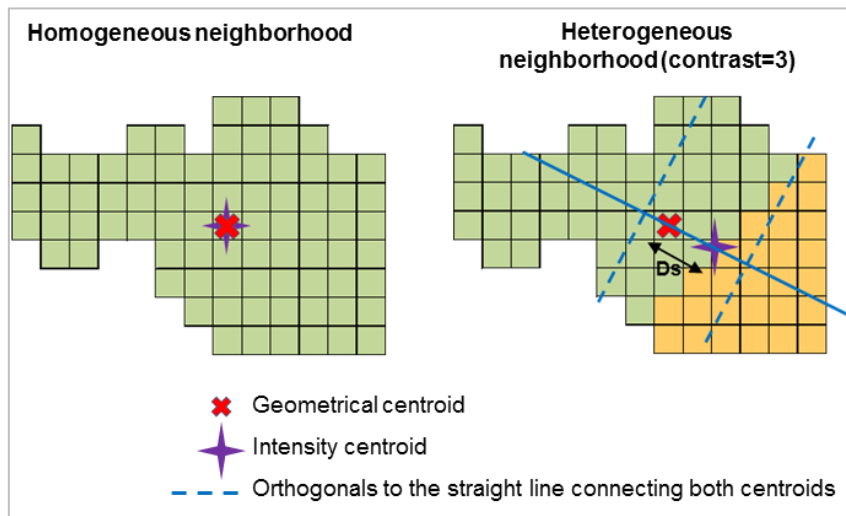
Fig. 8.5. Schematic of the Ds anisotropy measure.
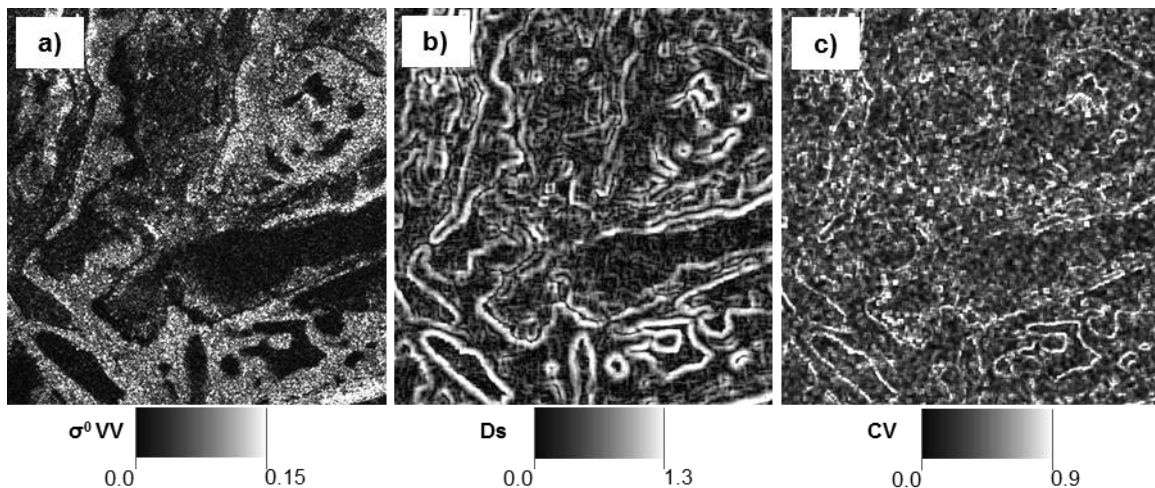
Fig. 8.6. Comparison between the Ds and CV sensitivity the edge presence: a) fragment of the intensity ASAR image from 27 Feb. 2007 at swaths IS6 in VV polarization; b) Ds values computed in 7x7 pixel windows for the image in a); c) CV values computed in 7x7 pixel windows for the image in a).

Strictly speaking, a Ds threshold to discriminate between isotropic textures and edges would depend on the filtering neighborhood geometry. Work aimed at the threshold generalization to different geometries is being undertaken at present. Nevertheless, this study applied Ds thresholds (DsT) between 0.4 and 1.1 based on the image equivalent number of looks and adjusted on an image basis. Neighborhoods with CV > $1/\sqrt{L}$ and Ds <= DsT were considered textured and isotropic, and the corresponding pixel filtered value was computed again as the neighborhood average intensity.

A Ds value higher than the corresponding threshold DsT denotes a spatial imbalance in the region's intensity distribution. Such regions are iteratively cropped in a direction orthogonal to the segment between the region's geometrical centroid and the intensity centroid (e.g. dash lines in Fig. 8.4), until the sub-region including P verifies that Ds <DsT and contains more than 9 pixels. The filtered P value is then computed as the sub-region's intensity mean. If such region is not found, the P value is left unfiltered.

It has to be stressed that the presented filter does not aim at reconstructing the scene radar cross section as the Frost's or Lee's filters do. The goal in the presented work was to smooth intensity fluctuations in textured areas corresponding to single cover types to facilitate their classification. The normalized variance of averaged neighborhoods was saved, since it contains information on the target complementary to its mean value, and can assist a subsequent classification.

8.3   Results and Discussion

Fig. 8.7 depicts the great reduction in the pixel values dispersion achieved by the DTM-guided filtering over homogeneous regions on the IS3 ASAR scene from 20 March 2007.

Fig. 8.8, Fig. 8.9 and Fig. 8.10 show fragments of calibrated ASAR images and their filtered versions using the DTM-guided methodology described in the previous section. Results of applying the Frost filter (Frost 1982) in 9x9 pixel windows are included for comparison.

Fig. 8.8b, Fig. 8.9b and Fig. 8.10b show the significant degree of smoothing achieved by the proposed method over areas of the same class, while the edge sharpness among cover

types is remarkably preserved. The excellent edge definition is basically a consequence that the borders of the DTM-based filtering regions tend to coincide with natural boundaries.

Fig. 8.8c, Fig. 8.9c and Fig. 8.10c reveal that the DTM filtering attains a higher degree of smoothing than the Frost filter. The latter filter aims at reconstructing the target radar cross section by removing the speckle noise. Doñana cover types often present some texture, so intensity fluctuations in the ASAR images are a consequence of both, speckle and texture. In presence of texture, the local CV increases and the Frost filter impulse response is narrowed to preserve texture features. The result is that intensity fluctuations within textured cover classes are often significant and can obscure their classification as a single type.

Another significant observation about the filters performance, stemming from the comparison of vignettes b and c in Fig. 8.8, Fig. 8.9 and Fig. 8.10, is that the Frost filter impulse response operates isotropically, meaning that the influence of relatively bright or dark pixels is equally spread in all directions. As a result, the filtered image takes on a dotted appearance, with concentric artifacts around relatively bright and dark points, which are not related to the real target structure. Some bright pixels are found, for example, surrounding flooded areas. They correspond to recently emerged areas with high moisture level. These pixels emerged simultaneously because they are at approximately the same elevation. Consequently the bright pixels are averaged with each other by the DTM-based filter, even though they are not isotropically distributed. As a result the wet areas became more sharply defined after the DTM-filtering, as exhibited by Fig. 8.8b and Fig. 8.10b.

Rather than reconstructing the scene radar cross section, like the Frost or Lee filters, the goal of the presented method is to flatten intensity fluctuations due to both speckle and texture within areas of the same cover type in order to facilitate their classification. The DTM-based filter assesses the spatial isotropy of the filtering neighborhoods by means of the Ds operator and assumes that isotropic regions belong to a single class. This is a reliable assumption in Doñana marshes, (and presumably in many natural environments). If the region is considered to be of a unique class, the corresponding pixel is characterized by the region's average intensity regardless of its CV. Averaging within isotropic neighborhoods results in higher smoothing than if a speckle filter is used, because most Doñana cover types present some texture.
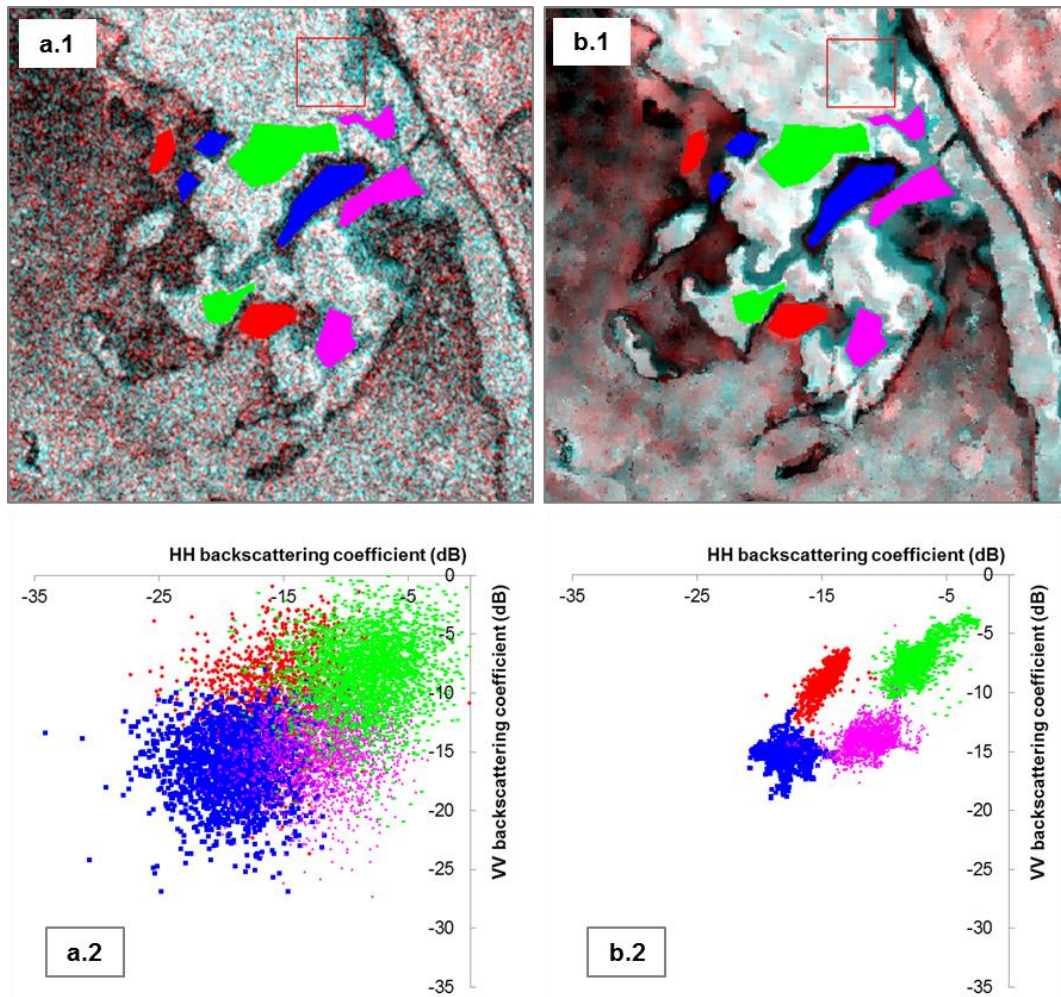
Fig. 8.7. Filtering degree achieved by the DTM-guided methodology over homogeneous regions: a.1) Fragment of the calibrated Doñana ASAR image from 20 March 2007, acquired at swath IS3. $\sigma^0 HH$ is displayed in cyan and $\sigma^0 VV$ in red. Colored polygons define homogeneous regions for four different land cover classes; a.2) Polygon's pixel values in the $\sigma 0HH$ and $\sigma 0VV$ space; b.1) Image in a.1 after applying the DTM-based filter; b.2) Scatter plot of the filtered pixels within the polygons in b.1.
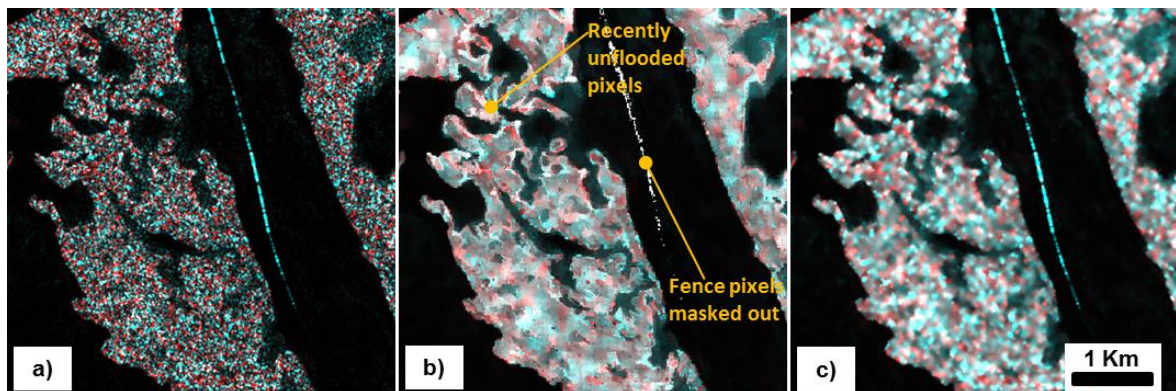
Fig. 8.8. Area in Doñana marshes captured by ASAR on 06 Jan. 2007 at swath IS2, HH/VV polarizations and ascending track. VV intensity is represented in red and HH in cyan: a) image calibrated to backscattering coefficient; b) image filtered with the DTM-based filter; c) image filtered with the Frost algorithm using 9x9 pixel windows.
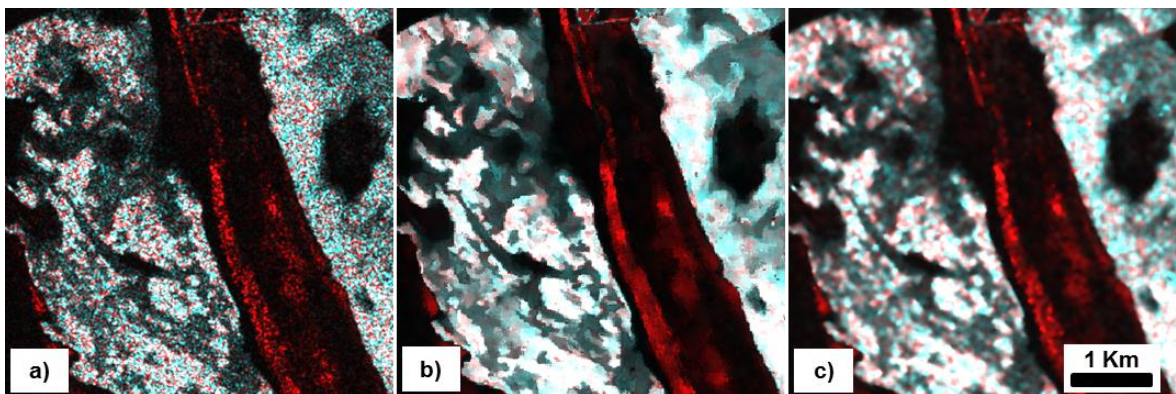
Fig. 8.9. Area in Doñana marshes captured by ASAR on 27 Feb. 2007 at swath IS6, HH/VV polarizations and descending track. VV intensity is represented in red and HH in cyan: a) image calibrated to backscattering coefficient; b) image filtered with the DTM-based filter; c) image filtered with the Frost algorithm using 9x9 pixel windows.
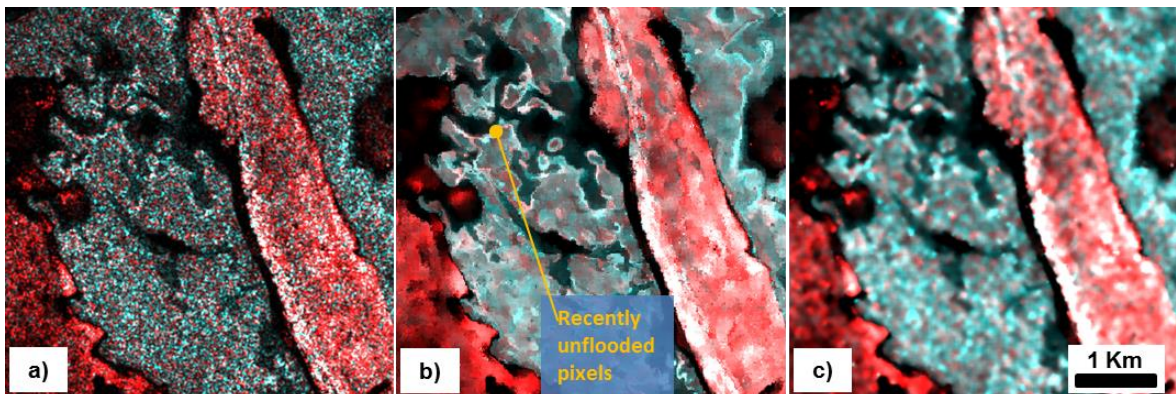
Fig. 8.10. Area in Doñana marshes captured by ASAR on 03 Apr. 2007 at swath IS6, HH/VV polarizations and descending track. VV intensity is represented in red and HH in cyan: a) image calibrated to backscattering coefficient; b) image filtered with the DTM-based filter; c) image filtered with the Frost algorithm in 9x9 pixel windows.

8.4 Conclusions

This chapter describes the filtering procedure applied to the Doñana ASAR images under the guidance of the DTM.

The use of irregular filtering neighborhoods fitting the elevation contours drastically improved the ASAR images filtering. Edge preservation was excellent, since natural edges closely follow terrain contours. Isotropic neighborhoods were assumed of a single class and their intensities were averaged. As a result, intensity fluctuations due to speckle and texture over areas of the same cover type were remarkably smoothed, facilitating the

subsequent clustering and classification tasks. The edge preservation and smoothing degree attained by the DTM-guided filtering was significantly better than that obtained by applying common speckle filters with square processing windows.

8.5 References

Frost, V. S., Stiles, J. A., Shanmugan, K. S., & Holtzman, J. C. (1982). A model for radar images and its application to adaptive digital filtering of multiplicative noise. IEEE Transactions On Pattern Analysis And Machine Intelligence, PAMI-4, 157–166.

Getis, A. (2010). Spatial Autocorrelation. In Handbook of Applied Spatial Analysis (pp. 255–278). doi:10.1007/978-3-642-03647-7_14

Griffith, D. A. (1987). Spatial Autocorrelation – A Primer. Washington D.C.: Association of American Geographers.

King, R. S., Baker, M. E., Whigham, D. F., Weller, D. E., Jordan, T. E., Kazyak, P. F., & Hurd, M. K. (2005). Spatial Considerations For Linking Watershed Land Cover To Ecological Indicators In Streams. Ecological Applications. doi:10.1890/04-0481

Kuan, D. T., Sawchuk, A. A., Strand, T. C., & Chavel, P. (1985). Adaptive noise smoothing filter for images with signal-dependent noise. IEEE Transactions On Pattern Analysis And Machine Intelligence, PAMI-2, 165–177.

Lee, J. S. (1980). Digital Image Enhancement and Noise Filtering by Use of Local Statistics. IEEE Transactions On Pattern Analysis And Machine Intelligence, PAMI-2(2), 165–168.

Lee, J. S. (1983). Refined filtering of image noise using local statistic. Computer graphics and image processing, 24, 255–269.

Legendre, P., & Legendre, L. (1998). Numerical ecology. Numerical Ecology Second English Edition (Vol. 20, p. 870). doi:10.1021/ic050220j

Lopes, A., Nezry, E., Touzi, R., & Laur, H. (1993). Structure detection and statistical adaptive speckle filtering in SAR images. International Journal of Remote Sensing, 14, 1735–1758. doi:10.1080/01431169308953999

Lopes, A., Touzi, R., & Nezry, E. (1990). Adaptive speckle filters and scene heterogeneity. IEEE Transactions on Geoscience and Remote Sensing, 28. doi:10.1109/36.62623

Martí-Cardona, B, López-Martínez, C., & Dolz-Ripollés, J. (2012). Local texture stationarity indicator for filtering Doñana wetlands SAR images. Geoscience and Remote Sensing Symposium (IGARSS), 2012 IEEE International. doi:10.1109/IGARSS.2012.6352513

Martí-Cardona, Belen, López-Martínez, C., Dolz-Ripollés, J., & Bladé-Castellet, E. (2010). ASAR polarimetric, multi-incidence angle and multitemporal characterization of

Doñana wetlands for flood extent monitoring. Remote Sensing of Environment, 114(11), 2802–2815. doi:10.1016/j.rse.2010.06.015

Nezry, E., Lopes, A., & Touzi, R. (1991). Detection Of Structural And Textural Features For Sar Images Filtering. [Proceedings] IGARSS'91 Remote Sensing: Global Monitoring for Earth Management, 4. doi:10.1109/IGARSS.1991.575470

Ord, J. K., & Getis, A. (1995). Local Spatial Autocorrelation Statistics: Distributional Issues and an Application. Geographical Analysis, 27, 286–306. doi:10.1111/j.1538-4632.1995.tb00912.x

Overmars, K. P., de Koning, G. H. J., & Veldkamp, A. (2003). Spatial autocorrelation in multi-scale land use models. Ecological Modelling, 164, 257–270. doi:10.1016/S0304-3800(03)00070-X

Touzi, R. (2002). A review of speckle filtering in the context of estimation theory. IEEE Transactions on Geoscience and Remote Sensing, 40. doi:10.1109/TGRS.2002.803727

Touzi, R., Lopes, A., & Bousquet, P. (1988). A statistical and geometrical edge detector for SAR images. IEEE Transactions on Geoscience and Remote Sensing, 26, 764–773.

Chapter 9:
Image Classification and Flood Mapping

9.1   Introduction

In Chapter 7 the temporal backscattering characteristics of Doñana's main land cover types were determined and discussed. These signatures were obtained by averaging the backscattering coefficient within control polygons, representative of the different covers. In Chapter 8, ASAR images were filtered with the aim to smooth out backscattering fluctuations due to speckle and texture, so that the filtered values were comparable to the previously determined backscattering characteristics.

In this chapter the filtered images are classified based on the land cover characterization undertaken in Chapter 7. The σ^0HH and σ^0VV coefficients are first shown to be insufficient for the temporal discrimination of cover types, due to the complex casuistic of the covers' backscattering. Ancillary information is then introduced in order to increase the land cover discrimination capacity and aid the classification process.

Once the images have been classified, flood maps are produced by simply reclassifying the flooded cover types.

9.2   Analysis of Cover Types in the $\sigma^0 HH$-$\sigma^0 VV$ Space

As discussed in Chapter 4, Doñana marshes can be subdivided into three main area types, with distinctive topographical and vegetation characteristics: paciles, ponds centers and transition zones. These main cover types are sketched and mapped in Fig. 4.18 and Fig. 4.15, respectively.

Control polygons representative of the main types were defined in Chapter 7 to determine the covers' backscattering signatures. Fig. 9.1 shows the polygons' average backscattering coefficient in all ASAR scenes from the 2006-2007 hydrologic year, in the $\sigma^0 VV/(\sigma^0 HH$-$\sigma^0 VV)$ space. Two observations can be readily drawn from Fig. 9.1. Firstly, σ^0 values from flooded pond centers (open water) and flooded transition zones show a large dispersion, as already pointed out in Chapter 7. Backscattering from open water areas can change capriciously up to 15 dB in time and space depending on the wind-induced surface roughness at the steepest swaths. A comparable σ^0 change is found in helophyte areas depending on the plants flooding and phenological stage. For this cover type, a large variation is also observed in the relative backscattering between polarizations, which can be up to 9 dB depending basically on the stems above-water height and spatial density.

Secondly, Fig. 9.1 reveals significant overlapping among different covers' backscattering, substantiating the difficulty to discriminate among them just from the two single-acquisition ASAR channel data. Backscattering from roughened open water at steep swaths, for instance, is similar to that from the emerged almajo regions, indicating the potential confusion among these classes. Flooded and emerged almajo areas show a significant overlap at swaths IS6 and IS7, as discussed in Chapter 7. Regarding the helophyte areas, they can coincide with virtually any class throughout their annual phenological evolution. Especially difficult to disentangle with ASAR data is the confusion between wind-roughened open water and flooded helophytes at the beginning of the stems emergence from the water surface.

It can be concluded from the figures and considerations above, that a land cover classification based exclusively on the $\sigma^0 HH$ and $\sigma^0 VV$ values of single ASAR acquisitions would lead to significant confusion among cover types at several hydrologic stages and incidence angles. However, the available data on Doñana's topography, vegetation and hydrological functioning are noteworthy. This information might be fed into a land cover classification algorithm in order to complement the σ^0 data and reduce the confusion

among classes. Section 9.4 is concerned with this issue.
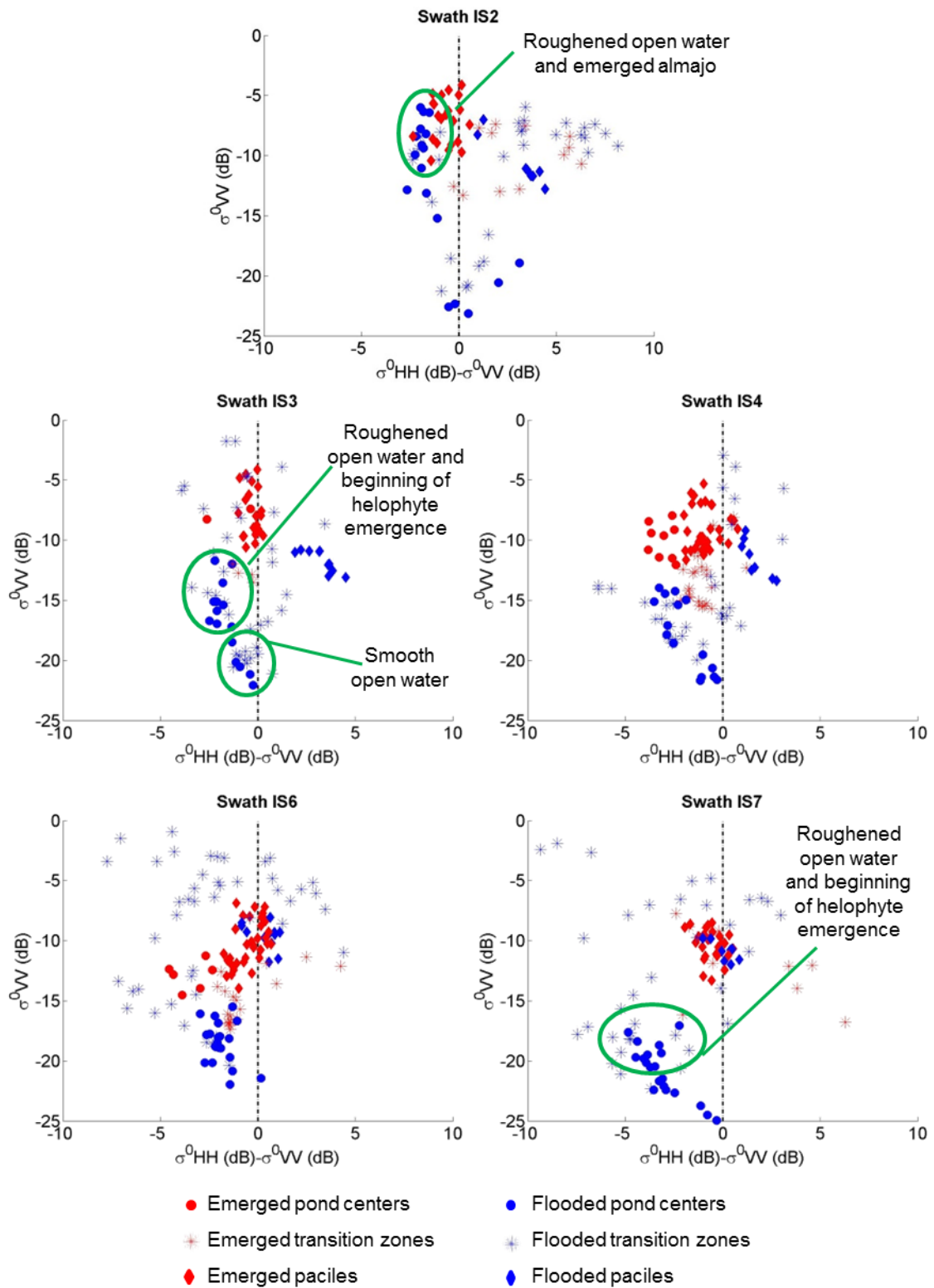
Fig. 9.1. Scatter plots of the control polygons' mean backscattering at five incidence angles. Overlapping between different classes backscattering characteristics is indicated with green lines.

9.3   Choice of Land Cover Classes

In a first approach, a reasonable cover classes' choice for flood mapping would be to consider two separate categories for each of the three main area types, depending on their flooded or emerged state. The classes set would then consist of: flooded pacil, emerged pacil, flooded transition zone, emerged transition zone, flooded pond center and emerged pond center.

However, the large dispersion of the transition zones backscattering advised a further subdivision of this cover type into different classes depending on the plants phenological stage, so the resulting classes could roughly approximate a cluster in the σ^0HH-σ^0VV space. Following this approach and always with the main goal of mapping the flooded areas in mind, the classes listed below were adopted. Photographs of these categories can be seen in Figs. 9.2 to 9.10.

- **Bare soil**, which corresponds to emerged pond centers;
- **Open water**, formed by flooded pond centers;
- **Dry emerged helophytes**, found in the transition zones at the beginning of the hydrologic year;
- **Flooded dry helophytes**, in the transition zones during the fall;
- **Flooded green helophytes at the beginning of the emergence**, which occurs approximately from the end of February until mid-March.
- **Flooded developed green helophytes**, found from mid-March on.
- **Green emerged helophytes**, from April on, depending on the flood duration;
- **Emerged almajo**;
- **Flooded almajo**, which might not be found in dry years.
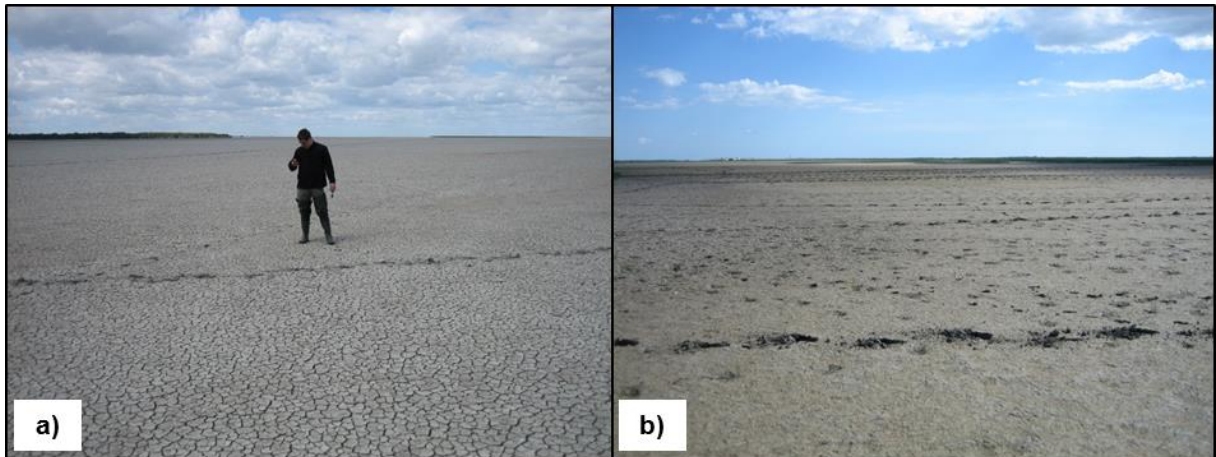
Fig. 9.2. Views of emerged pond centers which correspond to the cover class *bare soil:* a) dry bare soil; b) wet bare soil, with cattle footprints.
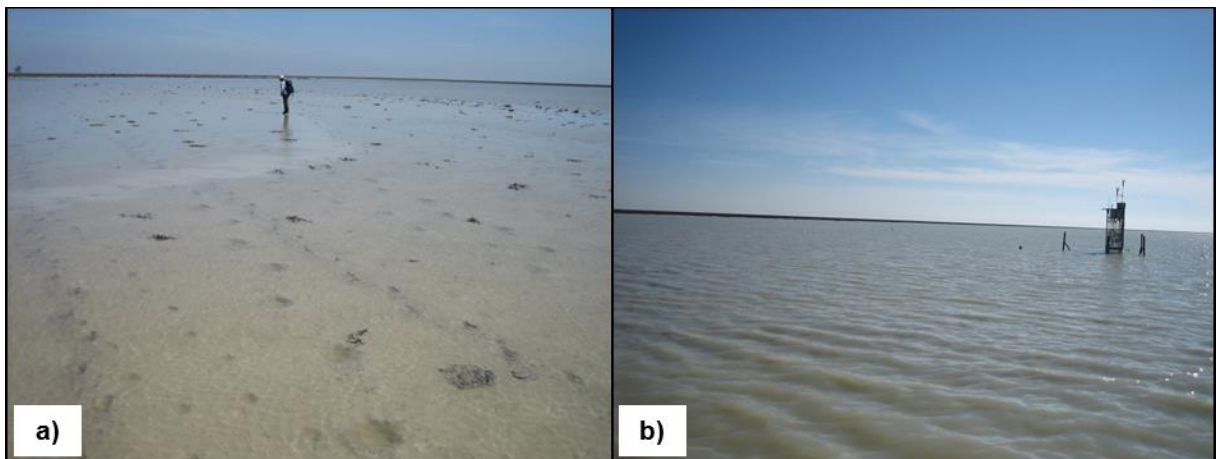
Fig. 9.3. Views of flooded pond centers which constitute the cover class *open water*: a) smooth open water; wind-roughened open water.
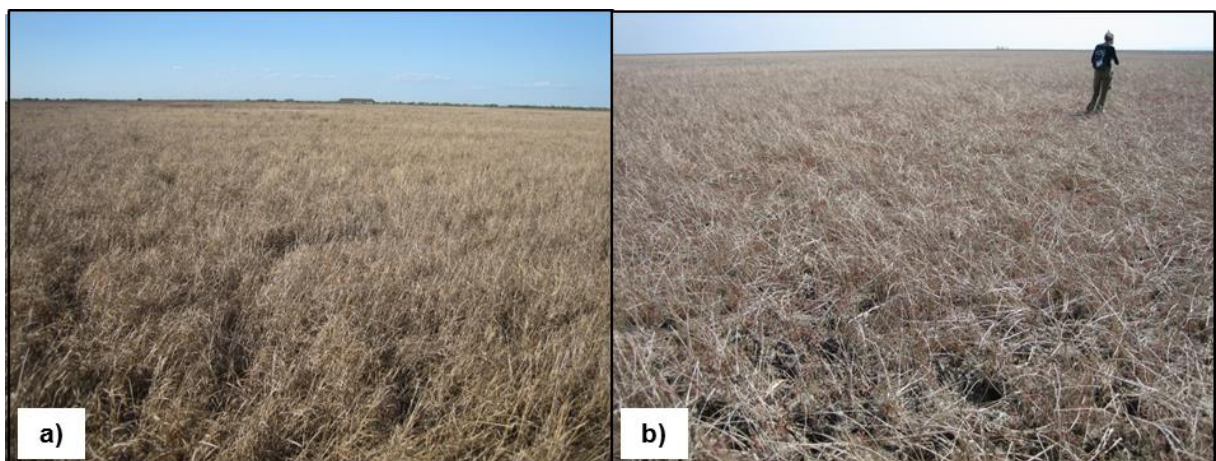
Fig. 9.4. Views of the class *dry emerged helophytes*.
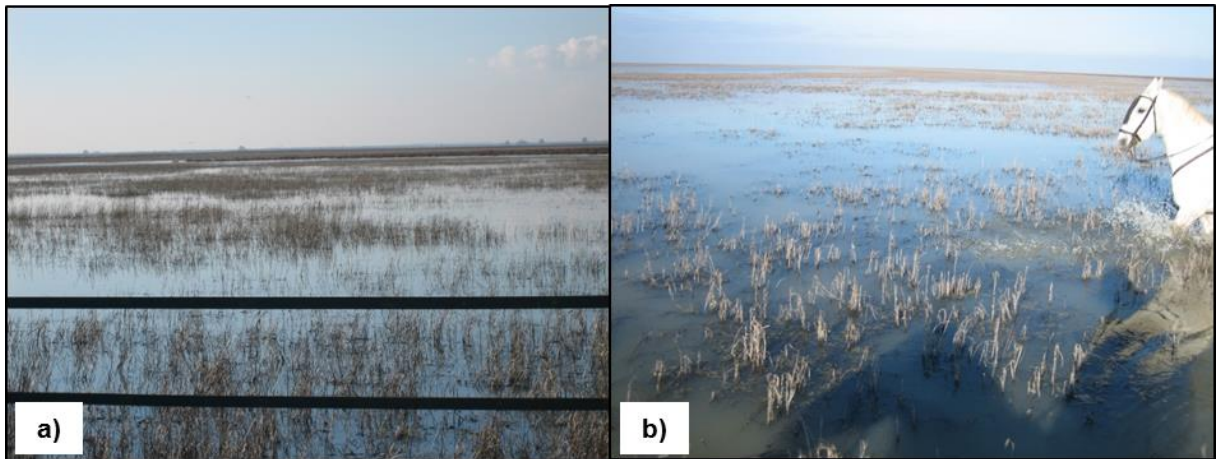
Fig. 9.5. Views of the class *flooded dry helophytes*.
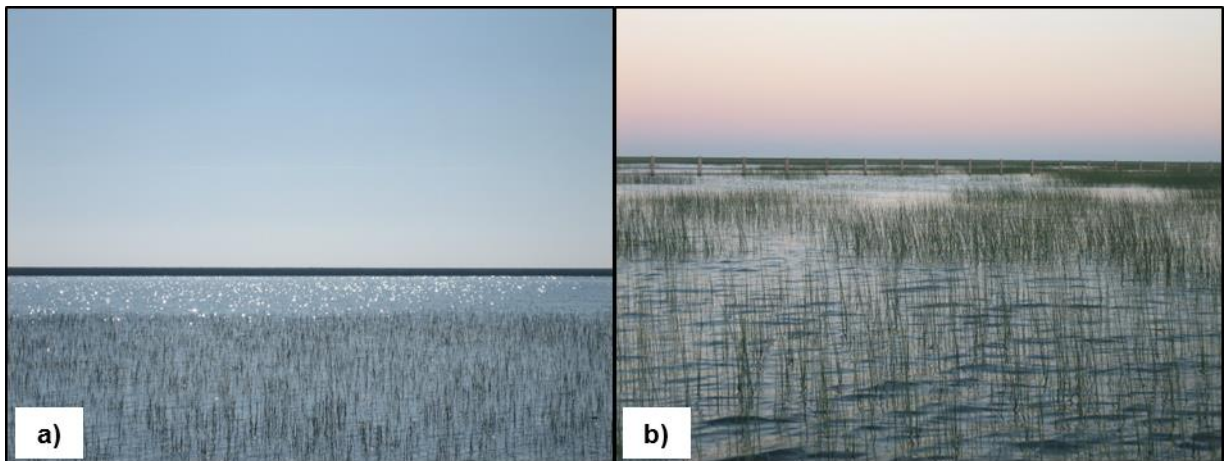
Fig. 9.6. Views of the class flooded green helophytes at the beginning of the emergence.
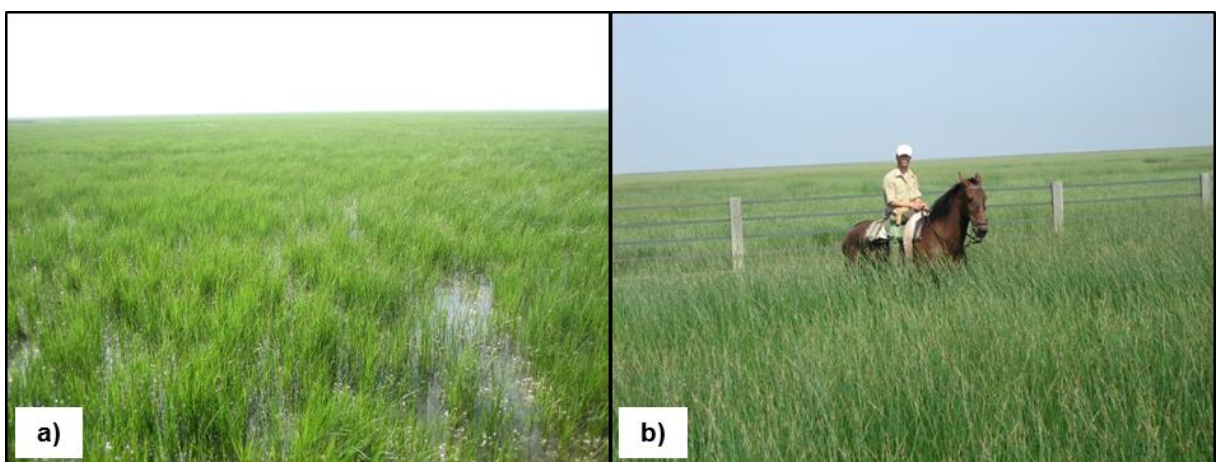
Fig. 9.7. Views of the class *flooded developed green helophytes*.
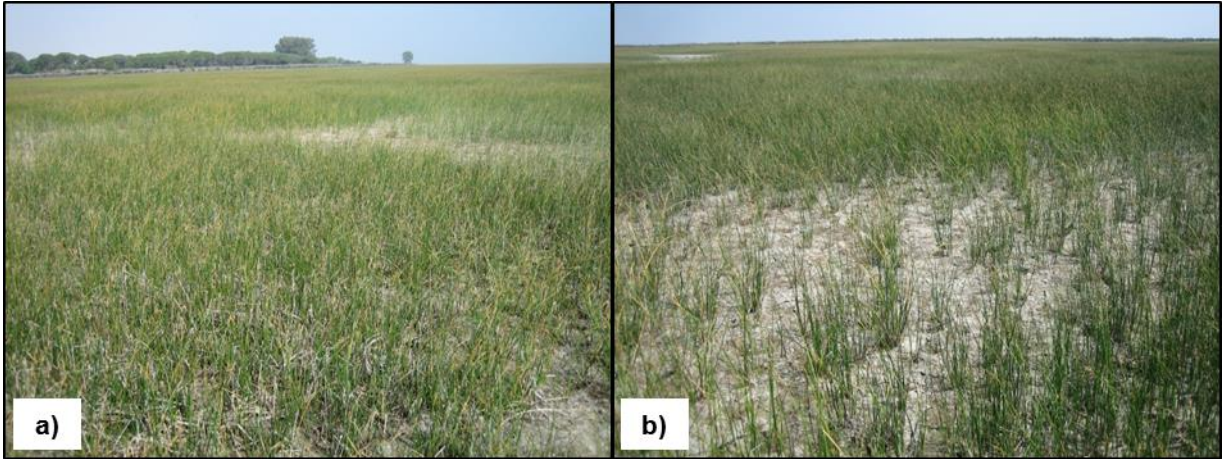
Fig. 9.8. Views of the class *emerged green helophytes.*
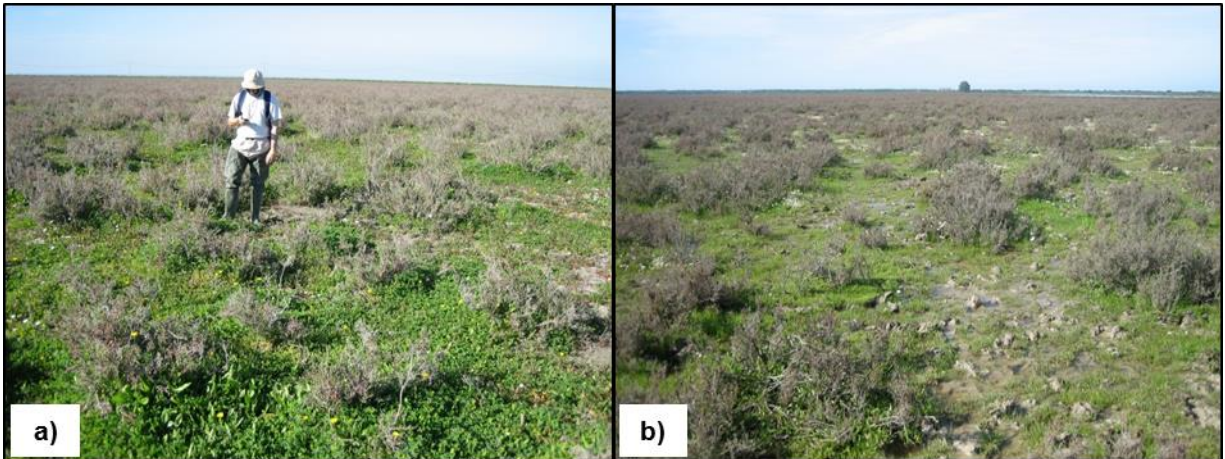
Fig. 9.9. Views of the class emerged almajar.
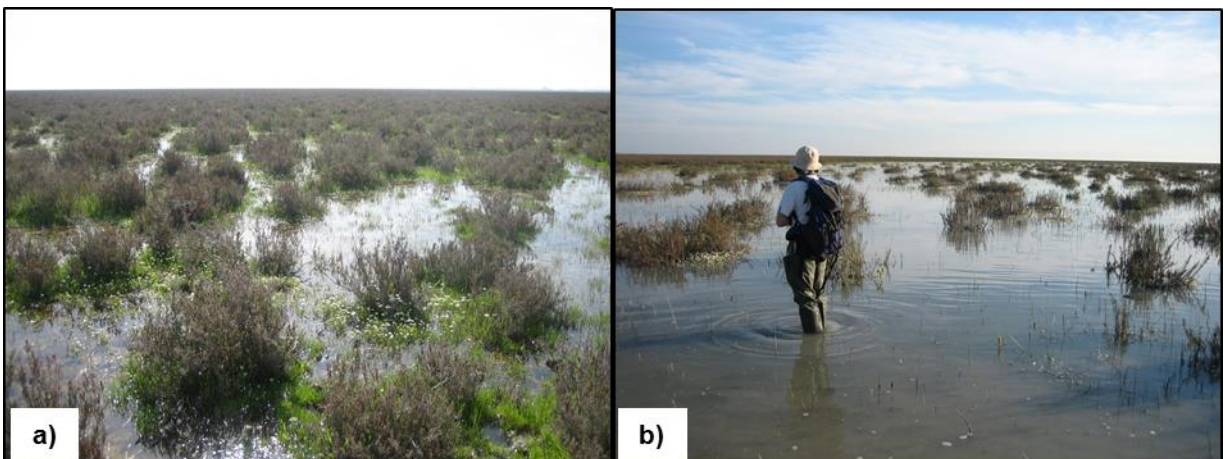
Fig. 9.10. Views of the class flooded almajar.

9.4   Ancillary Data to Aid the Land Cover Classification

It has been stressed in Section 9.2 that backscattering values of single ASAR acquisitions are insufficient for land cover classification and flood mapping of Doñana wetlands at several hydrologic stages and incidence angles. The following sections discuss different data sources to supplement the ASAR images for mapping purposes.

9.4.1   ANCILLARY SPATIAL DATA: THE LAND COVER MAP

Mean backscattering temporal signatures from Doñana main land covers were analyzed in Chapter 7 and conclusions regarding the flood detection feasibility at each incidence angle were drawn on a cover type basis. A straightforward way to implement the land cover map information into a classification algorithm would be to subdivide the ASAR images in a cookie-cut fashion into pond center, helophyte and pacil areas. Then, a decision on the inundation state of each area type could be based on the corresponding backscattering signature, according to Chapter 7's conclusions. In other words, the cover type label at every pixel would indicate the temporal signature to be considered in order to decide on its flooding state.

Nevertheless, this approach has important drawbacks. Firstly, the validity of the flood delineation would be subordinated to the correctness of the land cover map. Some relevant errors in the cover type map were pinpointed during the ground truth campaigns. But the most limiting aspect of the cookie-cut approach is that it does not account for inter-annual changes in the plant communities' spatial distribution. This is an important limitation in highly dynamic environments, such as coastal wetlands. And it is aggravated in the Doñana's case due to the fast change rate caused by hydrologic restoration actions and foreign species invasion.

The land cover data was exploited by the classification algorithm in a soft way, so it did not constrain the pixels' class to its corresponding cover type on the map. This was used only as a reference for the selection of those pixels with high confidence on their class membership, which are then used as seed regions in a clustering stage. High confidence pixels are searched for within their corresponding cover type areas, indicated by the land cover map. The precise utilization of the cover map in the classification procedure is described in Section Methodology.

9.4.2   ANCILLARY SPATIAL DATA: THE DTM

As it was discussed in Section 4.4, a close correspondence is found between the pixels' cover classes and their absolute elevation within the Doñana's sub-basins. Hence, the DTM can potentially provide relevant information on the pixels cover type and improve the classes' separability. Fig. 9.11 depicts the separability increment achieved by adding the terrain elevation (Z) data to the backscattering information of an ASAR image: a segment of the ASAR scene from 20 March 2007 is displayed on Fig. 9.11a, after having been filtered as explained in Chapter 8. Colored polygons define regions of interest (ROI's) for the land classes: open water, flooded helophytes, flooded almajar, and emerged almajar. Fig. 9.11b depicts the scatter plot of the ROI's pixel values in the σ^0HH and σ^0VV space and shows significant overlapping among the classes. The ROI's pixel values are represented in the σ^0VV-Z space in Fig. 9.11c, where the classes are clearly more separable.
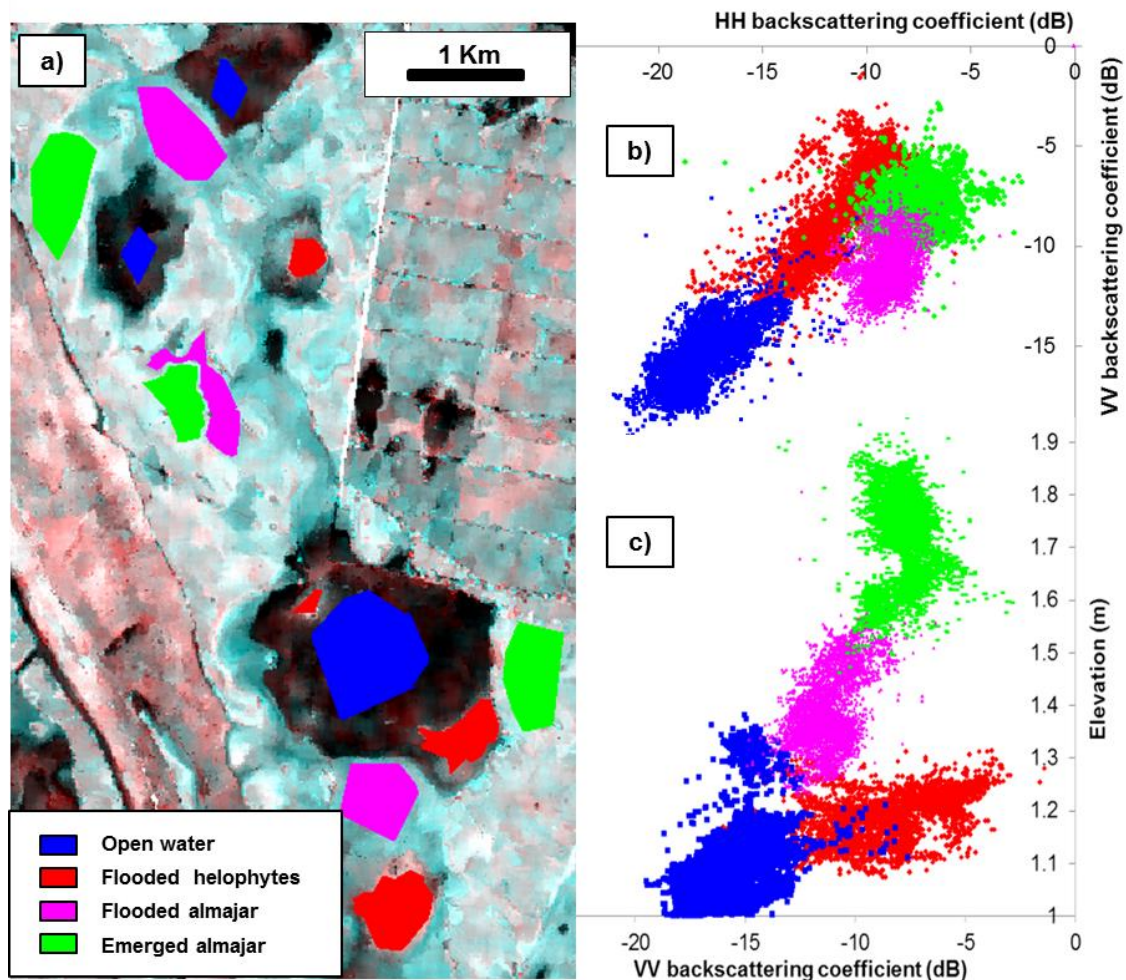
Fig. 9.11.Class separability increment achieved by adding the pixels' elevation data within sub-basins: a) Mari López sub-basin on the calibrated and filtered Doñana ASAR image from 20 March 2007, acquired at swath IS3. σ^0HH is displayed in cyan and σ^0VV in red. The colored polygons define ROIs for the main land classes; b) ROI's pixel values in the σ^0HH and σ^0VV space; c) ROI's pixel values in the σ^0VV and terrain elevation space.

Fig. 9.12 and Fig. 9.13 illustrate another example of the separability enhancement attained with the DTM. Fig. 9.12a is a segment of the ASAR image acquired on 1 November 2006. Figs. 9.12b, Figs. 9.12c and Figs. 9.12d represent a histogram plot of the ASAR segment's pixels in the σ^0VV/σ^0HH, σ^0HH/Z and σ^0VV/Z spaces, respectively. Bright pixels of the emerged almajar get confused with wet emerged brown helophytes in Fig. 9.12b. The pixels corresponding to each cover type separate in two different clusters when introducing the elevation data in the plots of Fig. 9.12c and 9.12d. Fig. 9.13 shows the correspondence between the histogram dots and the ASAR image. The cluster surrounded by a magenta line in the σ^0VV/σ^0HH space of Fig. 13b matches the pixels of emerged almajar and emerged helophytes in Fig. 9.13a. The same dots detach in two clusters in Fig. 9.13d, which correspond to emerged almajar (highlighted in red in Fig. 9.13c) and brown helophytes areas (in green in Fig. 9.13c).
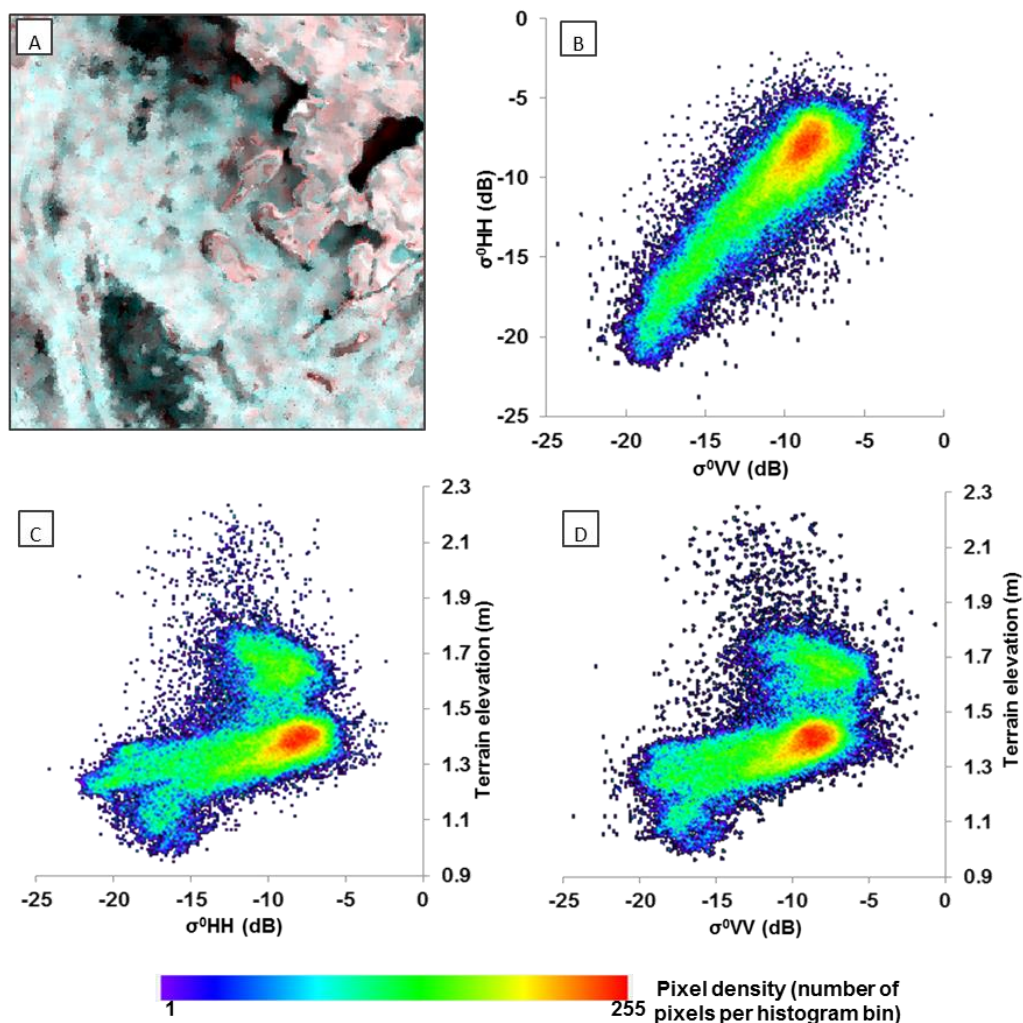
Fig. 9.12. Separability enhancement attained by using the pixels' elevation data within sub-basins: a) segment of the Hinojos sub-basin on the calibrated and filtered Doñana ASAR image from 1 November 2006, acquired at swath IS4. σ^0HH is displayed in cyan and σ^0VV in red; b) histogram plot of the ASAR segment's pixels in the σ^0VV/σ^0HH space; c) histogram plot in the σ^0HH/Z space; d) histogram plot in the σ^0VV/Z space.
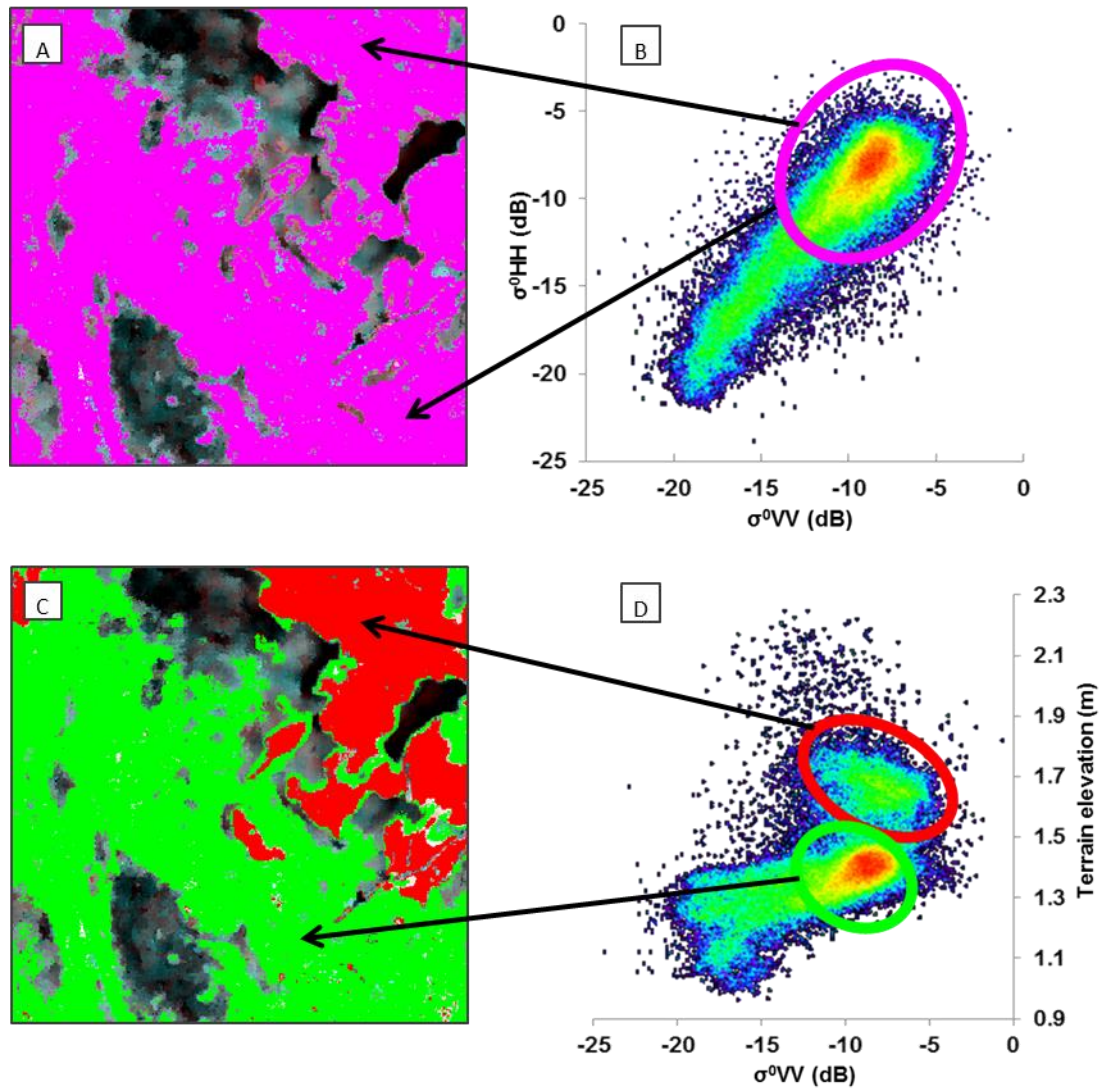
Fig. 9.13. Correspondence between the feature space histogram dots and the ASAR image: a) and b) emerged almajar and brown helophytes are confused in the σ⁰VV/σ⁰HH space; c) and d) emerged almajar and brown helophytes separate in the σ⁰VV/Z space

9.4.3   ANCILLARY TEMPORAL DATA: FLOODING AND DRYING OUT PERIODS

Fig. 4.4 in Chapter 4 depicts the water level evolution in Doñana marshes throughout the 2006-2007 hydrologic year. It could be thought to make assumptions on the inundation level and feasible classes in the target area as a function of the ASAR acquisition date, according to an average water level evolution trend. Such assumptions would be appropriate if Doñana's water cycles were reasonably regular and would greatly ease the classifications tasks. Nevertheless, Doñana's hydrology shows highly variable flooding cycles, as illustrated by the accumulated precipitation curves in Fig. 4.5. In addition,

according to historical records it is not unusual that one or more sub-basins in the marshes dry out completely during the filling up period, or that rainfall events fill up others during the drying out time. Fig. 9.14 shows an example: the deepest bare soil areas in the Membrillo and Ansares sub-basins flooded at the beginning of October 2007, as it can be observed in Fig. 9.14a. Following a normal cycle, these areas would have been flooded until the end of the spring or beginning of the summer. But the precipitation absence caused them to emerge and the bare soil class to reappear one month afterwards, as shown in Fig. 9.14b. This sort of out-of-time events would invalid assumptions on the feasible classes set at a given period of the hydrologic year.
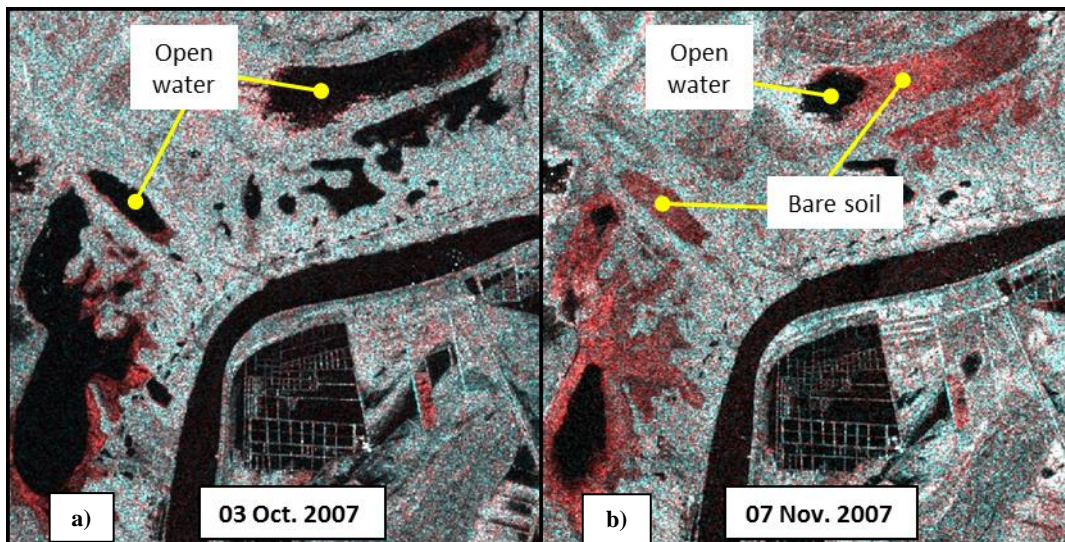
Fig. 9.14. The Membrillo and Ansares ponds on two ASAR images acquired 35 days apart in Fall 2007, at swath IS6. σ^0HH is displayed in cyan and σ^0VV in red

In general, classifications using temporal assumptions on the target characteristics would be largely undermined by the inter-annual variability, if images of different hydrological years were to be classified. Such assumptions were discarded since one of the requirements for the classification procedure developed here was the capability to map Doñana's flood extent from single ASAR acquisitions from different hydrologic cycles.

The only temporal input used for the image classification is the subdivision of the scenes as corresponding to the flooding or drying out period. The so-called flooding period goes from the beginning of the inundation until approximately mid-April. An automated classification algorithm has been developed for images acquired during this time. This algorithm is explained in detail in Section Methodology. In the last part of the inundation period, referred to as the drying out period, the water level declines steeply while

helophytes form thick vegetation canopies. Flood mapping at this stage was assisted by ancillary water level data.

9.4.4   ANCILLARY WATER LEVEL DATA

Section Methodology explains how thresholds are used together with the land cover map and the DTM in order to select seed regions for each class. These thresholds are stablished for flood mapping in the marshes filling up period and can be used in any hydrologic year.

In the marshes drying period, the helophytes can emerge from the flooded area at different developmental degrees, depending on the cycle's temporal accumulated precipitation. These variations introduce inter-annual differences in the thresholds needed for the selection of flooded and emerged helophytes seed regions.

In order to produce flood maps at the end of the flooding cycle, the selection of thresholds for the flooded and emerged transition zones had to be determined on an image basis with the aid of the water level records at the time of the corresponding ASAR acquisitions.

9.5   Methodology

The following sub-sections describe the algorithm developed for the classification and flood mapping of the Doñana wetlands' multi-incidence angle ASAR images. The algorithm is automated, meaning that it does not need the user's intervention, for the images acquired during the marshes filling up period, from the beginning of the inundation in fall until approximately mid-April. The more complex casuistic of land covers backscattering during the marshes drying out made the user intervention necessary to accomplish flood mapping, in May and June.

9.5.1   SUB-BASIN SEGMENTATION

The Doñana area was divided into sub-basins by applying the watershed segmentation algorithm to the marshes DTM (Meyer, 1994). Previously, the extended minima transform

described in Soille (2003) was applied to the DTM so local minima at each sub-basin were at least 0.40 m deeper than their surroundings. This transformation prevents the watershed algorithm from oversegmenting around shallow or irrelevant troughs. The value 0.40 m was one of the smallest thresholds for which all cover types were represented in the segments covering 90% of the marshes area: from the bare soil, the one with the largest hydroperiod, to the almajar at the top. Fig. 9.13 shows the sub-basins used in this study. Zones A and B were excluded from the analysis because no vegetation maps were available for them, and because their topography had been sensibly modified between the generation of the DTM and the ASAR scenes acquisition.
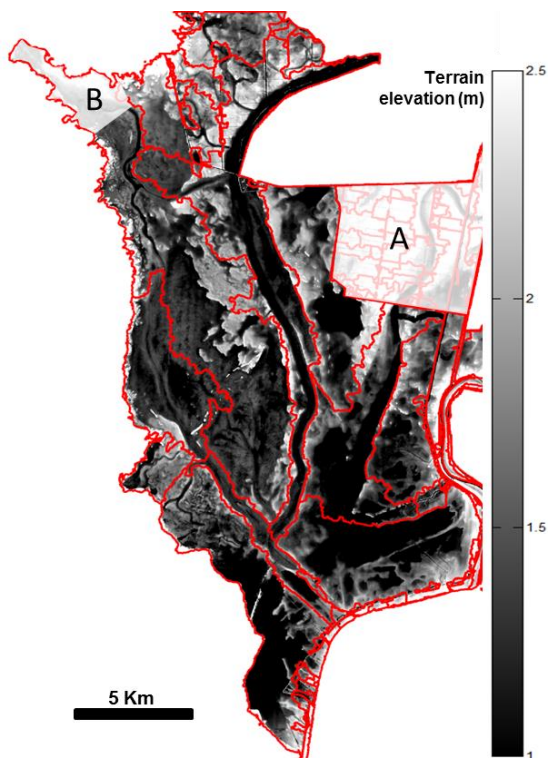
Fig. 9.15. Doñana marshes digital terrain model and sub-basins. Watersheds among sub-basins are shown in red. No accurate elevation data is available for areas A and B.
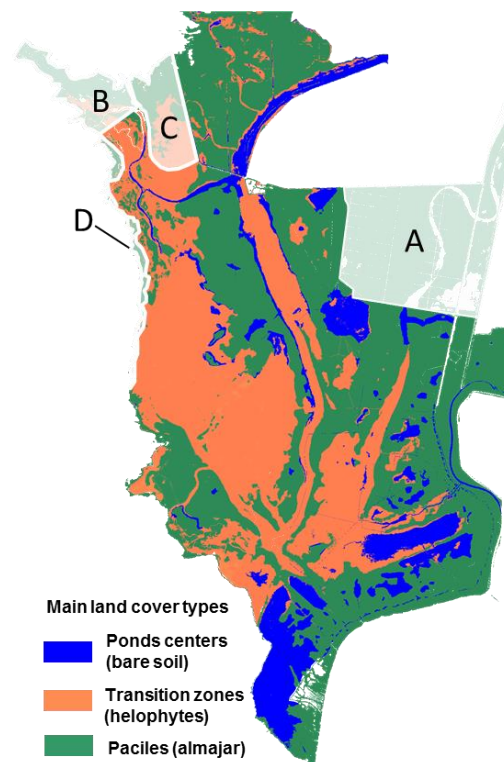
Fig. 9.16. Doñana main cover types. No vegetation cartography is available for areas A and B. No backscattering characterization was available for vegetation communities in C and D.

9.5.2   SELECTION OF THE CLASSES' SEEDS

Pixels highly likely to belong to the different cover classes were selected by combining the available vegetation map, the sub-basin segmentation and knowledge of the Doñana's

covers backscattering behavior. These pixels provide the classes' seeds or starting reference regions for a subsequent clustering algorithm.

The selection of the classes' seeds is performed on the ASAR images' regions defined by the corresponding cover type polygons in Fig. 9.16. In order to be selected as seeds, the pixels' backscattering needs to meet certain thresholds specific for each cover type and for each incidence angle. The majority of these thresholds were defined based on the covers backscattering behavior presented in Chapter 7. For instance, if a pixel in almajar areas shows low $\sigma^0 VV$ and high $\sigma^0 HH$ to $\sigma^0 VV$ ratio, then it is very likely to be flooded almajar. How low or high $\sigma^0 VV$ and $\sigma^0 HH/\sigma^0 VV$ need to be, depends on the thresholds defined for each incidence angle.

For the images acquired from mid-April to June, the thresholding needed to select flooded and emerged seed regions in the transition zones was determined by defining regions of interest (ROI's) for both classes on an image basis. The region definition was assisted by knowledge of the water levels from the on-site gauging stations at the moment of the image acquisition. The thresholds were then based on the corresponding ROIs pixel values.

All classes' thresholding is applied within sub-basins in order to reinforce the backscattering information with elevation data. Following with the almajar example, an emerged almajar seed pixel has to meet some backscattering thresholds, and additionally, it has to be higher than the flooded almajar pixels. Conditions such as "emerged almajar pixels being higher than flooded almajar ones" are much more consistent if applied within sub-basins.

A flow diagram sketching the selection of the classes' seeds is shown in 9.17. Thresholds used for the different ASAR swaths, except for the transition zones in May and June images, are shown in Table 9.1. Open water and bare soil targets were found to verify $/\sigma^0 VV-(0.92 x\sigma^0 HH+1.18)/<2.0$ at all ASAR incidence angles in Martí-Cardona et al., 2010. This relation is included as a necessary condition for the selection of such target pixels in the three decision trees. Fig. 18c shows an example of seed pixels selection.

It is worth stressing that the aim of the decision trees is not to perform a complete flooded areas classification of the scene, not even an approximation of the classes' center in the feature space. The aim is only to select pixels with high confidence on their class

membership. These pixels will serve as the classes' seeds or starting regions at the subsequent clustering stage where the rest of the pixels are grouped and assigned to a class according to their backscattering coefficients, and X-Y-Z location.
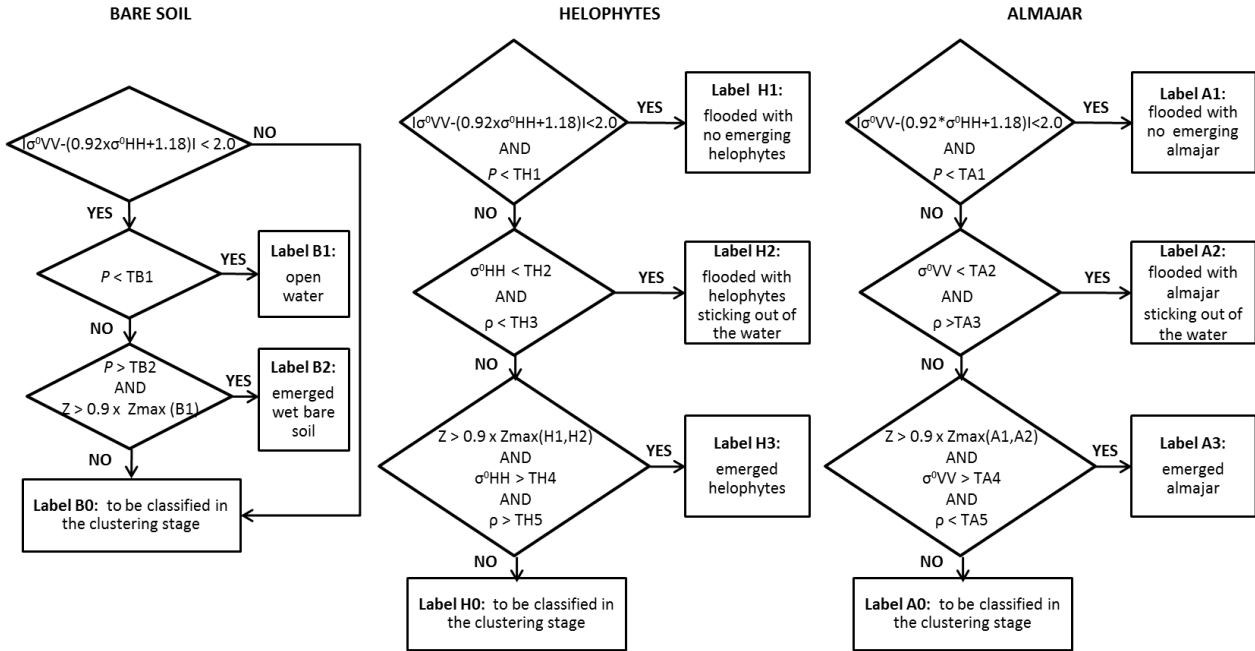
Fig. 9.17. Flow diagrams sketching the selection of the classes seed regions within polygons of bare soil, helophytes and almajar. All expressions consider backscattering magnitudes in dB units. P stands for $\sigma^0 HH + \sigma^0 VV$ computed in m^2/m^2 and expressed in dB; ρ stands for the $\sigma^0 HH$ to $\sigma^0 VV$ ratio, and was computed in dB units as $\sigma^0 HH$ (dB)-$\sigma^0 VV$ (dB); Thresholds TB, TH and TA are indicated in Table 9.1.

Table 9.1. Decision thresholds (dB) used in the flow diagram of Fig. 9.17 for each ASAR incidence angle.

Thresholds: ASAR swaths:	TB1	TB2	TH1	TH2	TH3	TH4	TH5	TA1	TA2	TA3	TA4	TA5
IS2	-6.0	-3.0	-6.0	-15.0	-1.0	-10.7	0	-6.0	-10.0	2.0	-7.0	0.5
IS3	-9.5	-6.0	-9.5	-15.0	-1.0	-11.4	0	-9.5	-10.0	2.0	-8.0	0.5
IS4	-12.0	-10.0	-12.0	-15.0	-2.0	-12.0	-1.0	-12.0	-10.0	1.0	-8.0	0.5
IS6	-14.0	-11.5	-14.0	-15.0	-3.0	-12.7	-1.50	-14.0	-10.0	0.5	-8.5	0.5
IS7	-15.0	-12.7	-15.0	-15.0	-4.0	-13.0	-1.50	-15.0	-10.0	0.0	-9.0	0.0

9.5.3   CLUSTERING

The classes' seeds selected by the decision trees typically comprised more than 70% of the marshes pixels. The rest of the pixels are clustered and assigned to one of the existing classes by means of a region growing algorithm and a final clustering performed in the $\sigma^0 VV$-$\sigma^0 HH$-Z space.

Region growing

The sample regions determined by means of the decision trees are grown as follows:

-   Image pixels adjacent to every region are selected.
-   The Mahalanobis distance (Mahalanobis, 1936) between every adjacent pixel and each class is computed. The seed regions are used as the reference sample needed for the Mahalanobis distance calculation.
-   If the minimum Mahalanobis distance between an adjacent pixel and a sample class happens for the contiguous class, then the pixel is assigned to that class.
-   When all assignments have been performed, the just classified pixels are adjoined to the sample regions. New adjacent pixels are determined and the whole process is repeated.
-   The process ends when no new assignments are made in two consecutive iterations.

Fig. 9.18d shows the result of the growing region procedure applied to the seed regions of Fig. 9.18c.
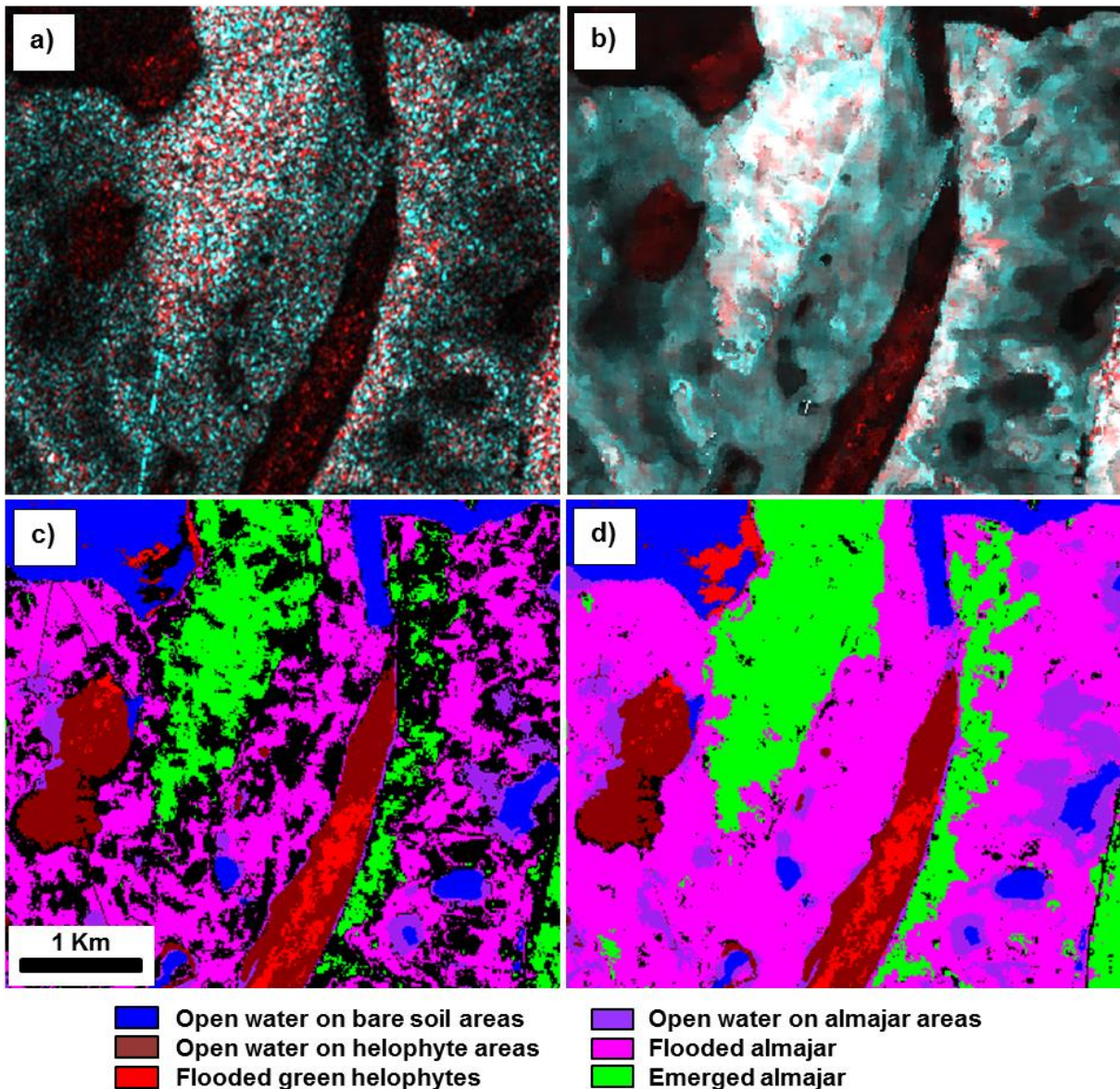
Fig. 9.18. Example of the filtering and clustering stages: a) area in Doñana marshes captured by ASAR on 02 Mar. 2007 at swath IS4, HH/VV polarizations. σ⁰VV is displayed in red and σ⁰HH in cyan; b) same image after applying the DTM-based filter; c) seed regions selected by the decision tree; d) classified pixels after the region growing stage.

Clustering in the feature space

After the region growing stage the large majority of the pixels are classified. However, some small clusters usually remain unclassified. This happens when no single seed pixel is selected by the decision tree within clusters detached from others of the same class. Since they are isolated, no region can reach them during the growing stage and they stay unclassified.

The remaining unclassified pixels, if compliant with constraints (1) and (2) below, are assigned to their closest Mahalanobis distance class in the $\sigma^0 HH$, $\sigma^0 VV$ space.

$$\min(Zc_j) < Zp < \max(Zc_j), \qquad c_j \in (C \cap S_p) \tag{1}$$

$$\text{Min } DMah(p,C) < 4, \tag{2}$$

Where: S_p is pixel p's sub-basin, *DMah(p,C)* is the Mahalanobis distance between pixel p and class C and Zp and Zc_j are respectively the elevations of pixels p and c_j.

Constraints (1) and (2) restrict the class assignment possibilities: pixels whose elevation is not within the elevation range of a given class are excluded from the possibility to belong to that class. On the other hand, virtually all minimum Mahalanobis distances in the region growing stage were observed to be lower than 4. Hence, any pixel whose closest distance to an existing class exceeded 4 was excluded from the clustering procedure, for being significantly different to any known class. This might happen for instance to pixels in the location of metallic fences or gauging stations solar panels.

9.5.4   FLOOD MAPPING

Once the image pixels are clustered and classified as explained above, flood mapping simply consists on reclassifying the different cover classes into flooded or emerged, as indicated in Table 9.2.

Table 9.2. Reclassification for flood mapping

Cover class	Flood map class
B1: Open water surface	Flooded
B2: Emerged bare soil	Emerged
H1: Flooded with no emerging helophytes	Flooded
H2: Flooded with emerging helophytes	Flooded
H3: Emerged helophytes	Emerged
A1: Flooded with no emerging almajar	Flooded
A2: Flooded with emerging almajar	Flooded
A3: Emerged almajar	Emerged

A few scattered pixels usually remain unclassified. A final refinement of the flood map is then performed as follows: unclassified pixels above the highest flooded pixel in the sub-basin and at least above one emerged pixel are classified as emerged. If they are below the lowest emerged pixel and at least below one flooded pixel, they are labeled as flooded.

9.6   Results and Discussion

Fig. 9.19 to Fig. 9.23 present examples of land cover and flood maps generated from ASAR scenes by means of the above presented methodology. Fig. 9.24 compares the flood map obtained from the image of 21 December 2006 with the ground truth data collected on the same day and reveals the good consistency between them. The flood mapping accuracy can also be assessed by comparison with the DTM contours at the water level recorded at the time of the ASAR acquisition. This is equivalent to assuming a horizontal water surface, which is a reasonable assumption in the vicinity of the gauging location, under low wind conditions and for low water velocities. Fig. 9.22 also reveals the good adjustment of the ASAR flood maps to the gauged water depth, though contours and mapped flood perimeters separate as they get away from the point of measure.

The overall accuracy of the flood mapping was assessed by comparing the classification results to the flood stage recorded at the sampling points on the image acquisition dates. Data from roughly 600 sampling points were available for the six ASAR scenes indicated in Chapter 5. This comparison yielded an overall accuracy of 92% when excluding areas C and D in Fig. 9.14. For regions C and D the accuracy went down to 73%. The inferior classification results in these regions were expected since no backscattering characterization of their cover types had been performed, and therefore no specific choice of seed regions could be designed. C and D covers usually appear darker than their assigned classes and, consequently, the presented methodology tends to overflood them.

A fair comparison among flood mapping accuracies per incidence angle is difficult, because target conditions such as soil moisture, flood stage or helophyte development changed between acquisitions and also different cover types were sampled on different dates. The assessment of the flood mapping accuracy was supplemented by using water surface elevation records simultaneous to the image acquisitions in the proximity of gauging stations. The flood perimeter was observed to be less precise at swaths IS6 and IS7 in

almajar areas. As noted in Chapter 7, at the large incidence angles of these swaths polarimetric signatures of flooded and emerged almajar get closer, and the use of the elevation information becomes critical to avoid confusion between both classes. This information is introduced in the selection of the classes' seed regions by constraining emerged almajar pixels to be higher than the flooded ones (9.15).

The accuracy of the cover types' classification is lower than for the flood maps. Some confusion has been observed for instance at steep incidence angles between flooded areas with scattered helophytes and wind-roughened open water areas. When selecting the classes' seeds, low σ^0 pixels are picked up by the decision tree to characterize the open water class. When the water surface is substantially roughened its backscattering increases, especially at VV polarization, and it can reach values close to those induced by the double bounce on vertically oriented sparse stems at swaths IS1, IS2 and IS3. The red area labeled as W in Fig. 9.17 is an example of an open water segment missclassified as flooded helophytes during the methodology stage of clustering in the feature space. Fig. 9.19a displays an IS2 image acquired on an unusually windy day. The brightest open water pixels in this area were selected as flooded helophytes seeds and gave rise to the corresponding class segments (red in Fig. 19b) during the region growing stage. Such misclassification could probably be addressed by adding a new cover category of "roughened open water". Nevertheless, the main goal of this study was to produce flood maps from the ASAR scenes. Since the above-mentioned confusion took place between two flooded classes, it did not affect the flood mapping accuracy and the roughened water surface class was obviated for simplicity. Additionally, the discrimination between roughened water and helophytes is expected straightforward by means of newer sensors with further polarimetric capabilities, such as Sentinel 1, in virtue of the different dominant backscattering mechanisms on both targets: surface and double bounce backscattering, for open water and vertical semi-flooded helophytes, respectively.
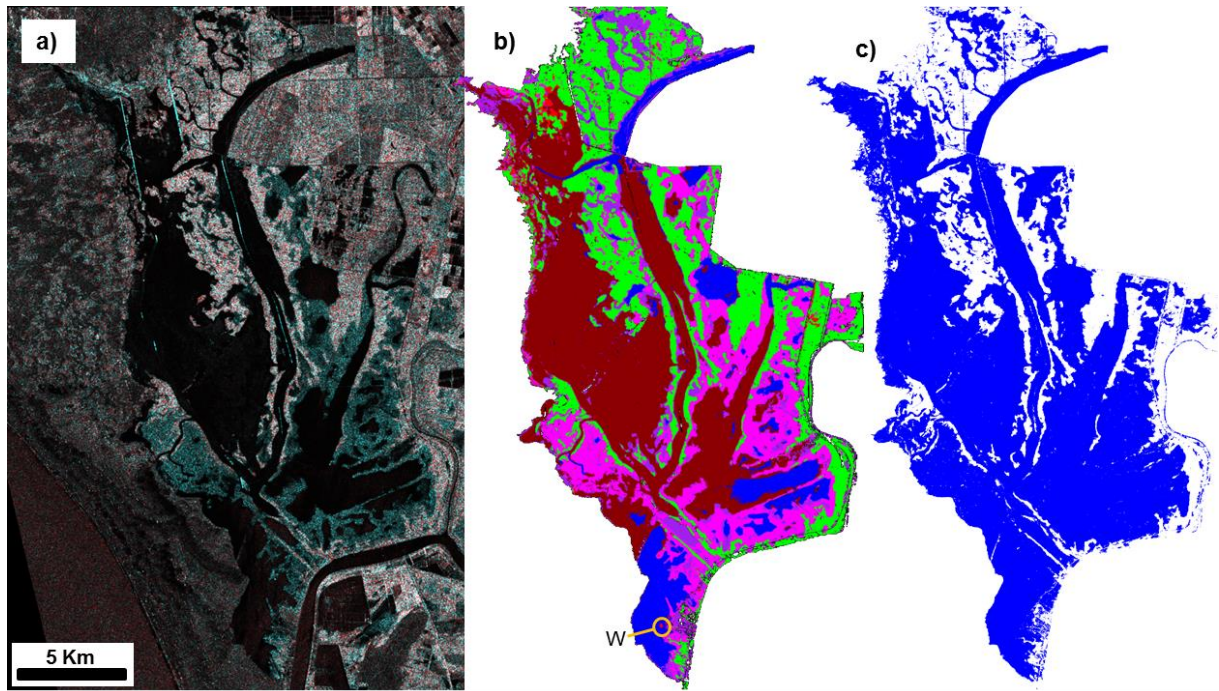
Fig. 9.19. Classification and flood mapping of Doñana ASAR image from 21 Dec. 2006, swath IS3: a) original ASAR image; b) classification of cover types; c) flood map.

Legend for Fig. 9.20 to Fig. 9.24

a)

Red: $\sigma^0 VV$
Green: $\sigma^0 HH$
Blue: $\sigma^0 HH$

b)

- ■ Open water on bare soil areas
- ■ Open water on helophyte areas
- ■ Emerged dry helophytes
- ■ Flooded green helophytes
- ■ Open water on almajar areas
- ■ Flooded almajar
- ■ Emerged almajar

c)

- ■ Flooded
- □ Emerged
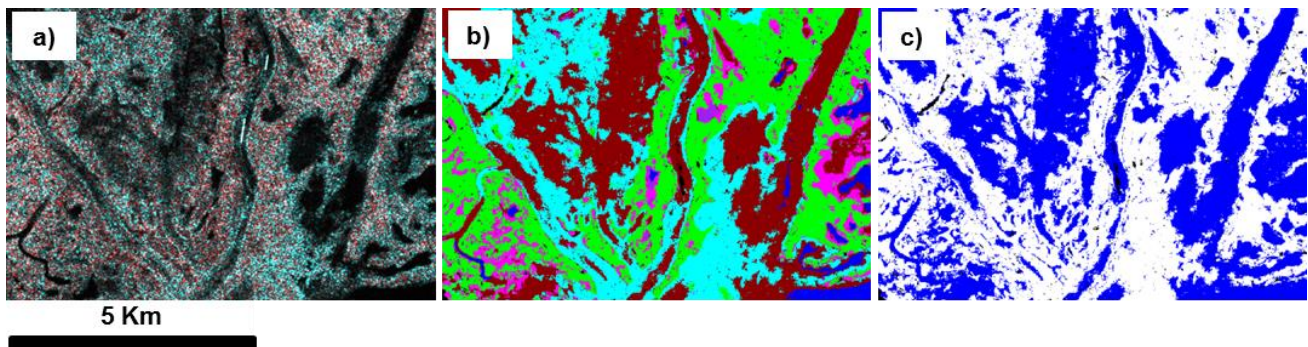
Fig. 9.20. Classification and flood mapping of Doñana ASAR image from 01 Nov. 2006, swath IS4:   a) original ASAR image; b) classification of cover types; c) flood map.
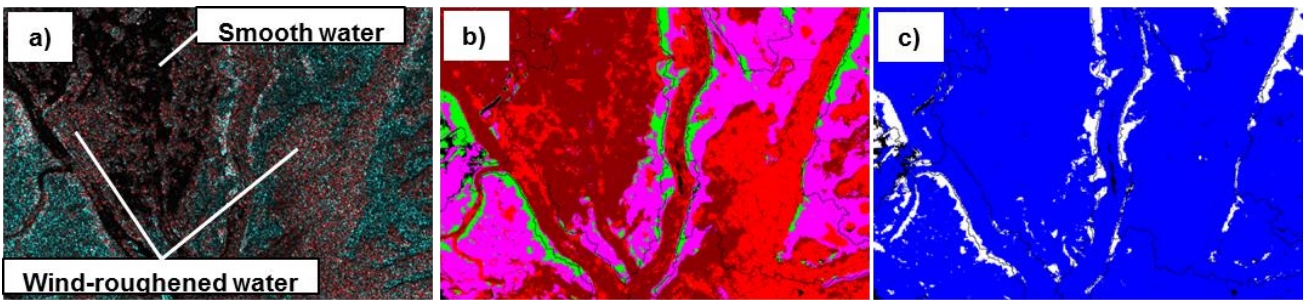
Fig. 9.21. Classification and flood mapping of Doñana ASAR image from 10 Feb. 2007, swath IS2: a) original ASAR image; b) classification of cover types; c) flood map.
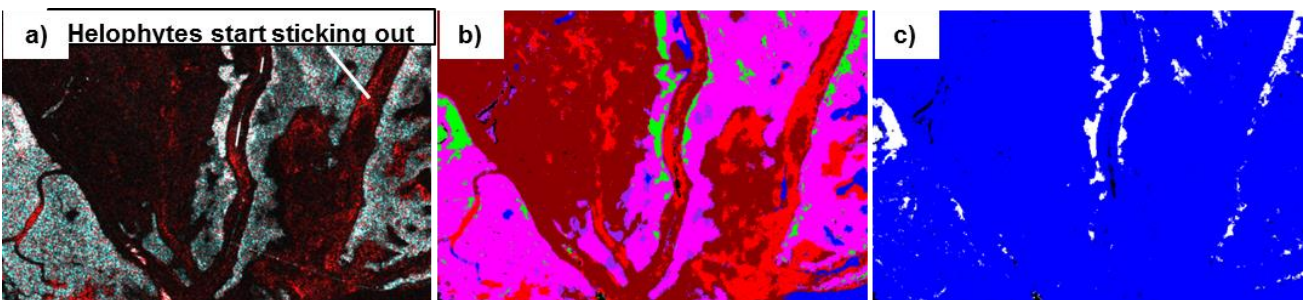
Fig. 9.22. Classification and flood mapping of Doñana ASAR image from 27 Feb. 2007, swath IS6: a) original ASAR image; b) classification of cover types; c) flood map.
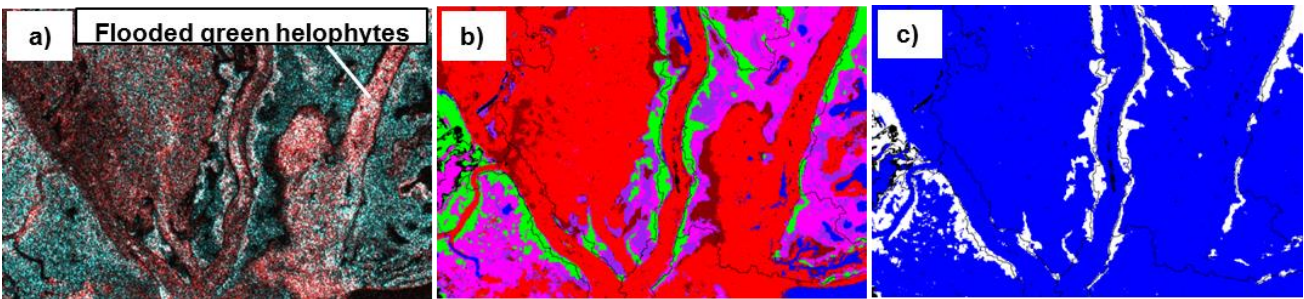
Fig. 9.23. Classification and flood mapping of Doñana ASAR image from 20 Mar. 2007, swath IS3: a) original ASAR image; b) classification of cover types; c) flood map.
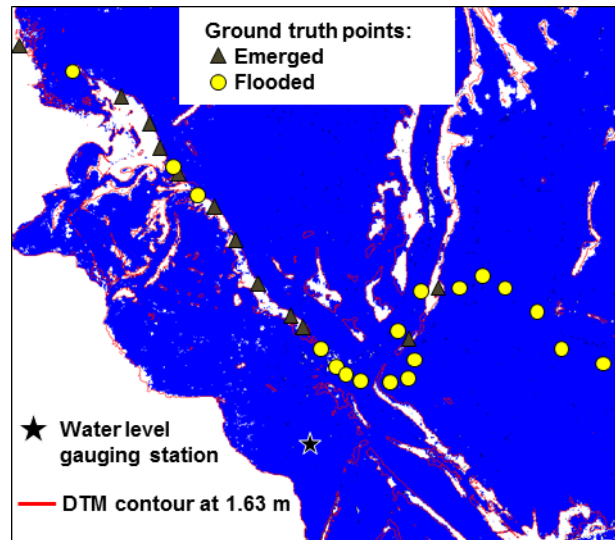
Fig. 9.24. Flood map of Doñana ASAR image from 21 Dec. 2006 (IS3), concurrent ground truth data and DTM contours at the water surface elevation gauged at the ASAR acquisition time.

A wide range of techniques was assayed during the completion of this work to accomplish the methodology clustering stage, such as the maximum likelihood, k-means, or hierarchical agglomerative algorithms (Jain and Dubes, 1988; Sneath and Sokal, 1973; King, 1967). At an initial stage of this research, backscattering coefficients characteristic of Doñana cover types had to be used together with standard classification methods to derive flood maps from the ASAR scenes. However, backscattering values often showed significant confusion among cover classes in the σ^0HH-σ^0VV space of single scenes. The vegetation cartography was then introduced in order to constrain the pixels' possible classes to those consistent with its vegetation type, and therefore prevent some misclassifications. Nevertheless, some errors were detected in the vegetation map during the ground truth campaigns. Additionally, the spatial distribution of plant communities undergoes subtle but detectable variations among years. Thus, by subordinating the pixels' possible classes to the vegetation map, the validity of the classification would depend on the correctness of the vegetation cartography and the detection of plant communities' spatial changes would be impeded.

On the other hand, Doñana backscattering signatures showed large temporal variations depending on the soil moisture content, helophyte height and density, wind and other environmental factors. The emerged almajar σ^0, for instance, was observed to increase 5 dB in HH and VV after a rainfall event. Consequently, the classification based on previously determined mean σ^0 values at a given time of the year, would be undermined by the inter-

annual variability in the amount and temporal distribution of the precipitation, if images of different hydrological years were to be classified.

Doñana covers σ^0 temporal variability brought up the need to select regions of interest for the different classes on each specific image to be classified. The vegetation maps were introduced into the analysis in order to assist the automated choice of the regions of interest on each image. The selection of the classes' representatives was restricted to their corresponding vegetation polygons, taken from the vegetation map, and also assisted by the DTM. Emerged almajar pixels, for example, need to be higher than the flooded ones. Within the set of pixels compliant with the vegetation and elevation constraints for a given class, only those clearly belonging to that class according to their backscattering coefficients are chosen as initial seeds. In other words, the initial seeds are located away from other classes' pixels in the σ^0VV-σ^0HH space. Continuing with the almajar example, pixels in low almajar areas according to the DTM and vegetation map, which exhibit low σ^0VV and much larger σ^0HH, correspond almost certainly to the flooded almajar class.

It is worth mentioning that the seed pixels do not necessarily capture the centroid and covariance of their corresponding classes. This is one of the reasons why the maximum likelihood algorithm was not an appropriate method to perform the subsequent classification, since it requires that the training set accurately describes the mean and covariance of the classes. Instead, the iterative region growing procedure described in Section Methodology was implemented. At each iteration only pixels adjacent to the seed regions were considered for classification. In this way, the spatial proximity to the classes' samples is considered in the classification. The Mahalanobis distance between surrounding pixels and classes is used to decide on the class membership. This distance accounts for the covariance between σ^0VV and σ^0HH, which is significant for all classes, and it is updated with the newly classified pixels at each iteration.

The use of the k-means algorithm, and hierarchical agglomerative algorithms such as the complete link, or average link were also considered for classifying the ASAR scenes in the σ^0HH-σ^0VV-Z feature space. For this purpose a distance involving backscattering coefficients and elevation measures had to be defined. Again, the Mahalanobis distance was applied. This distance makes use of the relative dispersion of the data, so it provides a proper tool to combine different magnitudes into the same measurement.

In the case of the k-means algorithm, while performed well on some images, it failed on others due to its sensitivity to extreme or spurious data. As pointed by Nagy 1968, the k-means algorithm is appropriate only on data sets having isotropic clusters. Additionally, clustering in the feature space misses the important information contained in the pixels spatial location, and some scattered missclassified pixels were output.

The use of hierarchical agglomerative algorithms using the Mahalanobis distance was also considered, but resulted computationally unfeasible.

As a final consideration, the flood maps produced in this work from the ASAR scenes showed excellent spatial consistency through watersheds. Inundation is mapped independently on each sub-basin by the algorithm and no constraint has been imposed to ensure such consistency. In the case that unconnected flooded regions were delineated, it was considered preferable that the user refines the choice of the seed pixels or revises the data for possible anomalies, instead of forcing the algorithm to output connected regions, which could result in data partitions through non-natural breaks.

9.7 Conclusions

It can be drawn from the analysis undertaken in this chapter that a flood mapping algorithm based exclusively on the $\sigma^0 HH$ and $\sigma^0 VV$ values of single ASAR acquisitions would lead to significant confusion among cover types at several hydrologic stages and incidence angles.

The combination of ASAR data with the vegetation cartography and the digital terrain model of the marshes enabled the discrimination of different cover types and the flood delineation from the ASAR images at the sensor's different incidence angles.

Clustering algorithms were developed for the automated generation of flood maps from the ASAR images, previously filtered by the DTM-guided methodology presented in Chapter 8. The clustering and classification algorithm operates on individual sub-basins, as the pixels elevation is more accurately related to cover classes within them. Vegetation and elevation maps plus knowledge of Doñana backscattering characteristics were initially used to select seed pixels with high confidence on their class membership. Selected seed

regions typically comprised more than 70% of the marshes pixels. This high percentage suggests that the characterization of the classes was fairly accurate and guarantees to a large extent a successful mapping. Next, a region growing algorithm extends the seed regions with new pixels based on their planimmetric adjacency and backscattering Mahalanobis distance to the seeds. The Mahalanobis distance accounts for the covariance between the ASAR channels, which is significant for all classes. During the seed regions growth, new pixels' possible classes are not constrained to their cover type according to the vegetation map, so the algorithm is able to capture changes in the vegetation spatial distribution.

Comparison of the resultant classification and concurrent ground truth yielded 92% of flood mapping accuracy over those marshes areas whose backscattering had been previously characterized.

The presented methodology does not require the user intervention for flood mapping in the filling up period. As a consequence of the interannual variability in the transition zones unflooding time, the selection of this class' seeds at the end of the hydrologic year requires approximate knowledge of the water level for at least one sub-basin. This information is likely to be available given, for example, the Park's rangers frequent trails. However, Fig. 7.9 and 7.13 show a drop in the helophytes backscattering coefficient between the flooded stage 4 and the emerged stage 5 at all incidence angles. The spatial observation of this drop, associated to an increase in the terrain elevation, can also indicate the flooded areas to an experienced user for the selection of the ROIs without the need for water level data. Furthermore, the availability of coherent HH and VV polarised data from Sentinel 1 in the near future is expected to facilitate such discrimination, in virtue of the increase in HH-VV phase difference of flooded helophytes versus the emerged ones.

9.8 References

Jain, A. K. & Dubes, R. C. (1988). *Algorithms for Clustering Data*, Prentice-Hall advanced reference series, Prentice-Hall, Inc., Upper Saddle River, NJ.

Jobs, S. (1995). The Wired Interview by Gary Wolf, Wired Digital, Inc. (http://www.wired.com/wired/archive/4.02/jobs_pr.html, last access: 11 Dec. 2013).

King, B. (1967). Step-wise clustering procedures, *J. Am. Stat. Assoc.,* 69, 86–101.

Mahalanobis, P. C. (1936). On the generalised distance in statistics. *Proceedings of the National Institute of Sciences of India*, 2, pp 49–55.

Martí-Cardona, B., López-Martínez, C., & Dolz-Ripollés, J. (2010). ASAR polarimetric, multi-incidence angle and multitemporal characterization of Doñana wetlands for flood extent monitoring. *Remote Sensing of Environment*, 114, 2802–2815.

Meyer, F. (1994). Topographic distance and watershed lines. *Signal Processing*, 38, 113-125.

Nagy, G. (1968). State of the art in pattern recognition. *Proc. IEEE*, 56, 836–862.

Ramos Fuertes, A., (2012). Hidrometeorología y Balance Térmico de la Marisma de Doñana, PhD dissertation, Universitat Politècnica de Catalunya, Barcelona, Spain.

Sneath, P. H. & Sokal, R. R. (1973). *Numerical Taxonomy*, Freeman, London, U.K.

Soille, P. (2003). *Morphological Image Analysis: Principles and Applications*. (2nd ed.). New York: Springer-Verlag.

Chapter 10:
ASAR Imagery for Understanding Doñana Marshes'Hydrodynamics and More

10.1 Introduction

The algorithms developed throughout this research focused on the 2006-2007 hydrologic year, for the reasons discussed in Chapter 5. Nevertheless, the Doñana ASAR images acquired during the completion of this study span from 2006 to 2010. The dates and sensor configuration details of these acquisitions are listed in Annex 3. In this chapter, hydrologic events and concurrent ASAR observations are selected from the entire image data base with the aim to gain understanding on the hydrodynamic processes taking place in the marshes and to obtain spatial data for modeling calibration purposes. Additionally, Chapter 10 identifies those hydrologic and biophysical parameters of Doñana marshes that the C-band SAR data are sensitive to, and therefore constitute a potential data source.

10.2 ASAR Imagery for Modelling the Wind Drag Action

The wind stress, as the vertical transfer of horizontal momentum between the atmosphere and the Earth surface, can be a major driving force for shallow water circulation and mixing (Ferrarin et al., 2009; Geyer, 1997; Magill and Kjerfve, 1989; Clarke and Brink, 1985). When the wind is sustained for sufficiently long periods, it produces a set-up of the water surface in the downwind direction. Various studies on shallow water bodies have documented the relationship between water level changes and local wind direction and intensity (Brownie et al., 2008; Pasternack and Hinnov, 2003; Clarke and Brink, 1985; Van

Dorn, 1953). Ramos Fuertes (2012) showed the water depth response to wind changes at different locations in the Doñana marshes. The wind drag effect was also observed during on-site work at the Ánsares pond on 23 December 2009. Some of the data acquired on that date are presented in Fig. 10.1 and explained as follows.

Fig. 10.1 shows the location of the ground truth sample points and the water depth measured at some of them. The blue arrows in Fig. 10.2 depict the wind velocity and direction registered at the Vetalengua gauging station during the on-site work. The red arrow was computed as the average vector of the wind records for the period encompassing approximately 1 h before the first and last sample acquisition, in attempt to approximate a mean wind action responsible for the observed water surface set-up. A similar averaging was successfully related to wind-induced water surface tilting and upwellings in inland waters by Martí-Cardona et al. (2008).

If the Ánsares water surface is being tilted by the wind, this surface should approximate a plane with its maximum slope in the wind direction. Fig. 10.3 depicts a terrain elevation vertical section of the Ánsares pond following approximately the pond's longitudinal axis, indicated by the blue line in Fig. 10.1. The water surface absolute level at the sampling points, obtained as the addition of the water depth plus the terrain elevation, is represented on the same figure. Their position in the x-axis is determined by the projection of the ground truth points' location on the Ánsares longitudinal axes, orthogonally to the averaged wind direction, since this orthogonal should approximate a horizontal line on the water surface plane.

Fig. 10.3 reveals the water surface tilting in the Ánsares pond at the time of the ground truth campaign. A linear interpolation of these points yields an estimate of the surface slope in the direction of the Ánsares longitudinal axis of roughly 0.11‰. The same interpolation in the average wind direction yields a maximum slope of 0.13‰, which is consistent with the values reported in the literature on wind-drag action (Wu, 1975; Hidy and Plate, 1966; Plate and Goodwin, 1965), strongly suggesting the wind stress as the cause of the observed water surface set-up.

The ground truth data presented above was not acquired with the objective to observe the wind drag effect. The author happened to find evidence of such phenomenon when walking along Ánsares, and especially when reaching the scale N26 at the pond's eastern end. The water surface slope estimation by the 4 points linear interpolation does not aim to be an accurate surface slope estimation, but just to give physical, direct evidence of the wind drag phenomenon. Rigorous observations of the wind drag action for hydrodynamic modeling calibration and validation were obtained from ASAR images, as discussed in the following sections.
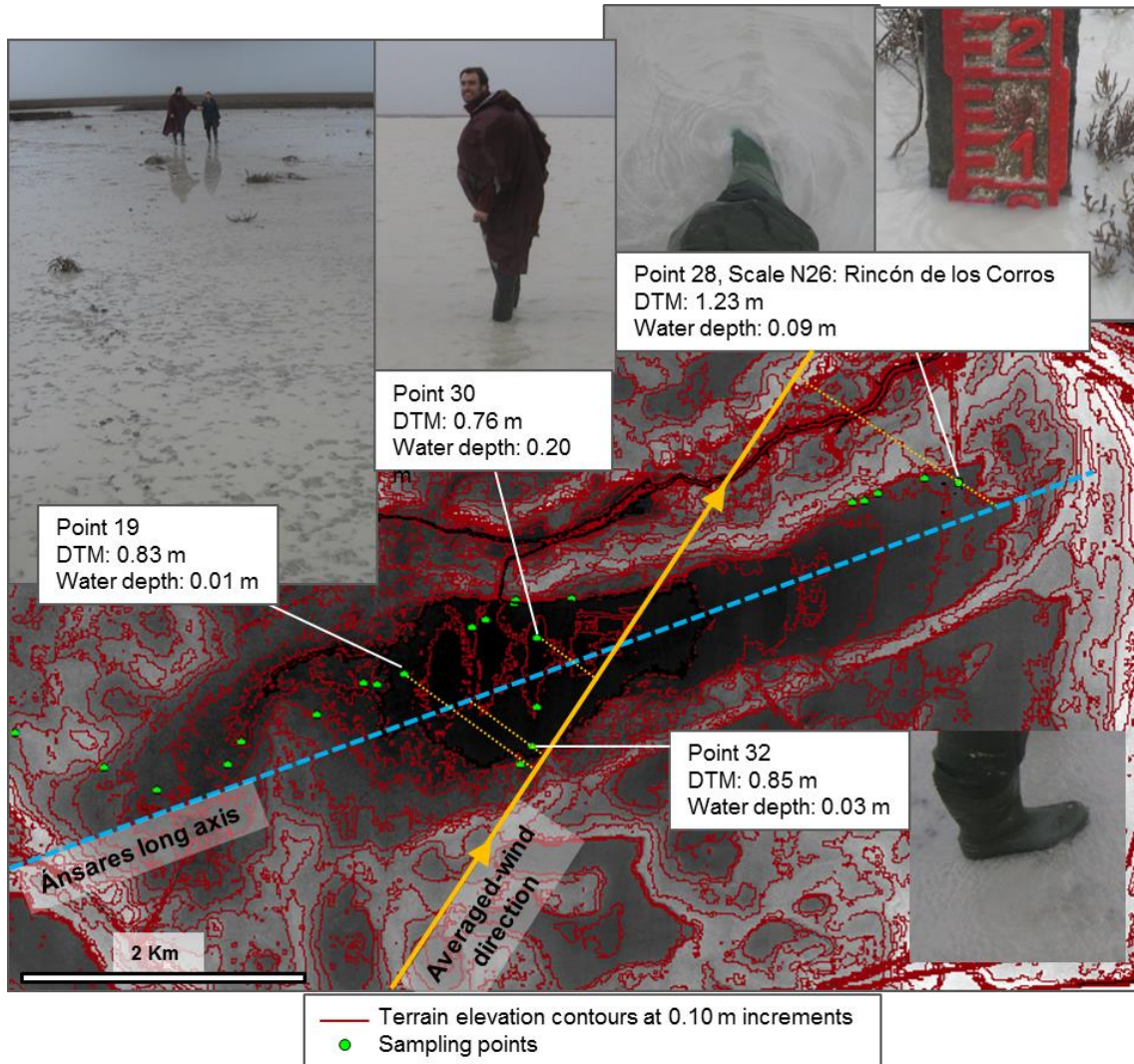
Fig. 10.1. On-site data acquired at the Ánsares pond on 23 December 2009.
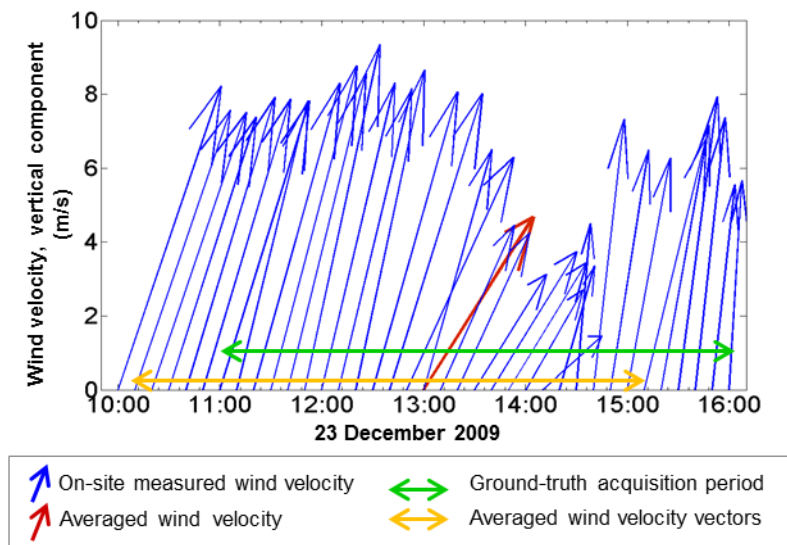
Fig. 10.2. Wind velocity gauged in the Doñana marshes during on-site work.
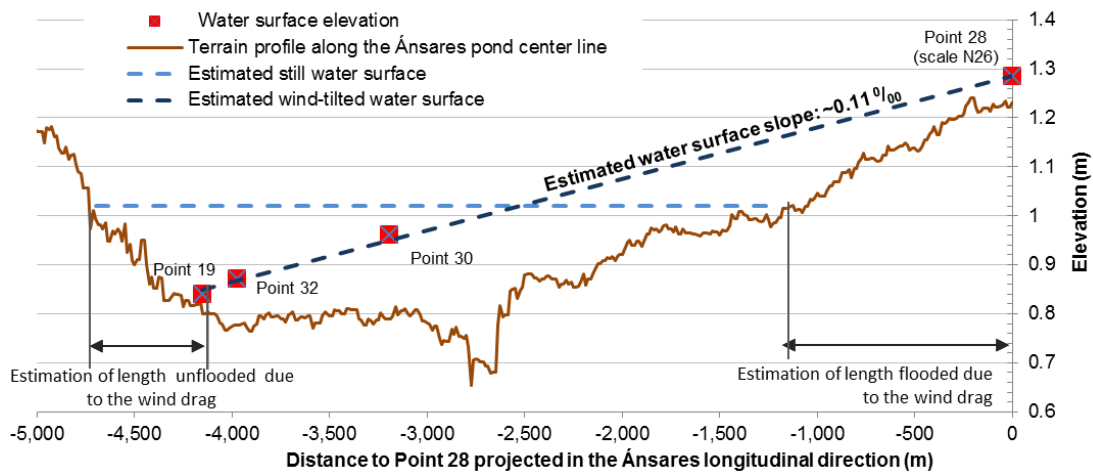
Fig. 10.3. Estimation of the water surface slope in the Ánsares long axes direction based on the on-site water depth measurements acquired on 23 December 2009 and assuming the maximum water surface slope in the average wind direction.

Given the flatness of Doñana's topography the wind-induced water surface tilting can cause the flooding or emergence of extensive areas, detectable in remote sensing images. Several Envisat/ASAR scenes were acquired during strong and persistent wind episodes. These scenes captured the wind-induced water displacement and corroborated the relevance of this action on the marshes hydrodynamics. The water displacement was especially notable in the marshes flattest areas which correspond to the Ánsares and the Membrillo ponds. The flood maps obtained from the ASAR images on these sites, together with concurrent records of wind speed and direction registered at the hydrometeorological gauging stations, enabled the calibration of the drag action exerted by the wind in the hydrodynamic model of Doñana marshes (Martí-Cardona et al., 2012; Ramos-Fuertes et al., 2013).

Table 10.1 lists several ASAR acquisitions which substantiate the hydrodynamic action exerted by the wind on Doñana water bodies. It also includes other wind-related phenomena observable on the scenes. Some of these ASAR images are included and commented in the following sub-sections. Details on the use of the ASAR-derived flood maps for the calibration of the wind action in the marshes hydrodynamic model can be found in Ramos Fuertes et al. (2013), included in Annex 6 to this document.

Table 10.1. List of Envisat/ASAR scenes showing wind related phenomena on Doñana's water bodies.

Wind and hydraulics related phenomena	ASAR acquisition			Observables
	Date	Incidence angle	Polarization configuration	
Wind drag action	4-Mar-2006	IS2	HH	Water mass displacement observable at the Membrillo pond. This observation was used for the marshes hydraulic model calibration/validation (Ramos Fuertes et al., 2013).
Wind drag action	23-Mar-2006	IS1	HH/HV	Water mass displacement observable at the Membrillo pond.
Wind drag action	19-Oct-06	IS1	HH/HV	Water mass displacement observable at the Ánsares pond. This observation was used for the marshes hydraulic model calibration/validation (Ramos Fuertes et al., 2013).
Wind drag action	02-Dec-06	IS2	HH	Water mass displacement observable at the Membrillo pond.
Wind drag action and uneven water surface roughness	10-Feb-07	IS2	HH/VV	Water mass displacement observable at the Membrillo pond. Strong differences in the backscattering from the open water in the Hinojos area.
Wind drag action	01-Mar-07	IS3	HH/VV	Water mass displacement observable at the Membrillo pond.
Wind drag action	26-May-07	IS2	HH/VV	Water mass displacement observable at the Membrillo pond.
Wind drag action	20-Jun-07	IS6	HH/VV	Two ASAR scenes acquired with a time interval of 12 hours show clear differences in the Membrillo pond flooded area. No precipitation was registered during that time and the observed water displacement is consistent with the wind direction.
	21-Jun-07	IS1	HH/VV	
Wind drag action	19-Jul-07	IS3	HH/VV	Great displacement of the Ánsares water mass in the wind direction.
	Landsat 5 TM: 24-07-2007			
Wind drag action	04-Oct-07	IS1	HH/VV	Water mass displacement observable at the Ánsares pond.

Table 10.1cont. List of Envisat/ASAR scenes showing wind related phenomena on Doñana's water bodies.

Wind and hydraulics related phenomena	ASAR acquisition			Observables
	Date	**Incidence angle**	**Polarization configuration**	
Wind drag action	16-Jan-08	IS6	HH/VV	Water mass displacement observable at the Ánsares pond.
Wind drag action	20-Mar_08	IS3	HH/VV	Great displacement of the Ánsares water mass in the wind direction.
Wind drag action	27-Mar-08	IS1	HH/VV	Water mass displacement observable at the Lobo and Mari López ponds. Modeled event.
Wind drag action	30-Apr-08	IS6	HH/VV	Water mass displacement observable at the Membrillo and Ánsares ponds.
Wind drag action	02-Jan-10	IS2	VV	Water surface tilting observable to the South of the Mari López and Ánsares ponds.
Wind drag action	24-Jul-10	IS2	HH/VV	Water mass displacement observable at the Membrillo pond.
Wind drag action	31-Jul-10	IS2	HH/VV	Water mass displacement observable at the Membrillo pond.
Wind drag action	30-Jun-07	IS2	HH/VV	The flood perimeters at the Membrillo pond extracted from these scenes clearly intersect.
	20-Oct-07	IS2	HH	
	31-Jul-10	IS2	HH/VV	
Uneven wind spatial distribution	01-Apr-10	IS1	HH/VV	Accused spatial differences in the wind-induced water surface roughness. The Lobo, Mari López and Ánsares ponds present smooth open water surfaces, while the Membrillo and North Hinojos appear notably wind-roughened.
Uneven wind spatial distribution	22-May-10	IS2	HH/VV	The flooded area at the Ánsares and Membrillo ponds appears notably wind-roughened while the open water surface in the nothern ponds seem to be smooth.

10.2.1   WIND-INDUCED WATER MOTION IN THE ÁNSARES POND: THE 19 OCTOBER 2006 CASE STUDY

Fig. 10.4a shows the Ánsares pond on the Envisat/ASAR image acquired on 19 October 2006 at swath IS1 and HH/HV polarization configuration. The HV backscattering coefficient is displayed in red and the HH in cyan. The perimeter of the flooded area in this pond was determined from the ASAR image following the filtering and classification procedures presented in Chapters 8 and 9, and is indicated by a red line on Fig. 10.4a and Fig. 10.4b.

The 19 October ASAR scene was acquired after an episode of relatively strong winds, as shown by the local wind records in Fig. 10.5. The wind-roughened open water surface in Doñana ponds induces little depolarization of the radar signal. As a consequence, the Ánsares flooded area presents low HV backscattering and is displayed at low red brightness values in Fig. 10.4a. Only the west end of the pond exhibits noticeable HV returns, due to the presence of helophyte stems sticking out of the water. In contrast, the water surface roughness does cause significant backscattering in like-polar channels. Consequently, the Ánsares open water area appears in bright cyan in Fig. 10.4a. The only exception are the dark elongated features on the east end of the pond. These dark features could be explained by the presence of very shallow water, whose surface ripples are too small to backscatter the C-band signal. The dark features could also correspond to recently unflooded flat areas, where a puzzle of very shallow puddles is usually retained on the soil after the waters retreat. Fig. 10.6 illustrates this type of surface, which is somehow on the border between flooded and emerged land. A more detailed interpretation of this and other ASAR images featuring the wind-drag effect on the Doñana's ponds can be found in Annex 6.

Fig. 10.4b depicts three DTM elevation contours together with the flood perimeter from Fig. 10.4a. It can be seen that the flood boundary approximately follows the 1.25 m contour line on the east end of the Ánsares pond but it is much closer to the 1.00 m one on the opposite side, thus revealing an elevation difference of 0.25 m between the water body's east and west ends. The local meteorological records show that the wind blew from the southwest and west for 31 hours before the ASAR acquisition (Fig. 10.5), suggesting that the wind action was the cause of the water surface tilting. No precipitation was registered in the previous days.
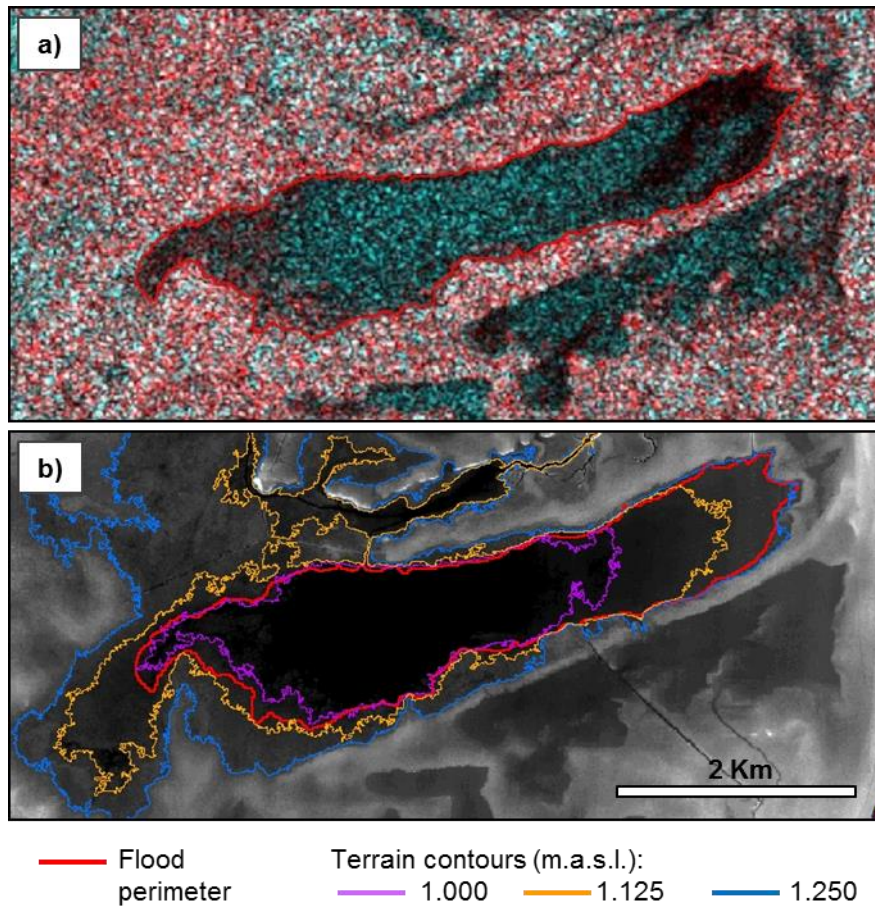
Fig. 10.4. Water surface tilting at the Ánsares pond: a) the Ánsares pond on the ASAR image from 19 October 2006 and flood perimeter. The HH backscattering is displayed in cyan and the HV in red; b) digital terrain model of the Ánsares pond on the background, elevation contours and flood perimeter from a).

This wind episode was simulated with the marshes hydrodynamic model. The flood map derived from the ASAR scene together with the pond's DTM enabled the estimation of the water volume comprised between the terrain and the flood patch, assuming the latter to be approximately a plane. This water volume was introduced at initial still condition into the hydrodynamic model. Then, the water motion was simulated using the on-site wind records for the 35 h prior to the ASAR acquisition.

Fig. 10.7 summarizes the simulation results. Fig. 10.7b reveals that the maximum displacement of the water mass towards the east coincides with the eastern flood perimeter determined from the ASAR image, but takes place 19 h before the satellite observation. The simulated inundation at the time of the ASAR acquisition is shown in Fig. 10.7c, and is remarkably coincident with the ASAR derived flood map, if the above mentioned dark eastern patches in the image are considered as recently unflooded land.

This and other wind-drag observed and simulated events are presented and discussed in Ramos Fuertes et al. (2013), in Annex 6 of this document.
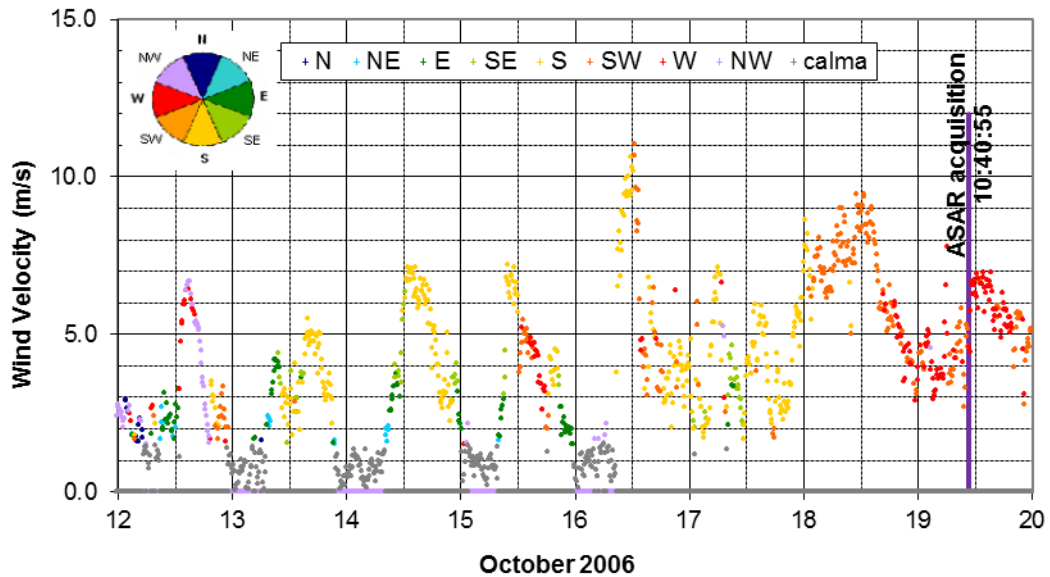
Fig. 10.5. Wind speed and direction recorded at the Vetalengua gauging station in October 2006, and acquisition time of the ASAR scene in Fig. 10.3.

Fig. 10.6. View of a bare soil area recently emerged due to the wind-induced water displacement.
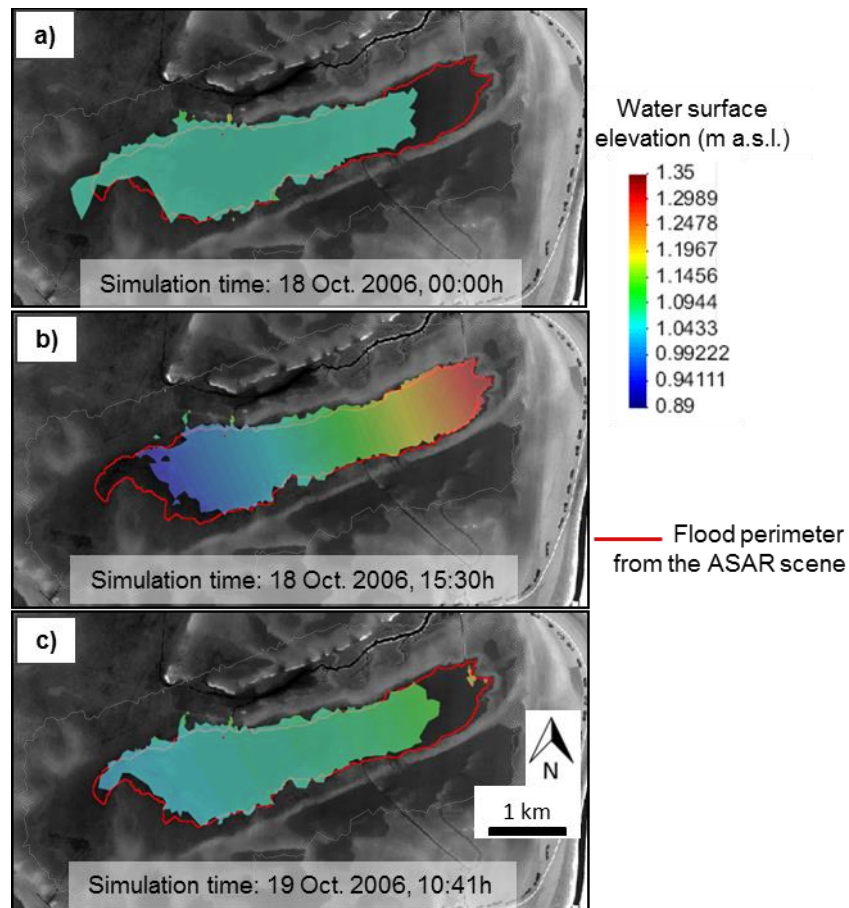
Fig. 10.7. Comparison between hydrodynamic modeling results and the ASAR derived flood perimeter: a) water surface elevation in Ánsares at the initial simulation time; b) maximum water displacement towards the East; c) water elevation at the ASAR acquisition time.

10.2.2 WIND-INDUCED WATER MOTION IN THE ÁNSARES POND: THE JULY 2007 CASE STUDY

Fig. 10.8a shows the Ánsares pond as captured by the ASAR image from 19 July 2007 at swath IS3 and HH/VV polarization configuration. The flooded area determined from the ASAR scene is depicted in Fig. 10.8b, together with the pond's terrain elevation contours. Doñana marshes were imaged again on 24 July 2007 by Landsat 5 Thematic Mapper (TM). Fig. 10.9a diplays the Ánsares pond in the Landsat 5 TM's bands 5 and 7. The flooded area was mapped from this scene by the Laboratorio de Sistemas de Información Geográfica y Teledetección de la Estación Biológica de Doñana (LAST-EBD) following the procedure presented in Aragonés et al. (2005). Fig. 10.9b shows the Ánsares flood map on 24 July 2007 together with the pond's terrain contours. The large decrease of the inundated area between 19 and 24 of July can be explained by the shallow water depths and the

evaporation losses, which approximate 60 mm a day at this time of the year (Ramos Fuertes, 2012).
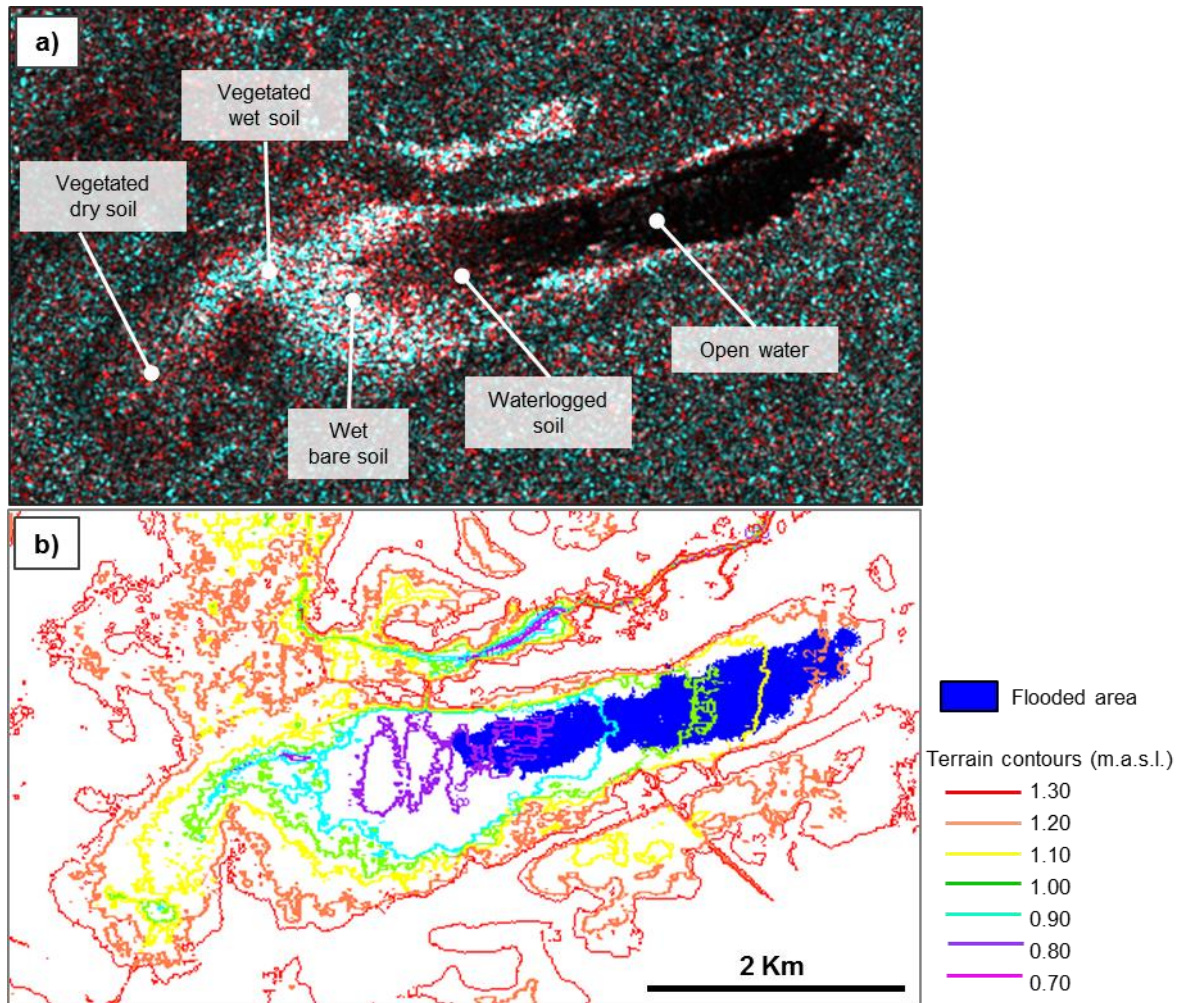
Fig. 10.8. The Ánsares pond on 19 July 2007: a) ASAR scene from 19 July 2007, at swath IS3 and HH/VV polarization configuration. VV displayed in red and HH in cyan; b) DTM contours and flooded area determined from de ASAR scene.

Fig. 10.8 and Fig. 10.9 reveal a large displacement of the flooded area in the Ánsares pond from what would be a horizontal surface. Wind records from the days prior to the image acquisitions are depicted in Fig. 10.10. These records show that the wind blew persistently from the West, which is consistent with the water mass displacement direction. The Ánsares images discussed in this section evidence one of the largest wind-induced water conveyance events observed by the hydrodynamic specialists in the Institut Flumen. However, the simulation of this wind-drag motion with the marshes hydrodynamic model has not been attempted at the time of this document writing. A comparable water displacement was observed at the Membrillo pond on the ASAR image from 4 March 2006. This event and the corresponding hydrodynamic simulation are addressed in Annex 6.
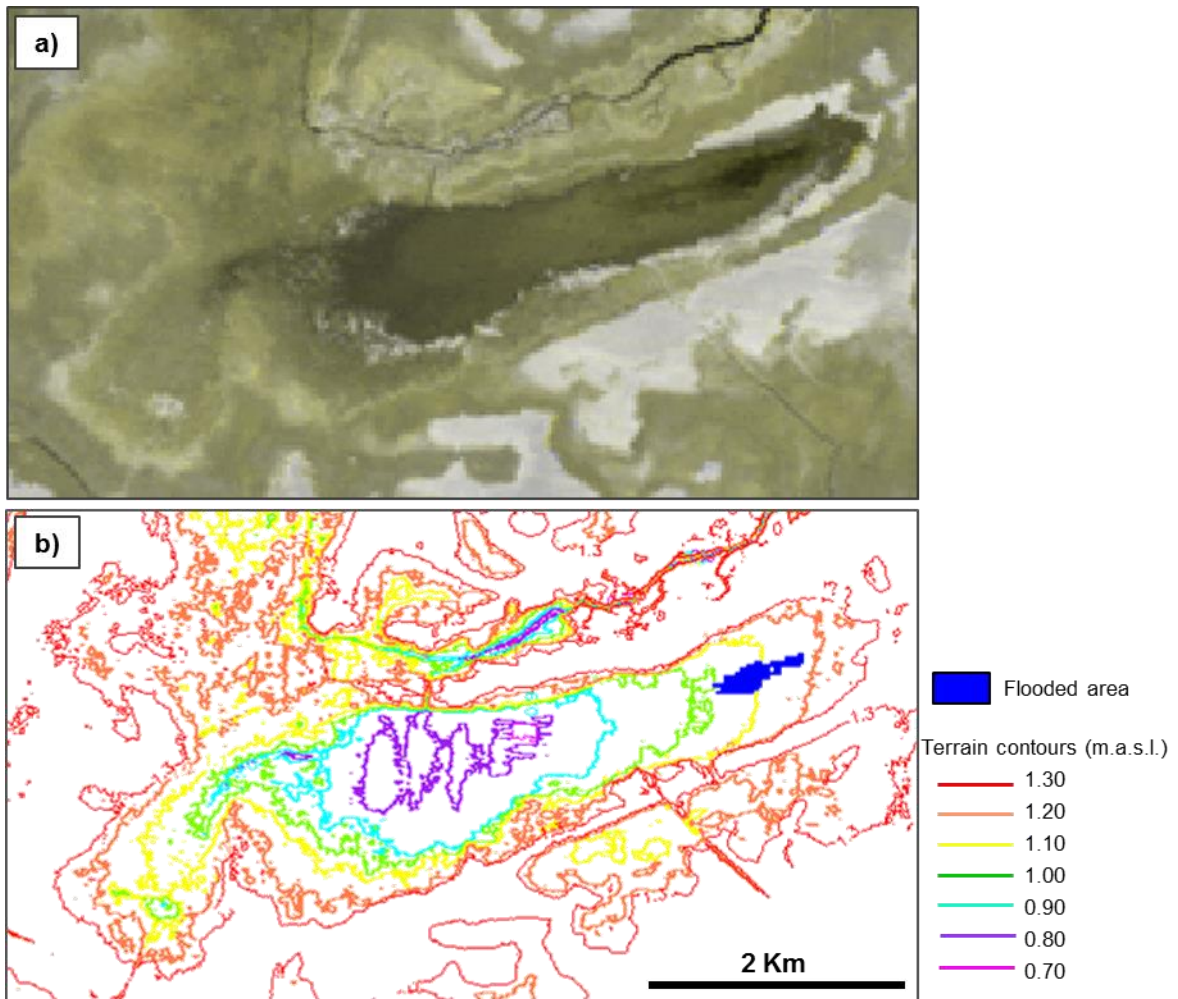
Fig. 10.9. The Ánsares pond on 24 July 2007: a) Landsat 5 TM's band 5 and band 7 from 24 July 2007. Band 5 is displayed in red and green, and band 7 in blue; b) DTM contours and flooded area determined from de Landsat 5 TM scene. Source of the flood map: LAST-EBD.
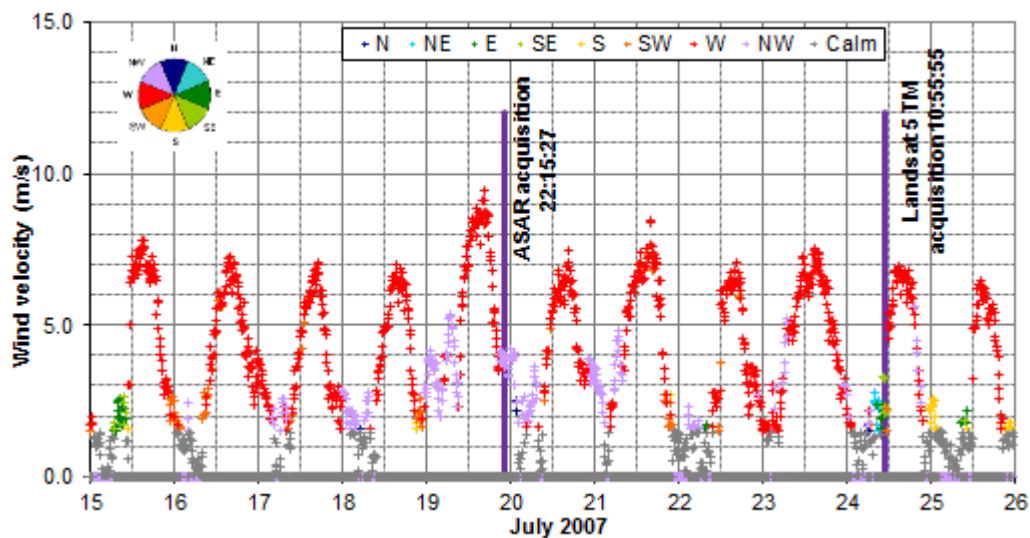
Fig. 10.10. Wind speed and direction recorded at the Vetalengua gauging station in July 2007. The Envisat/ASAR and Landsat 5 TM acquisition dates are also indicated.

10.2.3   THE ÁNSARES POND MORPHOLOGY: SHAPED BY THE WIND?

In addition to the wind drag events discussed above, further ASAR observation opportunities and water depth records have shown displacements of the water body at the Ánsares pond consistent with the wind direction.   In the author's opinion, the morphology of the Ánsares pond is likely to be the result of the wind-induced water motion. Fig. 10.11 depicts the wind direction and velocity frequency between 2007 and 2009, as recorded at the meteorological gauging station closest to Ánsares, and reveals the clear dominance of the Southwestern winds. As if it was a giant weathercock, the elongated shape of this pond is oriented in the clearly dominant Southwest-Northeast wind direction. Fig. 10.12 represents the Ánsares topography. The pond's maximum bottom gradients, though extremely subtle, follow the dominant wind orientation. In the orthogonal direction, the Ánsares bottom is approximately flat, with steep edges where the bare soil turns into a vegetated surface. This bottom and edge morphology suggests a frequent forth and back movement of the water mass in the pond's longitudinal dimension (the dominant wind direction), with the shear friction sharpening the lateral edges.
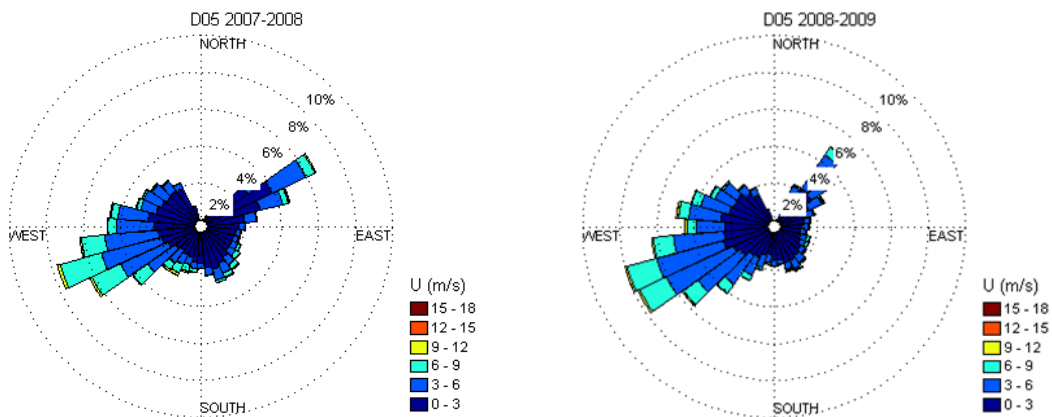
Fig. 10.11. Annual wind roses in Doñana marshes. Source: Ramos Fuertes, 2012.
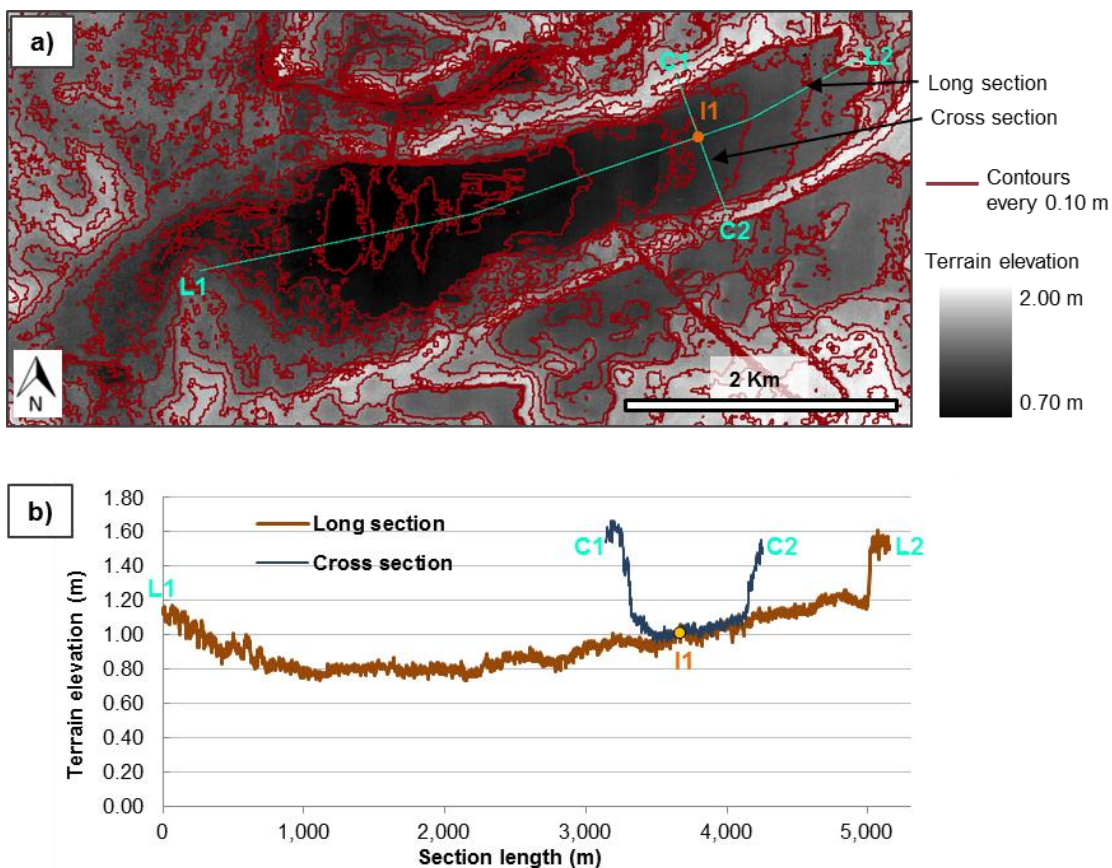
Fig. 10.12. Terrain morphology at the Ánsares pond: a) DTM, contours and location of the long and cross sections; b) Terrain elevation long and cross sections.

10.3 ASAR Imagery for Modelling Rainfall Events

ASAR images acquired shortly before and after rainfall events show the result of the precipitation on Doñana's inundation extent. The rainfall intensity was permanently recorded at the marshes gauging stations during the completion of this research (Ramos Fuertes, 2012). Both data sources, rainfall hyetographs and flood extent observations, contribute precious calibration and validation information for the hydrodynamic model of the marshes.

Fig. 10.13 presents an example of this calibration data. The ASAR image from 07 November 2007, in Fig. 10.13b, reveals relatively small flooded areas at the deepest troughs in Doñana. These areas flooded following the initial rainfall events in September and October 2007, which saturated the marshes soil. A rainfall event of 80 mm cumulated precipitation took place on November 20th. The corresponding hyetograph, registered at the marshes, is depicted in Fig. 10.13a. The spatial effect of this rainfall can be assessed in detailed on the ASAR image from 26 November (Fig. 10.13c): the deep bare soil areas in the Membrillo, Ánsares and Mari López ponds, as well as in the Caño Travieso, were completely inundated by this event. The water volume increase in the ponds can be estimated from the flood perimeter obtained from the satellite image and the DTM. The comparison of the water volume increment with the precipitation registered over the ponds' sub-basins provides a synoptic, integrating estimate of the precipitation transformed into flooding, and hence, of the rainfall losses.

Of special interest for the hydrodynamic modeling is the flood progression in the Madre de las Marismas watercourse, at the wetland Northwest end. Surface water inflows into the marshes come primarily from this region, through the watercourses of La Rocina, El Partido, Cañada Mayor, Soto Grande y Soto Chico, as explained in Chapter 4. It is close downstream those confluences, in La Madre de las Marismas watercourse, where the highest water velocities occur and the main erosive and sedimentation processes have been documented (Robredo et al., 2010; Robredo et al., 2007).

Unfortunately, the marshes tributaries' inflow hydrographs were not registered during the completion of this research. These data absence hinders the use of the ASAR derived flood maps for hydrodynamic calibration purposes at present. However, it is expected to estimate those input hydrographs in the near future by using historical precipitation records and a new distributed hydrologic model of the tributary basins, currently under

development (Caro and Bladé, 2012). Knowledge of the inflows discharged into the marshes would enable the numerical simulation of several flood events monitored with satellite imagery, and the comparison between the observed and simulated flooded areas for calibration and validation purposes.
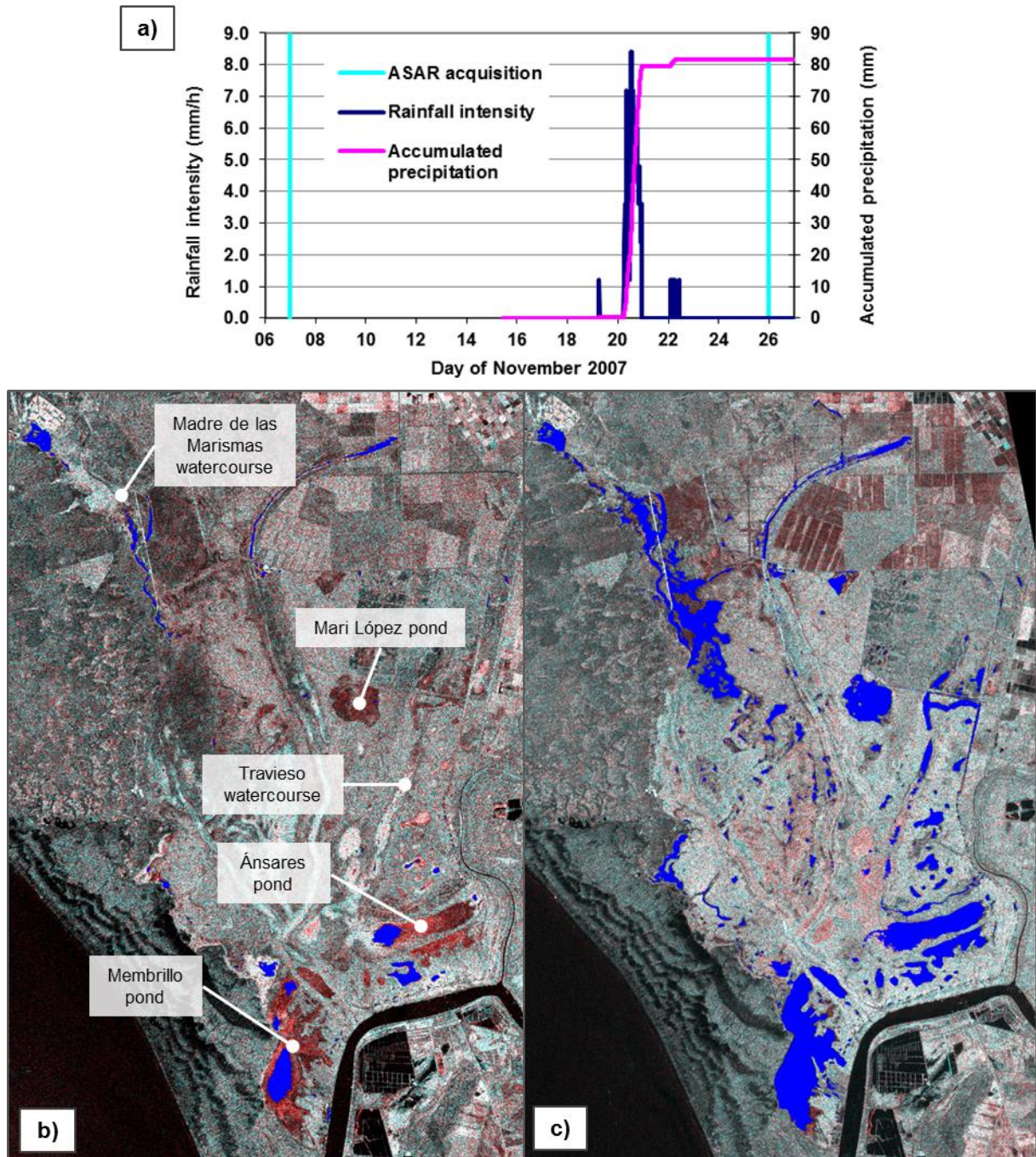
Fig. 10.13. Effect of the November 20th 2007 rainfall event on Doñana marshes's flood extent: a) rainfall intensity and accumulated precipitation registered at the marshes in November 2007; b) ASAR scene acquired on 7 Nov. 2007 at swath IS6 and HH/VV polarizations; c) ASAR scene acquired on 26 Nov. 2007 at swath IS7 and HH/VV polarizations. VV backscattering is displayed in red and HH in cyan for both scenes. The flooded area determined from each ASAR image is shown in blue.

10.4 ASAR Imagery to Determine the Tidal Influence

As pointed in Chapter 4, several culverts cross the levee detaching the Doñana marshes from the Guadalquivir River, known as Montaña del Río. These culverts are equipped with sluices, which allow a limited water exchange between the marshes and the river. One of these sluices is depicted in Fig. 10.14. For a given sluice gate opening, the direction of the water exchange is basically driven by the relative marshes and river water levels, the latter being mostly dependent on the ocean tides. Nevertheless, several ASAR scenes also revealed an important influence of the wind on the flow direction.

The spatial reach of the Guadalquivir river inflows into Doñana is clearly observable on ASAR and Landsat scenes when the marshes are dry. The water volume exchange between the marshes and the river during the study period was negligible in terms of the wetland water balance, but the observation of this phenomenon was used to test the hydraulic simulation model: Fig. 10.15 shows the location of the Figuerola and Nuevas watercourses and their culverts through the Montaña del Río on the marshes DTM. Two flooded patches can be seen at the upstream end of the Figuerola and Nuevas watercourses on the ASAR image from 10 October 2006 (Fig. 10.16). This flooding is the result of the Guadalquivir water flowing through the Figuerola and Nuevas streams when the river level is high enough.

The tidal inflow was simulated with the marshes hydrodynamic model, using the actual sluice gate height and the Guadalquivir water levels at the Figuerola and Nuevas downstream end as boundary conditions. The river levels were estimated based on the data from the Bonanza tide gauge, at the Guadalquivir river mouth. The tidal flow simulations were undertaken within the framework of the project *Estudio de la limnología de las Marismas del Parque Nacional de Doñana: balance térmico y transporte de masa..* Fig. 10.17 captures the simulation time of maximum river inflow penetration into the marshes, showing a close correspondence with the water extent observed on the satellite image.

Fig. 10.14. Culvert sluice on the river side of the Montaña del Río.
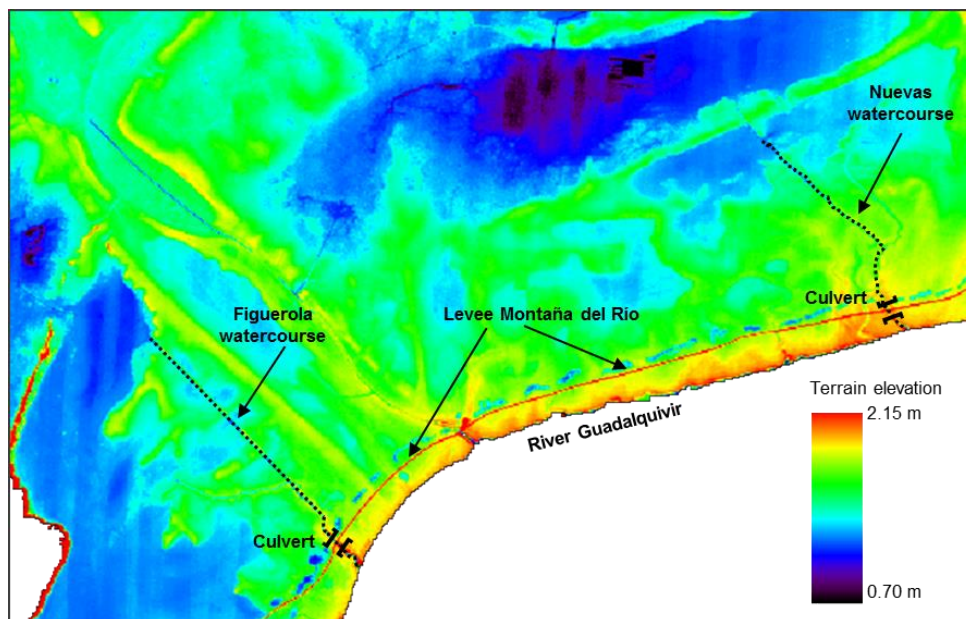
Fig. 10.15. Location of the Figuerola and Nuevas watercourses and their corresponding culverts trough the Montaña del Río levee.

Fig. 10.16. Flooded areas at the Figuerola and Nuevas upstream ends captured by ASAR on 10 Oct. 2006, at swath IS6 and HH/VV polarizations. VV backscattering is displayed in red and HH in cyan. Flooded areas are indicated in blue.
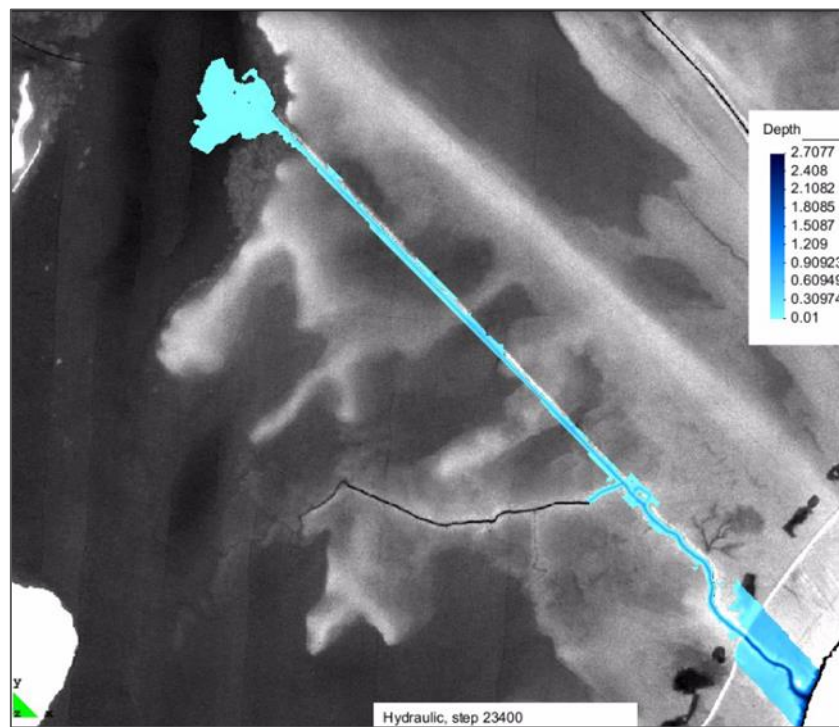
Fig. 10.17. Simulated maximum tidal inflow penetration through the Figuerola watercourse. Source: Bladé and Dolz (2011).

10.5 ASAR Flood Maps to Assist Water Losses Quantification

As discussed in Chapter 4, in periods of rain absence the water surface decrease in isolated ponds can be attributed almost entirely to evapotranspiration losses. Ten-minute water level records were registered at five different locations in the Doñana marshes during the study period (Ramos Fuertes, 2012; Fig. 4.2). This dataset provides detailed information on the total water loss temporal evolution in the gauged sub-basins. However, the losses derived from the water depth decrease are the combined result of two basic mechanisms of water transfer to the atmosphere: the evaporation from open water areas and the evapotranspiration from the flooded vegetation canopy. The quantification of these mechanisms and their relationship to the type and amount of vegetation are still under investigation. In this regard, the remote sensing observations enable the spatial delineation of open water and vegetated flooded areas. They can also provide estimates of the above-water vegetation biomass. Additionally, new radar systems with fully polarimetric capabilities and higher spatial resolution are expected to allow the discrimination among plant species of different structural characteristics. Hence, SAR imagery can provide quantitative spatial information essential to relate the water level losses to the different water transfer mechanisms.

Furthermore, the ASAR images provide timely discrete water volume estimates for those sub-basins with no gauging stations. The volume under a mapped flooded area can be estimated by means of the terrain elevation model, by assuming that the flood patch approximates a plane: the flood perimeter extracted from the satellite image is converted into a three-dimensional line by assigning to it the corresponding terrain elevations from the DTM. A surface is then interpolated within the three dimensional flood perimeter by means of a triangulated irregular network (TIN). The water volume can then be estimated by subtracting the DTM from the TIN. The volume decrease between consecutive images yields an estimate of the total water loss between acquisition dates.

Table 10.2 lists several ASAR image sets showing a progressive decrease in the flooded area at different isolated ponds in periods of rain absence. Needless to say, this image time series could be further enriched with optical observations, whose availability increases during the drying period.

Fig. 10.18 and Fig. 10.19 show two examples of the ASAR image series. Some of these sets were used to estimate water losses in ungauged sub-basins. The water volume decrease

between image dates was computed for those periods of rain absence and yielded average losses rates consistent with those computed from the continuous depth measurement at the gauging stations.

Table 10.2. ASAR image series showing the flooded area decrease in isolated ponds

Pond name	ASAR acquisition date						
Membrillo	5-Apr-06	10-May-06					
	21-Jun-07	30-Jun-07	19-Jul-07				
Mª López	12-May-06	15-May-06	23-May-06	26-May-06	28-May-06	8-Jun-06	11-Jun-06
	21-Jun-07	30-Jun-07					
Lobo	12-May-06	15-May-06	23-May-06	26-May-06	28-May-06	8-Jun-06	11-Jun-06
	21-Jun-07	30-Jun-07					
Ánsares	12-May-06	15-May-06	23-May-06	26-May-06	28-May-06	8-Jun-06	11-Jun-06
	8-Mar-08	20-Mar-08					
Small ponds South of Ánsares	16-Jan-08	2-Feb-08					
	1-Mar-08	8-Mar-08					
Vetalengua	31-May-06	8-Jun-06					
	21-Jun-07	30-Jun-07	19-Jul-07				
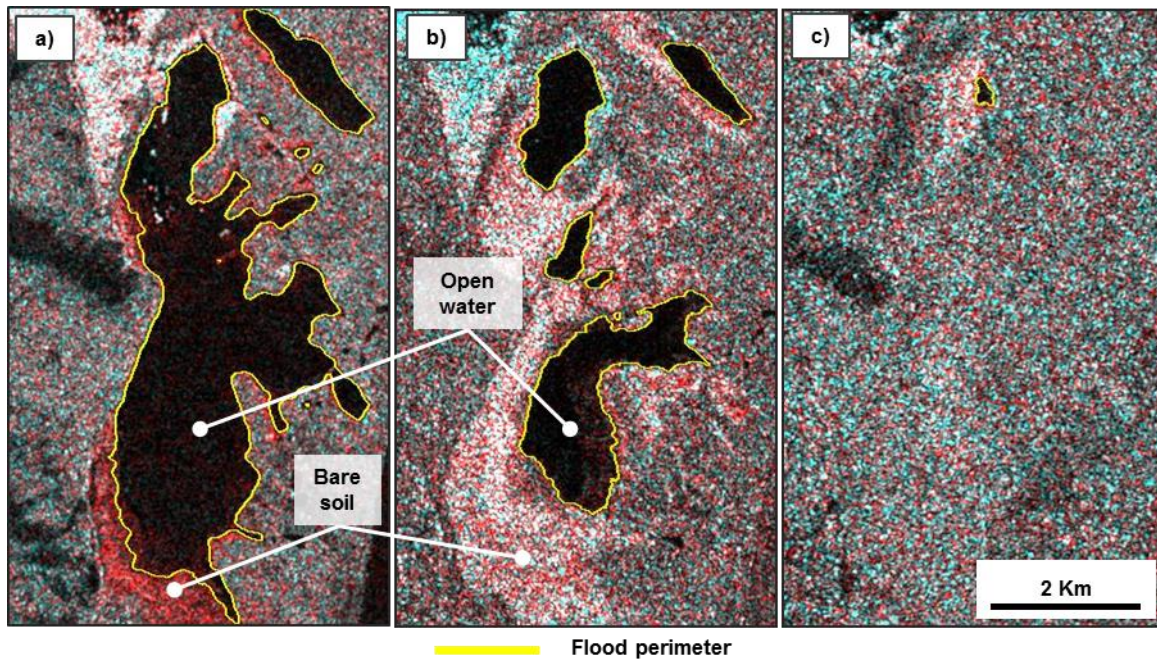
Fig. 10.18. Flooded area decrease in the isolated Membrillo pond as seen on three ASAR scenes acquired on: a) 20 June 2007at IS6, HH/VV, b) 30 June 2007 at IS2, HH/VV, c) 19 July 2007 at IS3, HH/VV. VV backscatter displayed in red and HH in cyan.
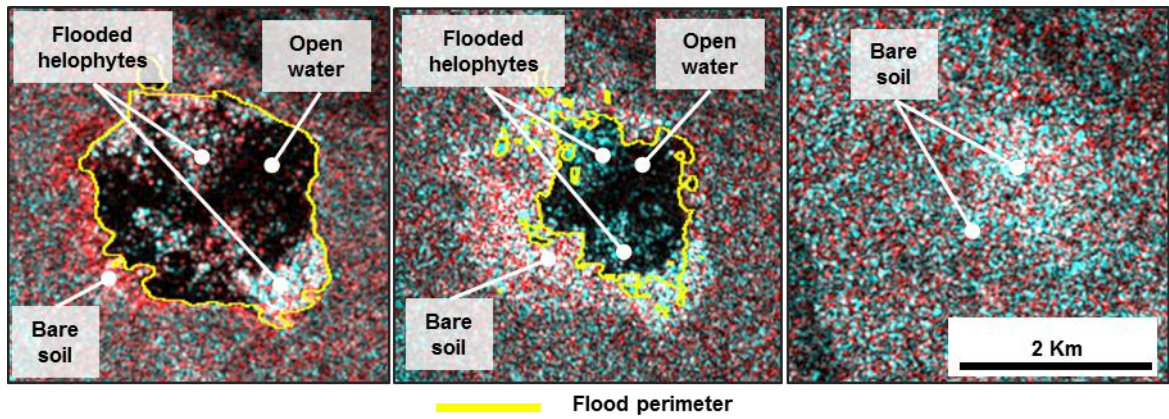
Fig. 10.19. Flooded area decrease in the isolated Mari López pond as seen on three ASAR scenes acquired on: a) 20 June 2007at IS6, HH/VV, b) 30 June 2007 at IS2, HH/VV, c) 19 July 2007 at IS3, HH/VV. VV backscatter displayed in red and HH in cyan.

10.6 Other Potential Applications of SAR Imagery to the Modeling and Monitoring of Doñana Marshes: Upcoming New SAR data

The ASAR sensitivity to the vegetation developmental stage and the soil moisture in Doñana has been highlighted in different occasions throughout this research. This section points at the potential applications of the mentioned sensitivity to surface water monitoring and conservation purposes. The exploration of these applications is, however, beyond the scope of the present research.

10.6.1 HELOPHYTE BIOMASS MAPPING

Fig. 10.20 illustrates the bayunco phenological evolution throughout the hydrologic year, as captured during on-site work. Bayunco and castañuela temporal signatures obtained in Chapter 7 for three control regions show a steep backscattering increase from the emergence of these plants and through their growth period (Fig. 7.9a and Fig. 7.9b), with overall increments in the order of 17 dB (Martí-Cardona et al., 2010). Fig. 10.21 shows the bayunco backscattering coefficient throughout the 2006-2007 hydrologic year at two incidence angles. The acquisition time of the photographs in Fig. 10.20 is also indicated.

The increment in the helophytes' backscattered power is directly related to the above water vegetation density and height (Grings et al., 2005; López-Sánchez et al., 2012;

Bouvet et al., 2009; Le Toan et al., 1997). Measurements of these vegetation parameters concurrent with ASAR acquisitions would allow relating the vegetation growth stage to the ASAR signal. Such relation would be of great value for mapping the distribution of the helophyte biomass.

The biomass increase observed in the backscattering signatures and in the photographs is not uniform in space at a given time. The development level of the plants depends on the inundation duration, which is spatially dependent on the terrain elevation. Interannual variability is also observed due to differences in pluviommetry and relative spatial changes in the species distribution. In addition to the mentioned pseudo-natural reasons, the most important factor for the uneven distribution of the helophyte biomass is the overgrazing by the cattle bred in Doñana. Fig. 10.22 illustrates the magnitude of this effect: the helophyte biomass in an area protected from grazing by a fence can be compared with the condition of the same vegetation outside the fence.

Mapping helophyte biomass from the ASAR images would enable the determination of spatially distributed hydrodynamic roughness coefficients associated to them. The same spatial information would be used as input data by two-dimensional evapotranspiration models, critical for understanding the water losses in the wetland. Furthermore, the biomass mapping would provide the national park's manager with a quantitative tool for the spatial monitoring of the cattle grazing impact over the autochthon vegetation.

September

December

February

March

Beginning of April

Mid April

May

June

Fig. 10.20. Bayunco phenological evolution throughout the hydrologic year, as observed during on-site work.
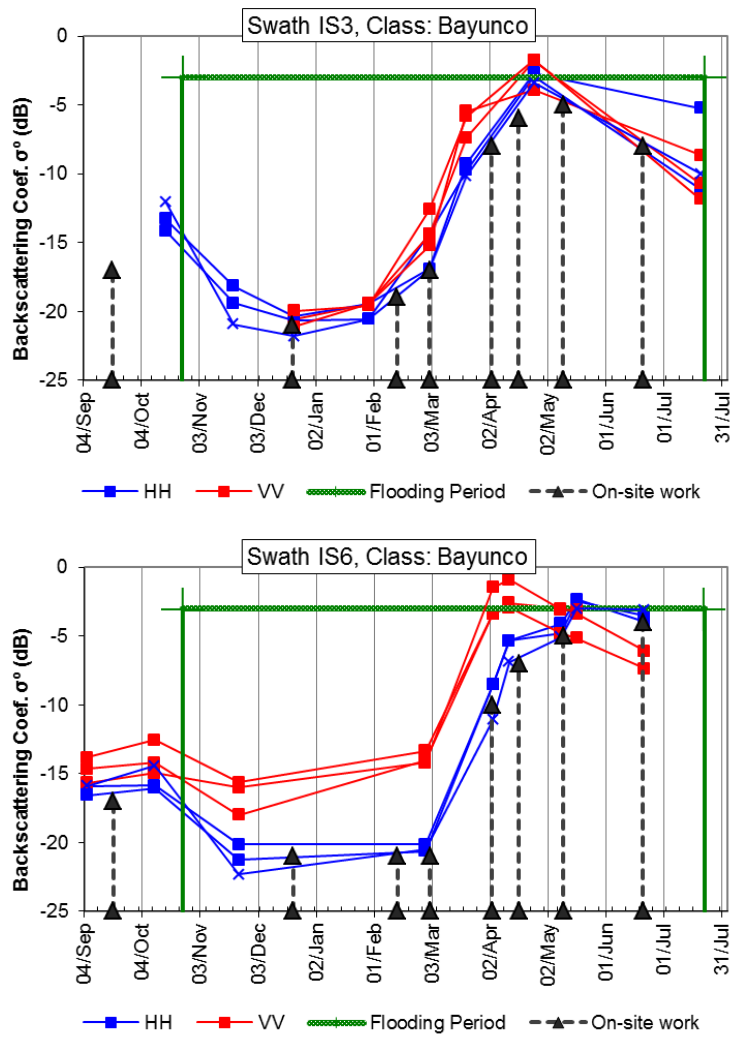
Fig. 10.21. HH and VV backscattering coefficient evolution in bayunco control regions during the 2006-2007 cycle at ASAR swaths IS3 and IS6. The black arrows indicate the acquisition dates for the photographs in Fig. 10.20.

Fig. 10.22. Grazing effect over the helophyte vegetation in the Marisma de Hinojos, near the Madre de las Marismas watercourse: castañuelar protected from grazing by a fence versus castañuelar leftovers after cattle grazing outside the fenced plot.

10.6.2 DISCRIMINATION OF VEGETATION COMMUNITIES

Some monitoring reports and on-site observations have pointed to the retreat of the bayuncar versus the castañuelar in the Doñana wetlands (Estación Biológica de Doñana, 2007). This regression might be exacerbated by the permeabilization of the Montaña del Río levee, which is currently being undertaken. Hence, mapping the spatial evolution of both emblematic vegetation communities becomes an important monitoring tool for the interest of conservation in Doñana.

The backscattering characteristics discussed in Chapter 7 and in Martí-Cardona (2010) show some differences between the bayunco and castañuela temporal signatures. Generally, these differences are too subtle to discriminate between both helophyte communities from a single ASAR acquisition, that is, without an entire image set and the corresponding temporal signatures. However, it has been observed that the ASAR data at large incidence angles, between IS4 and IS7, and in VV polarization capture the incipient emergence of helophyte stalks, towards the end of February and beginning of March. Steeper IS1 and IS2 swaths are blind to the same stalks. The location of these first detected helophytes closely resembles the spatial distribution of the bayunco communities according to Luque et al. (2005), as shown in Fig. 10.23. This spatial concordance could be explained by the fact that the bayunco emerges before the castañuela does and/or that its rigid, vertical stems of circular section yield a much stronger return in VV polarization than the catañuela leaves at this first developmental stage. If any of these hypotheses was confirmed, the SAR VV data acquired at large incidence angles at the beginning of March, would enable to map the bayunco presence and therefore to discriminate it from the castañuela.
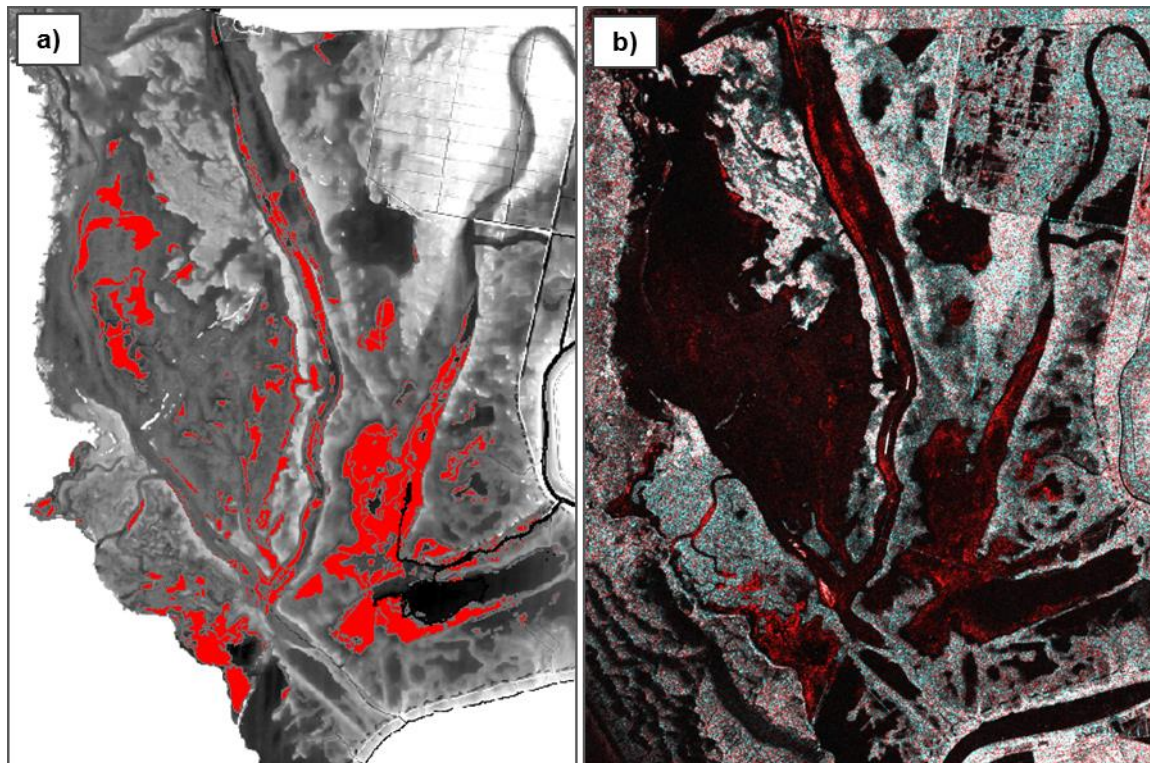
Fig. 10.23. Possible ASAR sensitivity to bayunco: a) Vegetation communities dominated by bayunco according to Luque et al. (2005) are highlitghted in red over the marshes DTM; b) ASAR image acquired on 27 Feb. 2007 at swath IS6 and HH/VV polarization. VV backscattering is displayed in red. The brightest areas in VV polarization resemble the spatial distribution of the bayuncar in a).

The Institut Flumen and the Remote Sensing Laboratory at the Universitat Politècnica de Catalunya have requested the acquisition of several image time series over Doñana from the following SAR sensors: the Japanese Space Agency's (JAXA) ALOS-2/PALSAR-2 operating at L-band, the Canadian Space Agency's (CSA) Radarsat-2 at C-band, and the future Spanish mission PAZ, which will use X-band radiation. All the acquisitions were requested in fully-polarimetric mode. The higher spatial resolution of these newer systems, under 10 m x 10 m, and the possibility to decompose the polarimetric data into the different backscattering mechanisms is expected to increase the capacity to discriminate and map different vegetation communities from the SAR images. In particular, the increase in spatial resolution might enable the detection of the invasive species *Spartina densiflora*, which grows in channels of tidal influence.

10.6.3 SOIL MOISTURE SENSITIVITY

The ASAR/Envisat data used in this study reveals the high sensitivity of the backscattered power to the soil moisture variations in Doñana. Fig. 7.6d and Fig. 7.9b4 depict the sharp backscattering coefficient increase from almajar and brown castañuela areas after the first rainfall events of the hydrologic year. Some areas recently affected by tidal floods were also distinguished by their high backscattering relative to dryer nearby areas of the same land cover type. The bright strip between the Montaña del Río and the Guadalquivir River in Fig. 10.16, close to the Figuerola watercourse sluice, reveals an area that had been inundated by tidal and maybe wind-induced flows, in virtue of its relatively greater wetness.

The high spatial resolution of the future PAZ sensor, able to acquire 1 m x 1m resolution data, in combination with the SAR sensitivity to soil moisture, might enable to spot and map the presence of groundwater surges in Doñana marshes, locally known as "ojos de la marisma" (Fig. 4.3 and Fig. 4.4).

10.7 Conclusions

Given the flatness of Doñana's topography, subtle changes in the water surface shape, such as the tilting induced by the wind drag action, can flood or emerge extensive areas observable on remote sensing images. Envisat/ASAR scenes acquired during persistent wind episodes have shown the displacement of several water bodies in the wind direction, corroborating the relevance of this action on the marshes hydrodynamics. These observations were used to compare and validate wind drag formulations in the marshes' two-dimensional hydrodynamic model.

The largest water displacements were observed in the Ánsares and Membrillo ponds, which are Doñana's flattest areas. The Ánsares terrain morphology, oriented in the direction of the clearly dominant winds, strongly suggests that the pond's shape is the result of the wind induced water motion. The fact that the Membrillo pond does not exhibit the same orientation could be explained by the presence of mobile sand dunes flanking the pond from the West.

ASAR images acquired before and after rainfall events provided synoptic observations of the precipitation effects over the inundation in Doñana. Rainfall hyetographs and concurrent flood extent observations constitute valuable calibration data for the two-dimensional hydrodynamic model of the marshes. The lack of input hydrographs records hindered the use of that data for hydrodynamic calibration purposes. Yet, estimations of those hydrographs are expected to be derived in the near future by means of a new distributed hydrologic model of the tributary basins (Caro and Bladé, 2012).

The spatial reach of the Guadalquivir river tidal inflows into Doñana is clearly observable on the ASAR scenes when the marshes are dry. This phenomenon was successfully reproduced by the hydraulic simulation model. Although the water volume exchange between the marshes and the river was negligible in terms of the wetland water balance during the completion of this research, the model's capacity to reliably simulate the tidal effect is of great interest in view of the planned partial demolition of the Montaña del Río.

Regarding the water depletion monitoring, the ASAR scenes enable estimations of volume losses between image acquisitions for the ungauged sub-basins. Furthermore, they allow measuring the flooded areas with emerging vegetation, what is needed for the study and spatial modeling of the evapotranspiration losses.

The temporal backscattering signatures derived in this study have shown great sensitivity of the ASAR data to the Doñana's helophyte vegetation developmental stage, pointing to the possibility to derive biomass maps from the ASAR images. These maps would supply temporal and spatially distributed roughness coefficients to the hydraulics model. On the other hand, the ASAR VV polarized data acquired at incidence angles between IS4 and IS7 towards the beginning of March seem to capture the presence of bayuncar, vegetation community reported to be in retreat. However, though seemingly feasible considering the presented findings, vegetation mapping from the ASAR data is beyond the scope of this research.

New SAR images of Doñana are to be acquired in the near future by the L-band system ALOS-2/PALSAR-2 from JAXA and the C-band sensor Radarsat-2 from CSA. Acquisitions are also expected from the ESA's new mission Sentinel-1, operating at C-band, and the future Spanish satellite PAZ, which will use X-band radiation. The enhanced technical capabilities of these systems will hopefully increase the current capacity for flood

mapping, vegetation communities' discrimination and invasive species detection in Doñana wetlands.

10.8 References

Aragonés, D., Díaz-Delgado, R., & Bustamante, J. (2005). Tratamiento de una serie temporal larga de imágenes Landsat para la cartografía de la inundación histórica de las marismas de Doñana. In M. Arbeló, A. González, & J. C. Pérez (Eds.), Teledetección. Avances en la Observación de la Tierra. Actas XI Congreso Nacional de Teledetección (pp. 407–410). Tenerife, Spain: Sociedad Española de Teledetección. Retrieved from http://www.ebd.csic.es/bustamante/publicaciones/Aragones_et_al_(2005)_XI_Congr eso_Teledeteccion_407-410.pdf

Bouvet, A., Le Toan, T., & Lam-Dao, N. (2009). Monitoring of the rice cropping system in the Mekong Delta using ENVISAT/ASAR dual polarization data. Geoscience and Remote Sensing, IEEE Transactions on, 47(2), 517-526.

Brownie, C., Kinder, C. A., Burkholder, J. M., Reed, R. E., & Dickey, D. A. (2008). Water level variations in the Neuse and Pamlico Estuaries, North Carolina due to local and remote forcing. Estuarine, Coastal and Shelf Science. doi:10.1016/j.ecss.2007.05.049

Caro Amargo, C. A., & Bladé Castellet, E. (2012). Modelo hidráulico – hidrológico contínuo basado en esquemas de volúmenes finitosleCaro Amargo, C. A., & Bladé Castellet, E. (2012). Modelo hidráulico – hidrológico contínuo basado en esquemas de volúmenes finitosle. In IAHR (Ed.), XXV Congreso Latinoameri. In IAHR (Ed.), XXV Congreso Latinoamericano de Hidráulica 2012 (pp. 1–10). San José de Costa Rica.

Clarke, A. J. & Brink K. H. (1985). The Response of Stratified, Frictional Flow of Shelf and Slope Waters to Fluctuating Large-Scale, Low-Frequency Wind Forcing. J. Phys. Oceanogr., 15, 439–453. doi: http://dx.doi.org/10.1175/1520-0485

Estación Biológica de Doñana, Equipo de Seguimiento de Procesos y Recursos Naturales (2007). Programa de Seguimiento de Procesos y Recursos Naturales en el Espacio Natural d eDoñana. Memoria Final: resultados del seguimiento en 2005-2006.

Ferrarin, C., Umgiesser, G., Scroccaro, I., & Matassi, G. (2009). Hydrodynamic modeling of the lagoons of Marano and Grado, Italy. GEOECOMARINA, 15, 13–20.

Geyer, W. R. (1977). Influence of Wind on Dynamics and Flushing of Shallow Estuaries. Estuarine, Coastal and Shelf Science 44, 713–722.

Grings, F., Ferrazzoli, P., Karszenbaum, H., Tiffenberg, J., Kandus, P. and Guerriero, L., 2005. Modeling Temporal Evolution Of Junco Marshes Radar Signatures, IEEE Transactions on Geoscience and Remote Sensing, 43, 2238–2245. Natural Doñana. Memoria Final: Resultados del Seguimiento en 2005-2006.

Hidy, G. M. & Plate, E. J. (1966). Wind action on water standing in a laboratory channel. Journal of Fluid Mechanics, 26, 04, pp 651-687. Doi: http://dx.doi.org/10.1017/S0022112066001460

Le Toan, T., Ribbes, F., Wang, L. F., Floury, N., Ding, K. H., Kong, J. A., ... & Kurosu, T. (1997). Rice crop mapping and monitoring using ERS-1 data based on experiment and modeling results. Geoscience and Remote Sensing, IEEE Transactions on, 35(1), 41-56.

López-Sánchez, J. M., Cloude, S. R. & Ballester J. D. (2012). Rice Phenology Monitoring by Means of SAR Polarimetry at X-Band. IEEE Trans. on Geoscience and Remote Sensing, Vol. 50, No. 7, pp. 2695-2709. doi:10.1109/TGRS.2011.2176740.

Luque, C. J., Rubio-Casal, A. E., Álvarez, A. A., Muñoz, J., Vecino, I., Doblas, D., ... Figueroa, E. (2005). Memoria de Vegetación: Parque Nacional de Doñana. Proyecto de Cartografía y Evaluación de la Flora y Vegetación Halófita y de los Ecosistemas de Marismas que se encuentren dentro de la Red de Espacios Naturales Protegidos de Andalucía.

Magill, K. ., & Kjerfve, B. (1989). Geographic and hydrodynamic characteristics of shallow coastal lagoons. Marine Geology. doi:10.1016/0025-3227(89)90097-2

Martí-Cardona, B, López-Martínez, C., & Dolz-Ripollés, J. (2012). Local texture stationarity indicator for filtering Doñana wetlands SAR images. Geoscience and Remote Sensing Symposium (IGARSS), 2012 IEEE International. doi:10.1109/IGARSS.2012.6352513

Martí-Cardona, B, Tran, T. D., Bladé-Castellet, E., Dolz-Ripollés, J., Neale, C. M. U., & Cosh, M. H. (2012). {ASAR/ENVISAT} images for the calibration of the wind hydrodynamic effect on Donana wetlands. Remote Sensing and Hydrology, 352, 459–463.

Martí-Cardona, B., & Dolz, J. (2005). Teledetección de la lámina de agua en la marisma de Doñana. Estudio comparativo de sensores. Flumen Internal Report.

Martí-Cardona, B., Dolz-Ripollés, J., & Gili-Ripoll, J. (2006). Monitoring of the Flooding and Dry-Out Processes in Doñana National Park for the Calibration of the Hydrodynamic Model of its Marshes. In Proceedings of the 1st GlobWetland Symposium: Looking at Wetlands from Space. European Space Agency and Ramsar Convention.

Martí-Cardona, B., López-Martínez, C., & Dolz-Ripollés, J. (2009a). Analysis of ASAR/Envisat Polarimetric Backscattering Characteristics of Doñana National Park Wetlands. In Proceedings of the 2009 IEEE International Geoscience and Remote Sensing Symposium. IGARSS'09.

Martí-Cardona, B., López-Martínez, C., & Dolz-Ripollés, J. (2009b). Efecto de la Inundación sobre el Coeficiente de Retrodispersión de las Marismas de Doñana en Distintos Swaths y Polarizaciones de ASAR/Envisat. Asociación Española de Teledetección.

Martí-Cardona, B., Dolz-Ripollés, J., & López-Martínez, C. (2013). Wetland inundation monitoring by the synergistic use of ENVISAT/ASAR imagery and ancilliary spatial data. Remote Sensing of Environment, 139, 171–184. doi:10.1016/j.rse.2013.07.028

Martí-Cardona, B., López-Martínez, C., Dolz-Ripollés, J., & Bladé-Castellet, E. (2010). ASAR polarimetric, multi-incidence angle and multitemporal characterization of Doñana wetlands for flood extent monitoring. Remote Sensing of Environment, 114(11), 2802–2815. doi:10.1016/j.rse.2010.06.015

Pasternack, G. B., & Hinnov, L. A. (2003). Hydrometeorological controls on water level in a vegetated Chesapeake Bay tidal freshwater delta. Estuarine, Coastal and Shelf Science. doi:10.1016/S0272-7714(03)00106-9

Plate, E. J. & Goodwin, C. R. (1965). "The Influence of Wind on Open Channel Flow," Coastal Eng., Santa Barbara Specialty Conference (ASCE), Chapter 17, October 1965.

Ramos Fuertes, A. (2012). Hidrometeorología y balance térmico de la marisma de Doñana. PhD dissertation. Universitat Politècnica de Catalunya. Retrieved from http://www.tdx.cat/handle/10803/110548

Ramos Fuertes, A., Martí-Cardona, B., Bladé Castellet, E., & Dolz, J. (2013). Envisat/ASAR images for the calibration of the wind drag action in Doñana wetlands 2D hydrodynamic model. Under review. Remote Sensing.

Robredo Sánchez, J. C., & Mintegui Aguirre, J. A. (2010). Proyecto de ampliación seguimiento y actualización del modelo sedimentario de la marisma del Parque Nacional de Doñana-Memoria Final. No Title (p. 223). Madrid (Spain).

Robredo Sánchez, J. C., Mintegui Aguirre, J. A., & Elorrieta Jove, J. (2007). Estudio del comportamiento de la solera en los lucios y caños de la marisma del Parque Nacional de Doñana en relación con los procesos de llenado y vaciado de la misma, a través demediciones en el campo en el periodo 1995-2006. Ecología, 21, 11–42.

Van Dorn, W.G. (1953). Wind stress on an artificial pond. Journal of Marine Research, 12, 249-276.

Wu, J. (1977). A note on the slope of a density interface between two stably stratified fluids under wind. Journal of Fluid Mechanics, 81, 02, pp 335 – 339. Doi: http://dx.doi.org/10.1017/S0022112077002079

Chapter 11:
Conclusions

The starting point of this research was the exploration of the remote sensing techniques as a tool for the regional and periodic monitoring of the Doñana marshes flood extent. An assessment of the available satellite sensors (Martí-Cardona and Dolz, 2005) pointed to the ASAR/Envisat instrument as the most appropriate sensor for the detailed monitoring of Doñana's filling period, in virtue of its all-weather imaging and pointable capabilities. A subsequent assessment of the ASAR's acquisition modes and polarization configurations advised the use of the AP mode and the HH/VV configuration (Martí-Cardona et al., 2006). All ASAR incidence angles were used in order to maximize the observation frequency.

More than 150 ASAR/Envisat images of Doñana were requested by the Flumen Institut and collected by the radar sensor from 2006 to 2010. The most detailed observation of the wetland filling up was achieved during the 2006-2007 hydrological year, which this study focuses on.

The analysis, processing and application of the ASAR scenes undertaken throughout this thesis underwent three clearly different stages:
- firstly, the backscattering from the main land cover types in Doñana was characterized;
- secondly, specific filtering and classification techniques were developed to achive flood mapping;
- finally, the derived products and observations were applied to the study of the marshes hydrodynamics and other potential conservationist applications were pointed out.

Contributions of this research can be identified for each of the abovementioned stages and are presented in separate sections as follows:

11.1 Backscattering Characterization

An initial assessment of the Envisat scenes showed that the ASAR backscattering enabled the discrimination among three main area types in Doñana, differing by their topographical and vegetation features: the paciles, the ponds' centers and the transition zones (Martí-Cardona 2006). Backscattering temporal signatures of those main cover types were obtained for the different incidence angles and polarizations (Martí-Cardona et al., 2009a; Martí-Cardona at al., 2009b; Martí-Cardona et al., 2010). The signatures were analyzed with the aid of miscellaneous site data in order to identify the effect of the flooding on the backscattering coefficient. Conclusions on the feasibility to discriminate emerged versus flooded land were drawn for the different incidence angles, land cover types and phenological stages, and are gathered as follows:

- Land cover type: bare soil, found at the center of ponds and watercourses.

Bare soil temporal signatures and scatter plots indicated that the flooding stages are separable at swaths IS3 and IS4. High amount of specular reflection can cause confusion between flooded and water-logged soil at large incidence angles. Confusion between open water and emerged land might also occur at steep incidence angles on windy days due to the increased backscattering from the roughened water surface.

- Land cover type: almajar, vegetation community dominated by the almajo shrub and found in the paciles.

Flooding in the almajar is clearly detectable at swaths IS2, IS3 and IS4, and presumably at IS1. The indicators of this class inundation are a significant backscattering decrease in both polarizations and a steep increase in the σ^0HH/σ^0VV ratio, as a result of a larger drop at VV than at HH. The smaller the incidence angle the higher the σ^0HH/σ^0VV value and therefore the distinction of flooded versus emerged pacil areas on a single image. At swaths IS6 and IS7 backscattering differences between flooded and emerged almajar are subtle. Hence, when water levels in the marshes are high enough to reach the pacil areas, a lower flood delineation accuracy is to be expected if IS6 or IS7 ASAR images are used for flood mapping.

- Land cover type: bayuncar and castañuelar, vegetation communitites dominated by the bayunco and castañuela helophytes and found in the transition zones.

Flooded brown castañuela can be discriminated at all incidence angles, except IS3, when the surrounding emerged regions are wet, because $\sigma^0 HH$ from the inundated areas is considerably lower than that from the emerged wet soil. There is no data for the same assertion about swath IS3. In the unlikely case of adjacent castañuela areas of flooded and emerged dry soil, the inundation may not be separable. Delineating inundation in brown bayunco areas is feasible at all swaths provided that HH data is available, since $\sigma^0 HH$ is always lower for flooded than for emerged brown bayunco.

In spring and summer images, backscattering from green flooded castañuela is substantially higher than that from the emerged plant at all swaths. However, certain confusion between emerged and low vegetated flooded areas can occur at IS2 and IS3. At IS6 and IS7 incidence angles the sustained increase in the HH/VV ratio at the end of the hydrologic year prevents the same confusion. Although no data on unflooded green bayunco ROIs is available, flood mapping is expected to be feasible at least at IS6 and IS7, because polarimetric effects enabling flood detection in the castañuela case are more accused in the bayunco areas.

Since the Doñana land covers require different observation swaths for flood detection, the composition of different incidence angle ASAR images close in time provided the optimum flood detection (Martí-Cardona et al., 2010). Such composition was possible four times per ASAR 35-day orbit cycle, using pairs of 12-hour apart IS1/IS6 and IS2/IS5 Doñana images.

11.2 *Filtering and Classification*

The delineation of the flooded areas on the ASAR images required filtering the scenes to smooth out pixel intensity fluctuations owing to speckle and texture within cover classes. Irregular filtering neighborhoods were defined at each pixel position so that they encompassed nearby connected pixels with similar terrain elevation, since natural edges closely follow terrain contours. The neiborhood stationarity was assessed by means of the intensity coefficient of variation. A new geometrical method, using the parameter named Ds (Martí-Cardona et al., 2012b), was proposed to assess the neighborhoods isotropy and discriminate high CVs caused by texture from those due to the presence of an edge. Isotropic neighborhoods were assumed of a single class and the pixel intensities within were averaged.

The use of irregular processing neighborhoods fitting the elevation contours drastically improved the ASAR image filtering (Martí-Cardona et al., 2013a; Martí-Cardona et al., 2013b). The edge preservation and smoothing degree attained by the DTM-guided filtering was significantly better than that obtained by applying common speckle filters with fixed-geometry processing windows, facilitating the subsequent clustering and classification tasks. It has to be stressed, however, that an accurate co-registration between the ASAR images and the DTM is critical for the quality of the DTM-based filtering results.

An analysis of the cover types backscattering in the σ^0HH-σ^0VV space revealed the large dispersion of the σ^0 values from flooded pond centers and flooded transition zones throughout the hydrologic year. On the other hand, significant overlapping among different covers' backscattering was found, substantiating the difficulty to discriminate among them just from the two single-acquisition ASAR channel data. It was concluded that a land cover classification based exclusively on the σ^0HH and σ^0VV values of single ASAR acquisitions would lead to significant confusion among cover types at several hydrologic stages and incidence angles.

Spatial data on Doñana's topography and vegetation was then used in order to complement the σ^0 data and reduce the confusion among classes. Clustering and classification algorithms were developed for the automated generation of flood maps from the ASAR images acquired by mid-April and previously filtered by the DTM-guided methodology (Martí-Cardona, 2013c). The algorithms operate on individual sub-basins, as the pixels elevation is more accurately related to cover classes within them. Vegetation and elevation maps plus knowledge of the Doñana backscattering characteristics were initially used to select seed pixels with high confidence on their class membership. Next, a region growing algorithm extends the seed regions with new pixels based on their planimmetric adjacency and backscattering Mahalanobis distance to the seeds. During the seed regions' growth, new pixels' possible classes are not constrained to their cover type according to the vegetation map, so the algorithm is able to capture changes in the vegetation spatial distribution.

Comparison of the resultant classification and concurrent ground truth yielded 92% of flood mapping accuracy over those marshland areas whose backscattering had been previously characterized, that is, over bare soil, bayuncar, castañuelar and almajar regions.

The accuracy is reduced at the northwestern part of the wetland, in areas C and D in Fig. 4.13. The vegetation communities found in these areas are short helophytes, herbaceous pasture and some foreign species associated to the near presence of El Rocío village. These vegetation types were not specifically characterized and considered by the classification algorithm.

A complete table of swath-dependent threshold values could not be defined for the automated selection of the transition zones seed regions at the end the flooding period, due to their complex backscattering casuistic. The thresholding was determined on an image basis, by defining regions of interest based on the water level records at the time of the image acquisition. Once the seeds had been determined, the clustering and classification algorithm previously developed for the marshes filling-up period was applied.

11.3 Applications of the ASAR Imagery to the Monitoring of the Doñana Wetlands

A final stage of this research focused on the selection of hydrologic events and concurrent ASAR observations with the aim to gain understanding on the Doñana marshes hydrodynamic processes and to obtain spatial data for modeling calibration purposes.

Envisat/ASAR scenes acquired during persistent wind episodes have shown the displacements of several water bodies in the wind direction, corroborating the relevance of this action on the marshes hydrodynamics. These observations were used to compare and validate different wind drag formulations on the marshes two-dimensional hydrodynamic model (Martí-Cardona et al., 2011; Martí-Cardona et al., 2012a; Ramos Fuertes et al., 2013).

The largest water displacements were observed in the Ánsares and Membrillo ponds, which are the flattest areas in the marshes. The Ánsares terrain morphology, oriented in the direction of the clearly dominant winds, strongly suggests that the pond's shape is the result of the wind induced water motion. In such a case, the pond's longitudinal slope, together with long-term wind records constitute a valuable insight into the sediment transport and deposition processes taking place in the Doñana marshes.

ASAR images acquired before and after rainfall events provided synoptic, spatial observations of the precipitation effects over the Doñana's inundation. Rainfall hyetographs registered in situ and simultaneous flood extent observations, contribute important calibration and validation data for the two-dimensional hydrodynamic model of the marshes. The lack of input hydrographs data hindered the use of the ASAR derived flood maps for hydrodynamic calibration purposes during the completion of this research. However, these input hydrographs can be estimated by means of a hydrologic model of the tributary basins.

The spatial reach of the Guadalquivir river tidal inflows into Doñana is clearly observable on the ASAR scenes when the marshes are dry. This phenomenon was successfully reproduced by the hydraulic simulation model. Although the water volume exchange between the marshes and the river was negligible in terms of the wetland water balance during the completion of this research, the model's capacity to reliably simulate the tidal effect is of great interest in view of the on-going partial demolition of the Montaña del Río.

It has been shown that the ASAR images can provide water loss estimates for ungauged sub-basins. Additionally, they enable the measurement of the flooded areas with emergent vegetation, needed for the study and modeling of the evapotranspiration losses.

Finally, this research work has identified some hydrologic and biophysical parameters of Doñana marshes that the C-band SAR data are sensitive to, and therefore constitute a potential data source. The temporal backscattering signatures have shown great sensitivity of the ASAR data to the Doñana's helophyte vegetation developmental stage, pointing to the possibility to derive biomass maps from the images. These maps would supply temporal and spatially distributed roughness coefficients to the hydraulics model.

Furthermore, the ASAR VV polarized data acquired at incidence angles between IS4 and IS7 at the beginning of March, seem to capture the presence of bayuncar, autochthon vegetation community reported to be in retreat (Estación Biológica de Doñana, 2007).

11.4 Future Developments

The work presented in this document initiated a new line of research on the explotaition of SAR satellite images for the biophysical data retrieval of the Doñana wetlands. A tool for flood mapping in all-weather, day and night conditions has been developed and its utility for hydrodynamic modeling has been substantiated. Other applications of the SAR imagery, which are of great interest for the management and conservation in Doñana, and hence, candidates for future developments of this research, were pinpointed in the previous section and are summarized as follows:

- Biomass mapping for the spatial assessment of overgrazing, evapotranpiration losses and distributed hydraulic roughness coefficients.
- Mapping of bayuncar vegetation communties;
- Spatial delineation of the tidal influence;

The Envisat satellite is no longer operative since April 2012. The ESA's Sentinel-1 mission, with its first satellite to be launch in spring 2014, will continue the C-band data acquisition over Europe. These research findings will still be applicable to the new Sentinel-1 data for the monitoring of Doñana marshes.

Furthermore, the Institut Flumen and the Remote Sensing Laboratory at the Universitat Politècnica de Catalunya have been granted the acquisition of long image time series over Doñana from the SAR sensors as follows:

- the Japanese Space Agency's (JAXA) ALOS-2/PALSAR-2, operating at L-band;
- the Canadian Space Agency's (CSA) Radarsat-2, at C-band;
- the future Spanish mission PAZ, which will use X-band radiation.

The acquisitions of these sensors over Doñana were requested in fully-polarimetric mode. The enhanced capabilities of all the abovementioned systems, in terms of their channel coherency, spatial resolution (lower than 10 m x 10 m) and revisit time, and the possibility to decompose the polarimetric signal into the different backscattering mechanisms' contribution is expected to increase to a great extent our current capacity for flood mapping and for the discrimination of vegetation communities in the Doñana wetlands.

These new SAR data will also offer the chance to assess the interferometric techniques for monitoring water level changes in Doñana. These techniques have been successfully applied to map centimeter-scale water level changes in other wetlands (Wdowinski et al., 2008; Hong et al., 2010; Gondwe et al., 2010; Wdowinski et al., 2013).

11.5 References

Estación Biológica de Doñana, Equipo de Seguimiento de Procesos y Recursos Naturales (2007). Programa de Seguimiento de Procesos y Recursos Naturales en el Espacio Natural d eDoñana. Memoria Final: resultados del seguimiento en 2005-2006.

Gondwe, B. R. N., Hong, S. H., Wdowinski, S., & Bauer-Gottwein, P. (2010). Hydrologic Dynamics of the Ground-Water-Dependent Sian Ka'an Wetlands, Mexico, Derived from InSAR and SAR Data. Wetlands, 30 (1), pp 1-13.

Hong, S. H., Wdowinski, S., Kim, S. W., & Won, J. S. (2010). Multi-temporal monitoring of wetland water levels in the Florida Everglades using interferometric synthetic aperture radar (InSAR). Remote Sensing of Environment, 114, (11), pp. 2436-2447, ISSN 0034-4257. Doi: 10.1016/j.rse.2010.05.019.

Martí-Cardona, B., & Dolz, J. (2005). Teledetección de la lámina de agua en la marisma de Doñana. Estudio comparativo de sensores. Flumen Internal Report.

Martí-Cardona, B., Dolz-Ripollés, J., & Gili-Ripoll, J. (2006). Monitoring of the Flooding and Dry-Out Processes in Doñana National Park for the Calibration of the Hydrodynamic Model of its Marshes. In Proceedings of the 1st GlobWetland Symposium: Looking at Wetlands from Space. European Space Agency and Ramsar Convention, 19-20 Oct. 2006, Frascati, Italy. ISBN: 92-9092-945-6.

Martí-Cardona, B., López-Martínez, C., & Dolz-Ripollés, J. (2009a). Analysis of ASAR/Envisat Polarimetric Backscattering Characteristics of Doñana National Park Wetlands. In Proceedings of the 2009 IEEE International Geoscience and Remote Sensing Symposium, IGARSS'09, 12-17 Jul, Cape Town, South Africa.

Martí-Cardona, B., López-Martínez, C., & Dolz-Ripollés, J. (2009b). Efecto de la Inundación sobre el Coeficiente de Retrodispersión de las Marismas de Doñana en Distintos Swaths y Polarizaciones de ASAR/Envisat. Asociación Española de Teledetección.

Martí-Cardona, Belen, López-Martínez, C., Dolz-Ripollés, J., & Bladé-Castellet, E. (2010). ASAR polarimetric, multi-incidence angle and multitemporal characterization of Doñana wetlands for flood extent monitoring. Remote Sensing of Environment, 114(11), 2802–2815. doi:10.1016/j.rse.2010.06.015.

Martí-Cardona, B., Ramos, A., Bladé, E., Duc Tran, T. & Dolz, J. (2011). "La teledetección como fuente de información para los modelos bidimensionales: aplicación al modelo Íber de las marismas de Doñana". In: JIA: Jornadas de Ingeniería del Agua: modelos numéricos en dinámica fluvial, Barcelona 5-6 Octubre 2011, pp. 1-8. Flumen (UPC). ISBN-13: 978-84-615-4023-5.

Martí-Cardona, B.; Duc Tran, T.; Bladé, E.; Dolz, J. (2012a). "ASAR/Envisat images for the calibration of the wind hydrodynamic effect on Doñana wetland", In: Remote Sensing and Hydrology 2010 Symposium, 27-30 September 2010, Jackson Hole, WY,. pp. 459 - 463. IAHS publication 352. ISSN 0144-7815. ISBN: 978-1-907161-27-8.

Martí-Cardona, B., López, C. & Dolz, J. (2012b). "Local texture stationarity indicator for filtering Doñana wetlands SAR images". In: IGARSS 2012: International Geoscience and Remote Sensing Symposium: remote science for a dynamic Earth: proceedings, 22-27 July 2012 Munich,. pp. 4903 - 4906. Institute of Electrical and Electronics Engineers (IEEE), 0007. ISBN 978-1-4673-1159-5.

Martí-Cardona, B., & Dolz, J. (2013a) "On the synergistic use of Envisat/ASAR imagery and ancillary spatial data for monitoring Doñana wetlands". In: ESA Living Planet Symposium 2013: proceedings, 9-13 September 2013, Edinburgh. European Space Agency (ESA): waiting for the corresponding proceedings publication.

Martí-Cardona, B., Dolz, J. & López-Martínez, C. (2013b). "Imágenes SAR para la cartografía de Doñana: beneficios del filtrado asistido por información espacial auxiliar". In: XV congreso de la Asociación Española de Teledetección: Sistemas operacionales de observación de la Tierra,. 22-24 Octubre, Torrejón de Ardoz. Instituto Nacinonal de Tecnología Aeroespacial (INTA): waiting for the publication of the proceedings.

Martí-Cardona, B., Dolz-Ripollés, J., & López-Martínez, C. (2013c). "Wetland inundation monitoring by the synergistic use of ENVISAT/ASAR imagery and ancilliary spatial data", Remote Sensing of Environment, 139(12), 171–184. Doi:10.1016/j.rse.2013.07.028.

Ramos-Fuertes, A., Martí-Cardona, B., Bladé, E., & Dolz, J., 2013. "Envisat/ASAR images for the calibration of the wind drag action in Doñana wetlands 2D hydrodynamic model", Remote Sensing, 6(1), 379-406. Doi:10.3390/rs6010379.

Wdowinski, S., Kim, S. W., Amelung, F., Dixon, T. H., Miralles-Wilhelm, F., & Sonenshein, R. (2008). Space-based detection of wetlands' surface water level changes from L-band SAR interferometry. Remote Sensing of Environment, 112 (3), pp.: 681-696, ISSN 0034-4257. Doi:10.1016/j.rse.2007.06.008.

Wdowinski, S., S.-H. Hong, A. Mulcan, and B. Brisco. 2013. Remote-sensing monitoring of tide propagation through coastal wetlands. Oceanography, 26(3), pp: 64–69. Doi: 10.5670/oceanog.2013.46.